UNIVERSITAT POLITÈCNICA DE CATALUNYA BARCELONATECH

Smart hybrid nanomaterials for biomimetic membranes

by

Maximilien Lopes Rodrigues

Smart hybrid nanomaterials for biomimetic membranes

Presented by

Maximilien Lopes Rodrigues

Supervised by

Prof. Carlos Alemán

Prof. Catherine Michaux

Thesis submitted to obtain the degree
Doctor of Philosophy in Polymers and Biopolymers
Universitat Politècnica de Catalunya

Barcelona, 2019

Department of Chemical Engineering

Innovation in Material and Molecular Engineering (IMEM)

Summary

The development of nanoscopic devices has pushed forward the possibilities in the fields of filtration, biosensing and nanofluidics. Combined with adapted materials such as biocompatible polymers, those innovative tools represent a promising technology for future biomedical applications.

The main topic of this thesis is the preparation of nanomaterials made of proteins and polymers. Even though the technology has advanced in the last decades to design new devices at the atomic scale, researchers are still inspired by what Nature has produced and optimized for millions of years. Following this concept, this work uses membrane proteins forming water-filled channels which regulate the flow of ions, nutrients and biomolecules in cells. They act as the gates of the membranes and determine if a molecule passes or not.

More specifically, the proteins involved in this project are the porins Omp2a and VDAC36. Omp2a is a 16-stranded β-barrel from the gram-negative bacterium *Brucella melitensis*. On the other hand, VDAC36 is a slightly larger barrel composed of 19 β-strands and located in mitochondria of *Solanum tuberosum*, a plant model. The following manuscript is divided in two main parts: 1) the thermomechanical study of proteins and polymers and 2) the development of a new hybrid nanomembrane.

The first part investigates the thermomechanical properties of the latest hybrid membrane developed by the IMEM group: an ultra-thin nanoperforated poly(lactic acid) (PLA) film loaded with Omp2a. For this purpose, a new equipment based on the microcantilever technology was employed: the SCAnning LAser analyzer (SCALA). SCALA analyses the surface of coated cantilevers by reflecting a laser beam on it. The sample (and the cantilever) placed in a thermocontrolled chamber is warmed up/cooled down with high precision. It allows following the cantilever bending induced by the compression/expansion of the sample coating (*i.e.* proteins or polymers in our case).

Using the aforementioned method, the intermolecular reorganization of Omp2a aggregates was evidenced as well as the protein secondary structure stability against temperature. The same method was employed to study the impact of nanofeatures on ultra-thin films of PLA. Nanopores, nanoperforations and nanodomains composed of organic drugs were added to the films. Those nanofeatures, by their size, abundance and location, affected the apparent glass transition and the cold crystallization temperatures. Those results suggest that the properties of future nanomaterials can be modulated by such treatments. Moreover, this work established a protocol for the study of biomolecules and polymers attached to microcantilevers, allowing an accurate analysis of the thermomechanical properties using very low amounts of sample.

The second part of the thesis is the development of a new hybrid nanomaterials composed of VDAC36, PLA and poly(3,4-ethylenedioxythiophene) (PEDOT). Contrary to Omp2a, no protocol was already established for VDAC36 production. For this purpose, the expression of the protein in bacteria and the subsequent purification by chromatography were optimized. Membrane proteins require a specific environment (*i.e.* amphiphilic) to retain their structure and activity. For this reason, a refolding step is necessary to recover its native form. The refolding was achieved using a protocol based on the combination of a detergent and a di-alcohol. The recovery of the secondary and tertiary structure was assessed by circular dichroism and intrinsic fluorescence, respectively. The formation of dimers and tetramers was then evidenced by cross-linking. Interestingly, the tetramers were degraded into dimers by a reducing agent, suggesting the involvement of an intermolecular disulphide bond. The protein was then reconstituted into lipid vesicles (*i.e.* liposomes) and the size of the channel was determined by swelling assay.

After that, the polymer material was prepared. The assembly of PLA and PEDOT nanofilms was achieved to take profit of the promising PEDOT electrochemical properties and the mechanical integrity and robustness of PLA. The PLA layers were prepared by spin-coating and nanoperforated by solvent etching. It allowed the PEDOT to grow by electropolymerization through the perforations and cover the entire surface of the PLA. The PEDOT layer was then covered by a new layer of nanoperforated PLA. The protein was finally immobilized on the surface by solvent evaporation. Fluorescence, FTIR and XPS evidenced its presence in the material and microscopy studies the correct superposition of each polymer layer. Electrochemical impedance spectroscopy was performed to thoroughly describe the electrical properties of the new 3-layered material. The addition of VDAC36 into the material induced a decrease in its electrical resistance and enhanced its supercapacitive properties. Moreover, the complete description of the electrical equivalent circuit demonstrated the ion diffusion process induced by addition of the protein.

Based on the previous results, a similar membrane was prepared using a mixture of EDOT and a modified EDOT monomer, containing an α-dodecyl chain instead of the ethylenedioxy group. The modification aimed to mimic the protein natural membrane made of lipids. Indeed, VDAC36, like all porins, has a high content of hydrophobic residues and may require a suitable matrix to maximize its activity. The mixture of both monomers could indeed successfully provide a higher content of retained proteins. An impedance study revealed again that the resistance was decreased and the supercapacitive properties enhanced after addition of the proteins. Finally, the biomaterial could detect biomolecules such as ATP and provide a response depending on the concentration of the electrolyte.

Acknowledgement

This thesis is the result of the work of many people and only words will not be enough to express how I am grateful to all of them.

I want to start to thank my supervisors who all had the patience to overview my work until the very end. Thank you Catherine Michaux for your daily support and all your investment during the entire thesis. No matter what happened, you continuously offered help and energy to move forward. Thank you Eric Perpète for sharing your scientific and life experiences and pushing me in the right direction. You hosted me in the best lab of the University of Namur since the master degree. You made me part of a solid group and I am very grateful for that. Thank you David Zanuy for all the help you offered me and for always being available. You provided me company, history lessons and showed me your strong vision of how Science should be. Thank you Carlos Alemàn for your leadership and very hard work. You always had a clear vision of the whole thesis and constantly could adapt to make it whole, designing new exciting projects and managing the entire laboratory without any flaw. Without you, my life would have been very different in many aspects and I am very grateful we could complete this thesis all together.

During those years, I had the chance to meet tons of people that marked my mind. Probably few of them will read those lines. A heartfelt "thank you" to all of them for just being present and make this chapter of my life a rich human experience.

Manu. this name resonates like a forgotten legend. Thank you for all the time spent together in the lab or anywhere else. You were definitely a pillar for me in Namur. Your wisdom, advises, nonsense talks, motivation to play cards really made my days. Thank you for being you. I wish every group had its own Manu.

In the CPB lab, I am grateful I had the chance to meet Guillaume, Thibaut, Raphael, Boris, Maes, Stéphanie, Anaïs, Amaury, Djora, Romain, Victor, Nicolas, Laurène, Lauriane, Delphine, Fabiola, Simon. Some of them contributed to this thesis by helping me a lot in the lab. I hope you keep good memories of the time spent there. Thank you to the members of the other labs in Namur for sharing good moments all together. Bench, Coco, Thomas, Junior, Arvind, Andrea, Simon *etc*. I also acknowledge the labs URBM and URBE for training me and sharing their equipment with us.

At the UPC, I had the chance to meet a lot of other students from all around the world. Thank you very much Anna, Brenda and Didac for your huge help and the funny moments we had in the lab. Ina and Hamidreza E. who form the amazing Best Team ever. Angelica, Guillem, Georgina, Hamidreza K., Reza, Amirmajid, Maryam, Jordi T., Jordi S., Guillem, Sonia, Maricruz, Neudys, Ludka, Lucas, Vitor, Ali and Omid, I will always keep the memories we have built as friends.

Thank you Nicolas and Alex, for our weekly meetings making those helmets flying! Thank you Pit, Guillaume, Maxime and the whole Maxi-foot team for all those memories.

Thank you Cinthia for showing me your determination, pushing me to the best version of myself and giving me motivation for all my actions.

Papa, maman et Nina, merci infiniment pour tout ce que vous avez toujours fait pour moi. Votre regard me donnera toujours la force de continuer.

Table of contents

List of figures

1. Introduction

2. Thermomechanical response of Omp2a

3. Effect of nanofeatures on the thermal transitions of PLA films

4. Structural and functional characterization of VDAC36

5. Biomimetic hybrid membranes made of PLA, PEDOT and VDAC36

6. Enhanced biomimetic membrane made of PLA, PEDOT-P3DT and VDAC36

List of tables

2. Thermomechanical response of Omp2a

4. Structural and functional characterization of VDAC36

5. Biomimetic hybrid membranes made of PLA, PEDOT and VDAC36

6. Enhanced biomimetic membrane made of PLA, PEDOT-P3DT and VDAC36

List of abbreviations

AFM	Atomic force microscopy
ATP	Adenosine triphosphate
BSA	Bovine serum albumin
CD	Circular dichroism
CP	Conducting polymer
CPB	Physical Chemistry of Biomolecules
DFDNB	1,5-difluoro-2,4-dinitrobenzene
DMA	dimethyl adipimidate
DMS	dimethyl suberimidate
DNA	Deoxyribonucleic acid
DOPC	1,2-dioleoyl-sn-glycero-3-phosphocholine
DLS	Dynamic light scattering
EIS	Electrochemical impedance spectroscopy
FTIR	Fourier-transform infrared spectroscopy
HFIP	Hexafluoroisopropanol
IMEM	Innovation Material and Molecular Engineering
IPTG	β-D-1-thiogalactopyranoside
LB	Lysogeny broth
LYS	Lysozyme
MPD	2-methyl-*2*,4-pentanediol
NADH	Nicotinamide adenine dinucleotide hydrogen
NM	Nanomembrane
OMP	Outer membrane protein
PBS	Phosphate-buffered saline
PCR	Polymerase Chain Reaction
PDB	Protein data bank

PEDOT	Poly(3,4-ethylenedioxythiophene)
PEG	Poly(ethyleneglycol)
PLA	Poly(lactic acid)
PNMPy	Poly(N-methyl-pyrrole)
PSD	Positive sensitive detector
PSS	Poly(styrene sulfonate)
PVA	Poly(vinyl alcohol)
SCALA	Scanning Laser Analyzer
SDS	Sodium dodecyl sulfate
SEM	Scanning electron microscopy
TEM	Transmission electron microscopy
TRP	Tryptophan
TYR	Tyrosine
VDAC	Voltage dependent anion channel
VMD	Visual Molecular Dynamics
WAXD	Wide angle X-ray diffraction
XPS	X-ray photoelectron spectroscopy

List of symbols

D_{eff}	Effective diameter
θ	Contact angle
$\lvert\Delta f\rvert/f$	Resonance frequency shift
ω	Resonance frequency
k	Spring rigidity
M	Effective mass
E	Young modulus
S	Displacement of the laser on the detector
Δz	Deflection of the cantilever
σ	Surface stress
T_g	Glass transition temperature
T_{cc}	Cold crystallization temperature
λ_{max}	Maximum absorption wavelength
D_{pore}	Diameter of the protein pore
R_S	Electrolyte resistance
R_p	Resistance of the film
CPE_{3L}	Capacitance of a 3-layered film
CPE_{st}	Capacitance of steel
W	Warburg impedance

1. Introduction

1. Introduction

1.1. Motivation of the research

The term nanotechnology was coined by Professor Taniguchi in 1974, defining the emerging field as “the processing of separation, consolidation and deformation of materials by one atom or one molecule” [1]. A broader conception of the now ubiquitous term refers to all components purposefully constructed at the nanoscale (*i.e.* one billionth of a meter) to fulfil a specific function. For systems at this scale, the manipulation of atoms and molecules is an intrinsic component of endeavours towards the dream of maximum accuracy. Implicit to this achievement is the equal necessity of precision while constructing the materials and the ingenuity to navigate around technological limitations such as instrument resolution. Nevertheless, scientists and engineers have developed numerous applications for a broad range of fields such as water purification, electronics, medicine, drug development or energy among many others [2–4].

Controlling the organization of molecules and atoms is far from an easy task. To circumvent this obstacle, researchers developed innovative methods to achieve their goal. Three different approaches to achieve the preparation of nanodevices are briefly described here (Figure 1.1). The first one, lithography, is a clever method to design the surface of a nanomaterial, especially in electronics [5]. Practically, a light or electron beam is directed towards a stencil that makes a pattern on the silicon surface. In that way, the irradiated atoms have a different reactivity which causes them to interact with other chemicals. Another method is to literally move or deposit the atom(s) on the surface of the material. Dip-pen patterning is achieved by using the very precise tip of an atomic force microscope (AFM) that can interact with one single atom or drop of solution [6]. Alternatively, self-assembling, in which a disordered system spontaneously turns into an organized structure, is commonly exploited to design nanostructure [7]. Taking advantage of the natural self-organization of matter, it permits a three-dimensional building compared to the above mentioned approaches. In a similar concept, taking directly profit of what the nature has built during millions of years can prove itself to be very efficient. Indeed, biomimetics stimulated the engineers and scientists during the last decades to design numerous technologies [8–10]. Planes, cars, trains, boats, adhesive surfaces, water filtration devices, ventilation systems are all technologies present in our daily life that were improved by learning from the nature. Biomimetics evolved from a simple imitation to an integration and combination of natural structures for the development of functional materials (Figure 1.2). The strategy consists in surveying the naturally occurring biological structures associated with the properties to be achieved by the new synthetic materials [11]. In all organisms, the proteins are present to ensure the vital functions.

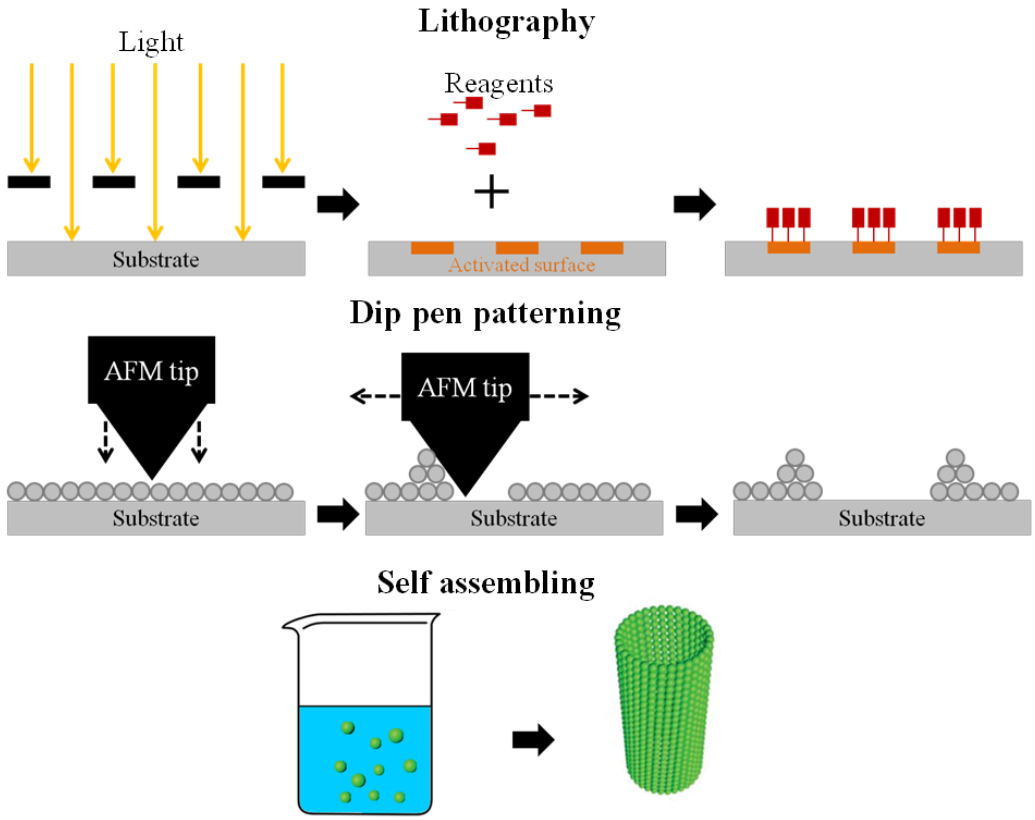

Figure 1.1: Schematic representation of three methods for designing nanomaterials. From top to bottom: Lithography, dip pen patterning and self-assembling.

In this framework, nanomaterials based on proteins offer countless potential nanosized devices such as nanoreactors [12], filtration devices [13], nanosensors [14], or drug delivery systems [15-16]. Many of these applications usually require channel shaped components which provide nanoscopic pathways for the passage of molecules. Appropriately, a family of proteins, called porins, can naturally form channels. They undoubtedly are serious candidates for the development of new applications and deserve particular attention from any learned person willing to develop nanodevices. The general purpose of the present thesis is to build new nanomaterials based on the integration of channel forming proteins.

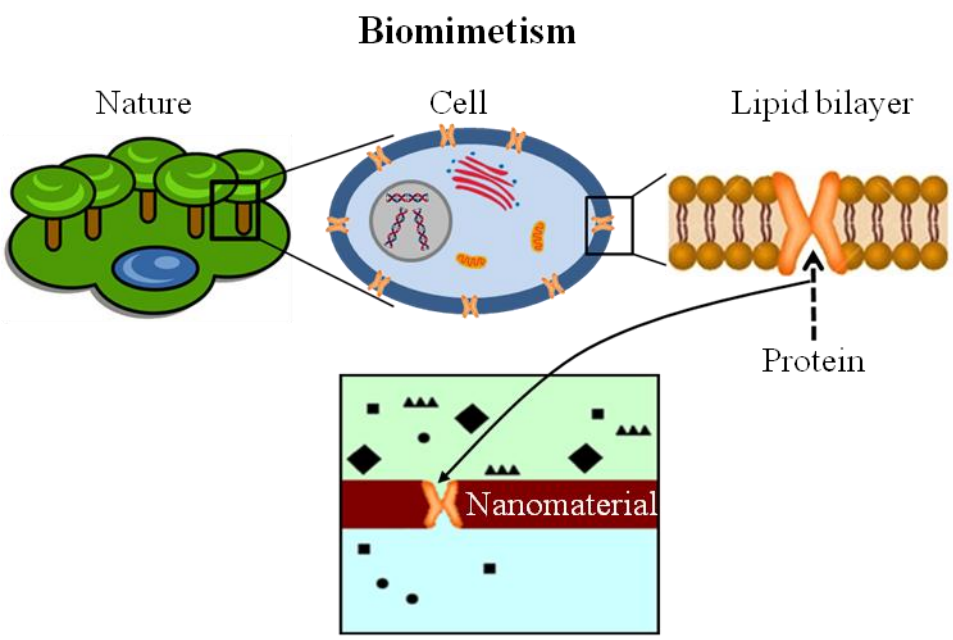

Figure 1.2: Schematic representation of biomimetics with the integration of biological elements (proteins) in synthetic nanomaterials.

1.2. Proteins, structure and function

Proteins are biological macromolecules synthesized by cells to ensure all functions of the organism. Each protein is composed of a specific combination of amino acids named primary structure and coded by a specific gene in the DNA. There are 20 natural amino-acids differing by their lateral chain. The length of proteins usually ranges from 100 to 1000 amino acids. This long chain folds itself into secondary structural elements such as α-helices or β-sheets (Figure 1.3). Those elements arrange themselves into a 3D tertiary structure, which exhibits specific features and shape ensuring the proper activity of the protein [17]. The process during which the protein acquires its correct tertiary structure is called (re)folding. Protein's structure is affected by the physicochemical conditions of the medium. If the latter fails to provide a suitable environment, the protein will lose its conformation and stay reversibly inactive. In some cases, multiples identical proteins gather to form an oligomer representing the quaternary structure. While the amino acids are covalently bonded, the tertiary structure is mainly stabilized by hydrogen bonds. Proteins have utility in a wide range of processes like structural purposes, performing and controlling chemical reactions or transporting ions and molecules [18]. Besides, proteins can be divided into two mains categories: soluble and membrane. The first category is composed of proteins soluble in water and, usually, they spontaneously adopt their active conformation. On the contrary, membrane proteins are not soluble in water. They are located in lipid bilayers that provide an amphiphilic environment that matches the hydrophobicity of the membrane protein.

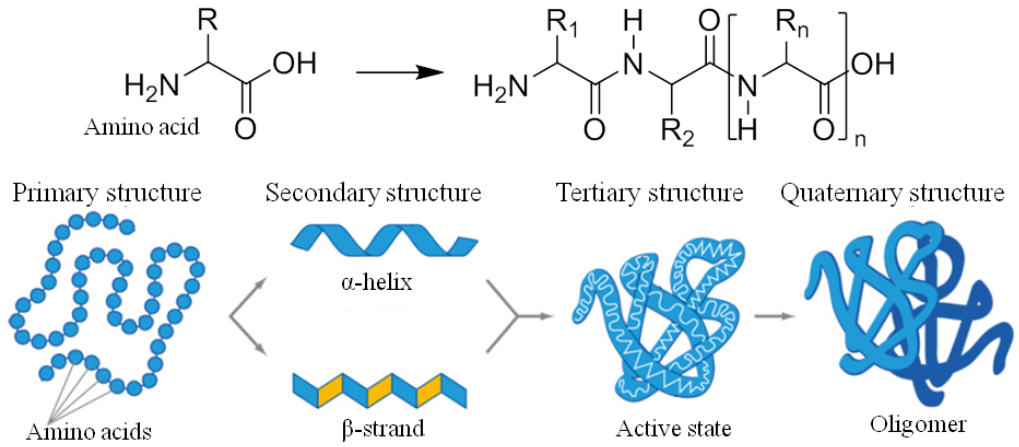

Figure 1.3: Structure of an amino acid and the peptide bond. Representation of the four levels of structures in proteins [17].

The function of transport is of particular interest in the design of nanoapplications. The type of transport in which this thesis is focused implies the move of molecules or ions across the biological membrane (lipid bilayer). The latter is impermeable to water or any hydrophilic molecule and protect the cell from its external environment [19]. To allow the passage of molecules from any side to the other, transport proteins are disseminated along the membrane. They act as the gates of the membrane and determine if a molecule passes or not. The solutes may be transported in two ways: actively and passively (Figure 1.4). The active way, performed by carrier proteins, is assimilated to a pump which transports the solutes from a low concentration to a high concentration environment. Because this is thermodynamically unfavourable, the process requires the use of energy, usually by ATP hydrolysis to modify the conformation of the protein. On the other hand, the passive transport does not use energy and solutes follow the concentration gradient. The proteins responsible of passive diffusion have a tertiary structure forming a channel [20]. Because of their location in the outer membrane of gram-negative bacteria or mitochondria, they are often referred as "outer membrane protein" (OMP). They generally adopt a barrel structure composed of anti-parallel β-strands, hence the name β-barrel (Figure 1.5) [21]. Some α-helices structure can also form channels, such as aquaporins [22].

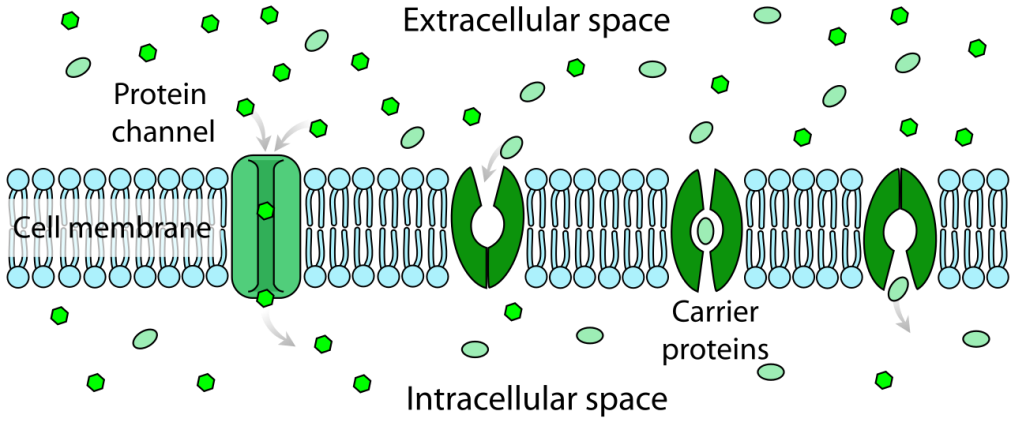

Figure 1.4: Representation of the lipid bilayer (membrane) of a cell with two types of transport proteins: channel proteins and carrier proteins respectively performing the passive and active modes of transport [19].

The smallest β-barrel contains 8 strands while the largest one has 24. The higher is the number of strands, the larger the diameter of the channel is. The outside facing part of the barrel is hydrophobic to match the alkyl chains of the lipids while the internal water-filled part contains charged and hydrophilic residues. The nature of the internal residues may determine the potential selectivity of the channel. The majority of the β-barrels does not present any particular substrate selectivity and allows the diffusion of various hydrophilic solutes like ions, sugars or amino acids to name a few. The size of the solute still limits the ability of the barrel to diffuse it. Generally, the diameter of the channel usually ranges from 10 to 40 Å and logically any molecule exceeding these dimensions is not able to pass. In addition, β-barrels exhibit exceptional robustness and stability over time and temperature [23]. Those features make them competitive for their insertion in non-biological synthetic environment such as polymers. Those particular proteins, called porins, are the biological material studied in the present Thesis for the development of new nanomaterials.

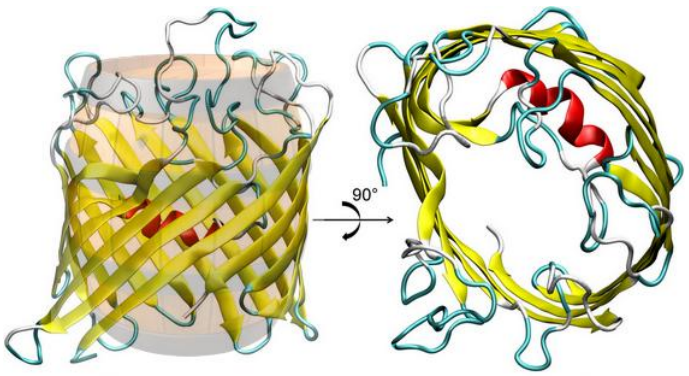

Figure 1.5: Cartoon representation of the protein Omp2a, a β-barrel protein. Secondary structure is displayed with the following colors: β-strands (yellow), α-helix (red), turns (cyan) and loops (white). The channel formed by the barrel is visible on the left picture [24].

1.3. Polymers

The particular amphiphilic environment that lipid bilayers provide is necessary for the membrane protein to retain its active form. Such requirement represents a challenge for the integration of β-barrels into a synthetic membrane. Hence, the latter should also provide amphiphilic conditions to retain the activity of the proteins. In this context, polymers appear as the obvious choice to provide a suitable matrix. Polymers are natural (DNA, cellulose, collagen...) or synthetic (plastics) macromolecules composed of numerous repeating structural units, the monomers, covalently bonded during the polymerization reaction. Polymers are mainly composed of carbon and hydrogen that constitute the main chain (backbone) but other elements such as oxygen, nitrogen, phosphorus or sulphur are also abundant. Inorganic polymers can have their backbone, for instance, made of silicon but they will not be discussed here.

Polymers can be composed of a unique repeating unit or can have two, three or more different species. In that case, they are named co-polymers and have different possible arrangements of subunits. The number of subunits is much larger than in proteins, with numbers rising up to 10^6 monomers. Monomers can assemble in a linear way to form long straight chains where each subunit reacts with the extremity. Branching can occur when the growth point is not only the last added subunit but also intermediate subunits. Moreover, distinct chains can connect with others to result in cross-linking. Branching and cross-linking can reduce the density of the material and therefore alter its rigidity, transparency, fluidity etc. Those parameters can be deliberately modified to obtain the properties wanted for the final product.

Another way to influence those properties is to control polymerization reactions. Doing so, the length of the chains can be adjusted as well as the stereochemistry of the polymer. The nature of the chemical groups present on the monomers generally leads the mechanism of reaction. Addition and condensation are the two main types of polymerization reaction. Addition requires the activation of a monomer containing a double carbon-carbon bond by a free-radical. The free-electron on the activated monomer is then propagated by opening the double bond of successive monomers, thus constructing the chain. Condensation on the other hand involves two different chemical groups (X-H and O-H) and the loss of a water molecule. Condensation needs higher temperature and longer time than addition and usually leads to shorter chains.

The nature of the chemical groups present on the monomers generally leads the mechanism of reaction. However one polymer can be produced by more than only one mechanism and the development of catalysts over the last decades increased the possibilities to influence the

mechanism. The choice of the monomer according to its hydrophilicity/hydrophobicity, molecular weight, reactivity is also important for the final applications [25]. In summary, polymers offer a wide range of assets such as great versatility, good resistance to chemicals, accessible preparation and good control of their morphology [26].

The large majority of polymers are electrical insulators. However, researchers evidenced that some particular polymers were electrical conductors. More precisely, conducting polymers (CPs) are considered as semiconductors as their conductivity still do not match metals. The electrical properties of CPs are essentially due to the organized distribution of π-bonds (Figure 1.6). Alternating single and double bonds (*i.e.* conjugation) allows the electrons to move across the entire polymer. Among the properties offered by CPs, electrical conductivity is of particularly interesting in the search of responsive nanodevices.

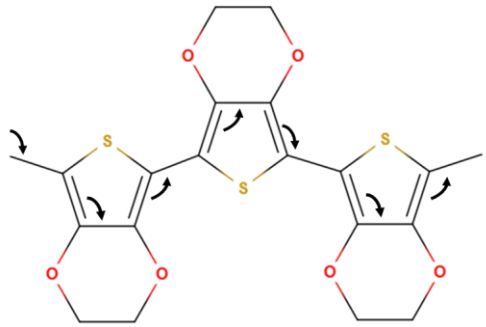

Figure 1.6: Structure of poly(3,4-ethylenedioxythiophene) (PEDOT), a conducting polymer and mechanism of conductivity by π-bonds conjugation.

1.4. State-of-the-art

Researchers have already considered polymers and channel proteins as important tools for nanotechnology. For instance, Balme *et al.* confined the protein Gramicidin-A in a polycarbonate nanoporous film with a thickness of 5 µm [27]. They demonstrated that the protein could be selectively confined inside the nanopores and with that the ionic conductance of the membrane was enhanced after integration of the channel. In another study, Güven *et al.* inserted FhuA, a large β-barrel of 22 strands, in a vesicle of poly(dimethyl siloxane) and poly(2-methyl-2-oxazoline) thereby achieving the control of the release of calcein, a fluorescent molecule [28]. They also engineered the protein by mutating key amino acids inside the channel, thus enhancing the release. FhuA, as a promising versatile channel, attracted other scientists who also modified the protein by extending its hydrophobic surface. They then inserted it in a membrane of poly(isobutylene) and poly(ethyleneglycol) for controlling drug release [29]. Using poly(dimethylsiloxane) and poly(2-methyl-2-oxazoline), Nardin *et al.* functionalized self-assembled copolymer vesicles by

reconstituting the channel protein OmpF, a 16-stranded β-barrel. The protein acted as a size-selective filter preventing the transport of molecules larger than 400 g/mol [30]. Similar vesicles were used for the insertion of Tsx, a channel of 12 β-strands specifically diffusing nucleotides [31]. In a different perspective, the eight stranded β-barrel aponitrobindin was used as a catalyst for the phenylacetylene polymerization [32]. The inner part of the channel contained a rhodium complex which usually yields the *trans*- isomer of the polymer. After its insertion into the protein, the *cis*-isomer was produced, proving the development of a stereoselective catalyst. In bioelectronics, Gramicidin-A was employed to achieve ionic to electronic signal transduction [33]. The protein was loaded on an electrical chip embedded in poly(dimethylsiloxane) to create ion-sensitives nanodevices.

Inspired by those promising works, the laboratories Innovation Material and Molecular Engineering (IMEM) from the Polytechnic University of Catalonia (Barcelona, Spain) and Physical Chemistry of Biomolecules from the University of Namur (Belgium) joined their expertise to develop new hybrid polymeric nanomaterials containing channel proteins. Two projects were achieved during this collaboration by using Omp2a, a β-barrel protein. The Omp2a protein is found in the bacterium *Brucella melitensis* and is composed of 16 β-strands with a channel diameter of 0.74 nm. Omp2a is considered as a general porin, meaning it has no definite selectivity. Nevertheless, an interesting behaviour was observed while the protein was embedded in the polymer films.

The first film was made of poly(N-methyl-pyrrole) (PNMPy), a conjugated conducting, biodegradable and biocompatible polymer [34]. It was previously used in biomedical and biotechnological applications (Figure 1.7) [35]. The porin Omp2a was added in the polymerization medium for its integration on a steel-supported PNMPy film with a thickness around 300 nm. The insertion of Omp2a promoted the exchange of ions between the support and the electrolyte solution. Electrochemical impedance spectroscopy analysis showed that the conductivity of the bionanomaterial was dependent of the ion concentration. This dependence was not observed in absence of protein. The results demonstrated that the resistance of the polymer film was reduced by 40%, due to the protein ability to diffuse ions. Interestingly, it was observed that Omp2a favoured the passive diffusion of Na^+ over K^+. The biofilm behaved as a smart ion-channel with potential for applications in biosensing. The major limitation of the PNMP-Omp2a film was its requirement to be supported on another material (steel in that case) for the electropolymerization of the polymer. To design innovative new applications, especially in biomedical fields, the development of free-standing materials may be crucial.

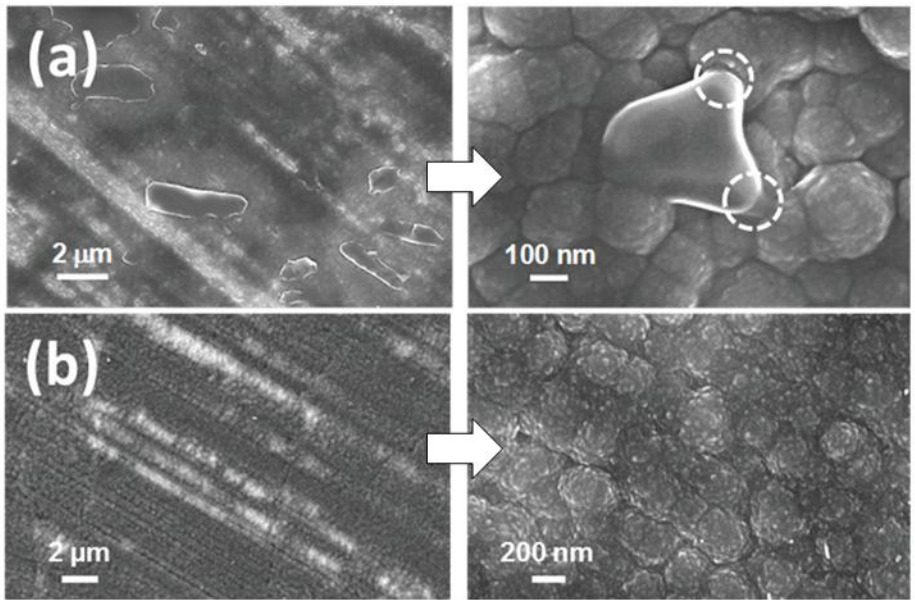

Figure 1.7: Surface characterization by SEM of a film of poly(N-methyl-pyrrole) (PNMPy). (a) PNMPy after integration of Omp2a, a channel protein, into the film and (b) PNMPy alone. The SEM pictures show the presence of the protein phase and the connection with the polymer phase is indicated by the dashed circles [34].

Another bionanomaterial based on Omp2a was prepared by using poly(lactic acid) (PLA) [36]. This insulating polymer can be produced from renewable biomass and is biodegradable and biocompatible. Unlike PNMPy, PLA films do not require a rigid support and can feature size-controlled nanoperforations (Figure 1.8). Self-supported PLA nanomembranes were prepared by spin-coating a mixture of PLA and poly(vinyl alcohol) (PVA). By selective solvent etching, the PVA domains were dissolved causing the formation of the nanoperforations. The films obtained had a thickness around 100 nm. The proteins were then loaded into the nanopores which increased the ion transport activity. The resistance of the nanomaterial was reduced by 60% with the presence of Omp2a. Besides, the diffusion of Na^+ was preferred over K^+ as measured in the PNMPy-Omp2a film. Those previous works motivated us to pursue the design of hybrid nanomaterials combining channel proteins and polymer films.

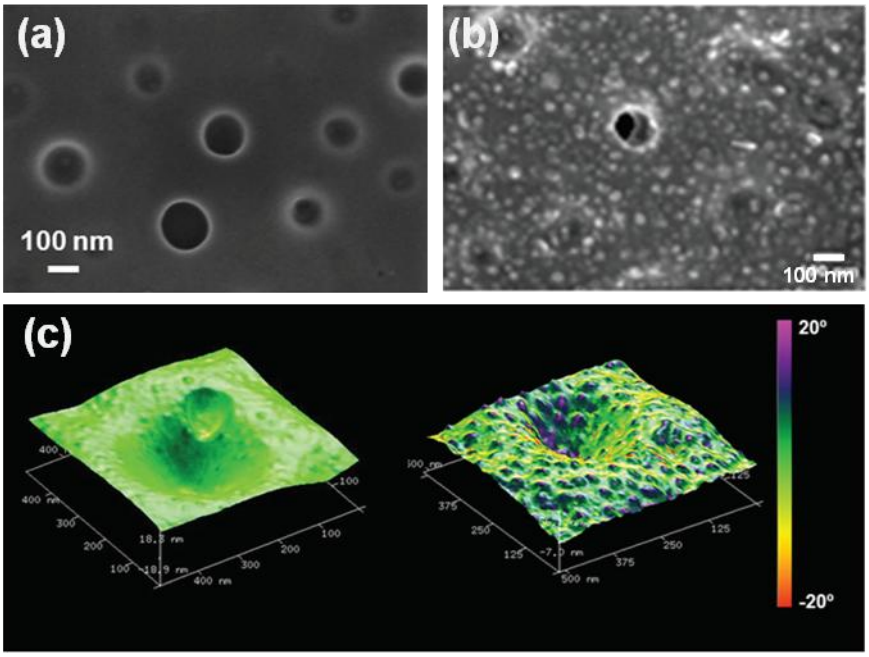

Figure 1.8: Surface characterization by of a free-standing film made of poly(lactic acid) (PLA). (a) Nanoperforated PLA film. (b) Nanoperforated PLA film after integration of the channel protein Omp2a. (c) 3D AFM images of the nanoperforated film before (left) and after Omp2a integration (right) [36].

1.5. Objectives

The present thesis hypothesizes that the combination of rationally selected polymers with β-barrel proteins could lead to the development of bionanosensors. The electrical response of such nanodevices would depend on the solutes crossing the protein channel towards the responsive polymer.

The main objective is to prepare a new nanomaterial including the protein VDAC36, a porin that forms a water-filled channel and presents a voltage-gating ability. The polymers retained as the material's support are a well-known conducting polymer, PEDOT, and PLA. PEDOT provides the electrical conductivity necessary for accurate sensing while PLA offers the robustness needed for a stable free-standing material. By combining the assets of the three components, the project aims at developing an innovative responsive nanobiosensor.

A side objective of this thesis is to understand better the features of the latest hybrid nanomaterial designed by the IMEM group. More specifically, it involves the study of the thermomechanical properties of the Omp2a porin and nanomodified poly(lactic acid) (PLA) films by using an innovative microcantilever technology.

To achieve the first objective, the next steps were followed:

- Produce and purify the VDAC36 protein
- Refold the VDAC36 using the sodium dodecyl sulfate (SDS) - 2-methyl-*2*,4-pentanediol (MPD) method
- Characterize VDAC36 and determine its pore size
- Optimize the assembling of PEDOT and PLA
- Insert VDAC36 into the polymer film
- Characterize the film and verify the insertion of the protein
- Study the electrical properties of the hybrid material by electrochemical impedance spectroscopy

Likewise, to accomplish the second objective the next steps were followed:

- Produce and purify the Omp2a protein
- Refold the Omp2a using the SDS-MPD method
- Study the effect of temperature on Omp2a using standard spectroscopic techniques
- Develop and optimize the fixation of Omp2a and PLA on microcantilevers
- Analyze the thermomechanical properties of Omp2a and PLA with the Scanning Laser Analyzer (SCALA)

1.6. Methodology

The present work involves the utilization of polymers and channel proteins and their combination for the preparation of hybrid nanofilms with enhanced ion transport activity. As a result of their structural relevance for the design of nanomaterials, the transport proteins Omp2a and VDAC proteins were selected.

Omp2a is located in the gram-negative bacterium *Brucella* responsible of the Brucellosis, a zoonotic infection affecting mammals [37]. The protein is composed of 367 amino acids for a total molecular weight of 39 kDa and it assembles into a trimer. Previous functional studies revealed the transport function of the protein and further topology prediction showed its β-barrel structure [38]. The barrel is made of 16 antiparallel β-strands separated by short turns on the intracellular side and longs loops on the extracellular side. The third loop, the longest, folds inside the barrel to form an α-helix constricting the channel. The minimum diameter of the inner channel of 0.74 nm allows molecules such as sugar (*e.g.* maltotetraose) to pass through the pore [39]. The model we have developed shows that the loops carry an excess of negative charges while the inner part of the channel is mainly positively charged [24]. Moreover, two pathways have been identified for the ions transport. This supports the preferential diffusion of some ions observed after integration of Omp2a into poly(pyrrole) and poly(lactic acid) nanomembranes [34-36].

VDAC36, for voltage-dependent anion channel, is a plant pore-forming protein found in the outer mitochondrial membrane of *Solanum tuberosum* [40]. It contains 277 amino acids for a total weight of 30 kDa. The function of VDAC proteins is associated with the permeability of the mitochondria. Specifically, they regulate the diffusion of ions and metabolites such as nicotinamide adenine dinucleotide hydrogen (NADH) or adenosine triphosphate (ATP). VDAC proteins adopt a β-barrel structure composed of 19 antiparallel β-strands. This conformation forms an inner channel restricted by an α-helix at the N-terminal extremity that folds into the pore [41]. The strands are separated by short turns on both sides of the protein, making the pore more accessible than the one of Omp2a. The diameter of the channel is about 2.0 nm allowing large molecules to pass through it [42]. Interestingly, VDAC proteins have a gating ability. Depending the electric potential, the inner α-helix undergoes conformational changes and the channel can switch from an open to a closed-state or vice-versa [43]. This feature is very promising for the development of smart bionanomaterials with controlled diffusion.

Regarding the matrix containing the channel proteins, PLA was chosen for its ability to be stable and free-standing as demonstrated in the previous works. Moreover, it is possible to obtain size-

controlled nanoperforations across the film and to select its thickness and shape [44]. Another polymer, PEDOT, was also considered for this study. It is a CP with supercapacitive properties promising for the development of sensors with tuneable electric response [45]. Both PLA and PEDOT are non-cytotoxic and their synergetic combination could lead to electroactive free-standing nanomaterials with potential biomedical applications.

The methodology followed to complete the study was divided into three tasks described below.

Task 1: Protein production

In order to perform the numerous analyses along this project, an appropriate quantity of protein is needed. When it comes to the production of transport proteins, as with all membrane proteins, the process is considered as challenging [46]. Indeed, their over-expression in bacteria often results in the formation of biologically inactive aggregates called inclusion bodies, which are incompetent elements for any meaningful structural or functional study [47]. Still, the over-expression in inclusion bodies can present several advantages compared to classical expression. First, it is less stressful for host bacteria and the produced proteins are less prone to degradation and high expression levels can be reached [48]. For those reasons, the selected proteins are produced in *E. coli* bacteria in inclusion bodies.

Task 2: Purification and refolding of the protein

The produced proteins are obtained in an inactive (*i.e.* unfolded) and impure form. They were therefore purified by fast protein liquid chromatography. The aforementioned requirement of membrane proteins to be surrounded by an amphiphilic medium to remain active makes their refolding difficult. Nevertheless, the CPB group for the University of Namur has demonstrated the reliability of an original protein refolding procedure, based on the synergistic association of the SDS anionic detergent with a diol-type organic cosolvent, the MPD [49-50]. This method has been extensively applied to various proteins such as β-barrel structures. The protocol simplicity and low economic costs make it a serious asset for the acquisition of active channel proteins. To characterize the proteins, diverse techniques are employed such as circular dichroism (CD), fluorescence, UV-vis absorbance to name a few. Functionality tests and oligomer formation studies are carried in order to understand better the channel properties and its tendency to aggregate.

Task 3: Polymers preparation and protein integration

The crucial step of this work is to prepare a suitable nanofilm that welcomes the active channel protein. PLA has proved itself to be able to host the protein but lacks the electroactivity that PEDOT provides. Stacking layers of PLA and PEDOT seems to be a smart option to combine the features of the two polymers. PLA nanomembranes are prepared by spin-coating a mixture of PLA and PVA. By selective solvent etching, the PVA is dissolved causing the formation of nanoperforations ready to receive the proteins. PEDOT is directly polymerized onto the underlying PLA layer. The process is repeated to create the final film. Then, the protein is immobilized in the PLA nanoperforations by deposition and solvent evaporation. The hybrid nanofilms are then characterized by an array of techniques (including electron and atomic force microscopies (SEM and AFM)) to assess their morphology at the nanoscale. The insertion of the protein is verified by X-ray photoelectron spectroscopy (XPS) and FTIR spectroscopy. Electrochemical impedance spectroscopy (EIS) is finally employed to study the response of the material with different solutes.

1.7. Bibliography

[1] A. Sandhu, "Who invented nano?," *Nat. Nanotechnol.*, 1, 2, 87–87, 2006.

[2] S. A. Edwards, *The nanotech pioneers : where are they taking us?* Wiley-VCH, 2006.

[3] J. Jeevanandam, A. Barhoum, Y. S. Chan, A. Dufresne, and M. K. Danquah, "Review on nanoparticles and nanostructured materials: history, sources, toxicity and regulations," *Beilstein J. Nanotechnol.*, 9, 1, 1050–1074, 2018.

[4] V. Prakash Sharma, U. Sharma, M. Chattopadhyay, and V. N. Shukla, "Advance Applications of Nanomaterials: A Review," *Mater. Today Proc.*, 5, 2, 6376–6380, 2018.

[5] J. E. E. Baglin, "Ion beam nanoscale fabrication and lithography—A review," *Appl. Surf. Sci.*, 258, 9, 4103–4111, 2012.

[6] Y.-S. Choi, X. Wu, and D.-W. Lee, "Selective nano-patterning of graphene using a heated atomic force microscope tip," *Rev. Sci. Instrum.*, 85, 4, 045002, 2014.

[7] H. Wang, L. Li, H.-W. An, B. Peng, and R. Zheng, "Self-Assembled Nanomaterials: Design Principle, Nanostructural Effect, Functional Mechanism as Antimicrobial or Detection Agent," *Mater. Horizons*, 2019.

[8] C. Sanchez, H. Arribart, and M. M. Giraud Guille, "Biomimetism and bioinspiration as tools for the design of innovative materials and systems," *Nat. Mater.*, 4, 4, 277–288, 2005.

[9] J. Hwang, Y. Jeong, J. M. Park, K. H. Lee, J. W. Hong, and J. Choi, "Biomimetics: forecasting the future of science, engineering, and medicine," *Int. J. Nanomedicine*, 10, 5701, 2015.

[10] J. F. V Vincent, "Biomimetics — a review," *Proc. Inst. Mech. Eng. Part H J. Eng. Med.*, 223, 8, 919–939, 2009.

[11] F. Baneyx, "Review of Biomimetic and Bioinspired Nanomaterials Biomimetic and Bioinspired Nanomaterials . Edited by Challa S. S. R.Kumar (Louisiana State University, Baton Rouge, LA). WILEY-VCH Verlag GmbH & Co KGaA : Weinheim . 2010 . xxii + 564 pp. $205.00. ISBN 978-3-527-32167-4 .," *J. Am. Chem. Soc.*, 133, 13, 5161–5161, 2011.

[12] Dennis M. Vriezema, Marta Comellas Aragonès, Johannes A. A. W. Elemans, Jeroen J. L. M. Cornelissen, and Alan E. Rowan, and R. J. M. Nolte*, "Self-Assembled Nanoreactors," 2005.

[13] J. R. Werber, C. O. Osuji, and M. Elimelech, "Materials for next-generation desalination and water purification membranes," *Nat. Rev. Mater.*, 1, 5, 16018, 2016.

[14] Y.-R. Kim, S. Jung, H. Ryu, Y.-E. Yoo, S. M. Kim, and T.-J. Jeon, "Synthetic biomimetic membranes and their sensor applications.," *Sensors (Basel).*, 12, 7, 9530–50, 2012.

[15] S. Majd, E. C. Yusko, Y. N. Billeh, M. X. Macrae, J. Yang, and M. Mayer, "Applications of biological pores in nanomedicine, sensing, and nanoelectronics," *Curr. Opin. Biotechnol.*, 21, 4, 439–476, 2010.

[16] S. Mura, J. Nicolas, and P. Couvreur, "Stimuli-responsive nanocarriers for drug delivery," *Nat. Mater.*, 12, 11, 991–1003, 2013.

[17] I. Rehman and S. Botelho, *Biochemistry, Tertiary Structure, Protein*. StatPearls Publishing, 2019.

[18] C. A. Ouzounis, R. M. R. Coulson, A. J. Enright, V. Kunin, and J. B. Pereira-Leal, "Classification schemes for protein structure and function," *Nat. Rev. Genet.*, 4, 7, 508–519, 2003.

[19] A. M. Seddon, P. Curnow, and P. J. Booth, "Membrane proteins, lipids and detergents: Not just a soap opera," *Biochim. Biophys. Acta - Biomembr.*, 1666, 1–2, 105–117, 2004.

[20] J.-M. Pagès, C. E. James, and M. Winterhalter, "The porin and the permeating antibiotic: a selective diffusion barrier in Gram-negative bacteria.," *Nat. Rev. Microbiol.*, 6, 12, 893–903, 2008.

[21] V. a Feher, A. Randall, P. Baldi, R. M. Bush, L. M. de la Maza, and R. E. Amaro, "A 3-

dimensional trimeric β-barrel model for Chlamydia MOMP contains conserved and novel elements of Gram-negative bacterial porins.," *PLoS One*, 8, 7, e68934, 2013.

[22] W. Xie, F. He, B. Wang, T.-S. Chung, K. Jeyaseelan, A. Armugam, and Y. W. Tong, "An aquaporin-based vesicle-embedded polymeric membrane for low energy water filtration," *J. Mater. Chem. A*, 1, 26, 7592, 2013.

[23] J. H. Kleinschmidt, "Folding and Stability of Monomeric β-Barrel Membrane Proteins," in *Protein-Lipid Interactions*, Weinheim, FRG: Wiley-VCH Verlag GmbH & Co. KGaA, 2006, 27–56.

[24] M. Lopes-Rodrigues, D. Zanuy, C. Alemán, C. Michaux, and E. A. Perpète, "3D structure of a Brucella melitensis porin: molecular modelling in lipid membranes," *J. Biomol. Struct. Dyn.*, 1–13, 2018.

[25] F. Seidi, R. Jenjob, and D. Crespy, "Designing Smart Polymer Conjugates for Controlled Release of Payloads," *Chem. Rev.*, 118, 7, 3965–4036, 2018.

[26] M. Kumar, J. E. O. Habel, Y. X. Shen, W. P. Meier, and T. Walz, "High-density reconstitution of functional water channels into vesicular and planar block copolymer membranes," *J. Am. Chem. Soc.*, 134, 45, 18631–18637, 2012.

[27] S. Balme, J.-M. Janot, L. Berardo, F. Henn, D. Bonhenry, S. Kraszewski, F. Picaud, and C. Ramseyer, "New Bioinspired Membrane Made of a Biological Ion Channel Confined into the Cylindrical Nanopore of a Solid-State Polymer.," *Nano Lett.*, 11, 2, 712–716, 2011.

[28] A. Güven, M. Fioroni, B. Hauer, and U. Schwaneberg, "Molecular understanding of sterically controlled compound release through an engineered channel protein (FhuA).," *J. Nanobiotechnology*, 8, 14, 2010.

[29] N. Muhammad, T. Dworeck, M. Fioroni, and U. Schwaneberg, "Engineering of the E. coli Outer Membrane Protein FhuA to overcome the Hydrophobic Mismatch in Thick Polymeric Membranes," *J. Nanobiotechnology*, 9, 1, 8, 2011.

[30] C. Nardin, J. Widmer, M. Winterhalter, and W. Meier, "Amphiphilic block copolymer nanocontainers as bioreactors," *Eur. Phys. J. E*, 4, 4, 403–410, 2001.

[31] A. Ranquin, W. Versées, W. Meier, J. Steyaert, and P. Van Gelder, "Therapeutic Nanoreactors: Combining Chemistry and Biology in a Novel Triblock Copolymer Drug Delivery System," *Nano Lett.*, 5, 11, 2220–2224, 2005.

[32] A. Onoda, K. Fukumoto, M. Arlt, M. Bocola, U. Schwaneberg, and T. Hayashi, "A rhodium complex-linked β-barrel protein as a hybrid biocatalyst for phenylacetylene polymerization," *Chem. Commun.*, 48, 78, 9756, 2012.

[33] N. Misra, J. A. Martinez, S.-C. J. Huang, Y. Wang, P. Stroeve, C. P. Grigoropoulos, and A. Noy, "Bioelectronic silicon nanowire devices using functional membrane proteins.," *Proc. Natl. Acad. Sci. U. S. A.*, 106, 33, 13780–4, 2009.

[34] M. M. Pérez-Madrigal, L. J. del Valle, E. Armelin, C. Michaux, G. Roussel, E. A. Perpète, and C. Alemán, "Polypyrrole-Supported Membrane Proteins for Bio-Inspired Ion Channels," *ACS Appl. Mater. Interfaces*, 7, 3, 1632–1643, 2015.

[35] D. T. McQuade, A. E. Pullen, and T. M. Swager, "Conjugated polymer-based chemical sensors.," *Chem. Rev.*, 100, 7, 2537–74, 2000.

[36] A. Puiggalí-jou, M. M. Pérez-madrigal, L. J. del Valle, E. Armelin, M. T. Casas, C. Michaux, E. A. Perpète, F. Estrany, C. Alemán, L. J. Valle, E. Armelin, M. T. Casas, C. Michaux, E. A. Perpète, F. Estrany, and C. Alemán, "Confinement of a β-barrel protein in nanoperforated free-standing nanomembranes for ion transport," *Nanoscale*, 8, 38, 16922–16935, 2016.

[37] G. Pappas, P. Papadimitriou, N. Akritidis, L. Christou, and E. V Tsianos, "The new global map of human brucellosis," 6, February, 91–99, 2006.

[38] J. Y. Paquet, M. A. Diaz, S. Genevrois, M. Grayon, J. M. Verger, X. De Bolle, J. H. Lakey, J. J. Letesson, and A. Cloeckaert, "Molecular, antigenic, and functional analyses of Omp2b

porin size variants of Brucella spp.," *J. Bacteriol.*, 183, 16, 4839–4847, 2001.

[39] J. Y. Paquet, C. Vinals, J. Wouters, J. J. Letesson, and E. Depiereux, "Topology prediction of Brucella abortus Omp2b and Omp2a porins after critical assessment of transmembrane beta strands prediction by several secondary structure prediction methods.," *J. Biomol. Struct. Dyn.*, 17, October 2014, 747–757, 2000.

[40] T. Salinas, S. El Farouk-Ameqrane, E. Ubrig, C. Sauter, A.-M. M. Duchêne, and L. Maréchal-Drouard, "Molecular basis for the differential interaction of plant mitochondrial VDAC proteins with tRNAs," *Nucleic Acids Res.*, 42, 15, 9937–9948, 2014.

[41] S. Hiller, R. G. Garces, T. J. Malia, V. Y. Orekhov, M. Colombini, and G. Wagner, "Solution Structure of the Integral Human Membrane Protein VDAC-1 in Detergent Micelles," *Science (80-.).*, 321, 5893, 1206–1210, 2008.

[42] M. Colombini, "The VDAC channel: Molecular basis for selectivity," *Biochim. Biophys. Acta - Mol. Cell Res.*, 1863, 10, 2498–2502, 2016.

[43] H. Rui, K. Il Lee, R. W. Pastor, and W. Im, "Molecular dynamics studies of ion permeation in VDAC," *Biophys. J.*, 100, 3, 602–610, 2011.

[44] A. Puiggalí-Jou, J. Medina, L. J. del Valle, and C. Alemán, "Nanoperforations in poly(lactic acid) free-standing nanomembranes to promote interactions with cell filopodia," *Eur. Polym. J.*, 75, 552–564, 2016.

[45] J. Bobacka, A. Lewenstam, and A. Ivaska, "Electrochemical impedance spectroscopy of oxidized poly(3,4-ethylenedioxythiophene) film electrodes in aqueous solutions," *J. Electroanal. Chem.*, 489, 1–2, 17–27, 2000.

[46] F. Junge, B. Schneider, S. Reckel, D. Schwarz, V. Dötsch, and F. Bernhard, "Large-scale production of functional membrane proteins.," *Cell. Mol. Life Sci.*, 65, 11, 1729–55, 2008.

[47] E. D. Clark, "Protein refolding for industrial processes.," *Curr. Opin. Biotechnol.*, 12, 2, 202–7, 2001.

[48] R. Laage and D. Langosch, "Strategies for prokaryotic expression of eukaryotic membrane proteins.," *Traffic*, 2, 2, 99–104, 2001.

[49] C. Michaux, N. C. Pomroy, and G. G. Privé, "Refolding SDS-Denatured Proteins by the Addition of Amphipathic Cosolvents," *J. Mol. Biol.*, 375, 5, 1477–1488, 2008.

[50] C. Michaux, G. Roussel, M. Lopes-Rodrigues, A. Matagne, and E. A. Perpète, "Unravelling the mechanisms of a protein refolding process based on the association of detergents and co-solvents," *J. Pept. Sci.*, March, 485–491, 2016.

2. Thermomechanical response of Omp2a

2. Thermomechanical response of Omp2a

Summary

The thermomechanical response of Omp2a, a representative channel protein recently used for the fabrication of smart biomimetic nanomembranes made of poly(lactic acid), has been characterized using microcantilever technology and compared with standard proteins. For this purpose, thermally-induced transitions involving the conversion of stable trimers to bigger aggregates, local reorganizations based on the strengthening or weakening of intermolecular interactions, and protein denaturation, have been detected by the microcantilever resonance frequency and deflection as a function of the temperature. Measurements have been carried out on arrays of 8-microcantilevers functionalized with proteins (Omp2a, lysozyme and bovine serum albumin). In order to interpret the measured nanofeatures, the response of proteins to temperature has been also examined using other characterization techniques, including real time wide angle X-ray diffraction. Results not only demonstrate the complex behaviour of porins, which exhibit multiple local thermal transitions before undergoing denaturation at temperatures higher than 105°C, but also suggest a post-treatment to control the orientation of immobilized Omp2a molecules in functionalized biomimetic nanomembranes and, thus, increase their efficacy in ion transport.

Disclaimer: this chapter was published as a regular article in the *Journal of the American Chemical Society Omega* with the following reference:

Maximilien Lopes-Rodrigues; Anna Puiggalí-Jou; Didac Martí-Balleste; Luis J. del Valle; Catherine Michaux; Eric A. Perpète and Carlos Alemán. Thermomechanical Response of a Representative Porin for Biomimetics. *ACS Omega* 2018, 3:7; 7856-7867.
https://pubs.acs.org/doi/10.1021/acsomega.8b00463

2.1. Introduction

This chapter and the following focus on the free-standing nanomaterial composed of poly(lactic acid) (PLA) and Omp2a that was developed in the IMEM laboratory [1]. It demonstrated promising results to modify the electrical activity (enhanced conductivity) of the material after addition of the proteins. Additionally, the selectivity of the material towards ions emerged after addition of the proteins. This previous work motivated us to deepen the understanding of the properties of the hybrid nanomaterial. More specifically, the following chapter studies the thermomechanical properties of the protein Omp2a using an innovative microcantilever technology.

Recently, there has been a paradigmatic shift in the experimental study of materials with applications in biomedicine: new methods have been developed to study phenomena associated to single molecules and their small supramolecular/nanostructured aggregates when embedded within complex platforms with functional interfaces for clinical applications. In particular, micro- and nano-sized mechanical techniques based on the principle that variations in electrostatic, van der Waals and steric intermolecular interactions on the surface of functionalized cantilever cause bending (deflection) of a few nanometers, are playing a fundamental role [2]. The combination of these miniaturized mechanical systems with electrical and, especially, optical displacement sensors has been applied for, among others, chemisorption measurements in air at room temperature with up to yoctogram (10^{-24} g) resolution [3-4], drug screening [5-6], characterization of the thermomechanical response and the glass transition temperatures of macromolecular ultra-thin films [7-8], detection of DNA strands [9], observation of the hydration-dehydration (swelling-deswelling) of molecular systems [10–12], and identification of biological species through their molecular mass and stiffness improving the capabilities of conventional mass spectrometers [13-14].

Porins are β-barrel outer membrane proteins (OMPs) that form water-filled open channels and allow the passive penetration of hydrophilic molecules. Due to their capacity in exchange ions and small nutrients over the outer membrane, porins have been used to fabricate smart biomimetic nanomembranes (NMs) that could incorporate biological functions, such as controlled ion transport [15]. For this purpose, OMPs are immobilized onto supported organic or inorganic nanomembranes [16–19], or even confined inside synthetic pores [1-20-21]. Apparently, in all cases the nanostructured porin aggregates formed in the resulting biointerfaces play a crucial role in the selective ion permeability. However, the size and shape of these structures are drastically influenced by the chemical environment, being usually different from those found in the natural state. For example, the individual trimeric units found in natural environments for Omp2a [22-23], a β-barrel OMP from *Brucella melitensis*, self-associate into hierarchical structures with around 6-8 trimeric

units when the protein incorporates onto the surface of supported NMs or inside the synthetic pores of polymeric free-standing NMs for biosensing, nanofluidics and ion-rectifying for energy conversion [1-18].

The organization of β-barrel OMPs in synthetic environments is investigated as a function of the temperature, thereby applying microcantilever deflection technologies to hierarchical structured Omp2a (367 residues, 39 kDa). The interpretation of these measurements has been carried out with the aid of the results obtained using other techniques, such as FTIR spectroscopy, circular dichroism (CD), dynamic light scattering (DLS), wide angle X-ray diffraction (WAXD), X-ray photoelectron spectroscopy (XPS) and atomic force microscopy (AFM). The distinctive thermal transitions identified for Omp2a, which compare with those observed for conventional proteins such as lysozyme (LYS; 129 residues, 14.4 kDa) and bovine serum albumin (BSA; 583 residues, 66.5 kDa), have been unraveled and their consequences and effects analyzed.

2.2. Methods

Materials. Octosensis Microcantilever-Arrays (chips with eight mono crystalline Si cantilevers, 500 μm in length) were obtained from Micromotive GmbH (Mainz, Germany). The following chemicals were purchased from Sigma-Aldrich and used as received without further purification: isopropanol, (3-glycidyloxypropyl)trimethoxysilane (98%), toluene (99.8%), N^{α},N^{α}-bis(carboxymethyl)-L-lysine hydrate (NTA-NH_2) (97%), 1-[(3-dimethylamino)propyl]-3-ethylcarbodiimide methiodide (EDC), N-hydroxysuccinimide (NHS), 2-(N-morpholino)ethanesulfonic acid (MES), 2-amino-2-(hydroxymethyl)-1,3-propanediol (Tris base), carbonate/bicarbonate buffer, phosphate buffered saline (PBS, pH7.4) Sodium chloride was purchased from Panreac (Spain). Bovine serum albumin (BSA, fraction V) and lysozyme (LYS) were purchased from BioLabs (England) and Fluka, respectively. The Omp2a protein was expressed, purified, and refolded using a previously reported procedure [22-23].

FTIR spectroscopy. FTIR spectra of BSA, LYS and Omp2a were recorded on a FTIR 4100 Jasco spectrophotometer. The samples were placed in an attenuated total reflection accessory with thermal control and a diamond crystal (Specac model MKII Golden Gate Heated Single Reflection Diamond ATR). For each sample 46 scans were performed with a resolution of 2 cm^{-1}. Spectra were recorded at 30°C and 100°C. FTIR spectroscopy was used to examine the secondary structure of the proteins. Specifically, the number and position of the peaks in the Amide I region, which were derived from the second derivative and deconvoluted spectra, provided information about the protein conformation. Fourier self-deconvolution was performed with the software PeakFit 4 (Jandel Scientific Software, AISN Software Inc.), the resulting profiles being fitted to Gaussian functions through the OriginPro 7.5 software.

Circular dichroism (CD). CD measurements of BSA and LYS were performed using a 1× commercial Dulbecco's Phosphate Buffered Saline (PBS) from Gibco with a protein concentration of 0.01 mg/mL, whereas a sodium dodecyl sulfate (SDS) – 2-methyl-2,4-pentanediol (MPD) buffer (60 mM SDS, 1.5 M MPD, 400 mM NaCl, 50 mM Tris-HCl pH 8) with a protein concentration of 0.005 mg/mL was used for Omp2a. It should be noted that the different buffer selection is due to the fact that the Omp2a structure is protected by amphiphilic SDS–MDP detergents.[22,23] Spectra were recorded between 190 and 250 nm using a Chirascan-plus *q*CD spectrometer (Applied Photophysics, APL; UK) equipped with a temperature-controlled cell. Spectra were obtained using heating (from 5°C to 90°C) and cooling (from 90°C to 5°C) runs stopping every 5°C for 5 minutes with a heating rate of 5°C/min. Machine settings were as follows: 1 nm bandwidth, 1 s response, 0.5 nm data pitch, 100 nm/min scan speed and cell length of 10 mm. All CD spectra presented in this

work correspond to the average from three independent measurements. Spectra were deconvoluted using the CDSSTR method of the DichroWeb server [24].

Dynamic light scattering (DLS). The influence of the temperature in the shape and aggregation of BSA, LYS and Omp2a was studied by DLS following the variation of the particle effective diameter (D_{eff}) when the temperature increases from 20 to 60°C. Proteins were dissolved in the buffers described above for CD measurement using the same concentrations. Measurements were performed using a NanoBrook Omni Zeta Potential Analyzer from Brookheaven Instruments Corporation. D_{eff} values correspond to average values of the corresponding particle size distributions, which were determined in steps of 10°C (heating/cooling rate 10°C/min) stopping for 2 minutes before the measurement.

Wide angle X-ray diffraction (WAXD). Time resolved WAXD experiments were carried out at the NCD beamline (BL-11) of the Alba synchrotron radiation light facility of Cerdanyola del Vallès (Catalunya). The beam was monochromatized to a wavelength of 1.5406 Å. Samples were confined between Kapton films and then held in a Linkam hot stage with temperature control within ±0.1°C. WAXD profiles were acquired during heating and cooling runs in time frames of 7.5 s and a rate of 4°C/min. The WAXD detector was calibrated with diffractions of a standard of a Cr_2O_3 sample. The diffraction profiles were normalized to the beam intensity and corrected considering the empty sample background. Deconvolution of WAXD peaks was performed with the PeakFit v4 program by Jandel Scientific Software using a mathematical function known as "Gaussian area".

Functionalization of silicon microcantilever chips. The functionalization protocol, which was applied to silicon microcantilever chips previously hydroxylated at the surface with a H_2O_2:H_2SO_4 (3:1 v/v) mixture, consisted of four steps:

1. *Silanization.* Hydroxylated microcantilevers were silanized with 0.2 % of (3-glycidyloxypropyl)trimethoxysilane in dry toluene overnight at room temperature under nitrogen atmosphere. Afterwards, samples were washed with toluene and milli-Q water.
2. *Carboxylation*. Silanized microcantilevers were incubated into 100 mM N^{α},N^{α}-bis(carboxymethyl)-L-lysine hydrate (NTA-NH_2) solution in 50 mM carbonate buffer (pH 9.5) overnight, at room temperature, and under gentle agitation. After this, carboxylated substrates were washed with 50 mM carbonate buffer (pH 9.5) and milli-Q water.
3. *Activation.* The carboxyl groups arising from NTA-NH_2 at the microcantilever surface were activated for direct reaction with primary amines via amide bond formation with a

mixture of 100 mM EDC and 150 mM NHS, both dissolved in 10 mM MES (pH5.5). Samples were incubated for 30 min at 37°C under gentle agitation and, then, extensively rinsed with 10mM MES (pH 5.5).

4. *Protein immobilization.* A solution of 0.1 mg/mL of protein (BSA, LYS or Omp2a) was prepared in 10mM MES (pH 5.5). The cantilevers were incubated for 2 h at 37ºC. After that, samples were washed with 10 mM MES (pH 5.5) and incubated for 45 minutes at 37°C with 1×PBS with 0.3 M NaCl to desorb proteins not covalently bonded to the surface.

X-ray photoelectron spectroscopy (XPS). XPS was used to analyze the chemical composition at the surface of silicon substrates. The system (SPECS Surface Nano Analysis GmbH, Berlin, Germany) was equipped with a non-monochromatic twin anode X-ray source XR50 of Mg/Al (1253 eV/1487 eV). Specifically, the Al anode was operated at 150 W. Detector pass energy was set at 25 eV and 0.1 eV for the survey and the narrow scans (high resolution spectra), respectively, at a pressure below 7.5×10^{-9} mbar. Casa XPS software (Version 2.3.16, Casa Software Ltd., Teignmouth, UK) was used to fit and perform peak integration of spectra. The C 1s peak was used as an internal reference (284.8 eV). High resolution XPS spectra were acquired by Gaussian–Lorentzian curve fitting after S-shape background subtraction.

Wettability. Contact angle measurements were conducted using the water drop method. 0.5 µL of milliQ water drops were deposited onto the surface of the substrate and recorded after stabilization with the equipment OCA 15EC (DataPhysics Instruments GmbH, Filderstadt). The SCA20 software was used to measure the contact angle, which is shown in this work as the average of at least 10 measures for each sample.

Atomic Force Microsco*py.* Atomic Force Microscopy (AFM) was conducted to obtain topographic images of the non-functionalized and functionalized surfaces using Si TAP 150-G probes (Budget Sensors, Bulgaria) with a frequency of 150 kHz and a force constant of 5 N/m. Images were obtained with an AFM VEECO Multimode under ambient conditions in tapping mode. The row scanning frequency was set between 0.6 and 0.8 Hz. The root-mean-square roughness was determined using the statistical application of the NanoScope Analysis software (1.20, Veeco).

Resonance frequency measurements and cantilever displacement. Cantilever resonance frequency and displacement measurements were carried out by means of the SCALA equipment (Scanning Laser Analyzer, from MecWins), a recently developed technology for the optical read-out of cantilevers [8-25-26]. The readout technique combines the optical beam deflection method

and the automated two-dimensional scanning of a single layer beam by voice-coil actuators. The equipment has been implemented with a thermal chamber containing a thermoelectric cooler and a cartridge heater. These elements are capable of sweeping the chamber's temperature from –50°C up to 220°C by flowing thermostatized N_2 to the sample. A holder containing multiple thermometer probes is placed inside the chamber for a better mapping of the temperature. All measurements were performed in nitrogen environment. The temperature control was regulated by software created by the MecWins Company.

Monocrystalline Si microcantilever chips containing arrays of eight cantilevers (Micromotive GmbH) were used for the measurements. Specifically, the nominal length, width, and thickness of the cantilevers were 500, 90±2 and 1 μm, respectively. Resonance frequency measurements were conducted in a nitrogen atmosphere at 25°C. The experimental setup is based on the shift induced in the resonance frequency by the added mass onto the cantilever through functionalization. The used platform consists in the automated two-dimensional scanning with a single laser (1 mW) beam by voice-coil actuators perpendicularly located.

The cantilever array is illuminated by the laser beam and a two-dimensional linear position detector (PSD) is arranged to collect the reflected beams. Location and characterization of cantilever sensors is carried out using TRACKER, an algorithm based on the recognition of reflected intensity patterns. This capability of SCALA allows the user to characterize a single sensor or an array of them in a fully automated process. A change in the local slope at the cantilever surface results into a displacement of the reflected laser spot on the PSD, which is denoted S. S is used to obtain the cantilever profile along its longitudinal axis, z(x), by integrating:

$$z(x) = \frac{1}{2D}\int_0^x S(x')dx' - \frac{1}{4}\frac{x^2}{D}\cos\beta \qquad (1)$$

where D is the distance between the cantilever and the PSD and β is the angle between the incident laser beam and the cantilever normal at its rest position. Coated cantilevers can be used as precise thermometers by exploiting the bimaterial effect, which refers to the measurable bending (*i.e.* differential stress) produced by temperature changes in substrates coated on one side by another material. Similarly, coated microcantilevers undergo a deflection as a result of temperature changes due to the thermal expansion coefficient difference between the coating material of the cantilever and the cantilever itself.

2.3. Results and discussion

The response of Omp2a to thermal stress has been compared with those of BSA and LYS. LYS exhibits an ellipsoidal shape in which both ordered (30% α-helix, 27% turn and 13% β-sheet secondary structures) and unordered (30%) regions coexist [27], while BSA structure is predominantly α-helical with the remaining polypeptide occurring in turns and loops (*i.e.* no β-sheet content) [28]. Omp2a has a cylindrical shape composed of β-strands separated by long unfolded loops [29]. Although the secondary structure of bacterial β-barrels is known to be sensitive to the polarity of the environment, they exhibit an increased thermal stability that has been typically attributed not only to the abundant β-strands barrel but also to their oligomeric architectures [30–33]. However, complete understanding of the thermal response of their supramolecular oligomeric architectures in synthetic environments, which is essential for the utilization of β-barrels in the fabrication of bioinspired nanodevices, is an unresolved question [34]. Before nanomechanical measurements, the effects of the heat shift on the secondary structure and aggregation tendency of the three proteins have been examined.

Secondary structure and diameter

Temperature-induced protein denaturation is frequently detected using FTIR spectroscopy and Circular Dichroism in various wavelength regimes. The vibrational spectrum in FTIR is selective in the absorption band frequency position, widths, and intensities in response to protein structural changes [35]. Specifically, the amide I band (1700 – 1600 cm^{-1}), which convolutes the major structural domain elements of proteins, including α-helix, β-sheet, turn and random coil (unstructured), has been used to visualize the response of BSA, LYS and Omp2a to heating. Circular Dichroism monitors the secondary structure of proteins. In CD, folded proteins have typical spectra for each secondary structure: the α-helix recognized by minima at ~220 and ~210 nm, while the β-sheet has a minimum at 218 nm and a maximum at ~195 nm [36]. These two structural motifs are detected in the spectra recorded for LYS and Omp2a at room temperature, whereas the spectrum of BSA mainly involves the helical motif.

CD (Figure 2.1) and FTIR (Figure 2.2) spectra were recorded in heating runs from 5ºC to 90ºC and reflect an increment of the disordered motifs at temperatures higher than ~55ºC for both BSA and LYS. Meanwhile, the content of ordered secondary structures, especially α-helix, decreases. The unfolding temperature estimated from CD results is 67ºC and 65ºC for BSA and LYS, respectively. These results are fully consistent with those early reported in previous studies in aqueous solution [37-38]. Specifically, the studies concluded that the proteins lose a small part of helical structures in the α-domain below 64ºC, undergoing irreversible (unless cooling start before reaching 75ºC)

thermal unfolding of the secondary structures at a temperature close to 75°C. On the other hand, Omp2a only exhibits slight variations in its secondary structures, the amount of unstructured content remaining practically constant from 5°C to 90ºC. Moreover, the thermal behavior of the three proteins is reversible, as is evidenced from the analyses of the CD spectra recorded in cooling runs (Figure 2.3).

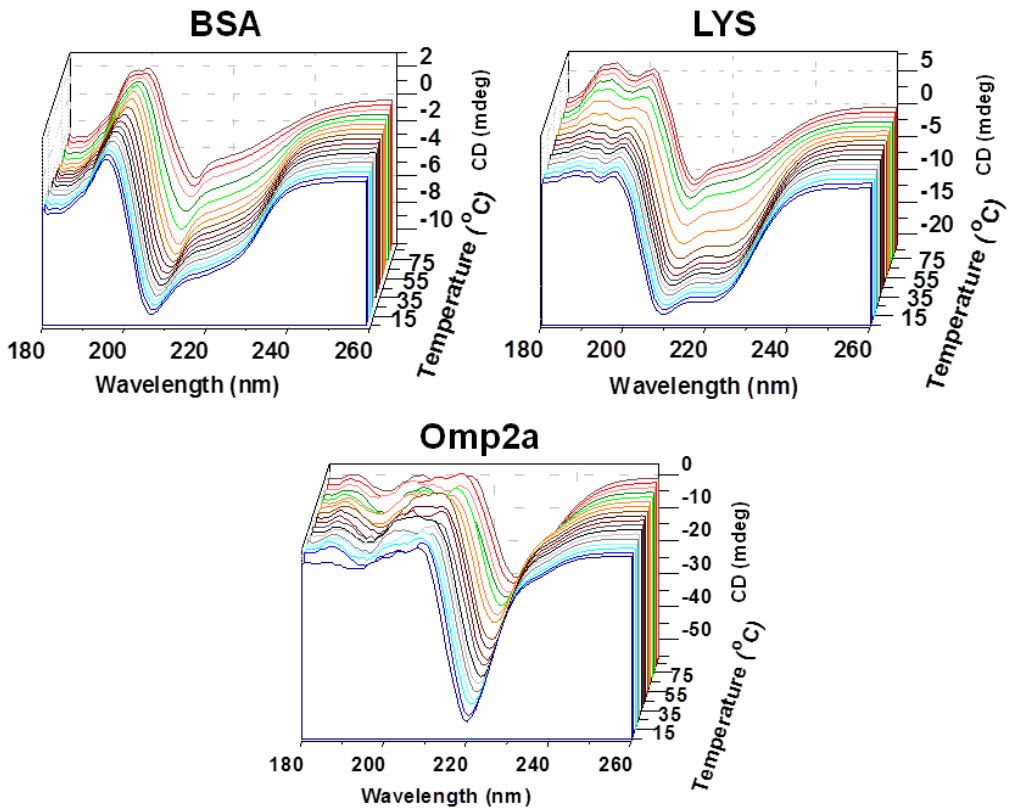

Figure 2.1: CD spectra recorded for BSA, LYS and Omp2a proteins at temperatures ranging from 5°C to 90°C (heating runs). Measurements for BSA and LYS were performed using a carbonate buffer, whereas a dodecyl sulfate (SDS) – 2-methyl-2,4-pentanediol (MPD) buffer was used for Omp2a.

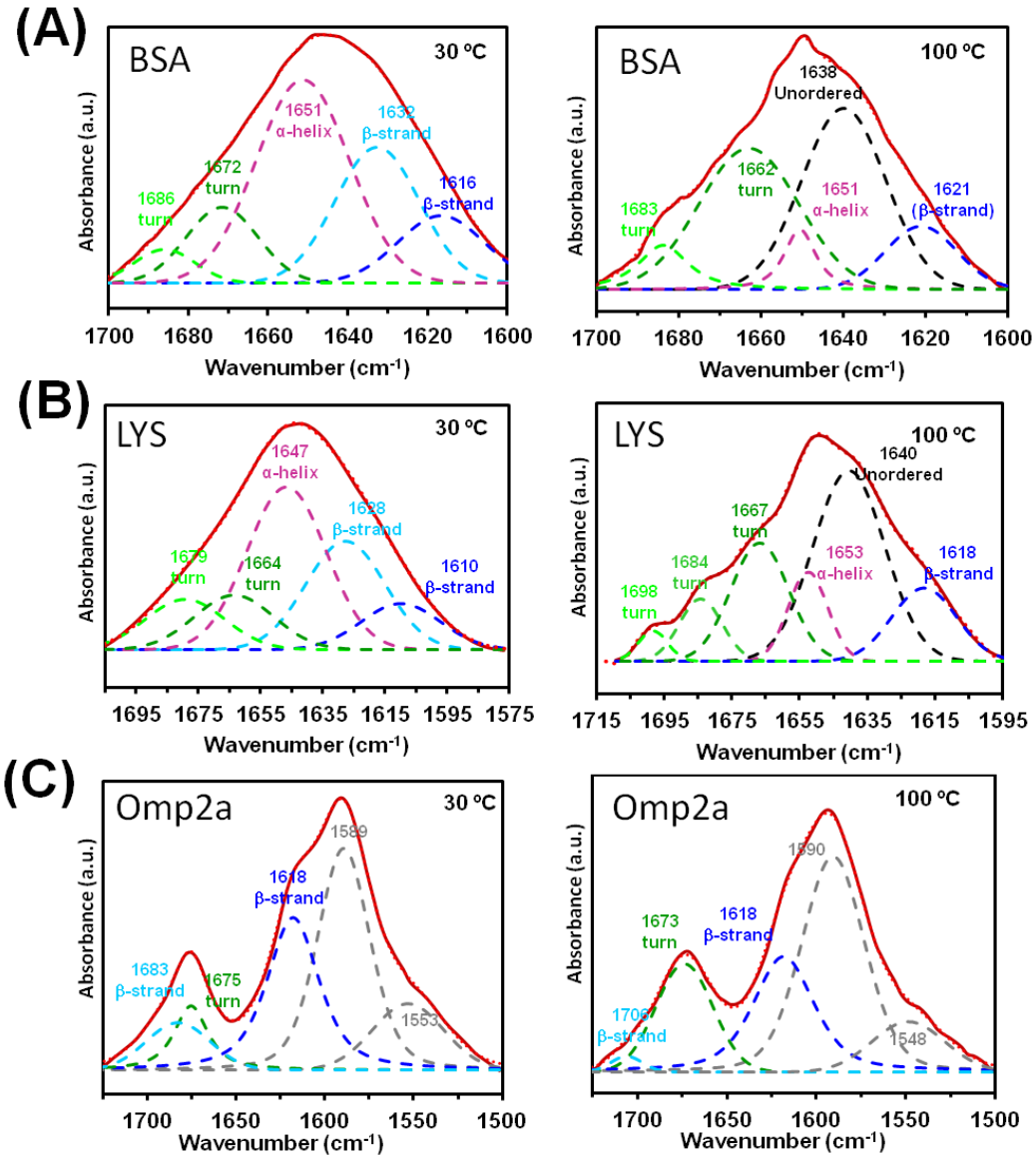

Figure 2.2: FTIR spectra in the region of amide I of (A) BSA, (B) LYS and (C) Omp2a at 30 ºC and 100 ºC (left and right, respectively). The deconvolution of the amide I absorption band is displayed in all cases.

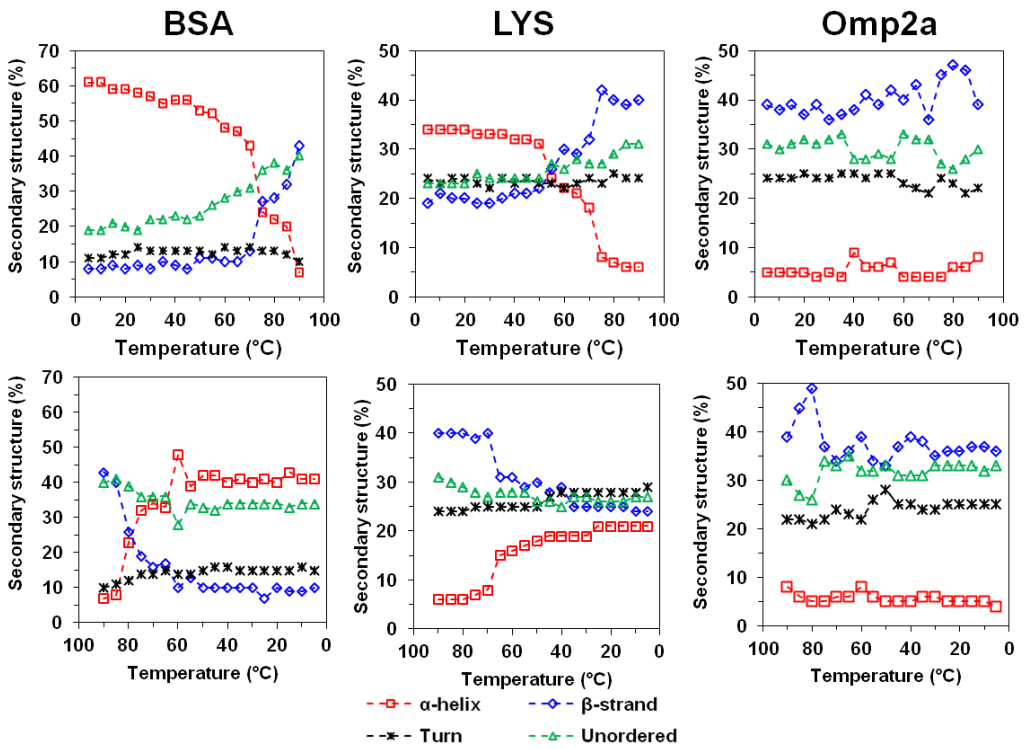

Figure 2.3: Secondary structure content of BSA, LYS and Omp2a obtained by deconvolution of the CD spectra for heating and cooling runs.

The FTIR and CD results of Omp2a prove that the efficient inter-strand hydrogen bond network preserves the protein secondary structure from thermal unfolding even outside the natural lipid environments. The heat-induced evolution of secondary structures in Omp2a has also been compared with conventional soluble proteins. The structural signatures of BSA and LYS significantly change beyond ~55ºC, evidencing the loss of secondary structure [39], while the CD spectrum of Omp2a remains practically unaltered until 90°C. At high temperature both BSA and LYS underwent a drastic unfolding, as is reflected by the apparition of an intense deconvoluted peak at ~1640 cm^{-1} in FTIR that has been associated to the unstructured protein. In contrast, the resemblance between all spectra recorded for Omp2a suggests that the β-barrel structure is preserved even at high temperatures.

The influence of the temperature in the shape and aggregation of the proteins was also assessed by Dynamic Light Scattering (DLS). Profiles displaying the variation of the particle effective diameter (D_{eff}) with the temperature are included in Figure 2.4 (both heating and cooling runs). Bimodal distributions were found for BSA at all examined temperatures and, therefore, two D_{eff} profiles are displayed in Figure 2.4. In the first mode, which corresponds to individual BSA molecules, D_{eff}

grows from 8.1 ± 1.4 nm at 20°C to 10.7 ± 1.4 nm at 60°C, evidencing that the unfolding process is accompanied by an increment of the molecular dimension. The lowest value, 8.1 ± 1.4 nm at 20°C, which is consistent with the dimensions of the prolate ellipsoid shape proposed for the protein monomer [40], increases by 30% with the temperature, due to the unfolding. The D_{eff} values of the second mode are approximately three times higher than the first one, indicating that BSA potentially forms trimers. In this case, D_{eff} increases from 23 ± 4 nm at 20°C to 46 ± 2 nm at 60°C. However, the highest value at 20°C, 23 ± 4 nm, grows more than twice when the temperature reaches 60°C. In this case, small aggregates (dimers or trimers) not only experience unfolding processes but also incorporate more protein molecules. Accordingly, it is concluded that BSA self-association is promoted by the temperature when already formed aggregates act as nuclei.

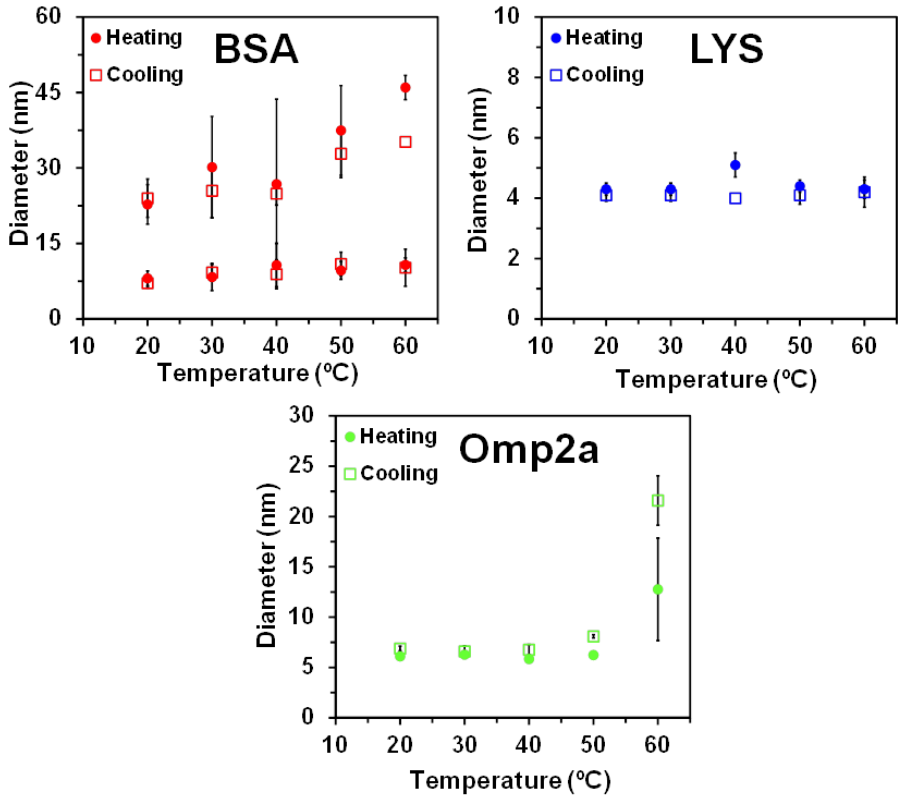

Figure 2.4: Effective diameter measured by DLS at temperatures ranging from 20ºC to 60ºC (heating and cooling runs are displayed) for BSA, LYS and Omp2a.

In contrast, LYS presents unimodal distributions, independently of the temperature, with similar D_{eff} values (*i.e.* 4.3 ± 0.2 nm and 4.3 ± 0.5 nm at 20 and 60°C, respectively). Although these results suggest that LYS volume is not affected by the unfolding, what actually occurs is that unfolding is accompanied by a reduction of the protein hydration. The latter was proved in early X-ray scattering

studies at 20°C and 80°C [37], which showed that the electron density of water in LYS crystals decreases with the crystallization temperature and, consequently, the radius of gyration remained practically invariant. Thus, it is hypothesized that changes in protein hydration offset the thermally induced protein motion. Similar observations have been found for other proteins [41], negative volume changes being detected in some cases [42]. The D_{eff} of LYS, which remains at 4.3 ± 0.2 nm for both 20 and 60°C, corresponds to the monomer diameter [40-43]. Thus, the contribution of aggregates, which are difficult to avoid completely even with dilute samples, was null in the case of LYS. These features combined with CD and FTIR data indicate that the unfolding is the only thermally-induced transition for LYS.

Omp2a also presents a unimodal distribution, even though D_{eff} increases from 6.1 ± 0.2 nm at 20°C to 12.6 ± 2.4 nm at 60°C. The former value has been associated to the trimeric state while the latter corresponds to bigger aggregates [1]. During the cooling run, D_{eff} decreases from 21.6 ± 5.1 nm at 60°C to 6.9 ± 0.4 nm at 20°C. The thermal stability observed for Omp2a combined with the significant D_{eff} variation indicates that the reversible aggregation of this β-barrel is notably affected by the temperature. DLS data reflect that Omp2a self-associates into the typical trimeric state found in the outer membranes of bacteria in the detergent buffer at room temperature. Thus, the D_{eff} measured by transmission electron microscopy (TEM) for Omp2a trimers in dried samples was recently found to be 9.3 ± 3.0 nm [1], which is consistent with the DLS value at 20°C aforementioned. However, the formation of bigger aggregates is detected by DLS when the temperature increases above 50°C, even though they are significantly smaller (D_{eff} = 12.6 ± 2.4 nm) than those also observed in dried samples at room temperature (D_{eff} = 25.9 ± 4.8 nm) by TEM. Thus, the van der Waals interactions between the side groups at the external side of the β-barrel are promoted through both drying and heating. This feature points out the importance of improving the understanding of Omp2a self-association processes in non-native environments, as for example those used to fabricate bioinspired nanomaterials for ion transport. Overall, FTIR, CD and DLS results probe that LYS and BSA are suitable controls for the present microcantileveler deflection studies due to their different behavior not only with respect to Omp2a but also among them.

Time resolved WAXD data on heating and cooling of lyophilized Omp2a

Real time WAXD experiments were performed using synchrotron radiation to examine the evolution of the β-strand structures in dried Omp2a during heating and cooling processes. Analyses were performed considering both Omp2a and blank samples, which were obtained by freeze drying the detergent buffer solution in presence and absence of protein, respectively. The one dimensional WAXD profile acquired for Omp2a at room temperature exhibits a sharp and intense peak at q =

15.64 nm^{-1} (Figure 2.5), which corresponds to an inter-strand spacing of d = 4.02 Å [44-45]. This peak is absent in the spectra recorded for blank samples, the broad peak centered at q = 15.40 nm^{-1} being attributed to the salts from the buffer (Figure 2.5). The presence and absence of the reflection associated to the β-strands in the Omp2a and blank samples, respectively, is clarified in the representative diffraction patterns showed in Figure 2.5d.

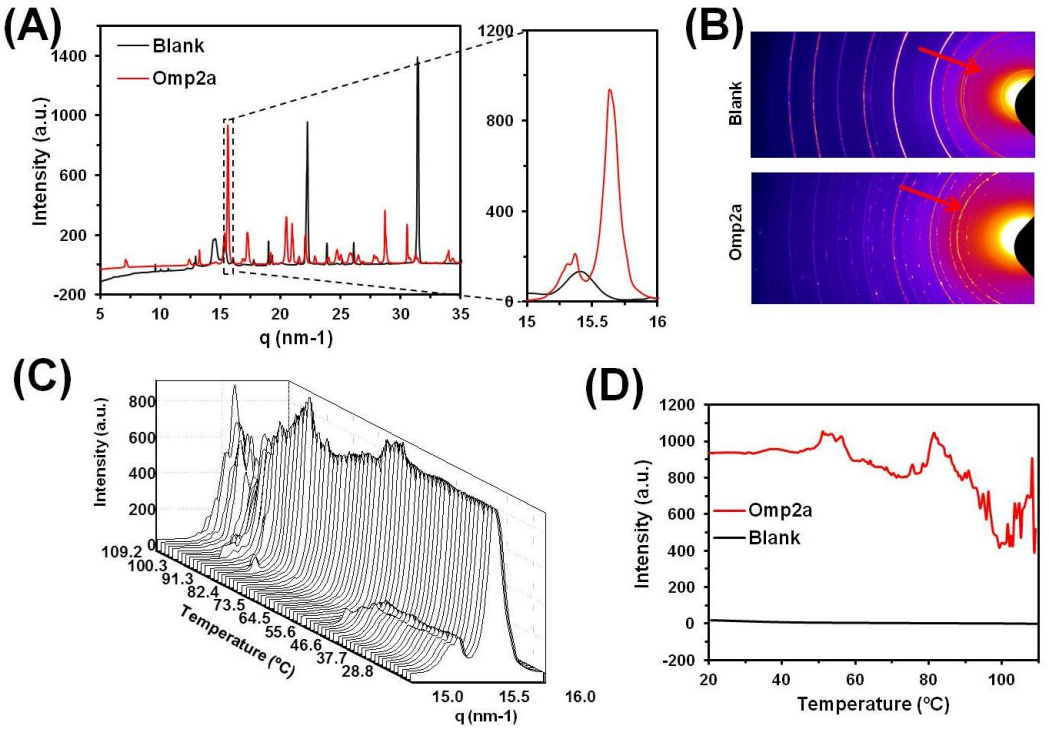

Figure 2.5: (A) 1D scattering patterns of blank (salts from the buffer solution) and Omp2a samples as dry powder at room temperature. (B) 2D scattering patters of the blank and Omp2a dried samples at room temperature. (C) 1D scattering pattern of Omp2a when a temperature ramp (heating) is applied. (D) Intensity of the peak profile for the blank and the Omp2a samples at q= 15.6 nm^{-1} during the temperature ramp.

Figure 2.5c displays a three-dimensional representation of the freeze dried Omp2a WAXD profiles in the β-strand region (q = 15-16 nm^{-1}) obtained by heating at a rate of 5°C/min from 25°C to 110°C. Figure 2.5d represents the variation in intensity of the peak at q = 15.6 nm^{-1} that occurs when heating both for Omp2a and blank samples. The variation with temperature of this narrow and intense peak has been used to monitor the effect of the different thermally-induced structural processes in inter-strand interactions. First, the intensity has a small increment at 50-55°C, which has been attributed to the reinforcement of neighboring intermolecular connections. According to DLS observations, which evidenced the transition from the trimeric form to bigger aggregates, this result has been interpreted as the formation of new hydrogen bonds between neighboring protein molecules. This hypothesis is also supported by the Omp2a trimer computational model [29]. After

this, from ~55°C to ~75°C the intensity decreases slowly and, suddenly, grows again at ~80°C. These changes suggest the restructuration of the newly formed aggregates during the heating process. Finally, the peak progressively broadened and becomes less intense at higher temperatures, evidencing that temperature has some effects in the local stability of the β-strands. In spite of this, the peak maintains 47% of its initial intensity at 100°C, which is consistent with the overall stability of the β-barrel structure observed by FTIR.

WAXD experiments indicate that temperature affects the β-sheet structure of Omp2a. This effect is focused in intermolecular interactions at temperatures lower than ~80°C and in both inter- and intramolecular interactions at higher temperatures. However, the amount of β-strands preserved at 110°C is still high enough to preserve the β-barrel structure, which supports FTIR and CD results. Thus, WAXD results corroborate the conversion of trimers into bigger aggregates at 50-55°C, which after equilibration through local reorganizations remain relatively stable until ~80°C. At higher temperatures, inter- and, probably, intramolecular β-strands, are affected by the thermal stress, these interactions being roughly halved. This interpretation is consistent with the well-known high thermal stability of bacterial porins, which exhibit temperature induced unfolding above 100°C [30]. This unusual stability is consequence of their β-barrel structural architecture composed of antiparallel β-sheets, in which strands are connected by short turns on one side and long loops on the other. Thus, the energy required to breakdown the secondary and quaternary structure of bacterial porins is significantly higher than that necessary to unfold BSA and LYS. Also, yet porin aggregates are stable, a variety of transitions associated to changes in their size (*i.e.* to dimers, trimers or bigger aggregates) has been detected at temperatures significantly lower than their unfolding temperatures but comparable to the typical unfolding temperatures of conventional proteins [46–48], which is in agreement with the opposite behaviours of Omp2a and BSA.

Protein immobilization onto the surface of silicon microcantilevers

The microcantilever-based biosensing technology has been applied in this work to monitor the response of porins in synthetic environments against the temperature change. Analysis of the results has been carried out by comparing their thermal behavior with the proteins BSA and LYS. Among other features, this nanomechanical platform is characterized by the high sensitivity, label-free detection, and small sample consumption due to the size of the microcantilevers (*ca.* 1000 μm^2) [49]. For successful characterization, the first step is the functionalization of silicon microcantilevers to achieve a stable and irreversible protein–surface binding.

In this work, a recently developed procedure to covalently bind peptides to silicon has been extrapolated and adapted to BSA, LYS and Omp2a proteins (Figure 2.6) [50]. This four-step protocol can be summarized as follows: 1) the microcantilever surface, previously hydroxylated with acids, is silanized with (3-glycodyloxypropyl)trimethoxysilane; 2) epoxy groups are opened with N^{α},N^{α}-bis(carboxymethyl)-L-lysine hydrate (NTA-NH_2) at basic pH; 3) the carboxylated surface derived from 2) is activated with a mixture of 1-[(3-dimethylamino)propyl]-3-ethylcarbodiimide methiodide (EDC) and N-hydroxysuccinimide (NHS); and 4) proteins are immobilized by incubating the activated surface in the corresponding protein solution. Before conducting any measurement, proteins not covalently bonded to the substrate were desorbed by washing with a phosphate buffer solution. Since the three proteins investigated contain a relatively large number of amine groups, corresponding to multiple lysine residues, in addition to the N-terminal amine, the study of protein-overhang interactions is limited by this immobilization procedure.

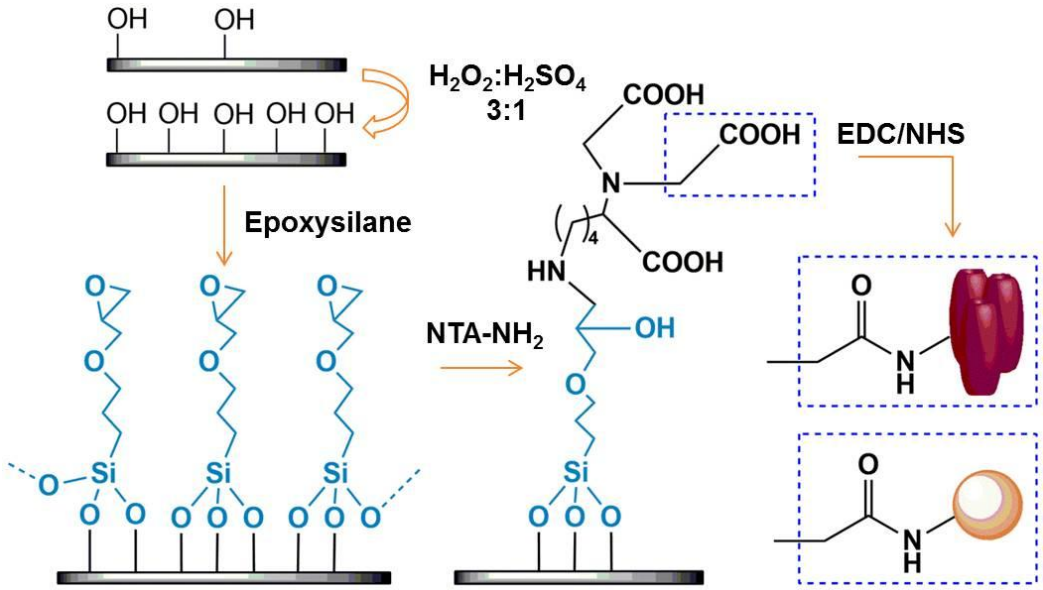

Figure 2.6: Protein functionalization protocol for silicon substrates.

Comparison of the characteristic XPS spectra in the N 1s, C 1s and O 1s regions of hydroxylated (non-functionalized) silicon and protein-functionalized substrates (Figure 2.7) chemically proves the success of the immobilization protocol. The presence of a peak in the C 1s region of the non-functionalized silicon spectrum has been attributed to the presence of organic contaminants from the environment. Whilst the latter makes more difficult the corroboration of the protein incorporation, the carbon content is significantly higher when silicon was functionalized with BSA, LYS and Omp2a (Table 2.1), showing a 4.5, 3.0 and 3.2 fold increase, respectively. Moreover, the apparition

of the N 1s peak, which was not detected for non-functionalized substrates, is an unequivocal chemical evidence of the proteins immobilization (Table 2.1).

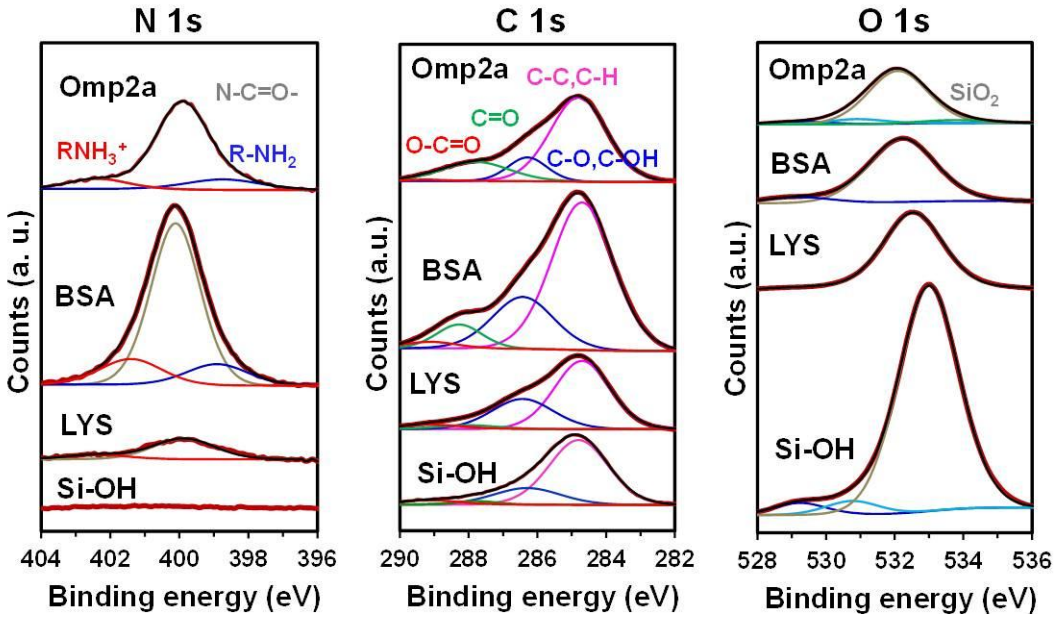

Figure 2.7: N 1s, C 1s and O 1s high-resolution XPS spectra for non-functionalized (hydroxylated; Si-OH) and protein functionalized (LYS, BSA or Omp2a) silicon substrates. Peaks from deconvolution are also displayed.

Table 2.1: Atomic percent composition (O 1s, C 1s, Si 2p and N 1s) obtained by XPS for non-functionalized (hydroxylated) and protein functionalized (*i.e.* with BSA, LYS or Omp2a covalently immobilized at the surface) silicon substrates.

	O 1s	**C 1s**	**Si 2p**	**N 1s**
Hydroxylated silicon	47.7	13.4	38.9	-
BSA-silicon	22.5	60.0	10.8	6.7
LYS-silicon	31.6	40.2	26.7	1.5
Omp2a-silicon	30.6	43.4	20.7	5.3

Changes in surface properties, as for example the wettability (Figure 2.8) provide indirect evidence of the binding between the substrate and the protein. Thus, contact angle (θ) measurements using deionized water showed that the hydrophilic character of silicon (θ = 30º ± 5º) decreased considerably upon the incorporation of protein (θ = 70º ± 3º, 47º ± 2 and 49º ± 6º for BSA, LYS and Omp2a, respectively).

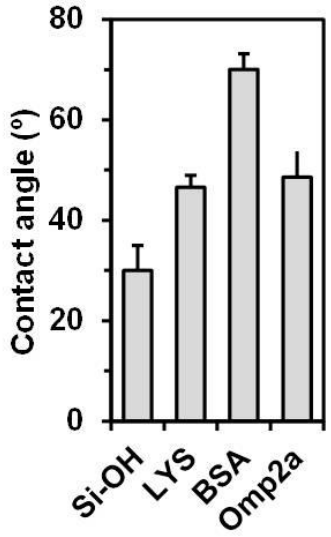

Figure 2.8: Average contact angle of non-functionalized and functionalized silicon substrates.

Similarly, 3D topographic AFM images reveal significant differences between the bare silicon substrate and the functionalized ones, which affect the root-mean-square roughness (Figure 2.9). Moreover, topographic images of protein functionalized surfaces, once biomacromolecules non-covalently bonded to the surface were eliminated, evidence heights and widths of 2-4 nm and 40-100 nm, respectively, demonstrating the immobilization of aggregates. As expected, the latter aggregates are much smaller and less abundant for LYS than for BSA and Omp2a, the former showing the flatter profile (root-mean-square roughness of non-functionalized, LYS-, BSA- and Omp2a-functionalized substrates is 4.9 ± 2.1, 6.1 ± 2.6, 10.5 ± 5.9 and 10.7 ± 3.0 Å, respectively). Inspection of the cross sectional profiles (Figure 2.10) are consistent with the immobilization not only of individual protein molecules but also of aggregates, diameter sizes ranging from 40 to 98 nm.

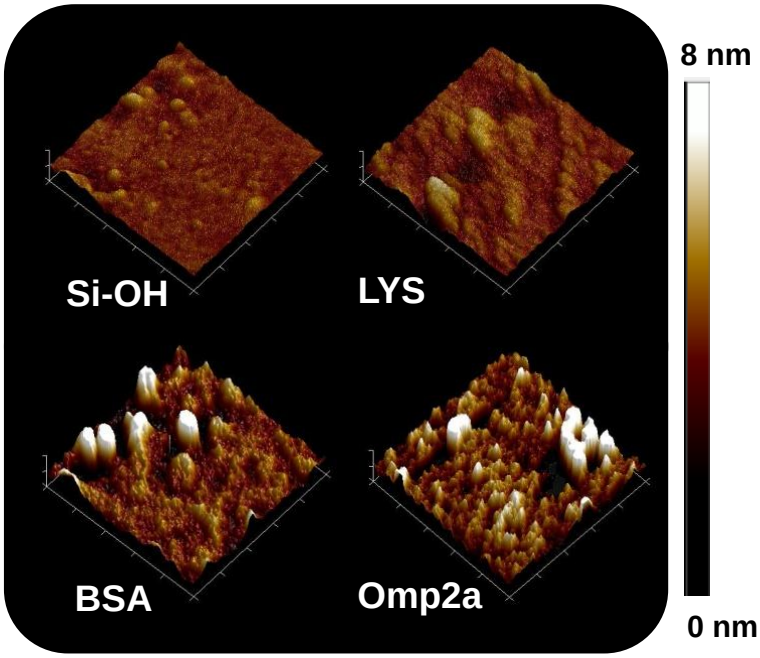

Figure 2.9: Topographic AFM images of non-functionalized and functionalized substrates (500 × 500 nm^2).

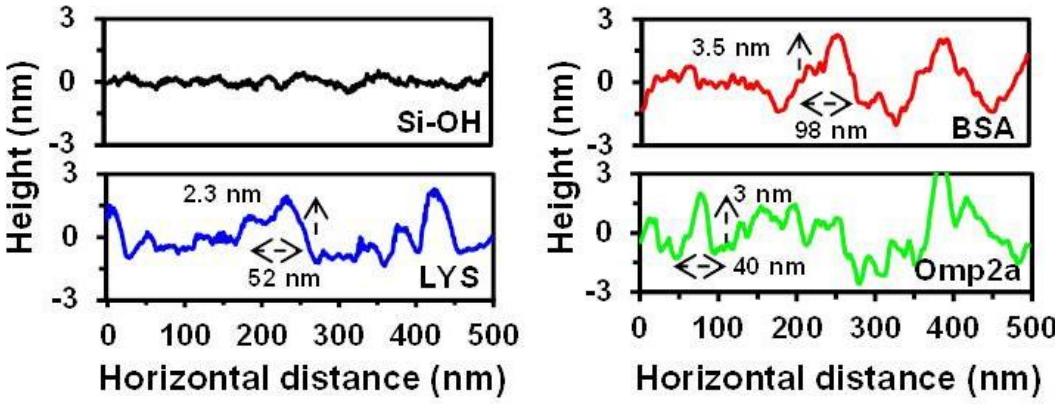

Figure 2.10: Representative cross sectional profiles for AFM images.

Proteins have been covalently linked via an epoxysilane-based protocol to silicon microcantilevers that had been efficiently activated by a hydroxylation treatment with a H_2O_2:H_2SO_4 mixture. The results derived from the different chemical and physical characterization techniques performed at each functionalized substrate have confirmed directly and indirectly, the suitability of the protocol to tether biomacromolecules onto the silicon surfaces.

Thermomechanical response of protein functionalized microcantilevers

Protein-functionalized silicon chips with arrays of eight cantilevers (*i.e.* using such number of sensors in parallel) were operated in dynamic mode (Figure 2.11). Piezoelectric excitation (*i.e.* an actuator is positioned below the chip base) and their first vibration mode were monitored by a scanning laser. After cleaning with isopropanol and hydroxylation with a H_2O_2:H_2SO_4 (3:1 v/v) mixture, hydroxylated chips (100 μm wide, 500 μm long and 1 μm thick) displayed a resonance frequency of 5206 ± 162 Hz measured in a N_2 atmosphere at 25°C.

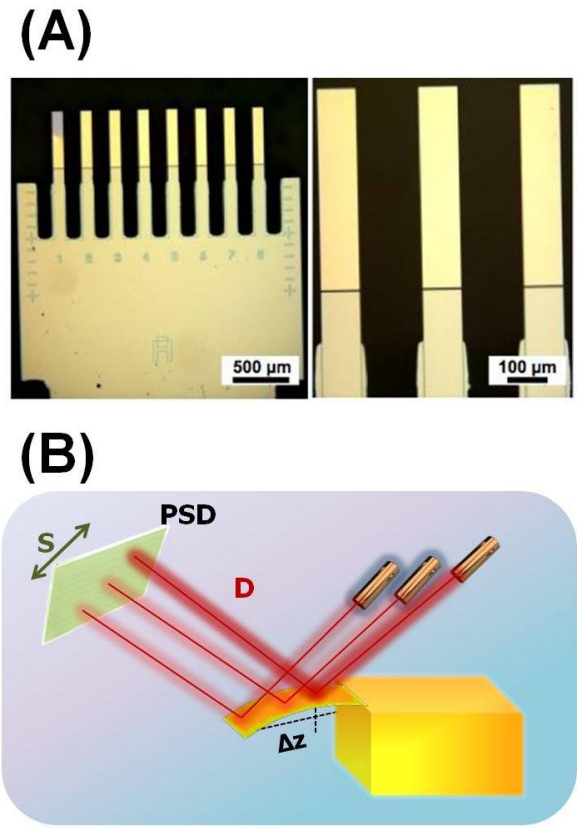

Figure 2.11: (A) Silicon chips with arrays of eight cantilevers used for nanomechanical measurements (Micromotive GmbH). (B) Scheme displaying the experimental setup used to evaluate the thermal response of LYS, BSA and Omp2a proteins.

Figure 2.12 shows the resonance frequency shift of at least 16 LYS-, BSA- and Omp2a-functionalized cantilevers. As it can be seen, the frequency shift value is significantly higher for Omp2a than for BSA and LYS. Provided the molecular weight of Omp2a is smaller than of BSA (*i.e.* 39 kDa vs 66.5 kDa), the formation of relatively big supramolecular aggregates is clearly evidenced. This feature is corroborated by comparing nanomechanical first mode resonances of hydroxylated and functionalized cantilevers (Figure 2.12), which provides a shift of 92, 182 and 313

Hz for LYS, BSA and Omp2a, respectively. On the other hand, the standard error of the mean calculated for Omp2a is significantly higher than for LYS and BSA. This has been attributed to the variability in the size of the Omp2a supramolecular aggregates, which induces fluctuations in the measured frequency shift values. However, it should be remarked that differences among LYS, BSA and Omp2a are large enough to be independent of such uncertainty.

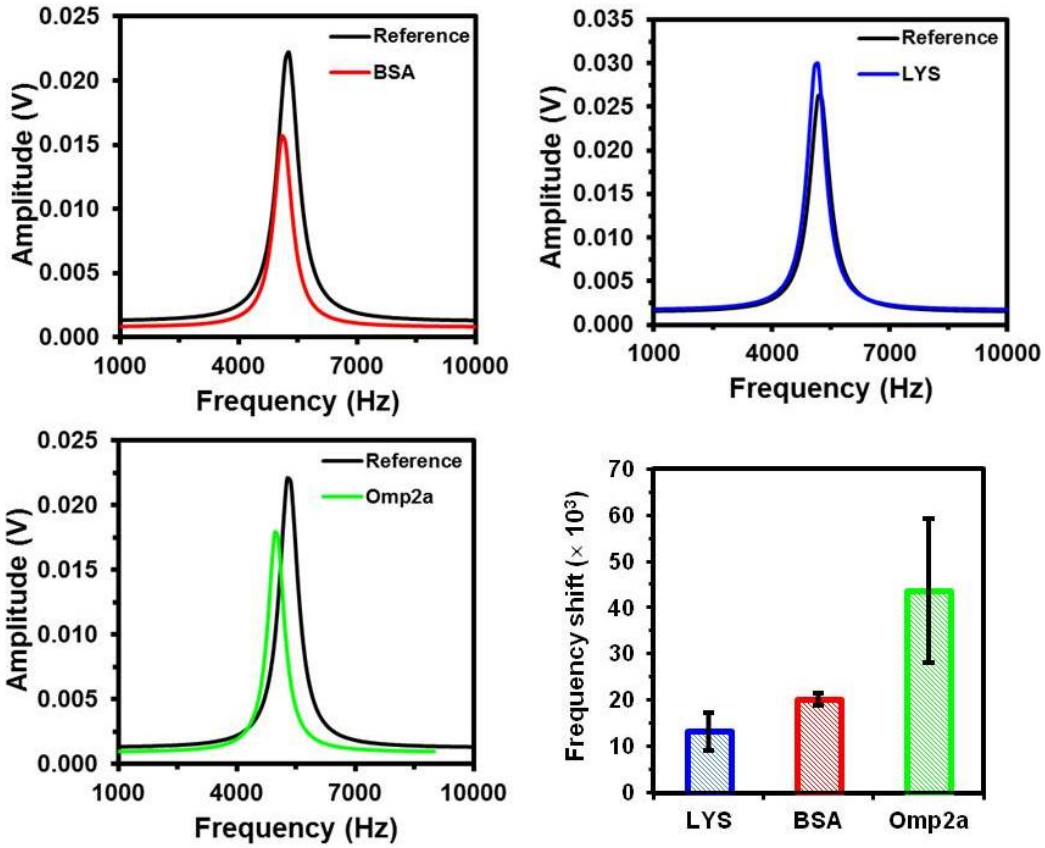

Figure 2.12: Nanomechanical resonance response of a silicon cantilever functionalized with LYS, BSA and Omp2a. The shift with respect to the hydroxylated (non-functionalized) cantilever used as reference is displayed. Resonance frequency shift (|Δf|/f), of functionalized cantilevers (mean values and standard error of the mean calculated with the data of at least 16 different cantilevers).

The resonance frequency of non-modified cantilevers (ω), which depends on their spring rigidity (k) and effective mass (M), is obtained by the elasticity theory as:

$$\omega = \frac{1}{2\pi}\sqrt{\frac{k}{M}} \qquad (1)$$

The constant k is obtained using the cantilever Young modulus (E) and dimensions, length (L), width (W) and thickness (T) [51]:

$$k = \frac{EWT}{4L^3} \qquad (2)$$

Upon protein-functionalization, the resonance frequency changes from ω to ν:

$$\nu = \omega + \Delta\omega = \frac{1}{2\pi}\sqrt{\frac{k}{M+m} + \Gamma(k,\eta)} \qquad (3)$$

where $\Delta\omega$ is the resonance frequency contribution due to the tethering of the protein, m is the total mass of the protein, and Γ is a function that depends on k and the surface stress (η) induced by protein···silicon surface interactions [52]. Particularly, the difference in frequency shift ($\Delta\omega/\omega$ x 10^3) for LYS, BSA and Omp2a was 13.2 ± 4.1, 20.2 ± 1.4 and 43.6 ± 15.6, respectively. These resonance frequency shifts suggest that protein···surface interactions predominate over m since the shift is two times higher for Omp2a than for BSA, whereas the molecular weight is 1.7 times higher for the latter than for the former. Accordingly, protein···surface interactions can be considered as a nanomechanical signature sensitive not only to the existence of protein aggregation phenomena but also to the distribution of the molecules in such aggregates.

The thermal response of proteins have been analyzed by plotting the displacement (S) of the reflected laser spot on the position sensitive detector (PSD), which originates from the variation of the local slope at the cantilever surface with the temperature and depends on the distance (D) between the cantilever and the PSD (Figure 2.11). It is worth noting that the variation of S with the temperature is analogous to the thermally induced cantilever deflection (Δz). As it was expected, the displacement of non-functionalized cantilevers increases slowly and progressively with the temperature (Figure 2.13), as the deflection of rectangular bare cantilevers of length L grows linearly with the change of temperature (ΔT), that is $\Delta z \propto L^2 \Delta T$ [53].

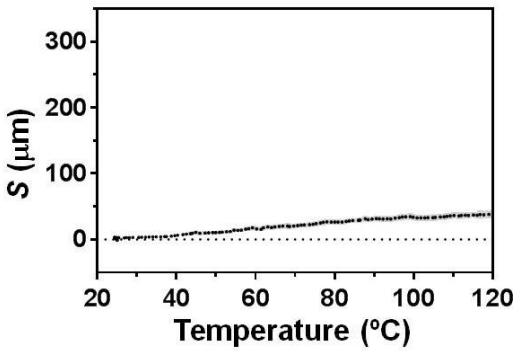

Figure 2.13: Relative displacement as a function of the temperature of a representative hydroxylated (non-functionalized) cantilever.

The average displacement curve obtained for LYS (Figure 2.14), which was obtained using 16 different microcantilever sensors, reflects a behaviour very different from that obtained for non-functionalized cantilevers. The slope of the displacement curve in the region comprised from room temperature to ~50°C is related to the deflection produced by the different thermal response of the two materials contained in the system (*i.e.* the silicon support and the attached proteins). More specifically, protein-functionalized cantilevers undergo a differential stress due to the thermal expansion coefficient difference between the protein and the microcantilever itself, giving rise to the cantilever deflection. After this, at ~50°C the protein starts to unfold, causing a redistribution of the mass and reducing the contact between the protein and the substrate. This situation enhances the cantilever deflection, as it is reflected by the sustained increasing displacement of the profile.

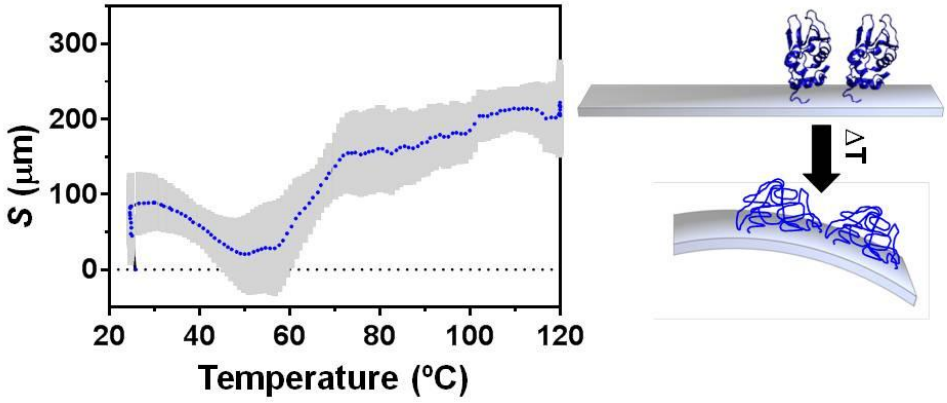

Figure 2.14: Thermomechanical response of cantivelevers functionalized with LYS proteins. Left: mean relative displacement as a function of the temperature and the corresponding standard error of the mean (thick light-grey lines), both calculated with the data of at least 7 different cantilevers. Right: cartoons representation of the folded → unfolded transitions.

Thus, the melting temperature of LYS, as determined thermomechanically, is approximately 60°C, which is consistent with the CD data. At ~70°C the slope of the displacement curve changes and the curve is similar to that observed for the hydroxylated silicon cantilevers (Figure 2.13). Thus, once LYS completes the conversion towards the unfolding state, the changes induced by the thermal dynamics of the random coil are not appearing in the deflection. At this stage the effects associated to the mass redistribution and the variation of the protein···surface interactions are negligible in average. Overall, the profile displayed for LYS should be considered as the fingerprint to recognize the thermomechanical response of conventional proteins, in which the folded → unfolded is the only occurring thermal transition.

Figure 2.15 displays the average displacement curve achieved for BSA. From a qualitative point of view, the behaviour of the curve is similar to that described above for LYS until ~100°C, even though the cantilever deflection is smaller for BSA. This has been attributed to the higher molecular weight of BSA and its tendency to aggregate, both reducing the differences in the stress distribution and the stress gradient between the protein and the substrate. Consequently, the impact of the bimetallic effects in the bending of the cantilever is relatively small before the protein denaturation at ~60°C. Moreover, the effect of the redistribution of the mass during the unfolding process is also smaller than for LYS. As the effect of the unfolding on the cantilever displacement is expected to be directly proportional to the amount of protein molecules, these results suggest that such amount is lower for cantilevers functionalized with BSA than with LYS. Although this could be in apparent contradiction with the nanomechanical first mode resonance shift, which is 90 Hz lower for the latter (Figure 2.12), it is worth noting that the molecular weight of BSA is four times higher than that of LYS.

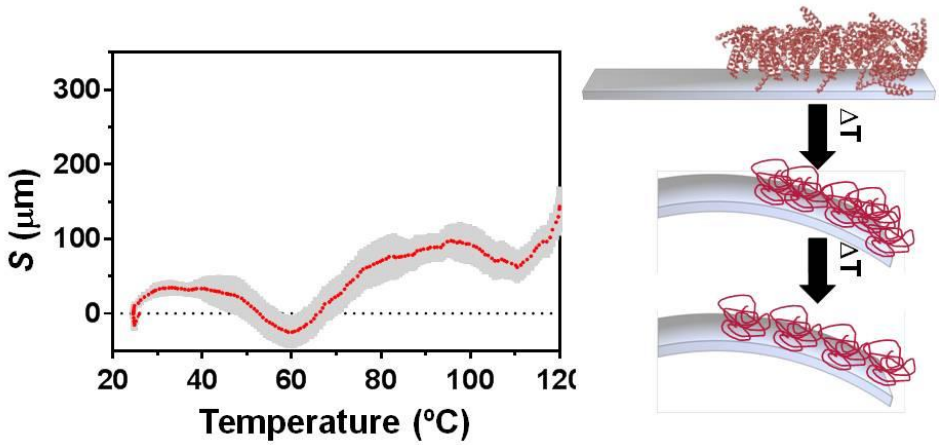

Figure 2.15: Thermomechanical response of cantivelevers functionalized with BSA proteins. Left: mean relative displacement as a function of the temperature and the corresponding standard error of the mean (thick light-grey lines), both calculated with the data of at least 7 different cantilevers. Right: cartoons representation of the folded → unfolded transitions.

In spite of this, the dynamics of the random coil causes a change in the cantilevers deflection. Thus, deflection downwards or upwards of the cantilever is mainly defined by the response of the protein within the studied temperature range and, as mentioned above, the deflection was relatively low before the unfolding. After this, the upward profile experiences an abrupt change at ~110°C, which is not detected for LYS. Although this sudden drop in the displacement could be hypothesized as a disaggregation of the proteins, a simple thermogravimetric analysis evidenced that it corresponds to the evaporation of water molecules that were strongly interacting with the protein. Accordingly, in addition to the molecular unfolding, thermomechanical characterization of BSA reveals sharp dehydration process that, suddenly, produces a change of the deflection.

The displacement profile recorded for Omp2a (Figure 2.16) exhibits unusual complexity. Although bimetallic effect initially affects the cantilever deflection, as in LYS and BSA, four regions can be distinguished above 40°C for Omp2a. In the first one, which extends from 40°C to 60°C, the variation of the displacement is practically null, suggesting that the redistribution of the molecular masses and the changes in the protein···substrate interactions are minimum (*region I*). This region has been associated with the alteration of intermolecular interactions before the transition from trimers to bigger aggregates, which is also consistent with WAXD observations. While initially they seem to become more intense, the step prior to the conversion into bigger aggregate is characterized by a weakening of interactions among neighbouring Omp2a molecules in trimers. This phase transition is evidenced by the increasing displacement (*region II*), which occurs in a relatively wide interval of temperatures (*i.e.* between ~60°C and ~77°C). After this (*region III*), the displacement undergoes small fluctuations, the average deflection increment along the whole region being very small. These fluctuations have been associated with local re-organizations in the newly formed aggregates. Above 105°C, the displacement drops sharply (*region IV*), suggesting that at such high temperatures the thermal stability of the β-barrel is finally lost. Therefore, the downward deflection of the cantilevers is a consequence of the folded → unfolded transition that alters both the mass distribution and the Omp2a···substrate interactions. These observations are fully consistent with the WAXD results.

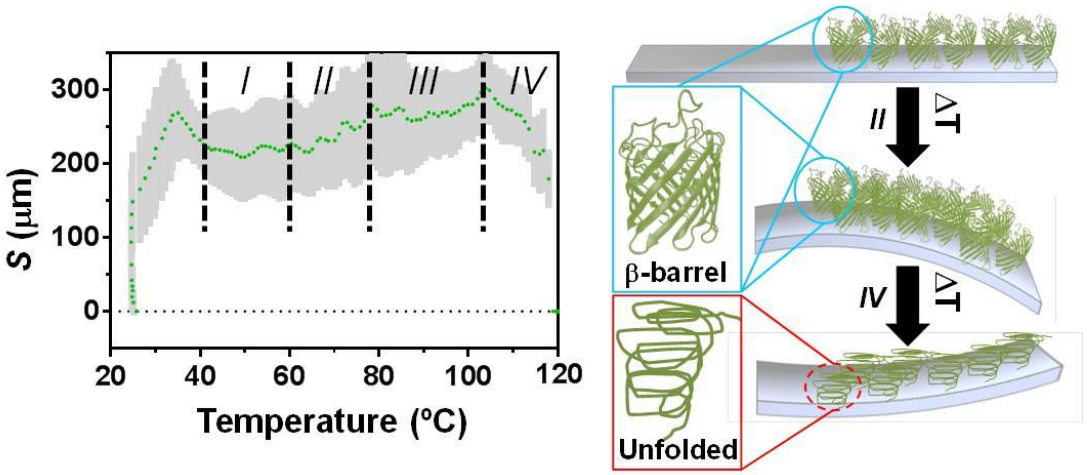

Figure 2.16: Thermomechanical response of cantivelevers functionalized with Omp2a proteins. Left: mean relative displacement as a function of the temperature and the corresponding standard error of the mean (thick light-grey lines), both calculated with the data of at least 7 different cantilevers. Right: cartoons representation of the trimer → large aggregate and β-barrel → unfolded transitions.

In addition to the mass redistribution onto the cantilever surface, which causes changes in the resonance frequency, and to the bimetallic effect, the main mechanical effect in microcantilevers is the surfaces stress (σ) that induces a nanoscale bending [2]. This effect, which occurs if only one of both cantilever sides are coated or, as in this work, functionalized, is quantified using the Stoney's equation [54]:

$$\sigma = \frac{1}{3}\left(\frac{T}{L}\right)^2 \frac{E}{1-\nu}\Delta z \qquad (4)$$

where L is the microcantilever effective length (450 μm), T is the microcantilever thickness (1 μm), E is the Young modulus of silicon (150 GPa), ν is the Poisson ratio of silicon (0.17) and Δz is the deflection of the cantilever. The surface stress is frequently associated to intermolecular interactions between molecules anchored onto the cantilever surface, such as van der Waals forces, hydrogen bonds, electrostatic interactions, steric repulsions, etc. Ideally, protein-functionalized cantilevers should not exhibit any static surface stress if the functionalization was identical for both sides. However, in practice, the experimental set-ups used during the functionalization process do not result in two identical cantilever sides. As a consequence, the surface stress is not negligible for protein-functionalized cantivelers. At 120°C, σ = 0.46 ± 0.12, 0.31 ± 0.05 and 0.30 ± 0.15 mN/m for LYS, BSA and Omp2a, respectively (Figure 2.17). This is significantly higher than the value for hydroxylated non-functionalized cantilevers (*e.g.* at 120°C, σ= 0.08 ± 0.012 mN/m). Moreover, the surface stress experiences a significant increment when the temperature is higher than ~50°C for all functionalized cantivelers (Figure 2.17).

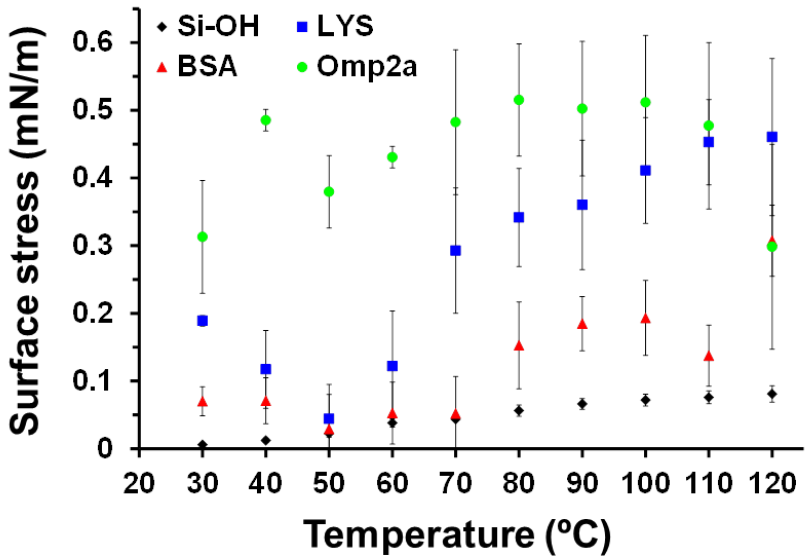

Figure 2.17: Variation of the surface stress for hydroxylated (control) and protein-functionalized cantilevers against the temperature.

Analyses of the displacement curves obtained for protein-functionalized cantilevers allowed distinguishing folded → unfolded conformational transitions from phase changes related with protein aggregates. Thus, the thermally-induced increment in the deflection of protein-functionalized cantilevers is not constant, as occurs for non-functionalized cantilevers. Proteins are much more sensitive than silicon to the temperature and, therefore, the general evolution of the displacement observed at relatively low temperatures (< 50°C) is mainly due to the differences in both stress distribution and stress gradient between the protein and the silicon substrate (*i.e.* the bimetallic effect). In such conditions, the bending of protein-functionalized cantilevers depends on the molecular weight and the presence of aggregates.

Conventional proteins exhibit an abrupt change in the evolution of the curve, which is ascribed to their unfolding process. This folded → unfolded transition occurs at temperatures close to ~50°C and ~60°C for LYS and BSA, respectively, which are lower than those observed in water (60-70°C). Consequently, in solution the folded structure of these soluble proteins is stabilized by intermolecular hydrogen bonds with surrounding water molecules, which are loss upon removal of the solvent. This instability induces a lower unfolding temperature.

2. Thermomechanical response of Omp2a

Once the denatured protein reaches a stable random coil, the dynamics of this state should not affect the thermomechanical response of the cantilever. This is true for LYS- and BSA-functionalized substrates, which show a behavior similar to that of non-functionalized cantilevers when the temperature exceeds ~55 and ~60°C, respectively. However, BSA-functionalized cantilevers display another transition at 110°C that has been ascribed to the evaporation of water molecules strongly interacting with protein molecules.

The thermomechanical response of Omp2a is more complex than those of LYS and BSA because of both its intrinsic thermal stability and the tendency to form not only trimers but also larger aggregates. The thermal behavior of this porin is characterized by local re-organizations, which affect the strength of intermolecular interactions among neighbouring Omp2a molecules, inducing the transition from trimers to larger aggregates. The formation of such larger aggregates is consistent not only with DLS results but also with previous TEM investigations [1]. The latter phase transition is poorly defined, as reflects the continuous increase of the displacement in the temperature interval comprised between ~60°C and ~77°C. This feature should be attributed to the fact that the size and shape of the aggregates formed at such temperatures are constrained by the functionalization of the cantilever, which defines the tethering position of the protein molecules and gives variability to the transition. Such heterogeneity explains the undefined character of the transition that, in spite of the monodisperse and precise chemical nature of Omp2a molecules, occurs within a wide interval of temperatures rather than at a precise temperature. On the other hand, the thermal unfolding of Omp2a is detected at ~105°C, this temperature representing the upper threshold in relation to the manipulation of stable protein aggregates.

2.4. Conclusion

In summary, thermomechanical measurements at the microscopic level on functionalized cantilevers have provided molecular insights that complement the information obtained from conventional characterization techniques on ensembles formed by a very large number of molecules. A serious limitation of conventional techniques is that they provide only a sample average response and are unable to give information on specific local features on or within the sample. Within this context, the unique thermomechanical response of Omp2a-functionalized cantilevers, which exhibits four well-defined regimes above 40°C, suggests practical approaches to improve the efficacy of smart biomimetic NMs with porins immobilized onto the surface or confined inside synthetic pores. Specifically, although the effectiveness of NMs is regulated by the amount of porin molecules active for the ion transport, controlling their orientation once immobilized onto the surface or inside nanopores is a challenge that has not been achieved yet. However, the identification of temperature intervals in which protein molecules experience local structural re-arrangements with an enhancement of intermolecular interactions, suggests that soft post-thermal treatments could be very advantageous to improve the efficacy of the NMs. Thus, this could be achieved by heating the proteins from their initial assembly state to denaturalization and, subsequently, cooling under controlled conditions to maximize favorable interactions. The amount of protein molecules contributing to the selective ion transport substrate could be substantially increased by enhancing the intermolecular interactions.

2.5. Bibliography

[1] A. Puiggalí-jou, M. M. Pérez-madrigal, L. J. del Valle, E. Armelin, M. T. Casas, C. Michaux, E. A. Perpète, F. Estrany, C. Alemán, L. J. Valle, E. Armelin, M. T. Casas, C. Michaux, E. A. Perpète, F. Estrany, and C. Alemán, "Confinement of a β-barrel protein in nanoperforated free-standing nanomembranes for ion transport," *Nanoscale*, 8, 38, 16922–16935, 2016.

[2] J. Tamayo, P. M. Kosaka, J. J. Ruz, Á. San Paulo, and M. Calleja, "Biosensors based on nanomechanical systems," *Chem. Soc. Rev.*, 42, 3, 1287–1311, 2013.

[3] M. Li, H. X. Tang, and M. L. Roukes, "Ultra-sensitive NEMS-based cantilevers for sensing, scanned probe and very high-frequency applications," *Nat. Nanotechnol.*, 2, 2, 114–120, 2007.

[4] J. Chaste, A. Eichler, J. Moser, G. Ceballos, R. Rurali, and A. Bachtold, "A nanomechanical mass sensor with yoctogram resolution," *Nat. Nanotechnol.*, 7, 5, 301–304, 2012.

[5] J. W. Ndieyira, M. Watari, A. D. Barrera, D. Zhou, M. Vögtli, M. Batchelor, M. A. Cooper, T. Strunz, M. A. Horton, C. Abell, T. Rayment, G. Aeppli, and R. A. McKendry, "Nanomechanical detection of antibiotic–mucopeptide binding in a model for superbug drug resistance," *Nat. Nanotechnol.*, 3, 11, 691–696, 2008.

[6] P. M. Kosaka, J. Tamayo, J. J. Ruz, S. Puertas, E. Polo, V. Grazu, J. M. de la Fuente, and M. Calleja, "Tackling reproducibility in microcantilever biosensors: a statistical approach for sensitive and specific end-point detection of immunoreactions," *Analyst*, 138, 3, 863–872, 2013.

[7] M. Soccio, G. Luongo, C. Esteves, A. Salvador-Matar, O. Ahumada, D. R. Rueda, M. C. García-Gutiérrez, N. Lotti, A. Munari, and T. A. Ezquerra, "Thermomechanical response of a semicrystalline polymer in the vicinity of the melting by using microcantilever technology," *Appl. Phys. Lett.*, 104, 25, 251904, 2014.

[8] O. Ahumada, M. M. Pérez-Madrigal, J. Ramirez, D. Curcó, C. Esteves, A. Salvador-Matar, G. Luongo, E. Armelin, J. Puiggalí, and C. Alemán, "Sensitive thermal transitions of nanoscale polymer samples using the bimetallic effect: Application to ultra-thin polythiophene," *Rev. Sci. Instrum.*, 84, 5, 053904, 2013.

[9] E. Rebollar, M. Sanz, C. Esteves, N. F. Martínez, Ó. Ahumada, and M. Castillejo, "Gold coating of micromechanical DNA biosensors by pulsed laser deposition," *J. Appl. Phys.*, 112, 8, 084330, 2012.

[10] G.-G. Bumbu, M. Wolkenhauer, G. Kircher, J. S. Gutmann, and R. Berger, "Micromechanical Cantilever Technique: A Tool for Investigating the Swelling of Polymer Brushes," *Langmuir*, 23, 4, 2203–2207, 2007.

[11] M. del Rey, R. A. da Silva, D. Meneses, D. F. S. Petri, J. Tamayo, M. Calleja, and P. M. Kosaka, "Monitoring swelling and deswelling of thin polymer films by microcantilever sensors," *Sensors Actuators B Chem.*, 204, 602–610, 2014.

[12] C. M. Domínguez, D. Ramos, J. I. Mendieta-Moreno, J. L. G. Fierro, J. Mendieta, J. Tamayo, and M. Calleja, "Effect of water-DNA interactions on elastic properties of DNA self-assembled monolayers," *Sci. Rep.*, 7, 1, 536, 2017.

[13] O. Malvar, J. J. Ruz, P. M. Kosaka, C. M. Domínguez, E. Gil-Santos, M. Calleja, and J. Tamayo, "Mass and stiffness spectrometry of nanoparticles and whole intact bacteria by multimode nanomechanical resonators," *Nat. Commun.*, 7, 1, 13452, 2016.

[14] A. K. Naik, M. S. Hanay, W. K. Hiebert, X. L. Feng, and M. L. Roukes, "Towards single-molecule nanomechanical mass spectrometry," *Nat. Nanotechnol.*, 4, 7, 445–450, 2009.

[15] Y. Shen, P. O. Saboe, I. T. Sines, M. Erbakan, and M. Kumar, "Biomimetic membranes: A review," *J. Memb. Sci.*, 454, 359–381, 2014.

[16] M. Ali, S. Nasir, Q. H. Nguyen, J. K. Sahoo, M. N. Tahir, W. Tremel, and W. Ensinger, "Metal Ion Affinity-based Biomolecular Recognition and Conjugation inside Synthetic

Polymer Nanopores Modified with Iron–Terpyridine Complexes," *J. Am. Chem. Soc.*, 133, 43, 17307–17314, 2011.

[17] X. Hou, W. Guo, and L. Jiang, "Biomimetic smart nanopores and nanochannels," *Chem. Soc. Rev.*, 40, 5, 2385, 2011.

[18] M. M. Pérez-Madrigal, L. J. del Valle, E. Armelin, C. Michaux, G. Roussel, E. A. Perpète, and C. Alemán, "Polypyrrole-Supported Membrane Proteins for Bio-Inspired Ion Channels," *ACS Appl. Mater. Interfaces*, 7, 3, 1632–1643, 2015.

[19] X. Zhang, W. Fu, C. G. Palivan, and W. Meier, "Natural channel protein inserts and functions in a completely artificial, solid-supported bilayer membrane.," *Nat. Sci. reports*, 3, 1, 2196, 2013.

[20] A. R. Hall, A. Scott, D. Rotem, K. K. Mehta, H. Bayley, and C. Dekker, "Hybrid pore formation by directed insertion of α-haemolysin into solid-state nanopores," *Nat. Nanotechnol.*, 5, 12, 874–877, 2010.

[21] S. Balme, J.-M. Janot, L. Berardo, F. Henn, D. Bonhenry, S. Kraszewski, F. Picaud, and C. Ramseyer, "New Bioinspired Membrane Made of a Biological Ion Channel Confined into the Cylindrical Nanopore of a Solid-State Polymer.," *Nano Lett.*, 11, 2, 712–716, 2011.

[22] G. Roussel, A. Matagne, X. De Bolle, E. A. a. Perpète, and C. Michaux, "Purification, refolding and characterization of the trimeric Omp2a outer membrane porin from Brucella melitensis," *Protein Expr. Purif.*, 83, 2, 198–204, 2012.

[23] G. Roussel, E. A. Perpète, A. Matagne, E. Tinti, and C. Michaux, "Towards a universal method for protein refolding: The trimeric beta barrel membrane Omp2a as a test case," *Biotechnol. Bioeng.*, 110, 2, 417–423, 2013.

[24] L. Whitmore and B. A. Wallace, "Protein secondary structure analyses from circular dichroism spectroscopy: Methods and reference databases," *Biopolymers*, 89, 5, 392–400, 2008.

[25] L. Lechuga Gomez, V. Alvarez-Sanchez, and F. J. Tamayo de Miguel, "System and method for detecting the displacement of a plurality of micro- and nanomechanical elements, such as micro-cantilevers," 7,646,494 B2, 2010.

[26] F. J. Tamayo de Miguel, J. Mertens, and M. Calleja-Gomez, "System and method for the inspection of micro and nanomechanical structures," 7,978,344 B2, 2011.

[27] M. S. Weiss, G. J. Palm, and R. Hilgenfeld, "Crystallization, structure solution and refinement of hen egg-white lysozyme at pH 8.0 in the presence of MPD," *Acta Crystallogr. Sect. D Biol. Crystallogr.*, 56, 8, 952–958, 2000.

[28] K. A. Majorek, P. J. Porebski, A. Dayal, M. D. Zimmerman, K. Jablonska, A. J. Stewart, M. Chruszcz, and W. Minor, "Structural and immunologic characterization of bovine, horse, and rabbit serum albumins," *Mol. Immunol.*, 52, 3–4, 174–182, 2012.

[29] M. Lopes-Rodrigues, D. Zanuy, C. Alemán, C. Michaux, and E. A. Perpète, "3D structure of a Brucella melitensis porin: molecular modelling in lipid membranes," *J. Biomol. Struct. Dyn.*, 1–13, 2018.

[30] K. Zeth and M. Thein, "Porins in Prokaryotes and Eukaryotes: Common Themes and Variations," *Biochem. J.*, 431, 1, 13–22, 2010.

[31] L. K. Tamm, H. Hong, and B. Liang, "Folding and assembly of β-barrel membrane proteins," *Biochim. Biophys. Acta - Biomembr.*, 1666, 1–2, 250–263, 2004.

[32] C. P. Moon, N. R. Zaccai, P. J. Fleming, D. Gessmann, and K. G. Fleming, "Membrane protein thermodynamic stability may serve as the energy sink for sorting in the periplasm," *Proc. Natl. Acad. Sci.*, 110, 11, 4285–4290, 2013.

[33] J. H. Kleinschmidt, "Folding and Stability of Monomeric β-Barrel Membrane Proteins," in *Protein-Lipid Interactions*, Weinheim, FRG: Wiley-VCH Verlag GmbH & Co. KGaA, 2006, 27–56.

[34] F. Rodríguez-Ropero, M. Fioroni, and T. Dworeck, *Channel Proteins as Tools in Nanotechnology*, Biology, B. Springer, 2014.

[35] K. Murayama and M. Tomida, “Heat-Induced Secondary Structure and Conformation Change of Bovine Serum Albumin Investigated by Fourier Transform Infrared Spectroscopy,” *Biochemistry*, 43, 36, 11526–11532, 2004.

[36] N. J. Greenfield, “Using circular dichroism collected as a function of temperature to determine the thermodynamics of protein unfolding and binding interactions,” *Nat. Protoc.*, 1, 6, 2527–2535, 2007.

[37] F. Meersman, C. Atilgan, A. J. Miles, R. Bader, W. Shang, A. Matagne, B. A. Wallace, and M. H. J. Koch, “Consistent Picture of the Reversible Thermal Unfolding of Hen Egg-White Lysozyme from Experiment and Molecular Dynamics,” *Biophys. J.*, 99, 7, 2255–2263, 2010.

[38] T. Knubovets, J. J. Osterhout, P. J. Connolly, and A. M. Klibanov, “Structure, thermostability, and conformational flexibility of hen egg-white lysozyme dissolved in glycerol,” *Proc. Natl. Acad. Sci.*, 96, 4, 1262–1267, 1999.

[39] P. Saha, C. Manna, J. Chakrabarti, and M. Ghosh, “Reversible thermal unfolding of a yfdX protein with chaperone-like activity,” *Sci. Rep.*, 6, 1, 29541, 2016.

[40] W. L. Stoppel, J. C. White, S. D. Horava, S. R. Bhatia, and S. C. Roberts, “Transport of biological molecules in surfactant–alginate composite hydrogels,” *Acta Biomater.*, 7, 11, 3988–3998, 2011.

[41] C. R. Chen and G. I. Makhatadze, “Molecular Determinants of Temperature Dependence of Protein Volume Change upon Unfolding,” *J. Phys. Chem. B*, 121, 35, 8300–8310, 2017.

[42] T. V. Chalikian and K. J. Breslauer, “On volume changes accompanying conformational transitions of biopolymers,” *Biopolymers*, 39, 5, 619–626, 1998.

[43] S. E. Hill, T. Miti, T. Richmond, and M. Muschol, “Spatial Extent of Charge Repulsion Regulates Assembly Pathways for Lysozyme Amyloid Fibrils,” *PLoS One*, 6, 4, e18171, 2011.

[44] S. K. Maji, L. Wang, J. Greenwald, and R. Riek, “Structure-activity relationship of amyloid fibrils,” *FEBS Lett.*, 583, 16, 2610–2617, 2009.

[45] D. Eisenberg, “The discovery of the -helix and -sheet, the principal structural features of proteins,” *Proc. Natl. Acad. Sci.*, 100, 20, 11207–11210, 2003.

[46] S. Sukumaran, K. Hauser, E. Maier, R. Benz, and W. Mäntele, “Structure–function correlation of outer membrane protein porin fromParacoccus denitrificans,” *Biopolymers*, 82, 4, 344–348, 2006.

[47] S. Sukumaran, C. Zscherp, and W. Mäntele, “Investigation of the thermal stability of porin from *Paracoccus denitrificans* by site-directed mutagenesis and Fourier transform infrared spectroscopy,” *Biopolymers*, 74, 1–2, 82–86, 2004.

[48] T. F. Solov’eva, G. N. Likhatskaya, V. A. Khomenko, A. M. Stenkova, N. Y. Kim, O. Y. Portnyagina, O. D. Novikova, E. V. Trifonov, E. A. Nurminski, and M. P. Isaeva, “A Novel OmpY Porin From *Yersinia Pseudotuberculosis* : Structure, Channel-Forming Activity and Trimer Thermal Stability,” *J. Biomol. Struct. Dyn.*, 28, 4, 517–533, 2011.

[49] N. F. Martínez, P. M. Kosaka, J. Tamayo, J. Ramírez, O. Ahumada, J. Mertens, T. D. Hien, C. V. Rijn, and M. Calleja, “High throughput optical readout of dense arrays of nanomechanical systems for sensing applications,” *Rev. Sci. Instrum.*, 81, 12, 125109, 2010.

[50] A. Puiggalí-Jou, L. J. del Valle, C. Alemán, and M. M. Pérez-Madrigal, “Weighing biointeractions between fibrin(ogen) and clot-binding peptides using microcantilever sensors,” *J. Pept. Sci.*, 23, 2, 162–171, 2017.

[51] M. Alvarez and L. M. Lechuga, “Microcantilever-based platforms as biosensing tools,” *Analyst*, 135, 5, 827, 2010.

[52] K. S. Hwang, K. Eom, J. H. Lee, D. W. Chun, B. H. Cha, D. S. Yoon, T. S. Kim, and J. H. Park, “Dominant surface stress driven by biomolecular interactions in the dynamical response of nanomechanical microcantilevers,” *Appl. Phys. Lett.*, 89, 17, 173905, 2006.

[53] J. R. Barnes, R. J. Stephenson, C. N. Woodburn, S. J. O’Shea, M. E. Welland, T. Rayment,

J. K. Gimzewski, and C. Gerber, “A femtojoule calorimeter using micromechanical sensors,” *Rev. Sci. Instrum.*, 65, 12, 3793–3798, 1994.

[54] G. Thakur, K. Jiang, D. Lee, K. Prashanthi, S. Kim, and T. Thundat, “Investigation of pH-Induced Protein Conformation Changes by Nanomechanical Deflection,” *Langmuir*, 30, 8, 2109–2116, 2014.

3. Effect of nanofeatures on the thermal transitions of PLA films

3. Effect of nanofeatures on the thermal transitions of PLA films

Summary

The influence of structural nanofeatures in the glass transition and cold crystallization temperatures (T_g and T_{cc}) of poly(lactic acid) (PLA) ultra-thin films has been investigated using a technology that detects the microcantilever deflection as a function of the temperature. Measurements have been conducted on arrays of 8-cantilevers spin-coated with PLA films with thickness of ~150 nm and weight of 6-9 ng. The deflection profiles recorded for compact, nanopored and nanoperforated PLA films of 120-1250 nm in thickness indicate that both nanopores and nanoperforations cause an increment of 7-12 ºC in the T_g while only the latter affect the T_{cc}, which increases by ~8 ºC. These phenomena have been attributed to the stress of the PLA molecules located at the interface of the pores and perforations and to the film-air interface effect, which is associated to the 2D nature of ultra-thin films. On the other hand, the thermomechanical response of PLA ultra-thin films loaded with curcumin (CUR) or stiripentol (STP), which form segregated nanodomains, also differs from that of unloaded PLA films. The size and abundance of CUR and STP nanodomains are directly related with the stress of the PLA chains at the interface and with the free volume, which affect the strength of the interactions and the mobility of polymer molecules (*i.e.* the T_g and the T_{cc}) with respect to neat PLA. Overall, results indicate that the thermal response of compact and homogeneous PLA ultra-thin films is close to that obtained for the bulk polymer, whereas the incorporation of nanofeatures (*i.e.* nanopores, nanoperforations and the segregated drug nanodomains) cause significant alterations in the properties of the polymeric nanosheets.

3.1. Introduction

In the last decades the use of nano- and micro-electromechanical systems (NEMs and MEMs, respectively) has become frequent for characterizing the properties of biological and synthetic macromolecules (*i.e.* proteins, DNA and polymers) at small scale. For example, these technologies have been used to study the response of such systems to pH changes [1-2], wetting and moisture uptake [3-4], swelling and de-swelling [5], the interfacial tension [6], the molecular folding [7-8], and the hydration of self-assembled monolayers [9]. The main advantages of NEMs and MEMs are high sensitivity and very small sample mass (from nano to attograms). Therefore, these technologies are able to capture the effects of air-sample or liquid-sample interfaces as well as nanofeatures in the sample.

The study of thermal transition temperatures of synthetic polymers using NEMs and MEMs is a topic of great interest. For example, Jeon and co-workers examined the glass transition temperature (T_g) of polystyrene, poly(vinyl acetate) and block copolymers using NEMs, which were coated with a polymer solution using inkjet printing [10–12]. The heat induced deflection of the NEMs, which was due to changes in volume and in elastic properties of the polymers, was used to determine the T_g. Similarly, different authors studied thermal transitions in ultra-small amounts of semicrystalline poly(lactic acid) (PLA) [13], amorphous poly(methylmethacrylate) [13], poly(thiophene) [14] and semicrystalline poly(propylene azelate) [15]. More recently, MEMs has been used to study the T_g, the amorphous α and β relaxations, and the liquid crystalline transitions of polymers [16], as well as the apparent denaturation temperature (T_{ad}) and other thermal transitions of different proteins [8].

In recent studies, we developed PLA free-standing nanomembranes (FSNMs) with nanopores crossing the entire ultra-thin film thickness as a solid support for different biomedical applications. Nanopores were obtained using spin-coating combined with phase segregation processes in immiscible PLA : poly(vinyl alcohol) (PVA) mixtures, and subsequent removal of PVA domains via selective solvent etching [17]. These PLA FSNMs were proposed as bioactive platforms for tissue engineering applications and as efficient biomimetic devices for selective ion transport in biosensing and biofiltration [18]. Thus, the diameter of nanoperforations obtained using 90:10 PLA:PVA mixtures was found to fit very well to the diameter of protruding finger-like cell filopodia, which play an important role in cell migration processes, promoting cell spreading and colonization [17]. Besides, the immobilization of Omp2a β-barrel membrane proteins inside nanoperforations enhanced the selective transport of ions across flexible PLA FSNMs, ion diffusion of Na^+ and Ca^{2+} through Omp2a-filled nanopores being significantly higher than for K^+ [18].

On the other hand, 2D (films and membranes) and 3D (fibres and particles) PLA scaffolds are frequently loaded with drugs for subsequent controlled delivery [19–24]. The efficiency of the regulation mechanism and kinetics of the release usually depend on the distribution and organization of the drug into the polymeric scaffold. Thus, crucial parameters to regulate the release are the affinity between the drug and PLA matrix, which essentially depends on the polarity of the drug, its ability to form polymer···drug specific interactions and the tendency of the drug to organize into nanoaggregates forming nanophases separated from the polymeric matrix.

This work reports on the thermal analysis of different PLA samples using a cantilever deflection technology to examine the influence of nanofeatures on the response of the material. More specifically, the thermal response of nanopored, nanoperforated and drug-loaded PLA ultra-thin films has been investigated using a technique named SCALA (SCAnning Laser Analyzer) [25-26], which is based on the optical read-out of microcantilevers. Our results show that both structural features in the nanometer-length scale and drug···polymer specific interactions cause important changes in the thermal properties of PLA ultra-thin films, which cannot be observed using conventional calorimetric techniques. Moreover, deflection profiles provide relevant information related with the evolution of the polymer···polymer and drug···polymer interactions with the temperature, which can be only detected using sensitive microcantilever-based technologies.

3.2. Methods

Materials. PLA 2002D, a product of Natureworks, was kindly supplied by Nupik International (Polinyà, Spain). According to the manufacturer, this PLA has a D content of ~1.5%, a residual monomer content of 0.3%, density of 1.24 g cm^{-3}, glass transition temperature (T_g) of 55-60 °C, and melting temperature (T_m) of 155-170 °C. The number and weight average molecular weight and polydispersity index, as determined by gel permeation chromatography, is M_n= 98100 g/mol, M_w= 181000 g/mol and 1.85, respectively. PVA (87-89% hydrolysed) with M_w= 13000 – 23000 g/mol was purchased from Sigma-Aldrich. Curcumin (CUR) and stiripentol (STP) were purchased from Sigma-Aldrich. 1,1,1,3,3,3-Hexafluoroisopropanol (HFIP) was purchased from Apollo Scientific Limit (UK).

Preparation of solutions and mixtures. For the fabrication of homogeneous PLA and PVA ultra-thin films without drug loading, 10 mg/mL polymer solutions in HFIP were prepared. Nanopored and nanoperforated films were obtained by blending PLA and PVA. PLA-PVA blends with 80:20 and 90:10 PLA:PVA v/v ratios were prepared by mixing PLA (8 and 9 mg/mL, respectively) and PVA (2 and 1 mg/mL, respectively) HFIP solutions. On the other hand, drug-loaded films with 80:20 and 90:10 PLA:CUR and PLA:STP v/v ratios were obtained by mixing PLA (8 and 9 mg/mL) and drug (2 and 1 mg/mL) HFIP solutions.

Preparation of ultra-thin films. 10 µL of PLA, PVA, PLA:PVA or PVA:drug solution was dropped onto a silicon microcantilevers chip, like that displayed in Figure 3.1a. The chip was fixed on a glass holder for spin-coating. The spin-coating was performed at 3500 rpm for 60 seconds in all cases. For the preparation of nanopored and nanoperforated PLA, samples coated with PLA-PVA films were incubated in milli-Q water during 1 h for the dissolution of the PVA nanophases [18]. Spin-coating was performed with a spin-coater (WS-400BZ-6NPP/A1/AR1 Laurell Technologies Corporation). Typically, 6-9 ng films were obtained in all cases. Samples were dried under vacuum for 24 h before analysis.

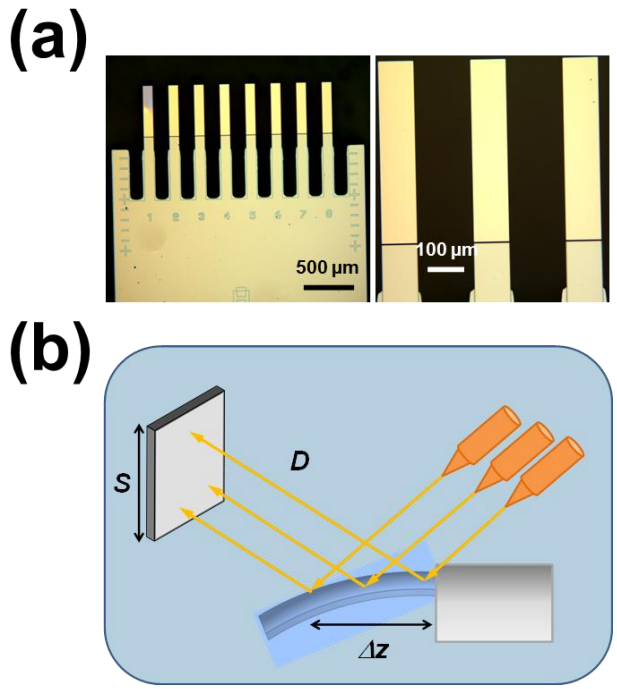

Figure 3.1: Low- and high-magnification optical images of a silicon chip of 8 microcantilevers. (b) Experimental set-up for the thermal analyses conducted with SCALA

Thermal analyses of microcantilevers. Deflection was measured by means of an equipment for the optical read-out of the microcantilevers named SCALA, (from MecWins) [25-26]. This technique combines the optical beam deflection method and the automated two-dimensional scanning of a single laser beam by voice-coil actuators. The equipment implements a thermal chamber with a thermoelectric cooler and cartridge heater. These elements are capable of sweeping the chamber's temperature by flowing thermostatized N_2 to the sample. A holder with multiple thermometer probes is placed inside the chamber for a better mapping of the temperature. All the measurements are performed in nitrogen environment to avoid the oxidation of the sample.

Figure 3.1b schematizes the experimental set-up. The cantilever array is illuminated by the laser beam and a two-dimensional linear position detector (PSD) is arranged to collect the reflected beams. Location and characterization of cantilever sensors is carried out using TRACKER, an algorithm based on the recognition of reflected intensity patterns. This capability of SCALA allows the user to characterize a single sensor or an array of them in a fully automated process. A change in the local slope at the cantilever surface results into a displacement of the reflected laser spot on the PSD, which is denoted S (Figure 3.1b). S is used to obtain the cantilever profile along its longitudinal axis, $z(x)$, by integrating:

$$z(x) = \frac{1}{2D}\int_0^x S(x')dx' - \frac{1}{4}\frac{x^2}{D}\cos\beta \quad (1)$$

where D is the distance between the cantilever and the PSD and β is the angle between the incident laser beam and the cantilever normal at its rest position.

Coated cantilevers can be used as precise thermometers by exploiting the bimaterial effect [27], which refers to the measurable bending (*i.e.* differential stress) produced by temperature changes in substrates coated on one side by another material. Similarly, coated microcantilevers undergo a deflection, Δz (Figure 3.1b), as a result of temperature changes due to the thermal expansion coefficient difference between the coating material of the cantilever and the cantilever itself [11]. The temperature control was regulated by software created by the MecWins Company. The average deflection curves discussed in this work were obtained using 16 different microcantilevers. Monocrystalline Si microcantilever chips containing arrays of eight cantilevers (Micromotive GmbH) were used for thermomechanical measurements (Figure 3.1a). Specifically, the nominal length, width, and thickness of the cantilevers were 500, 90 ± 2, and 1 μm, respectively.

Profilometry. Film thickness measurements were carried out using a Dektak 150 stylus profilometer (Veeco, Plainview, NY). Different scratches were intentionally caused on the films and measured to allow statistical analysis of data. At least eighteen independent measurements were performed for three samples of each examined condition. Imaging of the films was conducted using the following optimized settings: tip radius= 12.5 μm; stylus force= 3.0 mg; scan length= 1 mm; and speed= 100 μm/s.

Scanning electron microscopy (SEM). A Focus Ion Beam Zeiss Neon 40 instrument (Carl Zeiss, Germany) equipped with an energy dispersive X-ray (EDX) spectroscopy system and operating at 5 kV for characterization of the membranes was used. Films supported onto silicon sheets were mounted on a double-sided adhesive carbon disc and sputter-coated with an ultra-thin carbon layer (6-10 nm) to prevent sample charging problems. The diameter of the perforations was measured with the SmartTiff software from Carl Zeiss SMT Ltd.

FTIR spectroscopy. FTIR spectra were recorded on a FTIR Jasco 4100 spectrophotometer. Samples were deposited on an attenuated total reflection accessory (Top-plate) with a diamond crystal (Specac model MKII Golden Gate Heated Single Reflection Diamond ATR). For each sample, 64 scans were performed between 4000 and 600 cm^{-1} with a resolution of 4 cm^{-1}.

3.3. Results and discussion

Thermomechanical response of PLA and PVA ultra-thin films

Figure 3.2 show the ramp applied to the chips during the heating process (*i.e.* 1 ºC/min) and the thermal response of control non-coated cantilevers, which has been analysed by plotting the average deflection against the temperature. As it is expected, the deflection of uncoated cantilevers increases slowly and progressively with the temperature, as the deflection of rectangular bare cantilevers of length L grows linearly with the change of temperature (ΔT), that is $\Delta z \propto L^2 \Delta T$ [28]. However, the deflection is very small reaching a value of only -0.08 nm at 100 ºC indicating that changes discussed below for polymer-coated cantilevers are induced by the bimaterial effect (*i.e.* different thermal expansion/contraction behaviour of the polymer and the silicon cantilever). In this work, all thermal analyses with SCALA have been conducted from room temperature (25 ºC) up to 100 ºC. The latter is not only the denaturation temperature of the proteins typically used to prepare PLA nanomembranes for biofiltration but also a reasonable temperature to apply thermal treatments to drug-loaded PLA devices without causing melt [18].

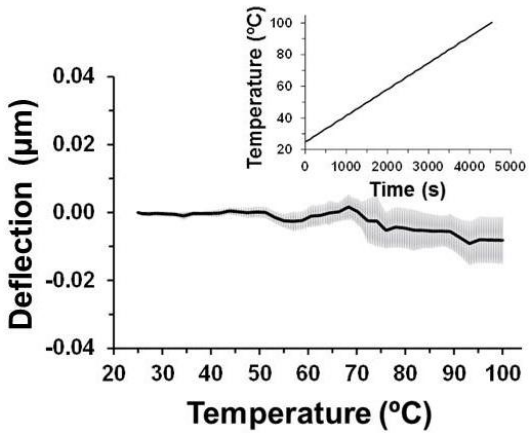

Figure 3.2: Mean deflection curves (obtained using 16 microcantilevers) measured for bare microcantilevers. In the deflection curve, the standard error of the mean is indicated by thick light-gray lines. The ramp of temperature is displayed in the inset.

PLA ultra-thin films were prepared by spin-coating a HFIP polymer solution onto previously cleaned bare microcantilevers chip. The thickness and roughness of the resulting films was 154±6 nm and 2.5±0.5 nm, respectively, indicating that they are also ultra-flat. This is evidenced in Figure 3.3a, which shows a representative SEM micrograph. Figure 3.4 shows the average deflection curve obtained for PLA, which is very different from that obtained for bare cantilevers. Thus, PLA-coated cantilevers undergo a differential stress due to the thermal expansion coefficient difference between the polymer and the silicon from the microcantilever, giving rise to significant net positive (upward)

deflection. This implies a contraction of the PLA volume, resulting from the reduction of the configurational entropy of PLA chains, which causes the reduction of the compressive forces on the silicon side of the cantilever.

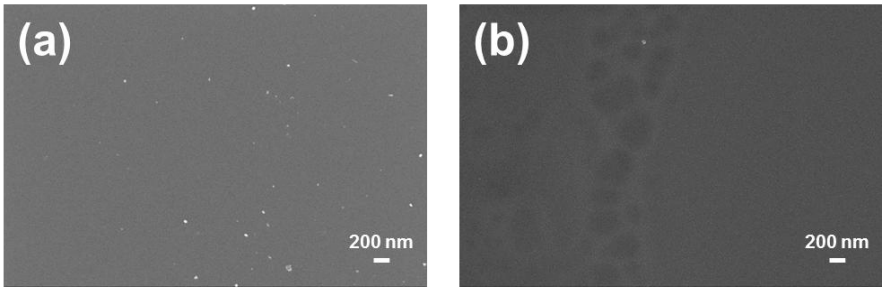

Figure 3.3: SEM micrographs of (a) PLA and (b) PVA.

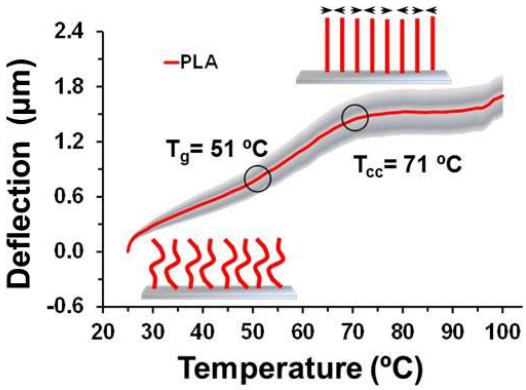

Figure 3.4: Mean deflection curves (obtained using 16 microcantilevers) measured for microcantilevers coated with PLA. In the deflection curve, the standard error of the mean is indicated by thick light-gray lines. Cartoons in schematize the tensile surface stress due to the attraction between PLA molecules, which leads to positive (upward) deflection.

The PLA deflection profile shows a subtle change in the slope that has been associated to the T_g, determined to be 51 ºC from the intersection of the tangents to the curves. This value is slightly lower that the T_g supplied by the manufacturer, which has been attributed to a small amount HFIP solvent molecules remaining after the spin-coating process. Thus, the ultra-thin nature of the film and the small weight of the sample (~8 ng) favour the plasticiser behaviour of residual HFIP solvent. After the T_g, a second change in the slope is detected at 71 ºC, associated to the crystallization of amorphous domains during heating from room temperature. This phenomenon, called cold crystallization, is observed for PLA and the cold crystallization temperature (T_{cc}) typically ranges from 70º to 165 º depending on the molecular weight and previous processing of the sample [29–33].

3. Effect of nanofeatures on the thermal transitions of PLA films

Since nanoperforated PLA ultra-thin films were prepared by blending PLA and PVA and by removing PVA domains via water etching, we decided to complete this section studying the thermomechanical response of PVA ultra-thin films. A representative SEM micrograph of such films, which exhibited thickness and roughness of 181±17 nm and 1.8±0.4 nm, respectively, is displayed in Figure 3.3b. The average deflection curve of PVA is shown in Figure 3.5. Unlike PLA, net negative (downward) deflection is observed, which has been attributed to increased repulsive forces on the silicon-coated surface of the microcantilevers. The interaction between PVA chains decreases with increasing temperature, whereas the opposite effect was detected for PLA.

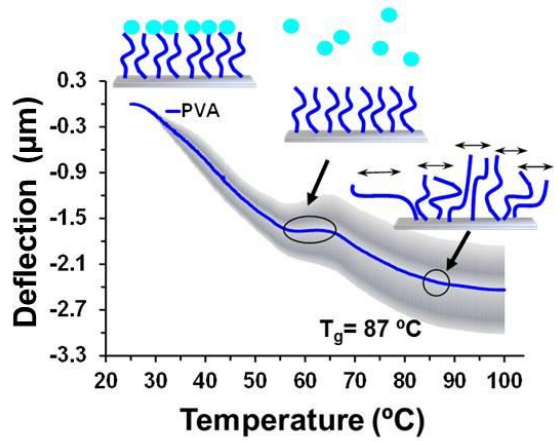

Figure 3.5: Mean deflection curves (obtained using 16 microcantilevers) measured for microcantilevers coated with PVA ultra-thin films. In the deflection curve, the standard error of the mean is indicated by thick light-gray lines. Cartoons schematize the compressive surface stress due to the repulsion between PVA molecules, which leads to negative downward deflection.

The complex deflection profile recorded for PVA shows an abrupt change in the slope starting at 56ºC, following a straight line until 66 ºC. This sharp change in the negative deflection tendency has been associated to the loss of mass produced by the detachment of superficially adsorbed water molecules. PVA is indeed a hydrophilic polymer that tends to capture water molecules at the surface. The vapour pressure of water being low, unbound of the superficially adsorbed molecules is expected at the indicated temperature interval. After this, the slope experiences a slight change that allows to determine the T_g = 87 ºC. This value is in agreement with the T_g values provided in the literature [34–36].

Thermomechanical response of nanopored and nanoperforated PLA ultra-thin films

PLA-PVA layers were deposited onto silicon microcantilevers by spin-coating 90:10 and 80:20 PLA:PVA mixtures in HFIP. As PLA and PVA are immiscible polymers, spin-coating promoted the segregation of both polymers and the subsequent formation of nanofeatures [17]. They consisted in

spherical PVA nanodomains homogeneously distributed in the resulting PLA film. According to previous work, PVA nanofeatures can be used to create nanopores or nanoperforations in PLA ultra-thin films by removing them via selective water etching [17-18]. More specifically, PVA nanofeatures transform into nanoperforations when their diameter is similar to the entire film thickness, while they create nanopores when the diameter is smaller. Moreover, both thickness and diameter depend not only on the operational conditions used for the spin-coating (see Methods section) but also on the substrate (*i.e.* silicon cantilevers in this case). It is worth noting that the use of an approach based on the combination of phase separation by spin-coating and selective solvent etching is expected to cause significant stress at the pore-air and/or perforation-air interfaces. Hereafter, solvent etched PLA ultra-thin films derived from spin-coated 90:10 and 80:20 PLA:PVA mixtures are denoted 90-PLA and 80-PLA, respectively.

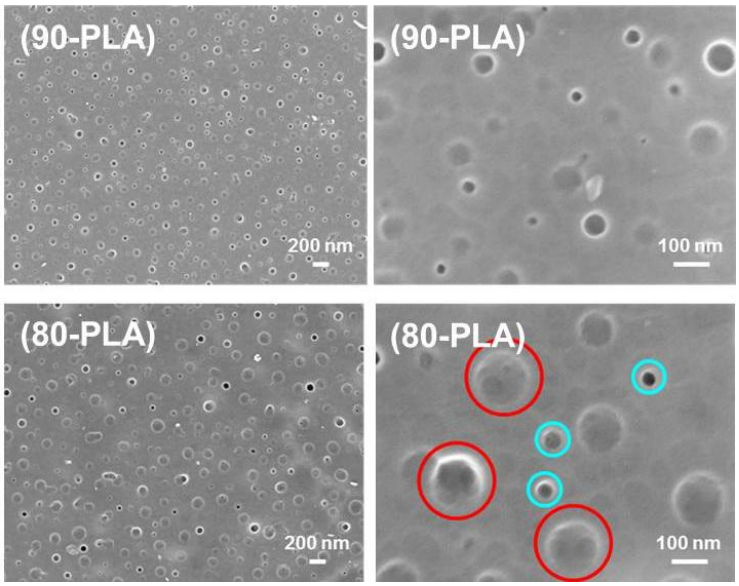

Figure 3.6: SEM micrographs of nanopored 90-PLA and nanoperforated 80-PLA. Examples of nanoperforations and nanopores are marked in (d) by red and blue circles, respectively.

The thickness of 90-PLA and 80-PLA films is 140±11 and 119±9 nm, respectively, whereas the average diameter of the created nanofeatures is 74±18 and 96±29 nm, respectively. According to such thickness / diameter ratios, the topography of these PLA nanofilms may involve nanopores and nanoperforations. Representative SEM micrographs of 90-PLA films are displayed in Figure 3.6. The surface of such nanofilms exhibits abundant nanopores of very different sizes, but in all cases smaller than ~100 nm and homogeneously distributed. In contrast, the surface of 80-PLA films can be described as distribution of both nanopores and nanoperforations, even though the former are more abundant than the latter. According to previous studies on nanoperforated PLA ultra-thin

films, nanopores and nanoperforations are distinguishable in Figure 3.6. Thus, nanoperforations correspond to nanofeatures with diameters around ~120 nm (some examples are marked with red boxes in Figure 3.6), while the diameter of nanopores is much lower, ~45 nm (some examples are marked with blue boxes in Figure 3.6). Obviously, nanofeatures affect the roughness of the films, which increases from 2.5±0.5 nm for neat PLA to 90±12 and 126±20 nm for 90-PLA and 80-PLA, respectively. More complete structural characterization of the nanoperforations was described in previous studies [17-18] and is not within the scope of this work, aiming to study the influence of nanopores and nanoperforations in the thermomechanical response of PLA nanosheets.

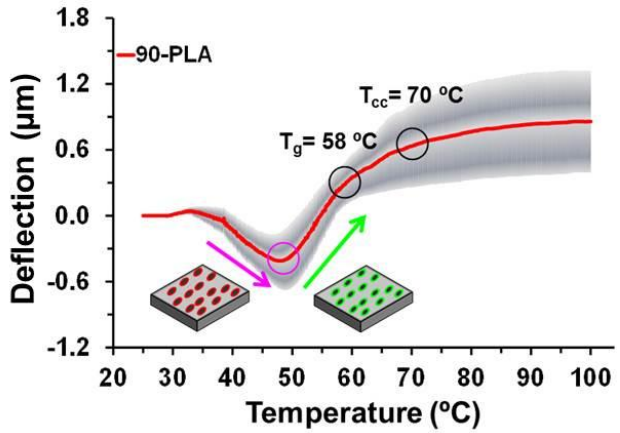

Figure 3.7: Mean deflection curves of nanopored 90-PLA ultra-thin films. Cartoons sketch of the rearrangement of the PLA molecules at the interface of the pores and perforations, which were affected by the PVA etching. Initially, molecules are stressed by repulsive interactions (red pores / perforations; negative deflection) but, after a temperature threshold, they are relaxed by attractive interactions (green pores; positive deflection).

The thermomechanical response of nanopored 90-PLA is completely different from that discussed above for the homogeneous PLA films (Figure 3.7). Two different regimes are clearly identified. The first is defined by the downward profile with negative deflection in the 32-to-48 ºC temperature interval, while the second corresponds to the subsequent ascending profile with positive deflection. This transition from one regime to the other has been interpreted as a rearrangement of the PLA molecules at the pores, which were probably stressed at the PLA–PVA interface before the water etching process. Once the PVA is removed, the increasing temperature ramp allows relaxing such interfacial molecules, changing repulsive interactions (negative deflection) into attractive ones (positive deflection). In the second regime, two changes in the slope are detected at 58 and 70 ºC, which have been associated with the T_g and T_{cc}, respectively. It is worth noting that the T_g of 90-PLA is 7 ºC higher that that found for compact PLA ultra-thin films (T_g= 51 ºC). According to previous observations, this shift is induced by the effect of film-air interface in the interactions among polymer chains [14]. Thus, the influence of the bulk and the film-air interface in nanopored

90-PLA films decreases and increases, respectively, in comparison to compact and homogeneous PLA, which was reported to increase the T_g. This phenomenon is consistent with the downward deflection at the lower temperature region (Figure 3.7), reflecting that both the surface stress and the thermal properties are affected by the interactions at the interface. On the other hand, the cold crystallization process in PLA ultra-thin films remains unaffected by the presence of nanopores, suggesting that the mobility of relaxed polymers molecules is preserved.

The thermomechanical response of 80-PLA films is completely dominated by nanofeatures (Figure 3.8). In these films, the diameter of nanopores is not only larger than in 90-PLA but also is close to the thickness of the film. Nanofeatures therefore consist in a mixture of nanopores and nanoperforations. Both elements favour the effects associated to the film-air interface in detriment of those of bulk PLA. Thus, the most striking feature of the profile obtained for 80-PLA is the continuous negative deflection indicating that repulsive interactions dominate attractive interactions throughout the whole temperature interval. Three changes in the slope of the deflection profile are detected. The first at 49 ºC has been associated to the relaxation of the PLA molecules located at the film-air interface. However, the size and depth of nanopores are significantly higher in 80-PLA than in 90-PLA. The extent of this relaxation is therefore lower in the former than in the latter, which explains the continuous negative deflection displayed in Figure 3.8. After this, two thermal transitions associated to the T_g and T_{cc} are detected at 63 ºC and 78 ºC, respectively. Again, these results indicate that the presence of nanofeatures induces a shift in the transition temperatures towards higher values. Moreover, this effect becomes more pronounced when the stress of the PLA molecules located at the interface of the pores and perforations predominate over the film-air interface associated to the 2D nature of the ultra-thin film.

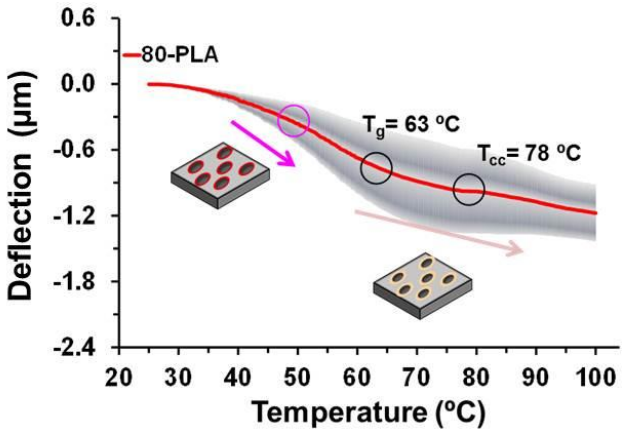

Figure 3.8: Mean deflection curves of nanoperforated 80-PLA ultra-thin films. Cartoons sketch of the rearrangement of the PLA molecules at the interface of the pores and perforations, which were affected by the PVA etching. Initially, molecules are stressed by repulsive interactions (red pores / perforations; negative

deflection) but, after a temperature threshold, they are less stressed by weaker repulsive interactions (less emphasized red perforations; negative deflection).

Thermomechanical response of PLA-drug ultra-thin films

Characterization of drug-loaded PLA ultra-thin films was performed considering curcumin (CUR), 1,7-bis(4-hydroxy-3-methoxyphenyl)-1,6-heptadiene-3,5-dione (Figure 3.9), and stiripentol (STP), (*R*,*S*)-(*E*)-4,4-dimethyl-1-[3,4(methylenedioxy)-phenyl]-1-penten-3-ol (Figure 3.10). CUR is a polyphenol soluble in lipids but not in water, which displays a wide spectrum of medical properties ranging from anti-bacterial, anti-viral, anti-protozoal, anti-fungal, and anti-inflammatory to anti-cancer activity [37–40]. However, CUR molecules were found to be unstable to a variety of physical and chemical environments (*i.e.* heat, pH, light or alkali medium), restricting its practical use. In order to overcome this drawback, researchers have encapsulated CUR into drug delivery systems improving drug stability and regulating release behaviour [41–44]. In particular, CUR-loaded PLA have shown good blood compatibility and healing properties [43-44].

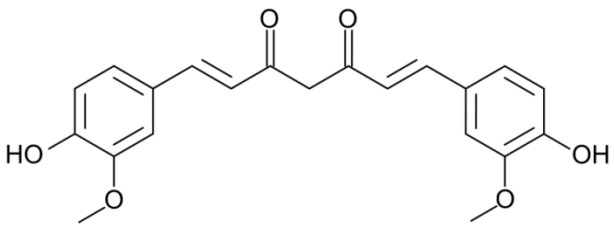

Figure 3.9: Molecular representation of curcumin

STP is an anticonvulsant drug used in the treatment of epilepsy that belongs to the group of aromatic allylic alcohols. It elevates the levels of γ-aminobutyric acid (GABA), a major inhibitory neurotransmitter that regulates electrical activity in the central nervous system [45]. The choice of STP for the present study was based on its molecular similarities with CUR. Indeed, in terms of potential intermolecular interactions, it mainly differs from CUR in the amount of hydrogen bonding acceptor and donor groups (*i.e.* CUR/STP contains 2/1 and 6/3, respectively). Thus, the integration and, indeed, the organization of CUR and STP into the PLA matrix is expected to be similar.

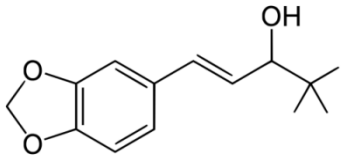

Figure 3.10: Molecular representation of striripentol

The surface morphology of films prepared using 90:10 and 80:20 PLA:CUR solutions in HFIP, hereafter denoted PLA/CUR(10) and PLA/CUR(20), respectively, is displayed in Figure 3.11. Although CUR is considered to be a lipophilic drug and, therefore, is expected to be miscible with

PLA, phase segregation occurred upon spin-coating the mixed CUR and PLA HFIP solutions. CUR separates from PLA forming well-defined phase-segregated nanodomains. This has been attributed to the hydrogen bonding capacity of CUR, which promotes the formation of CUR···CUR with respect to CUR···PLA when the solvent rapidly evaporates through the spin-coating process.

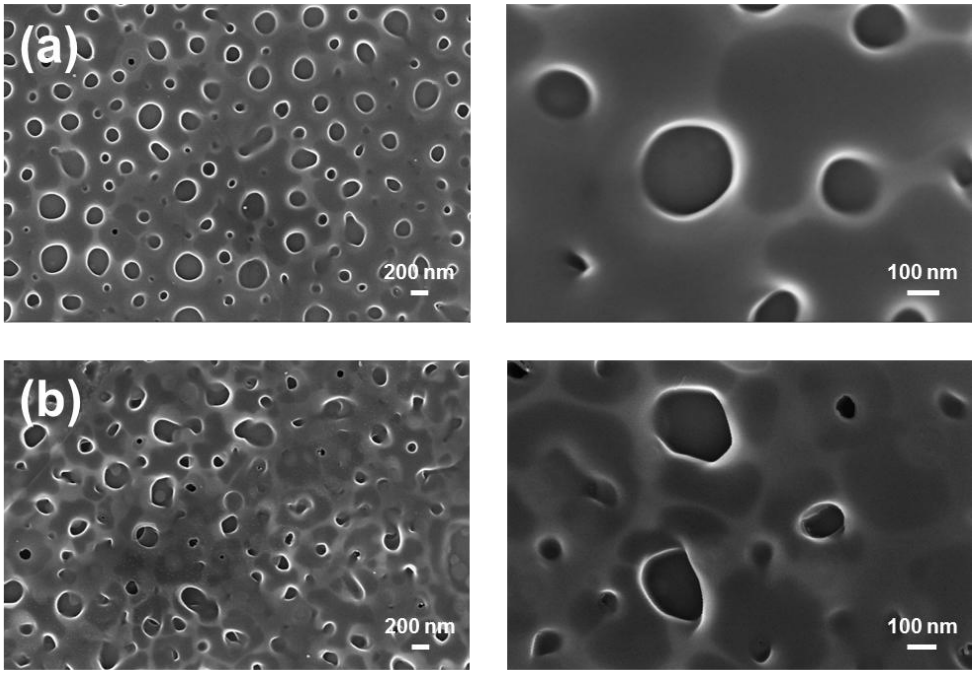

Figure 3.11: SEM micrographs of (a) PLA/CUR(10) and (b) PLA/CUR(20).

The average size of the CUR segregated phases is 76±25 and 88±22 nm for PLA/CUR(10) and PLA/CUR(20), respectively. Although the size of the segregated domains increases with the amount of CUR, Figure 3.11 shows that their abundance per surface unit (*i.e.* density) is maintained in both cases (*i.e.* 4.4 and 4.5 CUR domains per μm^2 is for PLA/CUR(10) and PLA/CUR(20), respectively). Accordingly, changes in the thermal response of the CUR-loaded PLA ultra-thin films should be attributed to the increment in the size of the nanodomains (see below). The thickness of PLA/CUR(10) films, 155±12 nm, is practically identical to that of neat PLA while that of PLA/CUR(20), 188±6 nm, is slightly higher. Comparison of the size of the CUR nanodomains and the thickness of the films suggests that some of such drug segregated phases cross the entire film thickness. On the other hand, the roughness of PLA/CUR(10) and PLA/CUR(20) films, 52±29 and 32±6 nm, respectively, are considerably higher than those of 90-PLA and 80-PLA.

Figure 3.12 shows the FTIR spectra of neat CUR, PLA and PLA/CUR(10). The spectrum of PLA/CUR(20) was practically identical to that of PLA/CUR(10). For PLA, peaks at 1749 cm^{-1} and 1085 cm^{-1} can be attributed to the stretching vibration of C=O and C–O bonds, respectively. In addition, asymmetrical vibrations of $–CH_3$ bonds at 1455 cm^{-1} and 1380 cm^{-1} and the CH–O stretching at 1180 cm^{-1} are also observed. PLA/CUR(10) kept the characteristic peaks at featured wave numbers, indicating that the polymer remained stable. The spectrum of pure CUR exhibited the characteristic peaks at 1625 cm^{-1}, 1507 cm^{-1}, 1427 cm^{-1}, 1273 cm^{-1} and 1027 cm^{-1}, which has been associated to the stretching vibration of C=O, C=C, olefinic C–H, C–O and C–O–C bonds, respectively. The lack of additional peaks in the spectrum of PLA/CUR(10) confirms a physical mixture of polymer and drug, proving that CUR was successfully immobilized in PLA ultra-thin films. Thus, no chemical reaction occurred during the spin-coating process and, therefore, segregated nanodomains in Figure 3.11 are properly ascribed to the drug.

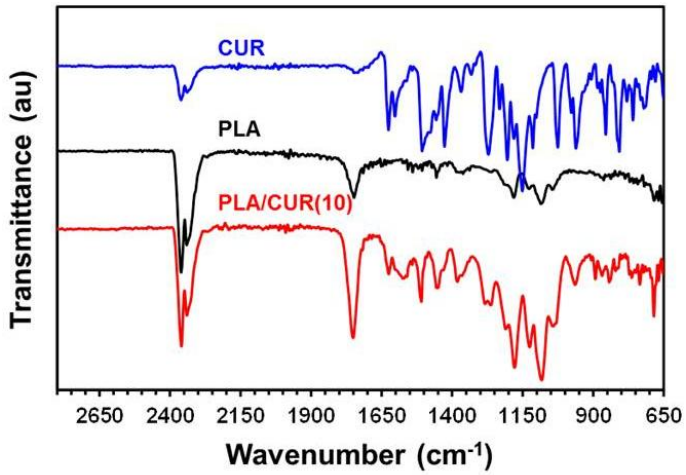

Figure 3.12: FTIR spectra of CUR, PLA and PLA/CUR(10).

Figure 3.13 compares the thermomechanical behaviour of PLA/CUR(10) and PLA/CUR(20), which is affected by the size of drug nanodomains. As occurred for PLA (Figure 3.4), attractive van der Waals forces among polymer molecules increase with the temperature, deflecting the cantilever upwards. The T_g determined for PLA/CUR(10) from the deflection profile is 60 ºC, which is 9º higher than that of PLA (Figure 3.4). Moreover, the regime associated to the cold crystallization is not detected below 100 ºC, indicating that CUR nanodomains are also interfering with this process. In contrast, the deflection profile of PLA/CUR(20) enables the identification of both the glass transition and the cold crystallization processes due to the size and abundance of the nanodomains. Specifically, the T_g and the T_{cc} of PLA/CUR(20) are 3º lower and 6º higher with respect to the values reached for neat PLA.

3. Effect of nanofeatures on the thermal transitions of PLA films

Calorimetric results on melt spun PLA microfibers loaded with 5 wt% CUR, which were prepared by melt spinning, showed an increment in the T_{cc} of 20 ºC [46]. This observation is consistent with the absence of the cold crystallization process in PLA/CUR(10), suggesting that the shift in the T_{cc} is higher than 30 ºC when the polymeric chains and the drug aggregates are confined in ultra-thin films. On the other hand, the T_g of electrospun and melt spun PLA/CUR microfibers remained practically unaltered when the drug was loaded in a concentration ≤ 10 wt% and decreased 4-5 ºC when the amount of drug was > 10 wt% [46-47]. Although the latter reduction is fully consistent with that displayed for PLA/CUR(20), the thermomechanical response of PLA/CUR(10) in the glass transition region seems to be largely influenced by the effect of the film thickness (*i.e.* by the confinement of the polymer chains).

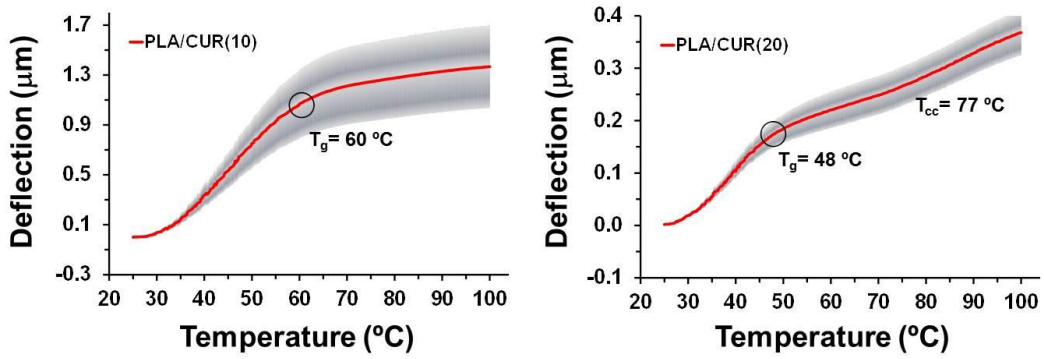

Figure 3.13: Mean deflection curves measured for microcantilever coated with PLA/CUR(10) and PLA/CUR(20).

Chen *et al.* reported the lack of PLA···CUR specific interactions (*e.g.* hydrogen bonds between the phenolic of CUR and the backbone ester groups of PLA backbone) for fibres loaded with CUR at ≤5 wt%. This feature is consistent with the FTIR spectra displayed in Figure 3.12 [43]. Accordingly, the changes induced in the T_g and T_{cc} of PLA ultra-thin films by the CUR loading should be associated to the effects exerted by nanodomains in the polymer molecules. CUR aggregates are expected to: (1) stress the PLA chains located at the interface; and (2) to enhance the free volume of the polymer matrix, reducing the strength of attractive polymer···polymer interactions. The predominant effect will depend on both the size of the drug aggregates and their abundance. Our results suggest that the T_g of PLA/CUR(10) is dominated by the stress of the PLA chains located at the interfaces, which causes rigidity to the chains of the rest of the film. In contrast, drug nanodomains act as a plasticizer in PLA/CUR(20). In this case, CUR nanodomains are big enough to make decisive the effect of the spaces between polymer chains at the interfaces, reducing the energy for molecular motion and, therefore, favouring the PLA mobility at lower temperature.

Independently of the drug concentration, the presence of CUR nanoaggregates acts against the cold crystallization process. Indeed polymer chains need to increase their mobility to reach some small amount of crystallization while heating. Thus, the increment of the T_{cc} in PLA/CUR(10) and PLA/CUR(20) with respect to neat PLA is due to the mobility restrictions imposed by the presence of drug nanodomains.

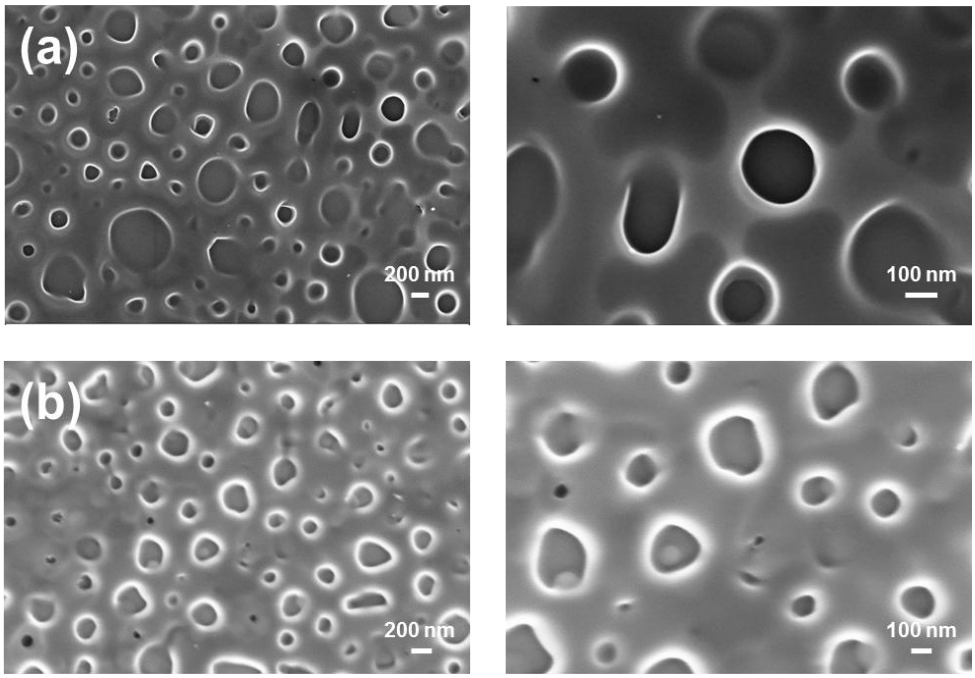

Figure 3.14: SEM micrographs of (a) PLA/STP(10) and (b) PLA/STP(20).

In order to corroborate these results, ultra-thin films were prepared using another drug. Figure 3.14 show representative SEM micrographs of films derived from 90:10 and 80:20 PLA:STP HFIP solutions, hereafter denoted PLA/STP(10) and PLA/STP(20), respectively. The thickness / roughness of these films, which is 161±9 nm / 60±25 nm and 180±12 nm / 36±8 nm, respectively, follow the same tendency of those loaded with CUR. Besides, the drug organizes in segregated nanodomains of average size / density 99±38 nm / 3.3 STP domains/μm^2 and 111±42 nm / 3.6 STP domains/μm^2 for PLA/STP(10) and PLA/STP(20), respectively. Accordingly, drug nanodomains are significantly larger for STP-loaded films than for CUR-loaded films, whereas the density is considerably lower for the former than for the latter. The FTIR spectrum of STP is characterized by a sharp peak at 3551 cm^{-1} corresponding to the OH group, the broad bands at 2951 and 2866 cm^{-1} associated to HC=CH and aliphatic C–H, respectively, and the sharp band at 1500 cm^{-1} ascribed to the stretching vibration of C=C (Figure 3.15). Inspection of the FTIR spectra recorded for PLA/STP(10) (Figure 3.15) and PLA/STP(20) (available upon request) indicates that the

distribution of the peaks in the physical mixtures is nearly identical to those of neat STP and PLA, which is attributable to the lack of drug···polymer interactions.

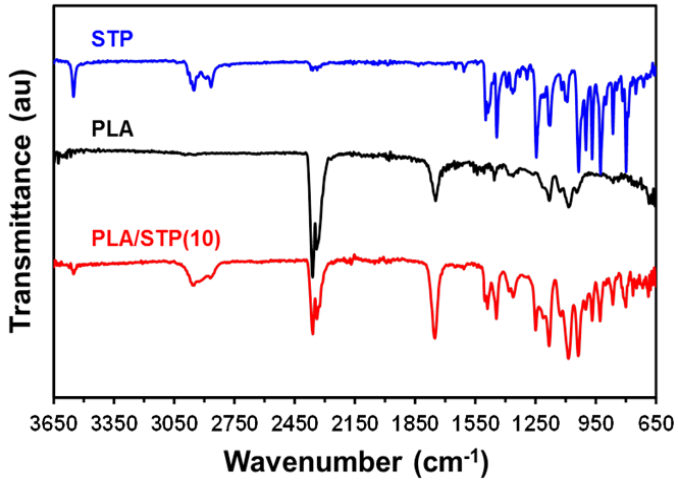

Figure 3.15: FTIR spectra of STP, PLA and PLA/STP(10).

Results from SCALA studies on PLA/STP(10) and PLA/STP(20) are in Figure 3.16. The T_g and T_{cc} determined for PLA/STP(10) (*i.e.* 61 ºC and 89 ºC, respectively) are higher than those obtained for neat PLA. The increment in the T_g, which is of 10 ºC, is very similar to that obtained for PLA/CUR(10). Again, this has been attributed to the rigidity of PLA chains confined in ultra-thin films, which is induced by the STP nanoaggregates. Comparison between PLA/STP(10) and PLA/CUR(10) suggests that the influence of the size of STP aggregates is offset by their abundance, which is significantly lower than for CUR-loaded films. Besides, the increment in the T_{cc} with respect to neat PLA (18 ºC) is lower than that observed in PLA/CUR(10). This has been associated to the fact that the amount of PLA chains affected by the drug in the cold crystallization process is mainly influenced by the density of nanodomains.

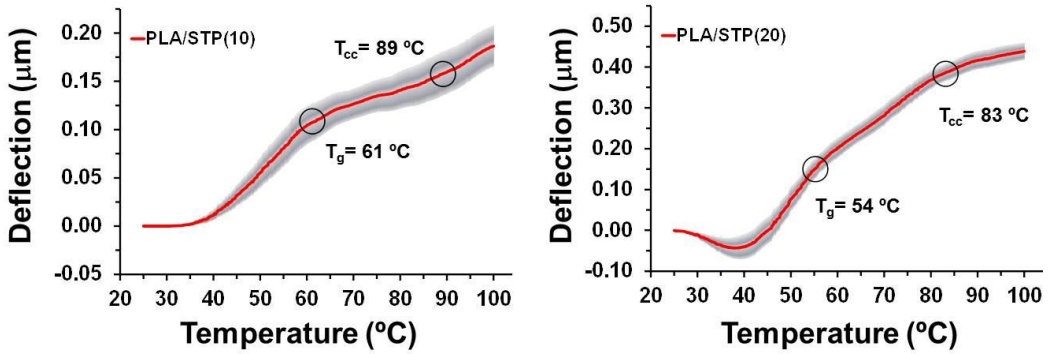

Figure 3.16: Mean deflection curves measured for microcantilever coated with PLA/STP(10) and PLA/STP(20).

On the other hand, the T_g and T_{cc} obtained for PLA/STP(20) (*i.e.* 54 ºC and 83 ºC, respectively) are intermediate between those of neat PLA and PLA/CUR(20). This observation suggests that, in this case, STP aggregates are not acting as a plasticizer. Thus, the increment in the size and the reduction in the density of drug nanodomains with respect to PLA/CUR(20) indicate that the effects on the rigidity of the PLA chains predominates over those on the mobility (*i.e.* the plasticising effect). In summary, results obtained for drug loaded PLA ultra-thin films demonstrate the sensitivity of the SCALA methodology, which allows identifying features in the nanometer-length scale that are usually undetectable by conventional calorimetric methods based on bulk samples.

3.4. Conclusion

SCALA microcantilevers technology has been used to investigate the influence of nanofeatures in the thermal response of PLA ultra-thin films. By comparing with conventional DSC analyses, the T_g and T_{cc} derived from the deflection profiles recorded for cantilevers coated with homogeneous and compact PLA and PVA ultra-thin films are very similar to those of the bulk polymers. Moreover, such deflection profiles provide information not only about the variation with the temperature of attractive and repulsive interactions between PLA and PVA chains, respectively, but also about the unbound of the water molecules from the surface of the latter polymer. Incorporation of physical nanofeatures, as for example nanopores, nanoperforations and segregated CUR or STP nanodomains, to ultra-thin films causes stress in the polymer molecules located at the PLA-air and PLA-drug interfaces, altering the thermal response. In the case of nanopored and nanoperforated PLA, such stress is probably due to the methodology applied to generate nanofeatures (*i.e.* phase separation through spin-coating followed by selective solvent etching), resulting in a significant increment of both the T_g and the T_{cc} with respect to homogeneous and compact PLA ultra-thin films. The thermal response of drug-loaded PLA films depends on the size and abundance of the nanodomains, which affect enhancing or reducing the strength of polymer···polymer interactions and increasing the mobility of polymer chains. Consequently, the T_g can increase or decrease with respect to neat PLA, while the T_{cc} increases in all cases. In summary, the used microcantilever-based technology has provided important microscopic information about the influence of nanofeatures on the thermal response of PLA, unreachable using conventional calorimetric methods, which was never reported before.

3.5. Bibliography

[1] F. Zhou, W. Shu, M. E. Welland, and W. T. S. Huck, "Highly Reversible and Multi-Stage Cantilever Actuation Driven by Polyelectrolyte Brushes," *J. Am. Chem. Soc.*, 128, 16, 5326–5327, 2006.

[2] T. Chen, D. P. Chang, T. Liu, R. Desikan, R. Datar, T. Thundat, R. Berger, and S. Zauscher, "Glucose-responsive polymer brushes for microcantilever sensing," *J. Mater. Chem.*, 20, 17, 3391, 2010.

[3] S. Lenz, S. K. Nett, M. Memesa, R. F. Roskamp, A. Timmann, S. V. Roth, R. Berger, and J. S. Gutmann, "Thermal Response of Surface Grafted Two-Dimensional Polystyrene (PS)/Polyvinylmethylether (PVME) Blend Films," *Macromolecules*, 43, 2, 1108–1116, 2010.

[4] G. M. A. Alves, S. B. Goswami, R. D. Mansano, and A. Boisen, "Using microcantilever sensors to measure poly(lactic-co-glycolic acid) plasticization by moisture uptake," *Polym. Test.*, 65, 407–413, 2018.

[5] C. Bradley, N. Jalili, S. K. Nett, L. Chu, R. Förch, J. S. Gutmann, and R. Berger, "Response Characteristics of Thermoresponsive Polymers Using Nanomechanical Cantilever Sensors," *Macromol. Chem. Phys.*, 210, 16, 1339–1345, 2009.

[6] J. Zhao, R. Berger, and J. S. Gutmann, "Thermal contributions to the bending of bimaterial cantilever sensors," *Appl. Phys. Lett.*, 89, 3, 033110, 2006.

[7] R. Muñoz, F. Aguilar-Sandoval, L. Bellon, and F. Melo, "Detecting protein folding by thermal fluctuations of microcantilevers," *PLoS One*, 12, 12, e0189979, 2017.

[8] M. Lopes-Rodrigues, A. Puiggalí-Jou, D. Martí-Balleste, L. J. Del Valle, C. Michaux, E. A. Perpète, and C. Alemán, "Thermomechanical Response of a Representative Porin for Biomimetics," *ACS Omega*, 3, 7, 7856–7867, 2018.

[9] A. Cagliani, P. Kosaka, J. Tamayo, and Z. J. Davis, "Monitoring the hydration of DNA self-assembled monolayers using an extensional nanomechanical resonator," *Lab Chip*, 12, 11, 2069, 2012.

[10] N. Jung and S. Jeon, "Nanomechanical Thermal Analysis with Silicon Cantilevers of the Mechanical Properties of Poly(vinyl acetate) near the Glass Transition Temperature," *Macromolecules*, 41, 24, 9819–9822, 2008.

[11] N. Jung, H. Seo, D. Lee, C. Y. Ryu, and S. Jeon, "Nanomechanical Thermal Analysis of the Glass Transition of Polystyrene Using Silicon Cantilevers," *Macromolecules*, 41, 19, 6873–6875, 2008.

[12] M. Yun, N. Jung, C. Yim, and S. Jeon, "Nanomechanical thermal analysis of the effects of physical aging on glass transitions in PS/PMMA blend and PS-PMMA diblock copolymers," *Polymer (Guildf).*, 52, 18, 4136–4140, 2011.

[13] S. A. Manzoor Bukhari, M. F. Khan, A. Goswami, R. McGee, and T. Thundat, "Thermomechanical analysis of picograms of polymers using a suspended microchannel cantilever," *RSC Adv.*, 7, 14, 8415–8420, 2017.

[14] O. Ahumada, M. M. Pérez-Madrigal, J. Ramirez, D. Curcó, C. Esteves, A. Salvador-Matar, G. Luongo, E. Armelin, J. Puiggalí, and C. Alemán, "Sensitive thermal transitions of nanoscale polymer samples using the bimetallic effect: Application to ultra-thin polythiophene," *Rev. Sci. Instrum.*, 84, 5, 053904, 2013.

[15] M. Soccio, G. Luongo, C. Esteves, A. Salvador-Matar, O. Ahumada, D. R. Rueda, M. C. García-Gutiérrez, N. Lotti, A. Munari, and T. A. Ezquerra, "Thermomechanical response of a semicrystalline polymer in the vicinity of the melting by using microcantilever technology," *Appl. Phys. Lett.*, 104, 25, 251904, 2014.

[16] M. Karl, P. E. Larsen, V. P. Rangacharya, E. Te Hwu, J. Rantanen, A. Boisen, and T. Rades, "Ultrasensitive Microstring Resonators for Solid State Thermomechanical Analysis of Small and Large Molecules," *J. Am. Chem. Soc.*, 140, 50, 17522–17531, 2018.

[17] A. Puiggalí-Jou, J. Medina, L. J. del Valle, and C. Alemán, "Nanoperforations in poly(lactic acid) free-standing nanomembranes to promote interactions with cell filopodia," *Eur. Polym. J.*, 75, 552–564, 2016.

[18] A. Puiggalí-jou, M. M. Pérez-madrigal, L. J. del Valle, E. Armelin, M. T. Casas, C. Michaux, E. A. Perpète, F. Estrany, C. Alemán, L. J. Valle, E. Armelin, M. T. Casas, C. Michaux, E. A. Perpète, F. Estrany, and C. Alemán, "Confinement of a β-barrel protein in nanoperforated free-standing nanomembranes for ion transport," *Nanoscale*, 8, 38, 16922–16935, 2016.

[19] B. Dorj, J.-E. Won, O. Purevdorj, K. D. Patel, J.-H. Kim, E.-J. Lee, and H.-W. Kim, "A novel therapeutic design of microporous-structured biopolymer scaffolds for drug loading and delivery," *Acta Biomater.*, 10, 3, 1238–1250, 2014.

[20] J. M. Anderson and M. S. Shive, "Biodegradation and biocompatibility of PLA and PLGA microspheres," *Adv. Drug Deliv. Rev.*, 64, 72–82, 2012.

[21] J. Delmote, L. Teruel-Biosca, J. L. Gómez Ribelles, and G. Gallego Ferrer, "Emulsion based microencapsulation of proteins in poly(L-lactic acid) films and membranes for the controlled release of drugs," *Polym. Degrad. Stab.*, 146, 24–33, 2017.

[22] A. Gao, F. Liu, Z. Xiong, and Q. Yang, "Tunable adhesion of superoleophilic/superhydrophobic poly (lactic acid) membrane for controlled-release of oil soluble drugs," *J. Colloid Interface Sci.*, 505, 49–58, 2017.

[23] J. Pang, Y. Luan, F. Li, X. Cai, J. Du, and Z. Li, "Ibuprofen-loaded poly(lactic-co-glycolic acid) films for controlled drug release," *Int. J. Nanomedicine*, 6, 659, 2011.

[24] A. Puiggalí-Jou, A. Cejudo, L. J. del Valle, and C. Alemán, "Smart Drug Delivery from Electrospun Fibers through Electroresponsive Polymeric Nanoparticles," *ACS Appl. Bio Mater.*, 1, 5, 1594–1605, 2018.

[25] L. Lechuga Gomez, V. Alvarez-Sanchez, and F. J. Tamayo de Miguel, "System and method for detecting the displacement of a plurality of micro- and nanomechanical elements, such as micro-cantilevers," 7,646,494 B2, 2010.

[26] F. J. Tamayo de Miguel, J. Mertens, and M. Calleja-Gomez, "System and method for the inspection of micro and nanomechanical structures," 7,978,344 B2, 2011.

[27] R. Berger, C. Gerber, J. K. Gimzewski, E. Meyer, and H. J. Güntherodt, "Thermal analysis using a micromechanical calorimeter," *Appl. Phys. Lett.*, 69, 1, 40–42, 1996.

[28] J. R. Barnes, R. J. Stephenson, C. N. Woodburn, S. J. O'Shea, M. E. Welland, T. Rayment, J. K. Gimzewski, and C. Gerber, "A femtojoule calorimeter using micromechanical sensors," *Rev. Sci. Instrum.*, 65, 12, 3793–3798, 1994.

[29] E. S. Trofimchuk, A. V. Efimov, T. E. Grokhovskaya, N. I. Nikonorova, M. A. Moskvina, N. G. Sedush, P. V. Dorovatovskii, O. A. Ivanova, E. G. Rukhlya, A. L. Volynskii, and S. N. Chvalun, "Cold Crystallization of Glassy Polylactide during Solvent Crazing," *ACS Appl. Mater. Interfaces*, 9, 39, 34325–34336, 2017.

[30] C. Zhou, H. Li, W. Zhang, J. Li, S. Huang, Y. Meng, J. de Claville Christiansen, D. Yu, Z. Wu, and S. Jiang, "Thermal strain-induced cold crystallization of amorphous poly(lactic acid)," *CrystEngComm*, 18, 18, 3237–3246, 2016.

[31] R. Androsch, H. M. N. Iqbal, and C. Schick, "Non-isothermal crystal nucleation of poly (l-lactic acid)," *Polymer (Guildf).*, 81, 151–158, 2015.

[32] R. Androsch and M. L. Di Lorenzo, "Crystal Nucleation in Glassy Poly(l -lactic acid)," *Macromolecules*, 46, 15, 6048–6056, 2013.

[33] Pengju Pan, Weihua Kai, Bo Zhu, and Tungalag Dong, and Y. Inoue*, "Polymorphous Crystallization and Multiple Melting Behavior of Poly(l-lactide): Molecular Weight Dependence," 2007.

[34] J. Rault, R. Gref, Z. H. Ping, Q. T. Nguyen, and J. Néel, "Glass transition temperature regulation effect in a poly(vinyl alcohol)—water system," *Polymer (Guildf).*, 36, 8, 1655–1661, 1995.

[35] E. Fathi, N. Atyabi, M. Imani, and Z. Alinejad, "Physically crosslinked polyvinyl alcohol–dextran blend xerogels: Morphology and thermal behavior," *Carbohydr. Polym.*, 84, 1, 145–152, 2011.

[36] A. Stavropoulou, K. G. Papadokostaki, and M. Sanopoulou, "Thermal properties of poly(vinyl alcohol)-solute blends studied by TMDSC," *J. Appl. Polym. Sci.*, 93, 3, 1151–1156, 2004.

[37] D. Karunagaran, R. Rashmi, and T. Kumar, "Induction of Apoptosis by Curcumin and Its Implications for Cancer Therapy," *Curr. Cancer Drug Targets*, 5, 2, 117–129, 2005.

[38] C.-H. Hsu and A.-L. Cheng, "Clinical studies with curcumin," in *The Molecular Targets and Therapeutic Uses of Curcumin in Health and Disease*, Boston, MA: Springer US, 2007, 471–480.

[39] B. B. Aggarwal and B. Sung, "Pharmacological basis for the role of curcumin in chronic diseases: an age-old spice with modern targets," *Trends Pharmacol. Sci.*, 30, 2, 85–94, 2009.

[40] P. Anand, S. G. Thomas, A. B. Kunnumakkara, C. Sundaram, K. B. Harikumar, B. Sung, S. T. Tharakan, K. Misra, I. K. Priyadarsini, K. N. Rajasekharan, and B. B. Aggarwal, "Biological activities of curcumin and its analogues (Congeners) made by man and Mother Nature," *Biochem. Pharmacol.*, 76, 11, 1590–1611, 2008.

[41] D. Chopra, L. Ray, A. Dwivedi, S. K. Tiwari, J. Singh, K. P. Singh, H. N. Kushwaha, S. Jahan, A. Pandey, S. K. Gupta, R. K. Chaturvedi, A. B. Pant, R. S. Ray, and K. C. Gupta, "Photoprotective efficiency of PLGA-curcumin nanoparticles versus curcumin through the involvement of ERK/AKT pathway under ambient UV-R exposure in HaCaT cell line," *Biomaterials*, 84, 25–41, 2016.

[42] A. Puiggalí-Jou, P. Micheletti, F. Estrany, L. J. del Valle, and C. Alemán, "Electrostimulated Release of Neutral Drugs from Polythiophene Nanoparticles: Smart Regulation of Drug-Polymer Interactions," *Adv. Healthc. Mater.*, 6, 18, 1700453, 2017.

[43] Y. Chen, J. Lin, Y. Wan, Y. Fei, H. Wang, and W. Gao, "Preparation and blood compatibility of electrospun PLA/curcumin composite membranes," *Fibers Polym.*, 13, 10, 1254–1258, 2012.

[44] T. T. T. Nguyen, C. Ghosh, S.-G. Hwang, L. D. Tran, and J. S. Park, "Characteristics of curcumin-loaded poly (lactic acid) nanofibers for wound healing," *J. Mater. Sci.*, 48, 20, 7125–7133, 2013.

[45] J. L. Fisher, "The anti-convulsant stiripentol acts directly on the GABAA receptor as a positive allosteric modulator," *Neuropharmacology*, 56, 1, 190–197, 2009.

[46] I. S. S. Sharifah, A. A. B. Qairol, H. N. Azlina, and M. K. N. Khairusshima, "Thermal, Structural and Mechanical Properties of Melt Drawn Cur-loaded Poly(lactic acid) Fibers," *Procedia Eng.*, 184, 544–551, 2017.

[47] G. Perumal, S. Pappuru, D. Chakraborty, A. Maya Nandkumar, D. K. Chand, and M. Doble, "Synthesis and characterization of curcumin loaded PLA—Hyperbranched polyglycerol electrospun blend for wound dressing applications," *Mater. Sci. Eng. C*, 76, 1196–1204, 2017.

4. Structural and functional characterization of VDAC36

4. Structural and functional characterization of VDAC36

Abstract

Forming water-filled channel in the mitochondria outer membrane and diffusing essential metabolites such as NADH and ATP, the VDAC (voltage-dependent anion channel) protein family plays a central role in all eukaryotic cells. Little is known about the structural and functional properties of plant VDACs in comparison with their mammalian homologues. In the present contribution, one of the two VDACs isoforms of *Solanum tuberosum*, stVDAC36, has been successfully overexpressed and refolded by an in-house method. Circular dichroism and intrinsic fluorescence could give information on its secondary and tertiary structure. Cross-linking and molecular modelling studies could evidence the presence of dimers and tetramers, and suggest the formation of a potential intermolecular disulphide bond between two stVDAC36 monomers. The pore-forming activity was also assessed by liposome swelling assays, highlighting a pore diameter between 2.0 and 2.7 nm. Finally, insights about the ATP binding inside the pore are pointed out by docking studies and electrostatic calculations.

4.1. Introduction

Voltage Dependent Anion Channels (VDACs) are pore-forming proteins found in the outer mitochondrial membrane of all eukaryotic cells. The function of those proteins is associated with the permeability of mitochondria. Indeed, they regulate the diffusion of ions and metabolites such as nicotinamide adenine dinucleotide hydrogen (NADH) or adenosine triphosphate (ATP). In addition, VDAC proteins are involved in apoptosis, as well as in transport of DNA and tRNA [1–4]. Their structural properties are highly conserved and they adopt a β-barrel structure generally composed of 19 antiparallel β-strands. This conformation leads to the formation of an inner channel restricted by a N-terminal α-helix that folds into the pore [5]. The VDAC proteins usually show poor selectivity and are consequently described as general diffusion pore. As a result, the diffusion is mainly controlled by the size of the pore, which may change with the conformation of the α-helix [6]. Nevertheless, the chemical nature of the inner cavity can also affect the selectivity as preferential diffusion of anions over cations was observed [7].

Up to now, only ten VDAC 3D-structures have been fully experimentally described. The Protein Data Bank (PDB) contains seven VDAC1 from human, two VDAC1 from mouse, and one VDAC2 from fish. In contrast to VDAC1, structural and functional characterizations of the other VDAC isoforms (2 and 3) are rather limited. Moreover, no consensus has been reached regarding the oligomeric state of VDAC proteins and their actual role in nucleotides transport and apoptosis. Being integral membrane proteins, it remains indeed a challenge to overexpress and characterize VDACs. Particularly, the structure and properties of plant VDACs are less described than their mammalian counterparts. In this framework, we have studied one of the VDAC isoforms of the *Solanum tuberosum* outer mitochondrial membrane, stVDAC36 [8]. The latter recently showed their relevance in the tRNA mitochondrial transport system [9].

To gain insight into the structure and function of stVDAC36, it was expressed, refolded and characterized. To do so, a protocol based on bacterial expression into inclusion bodies followed by an in-house SDS-MPD refolding method is proposed here. The latter procedure has already been proven efficient for membrane proteins, including bacterial porins [10–12]. The stVDAC36 was then reconstituted into liposomes allowing, by swelling assay, to assess its inner channel size. The oligomeric states of stVDAC36 were investigated by cross-linking experiments. A molecular model was built to investigate the stVDAC36 structure at the atomic scale. Comparisons to experimental data were successfully carried out, whereas the residues forming the inner channel and potentially binding ATP were also identified by docking studies and electrostatic calculations.

4.2. Methods

Expression and purification of stVDAC36. The cDNA encoding stVDAC36 was cloned into pQE60 vector by Salinas *et al.* [13], while *Escherichia coli* BL21 (DE3) were transformed with the vector to overproduce 6-His-tagged -stVDAC36 proteins in inclusion bodies. Bacteria were grown in 800 mL of lysogeny broth **(**LB) medium at 37 °C under constant agitation. When the optical density at 600 nm reached 0.7, isopropyl β-D-1-thiogalactopyranoside (IPTG) was added (final concentration of 2 mM) to stimulate the protein expression during 3h. Bacteria were then pelleted by centrifugation at 4000 g for 30 minutes at 4 °C. The pellets were then suspended in the lysis buffer (50 mM Tris-HCl pH 8, 5 mM $MgCl_2$, 17 mM NaCl, 1% (w/v) Triton X-100, 1 mg/mL lysozyme, 1 mM PMSF). Sodium deoxycholate and DNAse I were added (final concentrations of 0.2% (w/v) and 0.125 mg/mL, respectively). The lysed solution was agitated at 37°C for two hours and then centrifuged at 9000 g for 30 minutes at 4 °C. The supernatant was discarded and the pellet was washed twice with the washing buffer (20 mM Tris-HCl pH 8, 500 mM NaCl, 2% (w/v) Triton X-100). The washed solution was centrifuged at 5000 g for 10 minutes at 10°C. The final pellet corresponding to the inclusion bodies was solubilized in the solubilizing buffer (20 mM phosphate pH 8, 1% (w/v) SDS).

The solubilized proteins were then loaded on a 5 mL HiTrap IMAC FF (GE Healthcare) previously loaded with Ni^{2+}. The column was previously equilibrated with buffer A (20 mM phosphate pH 8, 100 mM NaCl, 0.1% (w/v) SDS), and stVDAC36 was then eluted with a gradient of buffer B (20 mM phosphate pH 8, 100 mM NaCl, 0.1% (w/v) SDS, 250 mM imidazole). Depending of the following treatments, the protein buffer was exchanged using a PD-10 desalting column (GE Healthcare).

Circular Dichroism. Measurements were performed with a Jasco J-810 in the far UV region (260 – 190 nm) at 20°C. Data pitch was set to 0.1 nm and the bandwidth to 1.0 nm. Spectra were accumulated four times at 20 nm/min and corrected by the subtraction of the buffer spectra. The secondary structure contents were calculated with Dichroweb using the CDSSTR method and the SMP180 reference set [14].

Steady-state Trp-Fluorescence. Steady-state measurements were performed with a Varian Cary Eclipse spectrophotometer with a 2-mm path length cell. The excitation wavelength was 280 nm and the emission spectra were recorded from 290 to 500 nm with 1 nm-step.

Reconstitution of stVDAC36 in liposome and swelling assay. The appropriate amount of pure 1,2-dioleoyl-sn-glycero-3-phosphocholine (DOPC) was dissolved in chloroform. The latter was then evaporated using a rotary evaporator to obtain a thin homogenous film. The flask was then left one hour in a desiccator, and the lipid film was suspended in a buffer (20 mM phosphate pH 7.4, 1 mM PEG6000) to obtain a final concentration of 2 mg/mL. The turbid solution was subsequently loaded on a mini Extruder (AvantiLipids) with 100 nm filter and extruded 30 times, resulting in a clear final solution.

The stVDAC36 was transferred in a buffer containing 20 mM phosphate pH 7.4, 0.2% (w/v) Triton X-100 by using a desalting PD10 column and then added to the liposomes. The final concentrations of protein and DOPC were 0.27 mg/mL and 1.4 mg/mL, respectively. The mixture was agitated for one hour. After that, 0.2 g/mL of BioBeads SM-2 (Bio-Rad) were added and the mixture was agitated two hours more to adsorb the detergent. The solution was filtered for the beads removal.

Swelling assays were performed by adding 10 µL of proteoliposomes to 190 µL of solution test, *i.e.* 20 mM phosphate pH 7.4 and 1.05 mM of solute such as glycine, sugars or PEG. After addition of the proteoliposomes, the absorbance at 450 nm was recorded for five minutes. The absorbance values were normalized and the diffusion rate was calculated as the difference between the starting and final absorbance values.

Cross-linking. Three cross-linkers were used: dimethyl suberimidate (DMS, 11.0 Å), dimethyl adipimidate (DMA, 8.6 Å), and 1,5-difluoro-2,4-dinitrobenzene (DFDNB, 3.0 Å), that were dissolved in 20 mM phosphate buffer pH 8.5. Equal volumes of cross-linker solution and protein (~0.8 mg/mL) were mixed and incubated for 1.5 hours at 20°C under gentle agitation. The reaction was stopped by adding SDS-PAGE loading buffer (10% (w/v) SDS, 20% (w/v) glycerol, 0.2 M Tris-HCl pH 6.8, 0.05% (w/v) bromophenol blue). A 12% acrylamide SDS-PAGE was run for 50 minutes at 200V, and the gels were stained by Coomassie Blue.

Transmission electron microscopy. Transmission electron microscopy (TEM) pictures were obtained with a Philips TECNAI 10 microscope operating at 100 kV. Carbon-coated grids were hydrophilized by glow discharge. A 5 µL drop was deposited on the grid for 60 seconds. The grid was then rinced with water and 0.5% (w/v) of uranyl acetate was added for 120 seconds for a negative staining.

Model prediction and analysis. The RaptorX webserver (http://raptorx.uchicago.edu) was used to predict the 3D-model of stVDAC36 by using Zebrafish VDAC2 (PDB ID: 4BUM) as main template [15]. The secondary structure content was evaluated by the DSSP algorithm [16]. The software Visual Molecular Dynamics (VMD) was used for visualizing the models and creating images [17]. The electrostatic potential was calculated using the APBS software [18]. Docking studies of ATP inside the channel of stVDAC36 were performed using the GOLD program [19]. The binding region was defined as a 30 Å radius sphere centred on Arg-16, one of the residues in the α-helical N-terminal. For each of the 10 runs, a total of 100,000 genetic operations were carried out on five islands, each containing 100 individuals. The solutions were ranked by GOLD score.

4.3. Results and discussion

Expression, purification and refolding

The transformation of *E. coli* BL21 (DE3) strain was verified by Polymerase Chain Reaction (PCR) with the T7 promoter/terminator. The DNA band revealed on the agarose gel corresponds to the length of the VDAC36 nucleic acid sequence (Figure 4.1). The insertion being successful, the transformed bacteria were used to express the protein.

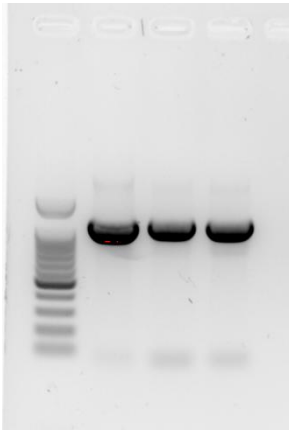

Figure 4.1: Agarose gel electrophoresis of PCR products of the stVDAC36 gene. The first column is the DNA size marker. Three samples were loaded and revealed a DNA size of 831 bp.

The purification yielded 9.3 mg of stVDAC36 per culture. It appeared on SDS-PAGE at a molecular weight of approximatively 30 kDa, close to the value calculated from the amino acid sequence (30.274 kDa) (Figure 4.2).

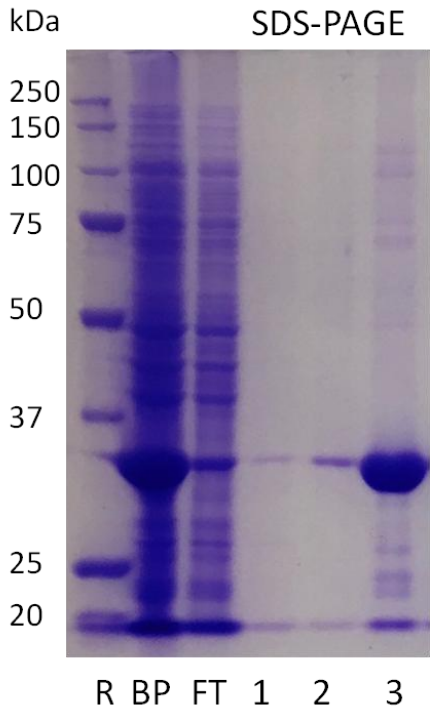

Figure 4.2: SDS-PAGE of the stVDAC36 gene. R: reference ladder, BP: sample before purification, FT: flow through obtained during the affinity chromatography, 1-3: samples eluted by imidazole.

Once produced as inclusion bodies in *E. coli* and purified under denaturing conditions, stVDAC36 has been refolded by dilution in a refolding buffer containing sodium dodecylsulfate (SDS) and 2-methyl-2,4-pentanediol (MPD). Indeed, this peculiar detergent-alcohol association was demonstrated be able to successfully refold β-barrel proteins [11-12]. Added MPD partially prevents SDS and water to interact with the protein, hence providing a suitable amphiphilic environment. To determine the optimal refolding conditions, a panel of refolding buffers has been considered, made of 20 mM phosphate pH 8, 66 mM NaCl and several concentrations of SDS and MPD. The protein was then characterized by both circular dichroism (CD) and intrinsic fluorescence. VDAC proteins possess high β-strands content which folded state is related to typical CD spectra [7-20]. As expected, SDS acts as a denaturing agent, leading to spectra that are usually associated to disordered structures, with a minimum at 208 nm (Figure 4.3) [21–23].

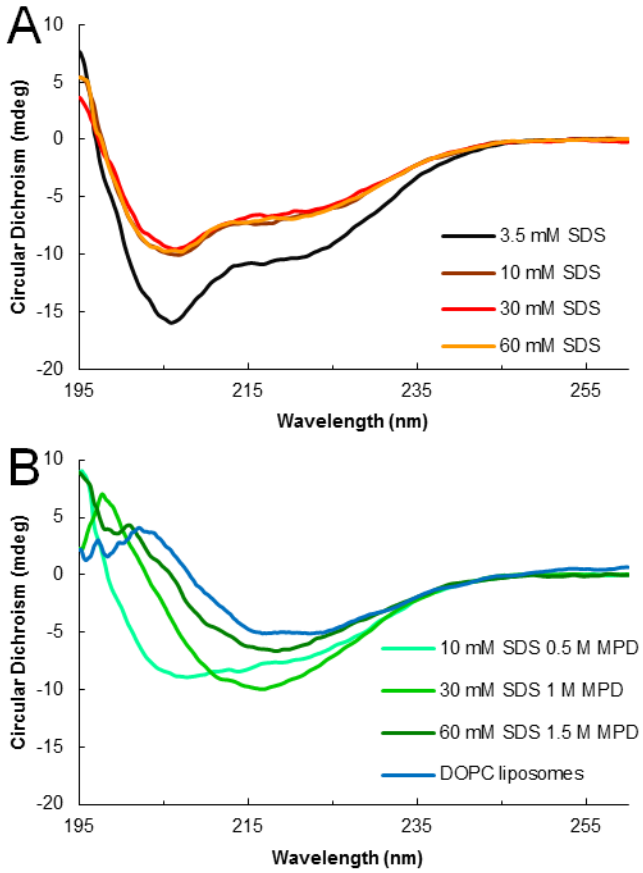

Figure 4.3: Far UV circular dichroism spectra of stVDAC36. After purification, the protein was placed in different refolding buffers composed of 20 mM phosphate pH 8 and 66 mM NaCl, and different concentrations of sodium dodecylsulfate (SDS) and 2-methyl-2,4-pentanediol (MPD). A) The protein is unfolded regardless the concentration of detergent. B) Spectra show a β-barrel signal after addition of MPD.

By adding an increasing amount of MPD, the CD spectra change to finally reach a signal corresponding to β-sheets and more particularly to a β-barrel structure (Figure 4.3B) [24–26]. With a MPD concentration of 0.5 M, the minimum at 208 nm is still present and it is concluded that this concentration is not sufficient to achieve the protein refolding. The CD spectrum corresponding to 30 mM SDS and 1 M MPD does not have the minimum at 208 nm and represents the transition between the unfolded state and the β-barrel structure. A suitable environment for the refolding is reached for the ratio 60 mM SDS and 1.5 M MPD and a β-barrel CD spectrum is obtained. Interestingly, the same ratio was also required to obtain the highest refolding yield for Omp2a, a bacterial porin also forming β-barrel [12]. This is a new evidence of the effectiveness of the SDS-MPD refolding method.

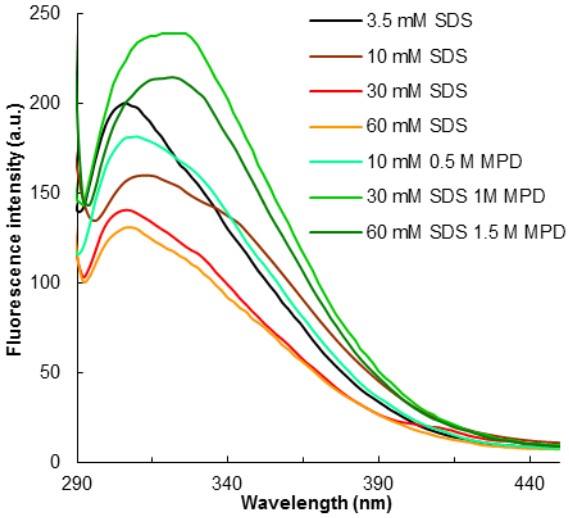

Figure 4.4: Steady-state intrinsic fluorescence spectra of stVDAC36 in buffers composed of 20 mM phosphate pH 8 and 66 mM NaCl, and with different concentrations of SDS and MPD. The λ_{max} is shifted from 309 to 320 nm upon addition of MPD into the refolding buffer.

The tryptophan (Trp) fluorescence is a common method to study the refolding of proteins and complements the CD analysis. More specifically it provides insights into the polarity of the Trp vicinity, thereby indicating the orientation of the residue (*e.g.* pointing towards the hydrophilic inner channel or the lipid membrane). In the SDS buffers, the stVDAC36 λ_{max} is at 309 nm with a decreasing intensity when the SDS concentration increases (Figure 4.4). This trend was also observed for peptides denatured in SDS [27]. With the addition of MPD, a bathochromic shift is observed to a λ_{max} of 320 nm, corresponding to a more polar environment. This result supports the recovery of the β-barrel conformation by addition of the MPD, as demonstrated by the CD analysis. This red-shift between the SDS-unfolded and the native state was also pointed out for peptides [28]. The increasing of the fluorescence intensity indicates that the Trp residue is less hindered after refolding. To sum up, the fluorescence results are in accordance with the information gathered from the CD analysis and support the evidences of the successful stVDAC36 refolding by the SDS/MPD method. The latter has proven itself a reliable and fast method for the refolding of membrane proteins.

Structural studies of stVDAC36: secondary and tertiary structure

The CD data were analyzed in order to extract the percentage of each secondary structure and to understand better the conformational changes underwent by the protein during its refolding (Table 4.1).

Table 4.1: Secondary structure content of stVDAC36 in different refolding conditions. Percentages were obtained by deconvolution of circular dichroism spectra.

%	**α-helices**	**β-strands**	**Turns**	**Unordered**
3.5 mM SDS	43	21	10	26
10 mM SDS	32	14	16	38
30 mM SDS	29	17	16	38
60 mM SDS	29	19	16	36
10 mM SDS + 0.5 M MPD	6	45	10	39
30 mM SDS + 1 M MPD	4	52	9	35
60 mM SDS + 1.5M MPD	1	68	9	22
Theoretical model	5	64	10	21

The β-strands content is higher for a SDS concentration of 3.5 mM than for the higher concentrations. This particularity can be related with the micelles formation. Indeed, above 3.5 mM the SDS could form micelles that alter the properties of the medium, hence modifying the detergent-protein interactions. Another interesting phenomenon is that SDS promotes the formation of helix-like structures [29], as illustrated by the high α-helix content for the conditions without MPD. With the alcohol, the micelles organization is perturbed and the protein accessible surface for detergents is reduced [30]. Consequently, the α-helix content drops significantly. The turn content remains almost unchanged, independently of the SDS/MPD ratio. With 0.5 M and 1 M of MPD, the unordered structure contents are similar to that of the denatured protein whereas the β-strands formation is largely intensified by MPD. Finally, concentrations of 60 mM SDS and 1.5 M MPD give the highest amount of β-structures and the smallest of unordered structures, which perfectly matches the structural data found in the Protein Data Bank (PDB) for other VDAC proteins.

Membrane proteins remain a challenge for crystallographic studies and no plant VDAC structure has been resolved yet making stVDAC36 structure still undescribed. To answer the need for atomic structural information, molecular modelling has become a cost and time effective alternative. A 3D model of the protein was therefore built by threading, based on the VDAC2 structure from *zebrafish*

(PDB: 4BUM) [31]. As observed in experimental VDAC structures [32], the resulting stVDAC36 model is composed of 19 β-strands separated by short loops on the cellular side and turns on the intermembrane space. The β-strands contribute the most to the secondary content with a percentage of 64% (Table 4.1), accordingly to the previously described CD spectra. The stVDAC36 model presents two girdles of aromatic residues similarly to other β-barrels like porins [33]. The N-terminal chain folds inside the barrel into an α-helix that forms a bottleneck restricting the size of the channel (Figure 4.5). The resulting pore diameter (D_{pore}) is 1.56 nm, while the diameter of the channel with the α-helix outside the barrel is 2.16 nm. The D_{pore} calculated from the model are in accordance with the literature [34–36]. It is important to note that the open state of VDAC proteins is dependent of the solute trying to cross the channel. Small ions such as sodium or chloride will see the protein as an open gate wherever the α-helix is located. On the contrary, bulkier molecules may not be able to pass through the channel when the α-helix restrains the pore.

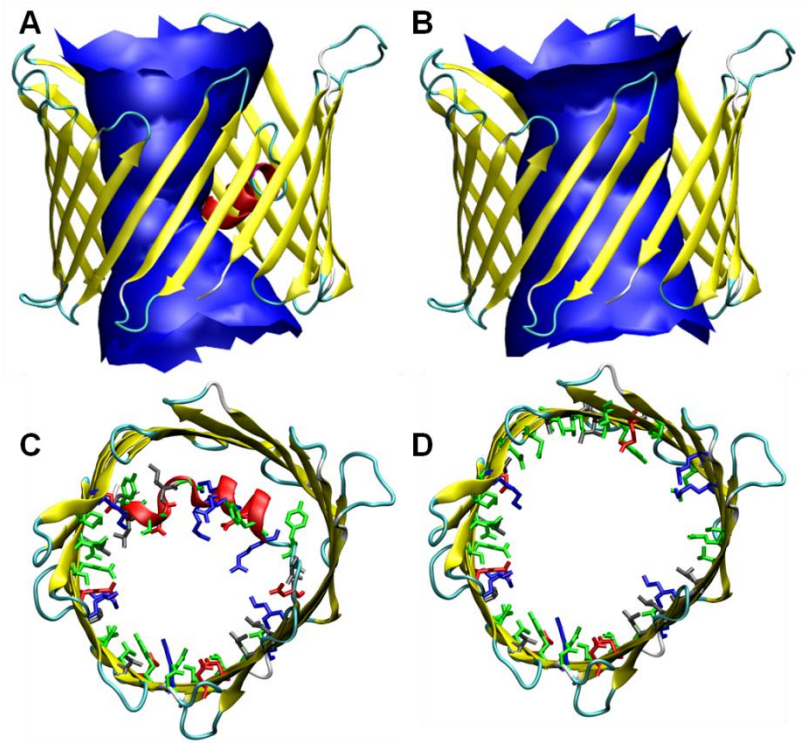

Figure 4.5: Cartoon representation of the stVDAC36 model built by threading. Secondary structure is displayed with the following colors: β-strands (yellow), α-helix (red), turns (cyan) and loops (loop). A) Side views with the maximum diameter of the channel in blue. B) Side view without the N-terminus α-helix. C) Top view of the stVDAC36 model with the residues constituting the inner channel. The colors correspond to the nature of the amino acids as follow: polar (green), apolar (gray), positive (blue) and negative (red). D) Top view of the stVDAC36 model without the N-terminus α-helix.

The fifty-five residues facing the inside of the channel and participating in the properties of the inner pore were identified in the model. The channel is composed of 34% polar (neutral), 19%

apolar, 9% aromatic, 21% positively charged, 17% negatively charged. Such proportions designate the channel as a polar environment with an almost neutral overall charge (*i.e.* +2). stVDAC36 does not have any particular distribution of the residues inside the pore. Indeed, the repartition is balanced with an alternation of positively and negatively charged residues all over the circumference of the channel (Figure 4.5C). With the α-helix removal, the pore is composed of 45% polar (neutral), 29% apolar, 3% aromatic, 13% positively charged and 10% negatively charged residues. The pore remains mainly polar and the charges distribution across the channel is modified. The translocation of charges was previously observed to explain the anion selectivity of VDAC proteins and supports the validity of our model [37].

Oligomerization studies by cross-linking

Some VDAC proteins have already been investigated in structural and functional studies but their oligomeric state is still uncertain. In previous works, monomers, dimers, trimers, tetramers and even hexamers have been mentioned for this protein family [38–40]. VDAC proteins retain their activity both in monomer and in oligomer state, making difficult to establish any solid structure-property correlation. Meanwhile, evidencing the nature of the stVDAC36 oligomeric states would help understanding the structural organization of the mitochondria outer membrane and its components as well as the role of oligomerization in biological processes [40–42]. Indeed, a correlation between VDAC oligomerization and apoptosis has previously been reported [4]. In that context, cross-linking is the method of choice to characterize the quaternary structure of proteins. Three homobifunctional and irreversible cross-linkers were selected with different spacer arm length: DMS (11.0 Å), DMA (8.6 Å) and DFDNB (3.0 Å). DMS and DMA have an amine-reactive imidoester groups and react with the N-terminal α-amines and lysine ε-amines at pH 7-10. They have the advantages to not change the charge of the protein thus retaining native structure and do not overreact with other nucleophilic groups. However, they present the risk to form a wide range of poorly defined oligomers and large aggregates of polymerized proteins. DFDNB contains active fluorine atoms reacting with amines but it is less selective than both DMS and DMA. This drawback can be partially countered by using very low concentrations of cross-linkers and a short incubation time.

The tests were carried out with/without the β-mercaptoethanol reducing agent and resolved by SDS-PAGE (Figure 4.6). The optimal refolding buffer, *i.e.* giving the highest β-sheets content, was selected for those experiments (60 mM SDS, 1.5 M MPD, 20 mM phosphate pH 8, 66 mM NaCl). Without β-mercaptoethanol, both DMA and DMS give strong bands at ~120 kDa, potentially evidencing the presence of tetramers. Interestingly, the intensity of this band is stronger than the one corresponding to the monomer. Large oligomers (> 250 kDa) could also be observed at the top of the gels. With DFDNB, weaker bands appear at about 30 and 90 kDa for monomer and trimers, respectively and the majority of the protein has aggregated.

When adding the reducing agent, stVDAC36 monomers remain at the same apparent molecular weight of 30 kDa but the band at ~120 kDa was worn away. This result suggests that β-mercaptoethanol can prevent the formation of stable tetramers even though it does not alter the abundance of large aggregates. Interestingly a weak band appears at ~60 kDa, hypothetically resulting from the degradation of the tetramers into dimers. The cross-linking experiments suggest that stVDAC36 can form dimers, trimers and tetramers, the latter being predominant but sensible to

chemical conditions. Trimers are associated to the weakest band which suggests a less probable state, and they are therefore not retained for the following discussion.

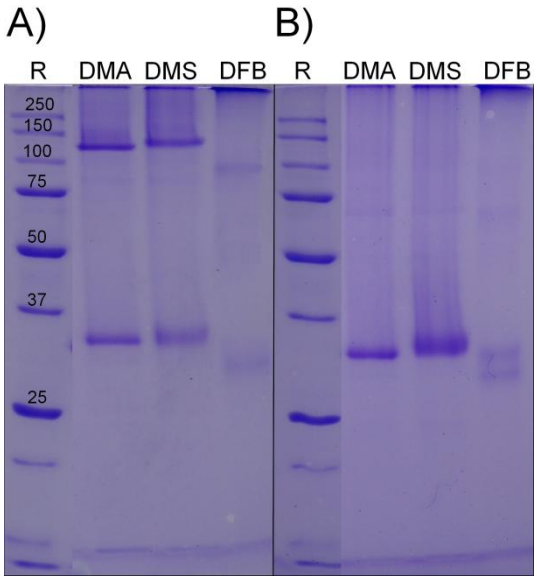

Figure 4.6: SDS-PAGE of stVDAC36 after incubation with three cross-linkers of different space arm length: dimethyl suberimidate (DMS, 11.0 Å), dimethyl adipimidate (DMA, 8.6 Å) and 1,5-difluoro-2,4-dinitrobenzene (DFDNB, 3.0 Å). The buffer is composed of phosphate pH 8, 66 mM NaCl, 60 mM SDS and 1.5 M MPD. The effect of a reducing agent in the loading buffer was studied: A) no β-mercaptoethanol, B) with β-mercaptoethanol.

The effect of the reducing agent brings us to consider the involvement of cysteine residues in the oligomerization process. A single cysteine residue is present in stVDAC36 and is, according to the model, located on the external part of the β-barrel, therefore available for intermolecular disulphide bridge. Studies on mammalian VDAC showed the involvement of cysteine in the oligomerization but this was only demonstrated for proteins with high content of Cys residues (up to nine) [43]. On the other hand, it was proved that cysteines in human VDAC2 mainly exist in their reduced form in the mitochondrial outer membrane and are more likely to stabilize the barrel with their apolar environment [44]. Actually, the number of cysteines is variable across the mammalian isoforms and their role still need to be elucidated. In the case of plants, no study has been yet performed on the role of cysteines. This first study would therefore give hypotheses on the relation between cysteines and oligomerization.

A dimer model with a disulphide bond formed by Cys158 was constructed using our stVDAC36 model (Figure 4.7). The *zebrafish* VDAC2, which served as a template for the stVDAC36 model, was proved to form dimer and also possesses a single Cys residue but not participating in the oligomerization [31]. The position of the Cys residue could be one reason of the different dimer

configuration: in stVDAC36 is at the top of the β-barrel on the cytoplasmic side while it is located at middle height of the barrel in *zebrafish* VDAC2.

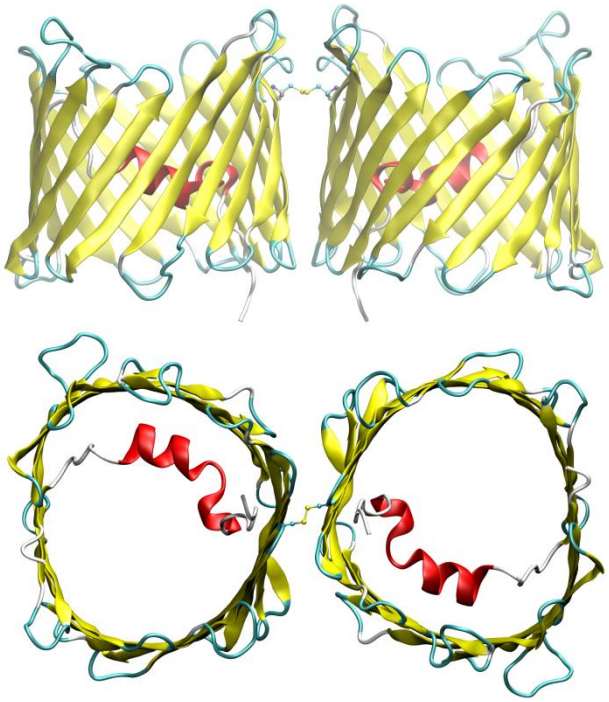

Figure 4.7: Cartoon representation of the dimer of stVDAC36 model with the intermolecular disulphide bond formed by Cys158. Secondary structure is displayed with the following colors: β-strands (yellow), α-helix (red), turns (cyan) and loops (loop). A) Side view. B) Top view.

Functional studies: pore-forming activity

Phosphatidylcholine lipids represent the main constituent of the mitochondria outer membrane where VDAC proteins are located [45]. The purified stVDAC36 was therefore reconstituted into large unilamellar vesicles (LUV) of 1,2-dioleoyl-sn-glycero-3-phosphocholine (DOPC). The vesicles were prepared by extrusion to control their size. DLS measurements indicated a hydrodynamic diameter of 148.4 ± 15.8 nm. The liposomes were also observed by TEM and showed an average diameter of 202.84 ± 31.35 nm (Figure 4.9). Micrographs were similar to the ones reported in literature [46]. The apparent bigger size of the liposomes by TEM is explained by the flattening of the vesicles after deposition onto the surface. The equation $d_{max} = \frac{\pi\, d}{2}$ gives the maximum diameter that a spherical object of diameter *d* can have after flattening [47]. Considering the latter equation, both DLS and TEM provided consistent sizes of the DOPC liposomes.

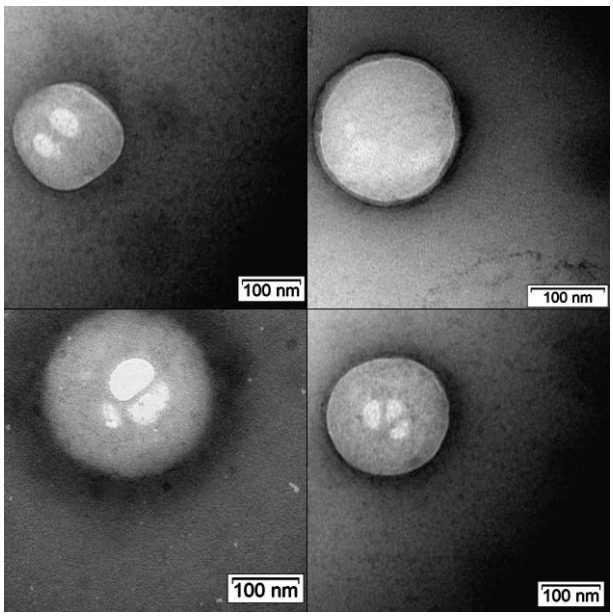

Figure 4.8: TEM images of negative stained DOPC liposomes prepared by extrusion.

Prior to functional assays, structural studies of stVDAC36 were conducted by CD to verify the conformational state of the protein after reconstitution. The spectrum of the proteoliposome is very similar to the refolded one (Figure 4.3), indicating a β-barrel structure. The calculated β-sheet content is 59% confirming the correct folding of the protein. However, a bathochromic shift is observed compared to the spectrum of the SDS-MPD refolding buffer sample. This effect was attributed to the differences in the physical properties of the amphiphilic environments SDS-MPD and DOPC liposomes [48].

Liposome swelling assays were then performed in test solutions containing substrates of different sizes. This method using sugars or polyethylene glycol (PEG) as diffusing solutes demonstrated its relevance to determinate the pore radius of membrane protein [49–52]. The selected solutes were classified according to their diameter (Table 4.2) considering that they adopt a spherical shape in water [49-51–57]. This approximation becomes less accurate as the size of the solute, especially PEG, increases.

Table 4.2: Size of the solutes used for the liposome swelling assay. The rate was calculated as the difference between the initial and last absorbance values (after 300 seconds).

Solute	Glycine	Glucose	Saccharose	Raffinose	Stachyose	PEG1000	PEG1500	PEG2000	PEG3500	PEG6000	PEG8000
Size (nm)	0.3	0.6	0.9	1.1	1.4	1.7	1.8	2.0	2.7	3.7	4.5
Rate of diffusion (%)	40.0	36.0	34.3	28.2	25.4	18.8	13.6	6.4	0.0	0.0	0.0

Liposomes without protein were added to the test solutions as negative controls, and no change in absorbance was observed. The swelling is more important with smaller solutes as previously reported for reconstituted pore-forming proteins [58]. No swelling was observed for PEG with a molecular weight equal or above 3500 Da (Figure 4.9). The assay demonstrated the ability of the reconstituted stVDAC36 to form a channel and diffuse solutes with a molecular weight below 3500 Da. The results also give an indirect determination of the pore size between 2.0 and 2.7 nm of diameter.

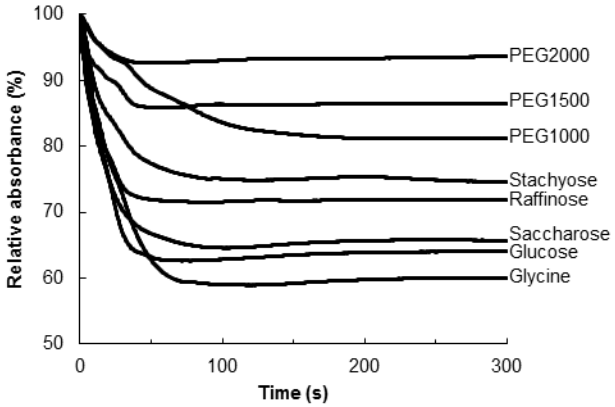

Figure 4.9: Liposome swelling assay of stVDAC36 reconstituted in DOPC liposomes. The absorbance was recorded at 450 nm after dilution of the proteo-liposomes into the test solutions containing glycine, saccharides or poly(ethyleneglycol) (PEG) of various sizes.

Those results are in agreement with the model and also with other VDAC from other organisms [35–37]. The discrepancies may be explained by the elliptical shape of the VDAC pore and the

spherical approximation of the long PEG molecules which can adopt an elongated shape. They could therefore orientate their long axis aligned with the main axis of the pore. The N-terminal extremity of VDAC forming the inner-pore α-helix is responsible of the channel gating [59-60]. The swelling data correspond to the protein conformation with the α-helix out of the barrel, as expected due to equal concentrations of ions in the internal and external media [61]. However the presence of high molecular weight PEG can induce ions partitioning in the vicinity of the proteins thus resulting in local changes of the electrical potential [62]. This phenomenon could play a role in the gating of the reconstituted stVDAC36, thus altering the diffusion of the solutes.

Functional studies: ATP binding to plant VDAC

A closer look into the channel provides essential information about the mechanism of selectivity of transport proteins. While ATP permeation through plant VDAC is totally unknown, some insights can be given using the present model.

VDACs were showed to have a high-conductance state, called the open state, and a lower-conductance state, called the partially closed state which reduces the flux of ATP molecules to zero [63–65]. Based on previous modelling studies and crystal structures on mammalian VDAC1 (mouse or human), our model is supposed to be in the open state [63]. ATP was assumed to permeate via a network of basic residues. As for mammalian VDAC1, electrostatic potential calculations show that the interior of the pore of stVDAC36 has a higher density of positive versus negative charges, partly due to the N-terminal α-helix, explaining the preference for transporting anions over cations in the open conformation (Figure 4.10) [66].

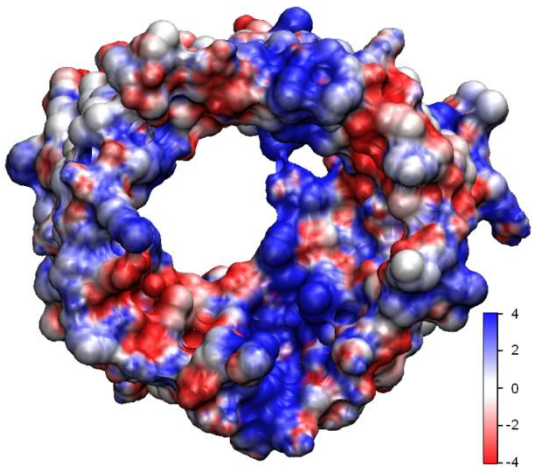

Figure 4.10: Electrostatic potential (units: $k_B T/e$) displayed on the accessible surface of stVDAC36.

A low-affinity binding site was identified in mVDAC1 for ATP in the N-terminal α-helical segment containing 3 positive (Lys-12, Lys-20, and Arg-15) and 2 negative (Asp-9 and Asp-16) charges facing the interior of the pore [66-67]. Interestingly these five residues are conserved in stVDAC36 (Lys-13, Arg-16, Asp-10, Asp-17) except Lys-20 which is replaced by an arginine (Arg-21). Replacing a serine in mVDAC, an additional lysine is present in the α-helix of stVDAC36, reinforcing the positive charge of the helix. Based on a docking study, several binding modes of ATP were identified inside the pore and interacting with the positive residues of the N-terminal, supporting the hypothesis of a low-binding affinity. One of these binding modes involved the specific Arg found in stVDAC36 and Lys-28 from the β1 sheet, interacting with the ATP phosphate group (Figure 4.11).

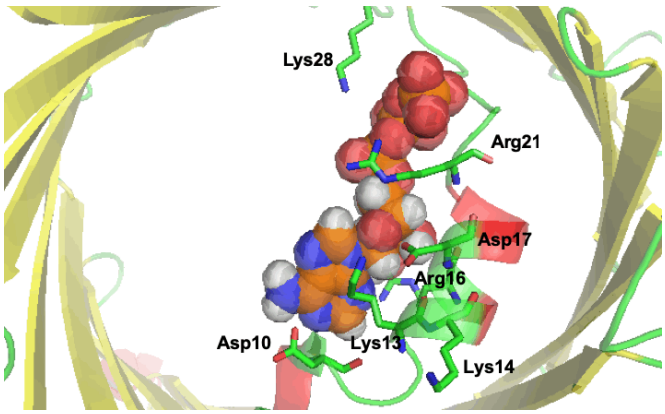

Figure 4.11: Potential ATP binding mode inside stVDAC36.

4.4. Conclusion

In this work, the stVDAC36 from *Solanum tuberosum* was first expressed and purified. The protein was subsequently refolded in one step by the SDS/MPD method. Circular dichroism was used to assess the secondary structure of the protein and verify the refolding. Doing so, a typical spectrum of β-barrels was obtained. The highest β-sheet content was attained with a SDS/MPD ratio of 60 mM and 1.5 M, respectively. Fluorescence measurements confirmed the conformation changes undergone by the protein after refolding. The formation of oligomers was then studied by cross-linking. Tetramers were predominant but were not stable against reducing agent such as β-mercaptoethanol. In such conditions, dimers were mainly present. The involvement of cysteine residues was therefore investigated and a realistic model of a stVDAC36 dimer with an intermolecular disulphide bond was constructed.

The protein was also reconstituted into lipid vesicles prepared by extrusion. The size of the vesicles could be controlled and the ability of the protein to diffuse solutes was evaluated by liposome swelling assays. The solutes varied in size in a range from 0.3 to 4.5 nm. It was concluded that stVDAC36 could not diffuse solutes bigger than 3500 Da, resulting of a pore diameter between 2.0 and 2.7 nm. This is in accordance with the size of the pore calculated from the model and other known similar channels.

4.5. Bibliography

[1] V. Shoshan-Barmatz and D. Ben-Hail, "VDAC, a multi-functional mitochondrial protein as a pharmacological target," *Mitochondrion*, 12, 1, 24–34, 2012.

[2] T. Salinas, A.-M. Duchêne, and L. Maréchal-Drouard, "Recent advances in tRNA mitochondrial import," *Trends Biochem. Sci.*, 33, 7, 320–329, 2008.

[3] F. Homblé, E.-M. Krammer, and M. Prévost, "Plant VDAC: Facts and speculations," *Biochim. Biophys. Acta - Biomembr.*, 1818, 6, 1486–1501, 2012.

[4] N. Keinan, D. Tyomkin, and V. Shoshan-Barmatz, "Oligomerization of the mitochondrial protein voltage-dependent anion channel is coupled to the induction of apoptosis.," *Mol. Cell. Biol.*, 30, 24, 5698–709, 2010.

[5] S. Hiller, R. G. Garces, T. J. Malia, V. Y. Orekhov, M. Colombini, and G. Wagner, "Solution Structure of the Integral Human Membrane Protein VDAC-1 in Detergent Micelles," *Science (80-.).*, 321, 5893, 1206–1210, 2008.

[6] O. Teijido, R. Ujwal, C.-O. Hillerdal, L. Kullman, T. K. Rostovtseva, and J. Abramson, "Affixing N-terminal α-Helix to the Wall of the Voltage-dependent Anion Channel Does Not Prevent Its Voltage Gating," *J. Biol. Chem.*, 287, 14, 11437–11445, 2012.

[7] M. Colombini, "VDAC structure, selectivity, and dynamics.," *Biochim. Biophys. Acta*, 1818, 6, 1457–65, 2012.

[8] L. Heins, H. Mentzel, A. Schmid, R. Benz, and U. K. Schmitz, "Biochemical, molecular, and functional characterization of porin isoforms from potato mitochondria.," *J. Biol. Chem.*, 269, 42, 26402–10, 1994.

[9] T. Salinas, S. El Farouk-Ameqrane, E. Ubrig, C. Sauter, A.-M. M. Duchêne, and L. Maréchal-Drouard, "Molecular basis for the differential interaction of plant mitochondrial VDAC proteins with tRNAs," *Nucleic Acids Res.*, 42, 15, 9937–9948, 2014.

[10] J. Kinzel, D. F. Sauer, M. Bocola, M. Arlt, T. Mirzaei Garakani, A. Thiel, K. Beckerle, T. Polen, J. Okuda, and U. Schwaneberg, "2-Methyl-2,4-pentanediol (MPD) boosts as detergent-substitute the performance of ß-barrel hybrid catalyst for phenylacetylene polymerization," *Beilstein J. Org. Chem.*, 13, 1, 1498–1506, 2017.

[11] C. Michaux, N. C. Pomroy, and G. G. Privé, "Refolding SDS-Denatured Proteins by the Addition of Amphipathic Cosolvents," *J. Mol. Biol.*, 375, 5, 1477–1488, 2008.

[12] G. Roussel, E. A. Perpète, A. Matagne, E. Tinti, and C. Michaux, "Towards a universal method for protein refolding: The trimeric beta barrel membrane Omp2a as a test case," *Biotechnol. Bioeng.*, 110, 2, 417–423, 2013.

[13] T. Salinas, A.-M. Duchene, L. Delage, S. Nilsson, E. Glaser, M. Zaepfel, and L. Marechal-Drouard, "The voltage-dependent anion channel, a major component of the tRNA import machinery in plant mitochondria," *Proc. Natl. Acad. Sci.*, 103, 48, 18362–18367, 2006.

[14] L. Whitmore and B. A. Wallace, "Protein secondary structure analyses from circular dichroism spectroscopy: Methods and reference databases," *Biopolymers*, 89, 5, 392–400, 2008.

[15] M. Källberg, H. Wang, S. Wang, J. Peng, Z. Wang, H. Lu, and J. Xu, "Template-based protein structure modeling using the RaptorX web server.," *Nat. Protoc.*, 7, 8, 1511–22, 2012.

[16] W. Kabsch and C. Sander, "Dictionary of protein secondary structure: Pattern recognition of hydrogen-bonded and geometrical features," *Biopolymers*, 22, 12, 2577–2637, 1983.

[17] W. Humphrey, A. Dalke, and K. Schulten, "VMD: Visual molecular dynamics," *J. Mol. Graph.*, 14, 1, 33–38, 1996.

[18] E. Jurrus, D. Engel, K. Star, K. Monson, J. Brandi, *et al.*, "Improvements to the APBS biomolecular solvation software suite," *Protein Sci.*, 27, 1, 112–128, 2018.

[19] G. Jones, P. Willett, R. C. Glen, A. R. Leach, and R. Taylor, "Development and validation of a genetic algorithm for flexible docking 1 1Edited by F. E. Cohen," *J. Mol. Biol.*, 267, 3,

727–748, 1997.
[20] M. Bayrhuber, T. Meins, M. Habeck, S. Becker, K. Giller, S. Villinger, C. Vonrhein, C. Griesinger, M. Zweckstetter, and K. Zeth, “Structure of the human voltage-dependent anion channel.,” *Proc. Natl. Acad. Sci.*, 105, 40, 15370–5, 2008.
[21] D. Otzen, “Protein-surfactant interactions: a tale of many states.,” *Biochim. Biophys. Acta*, 1814, 5, 562–91, 2011.
[22] K. K. Andersen, C. L. Oliveira, K. L. Larsen, F. M. Poulsen, T. H. Callisen, P. Westh, J. S. Pedersen, D. Otzen, G. W. Vej, D.-A. C, and D.-A. C, “The Role of Decorated SDS Micelles in Sub-CMC Protein Denaturation and Association,” *J. Mol. Biol.*, 391, 1, 207–226, 2009.
[23] D. E. Otzen, P. Sehgal, and P. Westh, “α-Lactalbumin is unfolded by all classes of surfactants but by different mechanisms,” *J. Colloid Interface Sci.*, 329, 2, 273–283, 2009.
[24] B. A. Wallace, J. G. Lees, A. J. W. Orry, A. Lobley, and R. W. Janes, “Analyses of circular dichroism spectra of membrane proteins.,” *Protein Sci.*, 12, 4, 875–84, 2003.
[25] G. Roussel, A. Matagne, X. De Bolle, E. A. a. Perpète, and C. Michaux, “Purification, refolding and characterization of the trimeric Omp2a outer membrane porin from Brucella melitensis,” *Protein Expr. Purif.*, 83, 2, 198–204, 2012.
[26] L. K. Tamm, H. Hong, and B. Liang, “Folding and assembly of β-barrel membrane proteins,” *Biochim. Biophys. Acta - Biomembr.*, 1666, 1–2, 250–263, 2004.
[27] G. Roussel, Y. Caudano, A. Matagne, M. S. Sansom, E. A. Perpète, and C. Michaux, “Peptide-surfactant interactions: A combined spectroscopic and molecular dynamics simulation approach,” *Spectrochim. Acta Part A Mol. Biomol. Spectrosc.*, 190, 464–470, 2018.
[28] C. Michaux, G. Roussel, M. Lopes-Rodrigues, A. Matagne, and E. A. Perpète, “Unravelling the mechanisms of a protein refolding process based on the association of detergents and co-solvents,” *J. Pept. Sci.*, March, 485–491, 2016.
[29] S. Micelli, D. Meleleo, V. Picciarelli, M. G. Stoico, and E. Gallucci, “Effect of nanomolar concentrations of sodium dodecyl sulfate, a catalytic inductor of alpha-helices, on human calcitonin incorporation and channel formation in planar lipid membranes.,” *Biophys. J.*, 87, 2, 1065–75, 2004.
[30] G. Roussel, S. L. Rouse, M. S. P. Sansom, C. Michaux, and E. A. Perpète, “The role of 2-methyl-2, 4-pentanediol in sodium dodecyl sulfate micelle dissociation unveiled by dynamic light scattering and molecular dynamics simulations,” *Colloids Surfaces B Biointerfaces*, 114, 357–362, 2014.
[31] J. Schredelseker, A. Paz, C. J. López, C. Altenbach, C. S. Leung, M. K. Drexler, J.-N. Chen, W. L. Hubbell, and J. Abramson, “High resolution structure and double electron-electron resonance of the zebrafish voltage-dependent anion channel 2 reveal an oligomeric population.,” *J. Biol. Chem.*, 289, 18, 12566–77, 2014.
[32] S. Hiller, J. Abramson, C. Mannella, G. Wagner, and K. Zeth, “The 3D structures of VDAC represent a native conformation.,” *Trends Biochem. Sci.*, 35, 9, 514–21, 2010.
[33] M. Lopes-Rodrigues, D. Zanuy, C. Alemán, C. Michaux, and E. A. Perpète, “3D structure of a Brucella melitensis porin: molecular modelling in lipid membranes,” *J. Biomol. Struct. Dyn.*, 1–13, 2018.
[34] M. Colombini, “VDAC structure, selectivity, and dynamics,” *Biochim. Biophys. Acta - Biomembr.*, 1818, 6, 1457–1465, 2012.
[35] J. Zimmerberg and V. A. Parsegian, “Polymer inaccessible volume changes during opening and closing of a voltage-dependent ionic channel,” *Nature*, 323, 6083, 36–39, 1986.
[36] M. Colombini, C. L. Yeung, J. Tung, and T. König, “The mitochondrial outer membrane channel, VDAC, is regulated by a synthetic polyanion,” *Biochim. Biophys. Acta - Biomembr.*, 905, 2, 279–286, 1987.
[37] M. Colombini, “The VDAC channel: Molecular basis for selectivity,” *Biochim. Biophys.*

Acta - Mol. Cell Res., 1863, 10, 2498–2502, 2016.

[38] V. Betaneli, E. P. Petrov, and P. Schwille, "The role of lipids in VDAC oligomerization.," *Biophys. J.*, 102, 3, 523–31, 2012.

[39] B. W. Hoogenboom, K. Suda, A. Engel, and D. Fotiadis, "The Supramolecular Assemblies of Voltage-dependent Anion Channels in the Native Membrane," *J. Mol. Biol.*, 370, 2, 246–255, 2007.

[40] R. Zalk, A. Israelson, E. S. Garty, H. Azoulay-Zohar, and V. Shoshan-Barmatz, "Oligomeric states of the voltage-dependent anion channel and cytochrome c release from mitochondria.," *Biochem. J.*, 386, Pt 1, 73–83, 2005.

[41] J. Krause, R. Hay, C. Kowollik, and D. Brdiczka, "Cross-linking analysis of yeast mitochondrial outer membrane.," *Biochim. Biophys. Acta*, 860, 3, 690–8, 1986.

[42] S. Peng, E. Blachly-Dyson, M. Colombini, and M. Forte, "Determination of the number of polypeptide subunits in a functional VDAC channel from Saccharomyces cerevisiae.," *J. Bioenerg. Biomembr.*, 24, 1, 27–31, 1992.

[43] V. De Pinto, S. Reina, A. Gupta, A. Messina, and R. Mahalakshmi, "Role of cysteines in mammalian VDAC isoforms' function," *Biochim. Biophys. Acta - Bioenerg.*, 1857, 8, 1219–1227, 2016.

[44] S. R. Maurya and R. Mahalakshmi, "Cysteine Residues Impact the Stability and Micelle Interaction Dynamics of the Human Mitochondrial β-Barrel Anion Channel hVDAC-2," *PLoS One*, 9, 3, e92183, 2014.

[45] A. I. P. . de Kroon, D. Dolis, A. Mayer, R. Lill, and B. de Kruijff, "Phospholipid composition of highly purified mitochondrial outer membranes of rat liver and Neurospora crassa. Is cardiolipin present in the mitochondrial outer membrane?," *Biochim. Biophys. Acta - Biomembr.*, 1325, 1, 108–116, 1997.

[46] P. Walsh, G. Vanderlee, J. Yau, J. Campeau, V. L. Sim, C. M. Yip, and S. Sharpe, "The mechanism of membrane disruption by cytotoxic amyloid oligomers formed by prion protein(106-126) is dependent on bilayer composition.," *J. Biol. Chem.*, 289, 15, 10419–30, 2014.

[47] U. Baxa, "Imaging of Liposomes by Transmission Electron Microscopy," in *Characterization of Nanoparticles Intended for Drug Delivery*, Humana Press, New York, NY, 2018, 73–88.

[48] A. J. Miles and B. A. Wallace, "Circular dichroism spectroscopy of membrane proteins," *Chem. Soc. Rev.*, 45, 18, 4859–4872, 2016.

[49] A. Godbole, R. Mitra, A. K. Dubey, P. S. Reddy, and M. K. Mathew, "Bacterial expression, purification and characterization of a rice voltage-dependent, anion-selective channel isoform, OsVDAC4," *J. Membr. Biol.*, 244, 2, 67–80, 2011.

[50] F. Jacob-Dubuisson, "Channel Formation by FhaC, the Outer Membrane Protein Involved in the Secretion of the Bordetella pertussis Filamentous Hemagglutinin," *J. Biol. Chem.*, 274, 53, 37731–37735, 1999.

[51] H. Nikaido and E. Y. Rosenberg, "Porin channels in Escherichia coli: studies with liposomes reconstituted from purified proteins.," *J. Bacteriol.*, 153, 1, 241–52, 1983.

[52] J. W. F. Robertson, C. G. Rodrigues, V. M. Stanford, K. A. Rubinson, O. V. Krasilnikov, and J. J. Kasianowicz, "Single-molecule mass spectrometry in solution using a solitary nanopore," *Proc. Natl. Acad. Sci.*, 104, 20, 8207–8211, 2007.

[53] C. M. Tam and A. Y. Tremblay, "Membrane pore characterization—comparison between single and multicomponent solute probe techniques," *J. Memb. Sci.*, 57, 2–3, 271–287, 1991.

[54] S. G. Schultz and A. K. Solomon, "Determination of the effective hydrodynamic radii of small molecules by viscometry.," *J. Gen. Physiol.*, 44, 6, 1189–99, 1961.

[55] C. J. Fee and J. M. Van Alstine, "Prediction of the Viscosity Radius and the Size Exclusion Chromatography Behavior of PEGylated Proteins," *Bioconjug. Chem.*, 15, 6, 1304–1313,

2004.
[56] S. Kuga, “Pore size distribution analysis of gel substances by size exclusion chromatography,” *J. Chromatogr. A*, 206, 3, 449–461, 1981.
[57] Z. Ma, D. N. LeBard, S. M. Loverde, K. A. Sharp, M. L. Klein, D. E. Discher, and T. H. Finkel, “TCR Triggering by pMHC Ligands Tethered on Surfaces via Poly(Ethylene Glycol) Depends on Polymer Length,” *PLoS One*, 9, 11, e112292, 2014.
[58] R. H. Senaratne, H. Mobasheri, P. Jenner, E. J. A. Lea, and K. G. Papavinasasundaram, “Expression of a Gene for a Porin-Like Protein of the OmpA Family from Mycobacterium tuberculosis H37Rv Expression of a Gene for a Porin-Like Protein of the OmpA Family from Mycobacterium tuberculosis H37Rv,” 180, 14, 3541–3547, 1998.
[59] D. A. Koppel, K. W. Kinnally, P. Masters, M. Forte, E. Blachly-Dyson, and C. A. Mannella, “Bacterial expression and characterization of the mitochondrial outer membrane channel. Effects of n-terminal modifications.,” *J. Biol. Chem.*, 273, 22, 13794–800, 1998.
[60] C. Guardiani, M. A. Scorciapino, G. F. Amodeo, J. Grdadolnik, G. Pappalardo, V. De Pinto, M. Ceccarelli, and M. Casu, “The N-Terminal Peptides of the Three Human Isoforms of the Mitochondrial Voltage-Dependent Anion Channel Have Different Helical Propensities,” *Biochemistry*, 54, 36, 5646–5656, 2015.
[61] H. Saidani, E.-M. Krammer, M. Prevost, and F. Homble, “Plant VDAC Selectivity and Voltage-Dependence are Uncoupled,” *Biophys. J.*, 106, 2, 791a, 2014.
[62] M. A. Aksoyoglu, R. Podgornik, S. M. Bezrukov, P. A. Gurnev, M. Muthukumar, and V. A. Parsegian, “Size-dependent forced PEG partitioning into channels: VDAC, OmpC, and α-hemolysin.,” *Proc. Natl. Acad. Sci. U. S. A.*, 113, 32, 9003–8, 2016.
[63] O. P. Choudhary, R. Ujwal, W. Kowallis, R. Coalson, J. Abramson, and M. Grabe, “The Electrostatics of VDAC: Implications for Selectivity and Gating,” *J. Mol. Biol.*, 396, 3, 580–592, 2010.
[64] S. R. Shuvo, F. G. Ferens, and D. A. Court, “The N-terminus of VDAC: Structure, mutational analysis, and a potential role in regulating barrel shape,” *Biochim. Biophys. Acta - Biomembr.*, 1858, 6, 1350–1361, 2016.
[65] T. Rostovtseva and M. Colombini, “VDAC channels mediate and gate the flow of ATP: implications for the regulation of mitochondrial function,” *Biophys. J.*, 72, 5, 1954–1962, 1997.
[66] R. Ujwal, D. Cascio, J.-P. Colletier, S. Faham, J. Zhang, L. Toro, P. Ping, and J. Abramson, “The crystal structure of mouse VDAC1 at 2.3 A resolution reveals mechanistic insights into metabolite gating,” *Proc. Natl. Acad. Sci.*, 105, 46, 17742–17747, 2008.
[67] O. P. Choudhary, A. Paz, J. L. Adelman, J.-P. Colletier, J. Abramson, and M. Grabe, “Structure-guided simulations illuminate the mechanism of ATP transport through VDAC1,” *Nat. Struct. Mol. Biol.*, 21, 7, 626–632, 2014.

5. Biomimetic hybrid membrane made of PLA, PEDOT and VDAC36

5. Biomimetic hybrid membranes made of PLA, PEDOT and VDAC36

Summary

Hybrid free-standing biomimetic materials are developed by integrating the VDAC36 β-barrel protein into robust and flexible three-layered polymer nanomembranes. The first and third layers are prepared by spin-coating a mixture of poly(lactic acid) (PLA) and poly(vinyl alcohol) (PVA). PVA nanofeatures are transformed into controlled nanoperforations by solvent-etching. The two nanoperforated PLA layers are separated by an electroactive layer, which is successfully electropolymerized by introducing a conducting sacrificial substrate below the first PLA nanosheet. Finally, the nanomaterial is consolidated by immobilizing the VDAC36 protein, active as an ion channel, into the nanoperforations of the upper layer. The integration of the protein causes a significant reduction of the material electrical resistance, which decreases from 21.9 to 3.9 $k\Omega \cdot cm^2$. Electrochemical impedance spectroscopy studies reveal that the hybrid material behaves as a supercapacitor. The combination of polymers and proteins is promising for the development of new devices in bioelectronics.

5.1. Introduction

Hybrid biomimetic membranes take advantage, on the one hand, of biomolecules having gained excellence on their specificity and efficiency during billions of years, and, on the other hand, of artificial materials loading the purified biological molecules as well as providing technological properties, such as robustness, scalability and suitable nanofeatures to confine the biomolecules. Molecular sensing, water purification and desalination, drug delivery and DNA sequencing are some striking applications of these 2D devices.

Porins are a class of outer membrane proteins (OMPs), which consist of β-barrel channels located in gram-negative bacteria and mitochondria [1]. β-Barrels are typically employed for the fabrication of hybrid biomimetic membranes [2–6], even though other biomolecules and materials have also attracted interest [7–13]. From the perspective of the employed materials, the approaches used to modify artificial membranes, which can be free-standing or tethered onto solid supports, with biomolecules are those based on the use of amphiphilic copolymers and nanostructured polymers.

In a recent study, the latter approach was used to embed an OMP, named Omp2a [14], in a supported conducting polymer (CP) membrane made of poly(*N*-methylpyrrole) (PNMPy) [5]. Electrochemical impedance spectroscopy (EIS) showed that PNMPy/Omp2a preferentially promotes the passive transport of K^+ in solutions with relatively high ionic concentrations. The PNMPy membrane was electrochemically synthesized onto a rigid stainless steel electrode, which represents a serious inconvenient for possible future applications. Later, self-standing poly(lactic acid) (PLA) nanomembranes were used as support for the Omp2a protein [6]. These membranes, which were prepared by spin-coating an immiscible mixture of poly(vinyl alcohol) (PVA) and PLA [15], showed nanoperforations (diameter: 51±22 nm) resulting from the combination of nanophase segregation processes and selective solvent etching. EIS assays evidenced that, with respect to protein-free nanoperforated PLA (npPLA) nanomembranes, the protein, confined around and inside the nanoperforations, enhanced the conductivity and selectivity against some ions [16].

5. Biomimetic hybrid membranes made of PLA, PEDOT and VDAC36

In this work we present a new approach to synergistically combine the advantages of supported and free-standing hybrid biomimetic membranes based on CPs, biodegradable PLA and OMPs. This approach is based on a smart strategy that merges the processing of npPLA nanosheets, the anodic polymerization of poly(3,4-ethylenedioxythiopene) (PEDOT), and the functionality of Voltage Dependent Anion Channels (VDACs), porins found in the outer mitochondrial membrane of all eukaryotic cells [17]. The function of VDACs is associated with the permeability of the mitochondria, regulating the diffusion of ions and metabolites [18-19]. Specifically, this work focus on the use of VDAC from *Solanum tuberosum*, a plant (potato) model organism, hereafter named VDAC36 [20]. Results show that npPLA/PEDOT/npPLA/VDAC free-standing membranes are biomimetic, exhibit low electrical resistance, and behave as a supercapacitor.

5.2. Methods

Materials. Poly(3,4-ethylenedioxythiophene):poly(styrenesulfonate) (PEDOT:PSS) 1.3 wt. % dispersion in H_2O, 3,4-ethylenedioxythiophene (EDOT), PVA 87-89% hydrolyzed and lithium perchlorate ($LiClO_4$) were purchased from Sigma-Aldrich (USA). PLA 2002D, a product of Natureworks, was kindly supplied by Nupik International (Polinyà, Spain). According to the manufacturer, this PLA has a D content of 4.25%, a residual monomer content of 0.3%, density of 1.24 g/cm^3, glass transition temperature (T_g) of 58 ^oC, and melting temperature (T_m) of 153 ^oC. Acetonitrile and hexafluoroisopropanol (HFIP) were purchased from Panreac Quimica S.A.U. (Spain).

Spin-coating. Spin-coating was performed using the conditions described in the main text with a spin-coater (WS-400BZ-6NPP/A1/AR1 Laurell Technologies Corporation). The PEDOT:PSS sacrificial layer was obtained by spin-coating a commercial water dispersion (1.3 wt. %) at a speed of 800 rpm for 1 min. Nanoperforated PLA (npPLA) layers were obtained by blending PLA and PVA with a ratio of 90:10 v/v (PLA:PVA), prepared by mixing PLA (10 mg/mL) and PVA (10 mg/mL) HFIP solutions. The spin-coating of the PLA:PVA mixture was conducted at 1200 rpm for 1 min. The resulting PLA:PVA nanomembrane was transformed into npPLA by eliminating the PVA phase. For this purpose, selective solvent etching was carried out by dropping milli-Q water on the surface for 1 h without agitation at 20 ºC.

Anodic polymerization. Anodic polymerizations were performed using a VersaStat II potentiostat-galvanostat connected to a computer controlled through a Metrohm Autolab Nova program. Electrochemical experiments were conducted in a three-electrode two-compartment cell under nitrogen atmosphere (99.995% in purity) at 20 ºC. The anodic compartment was filled with 40 mL of a 10 mM EDOT solution in acetonitrile containing 0.1 M $LiClO_4$ as supporting electrolyte, while the cathodic compartment was filled with 10 mL of the same electrolyte solution. Steel AISI 316L sheets, previously washed with acetone and ethanol, were employed as working (coated with a PEDOT:PSS layer) and counter (bare) electrodes. The reference electrode was an Ag|AgCl electrode containing a KCl saturated aqueous solution (E^o = 0.222 V at 25 ºC), which was connected to the working compartment through a salt bridge containing the electrolyte solution. All anodic polymerizations were conducted by chronoamperometry under a constant potential of +1.40 V and adjusting the polymerization charge to 90 mC.

Expression, purification and immobilization of the VDAC36 protein. Escherichia coli BL21 (DE3) bacteria were transformed to produce 6 His-tagged VDAC36 proteins in inclusion bodies.

Bacteria were then lysed and centrifuged to obtain the final pellet corresponding to the non-purified unfolded proteins. VDAC36 was then purified by Ni^{2+} affinity column. VDAC36 was eluted and the buffer was exchanged to 20 mM phosphate pH 8, 60 mM sodium dodecyl sulfate (SDS) and 1.5 M 2-methyl-2,4-pentanediol (MPD) with a PD10 desalting column. The supported npPLA/PEDOT/npPLA 3-layered film was used to immobilize the protein. For this purpose, samples were placed on a 24-well plate and incubated with 1000 µL of a protein solution, which contained 0.85 mg/mL VDAC36, 60 mM SDS and 1.5 M MPD, for 12 h at 20 ºC.
The resulting npPLA/PEDOT/npPLA/VDAC samples were rinsed three times with milliQ water to remove residues. Blank film was obtained using the same procedure (*i.e.* 60 mM SDS and 1.5 M MPD) but without VDAC36.

Profilometry. Film thickness measurements were carried out using a Dektak 150 stylus profilometer (Veeco, Plainview, NY). Different scratches were intentionally caused on the films and measured to allow statistical analysis of data. At least eighteen independent measurements were performed for three samples of each examined condition. Imaging of the films was conducted using the following optimized settings: tip radius = 2.5 µm; stylus force = 3.0 mg; scan length = 1 mm; and speed = 50 µm/s.

Scanning electron microscopy. Detailed inspection of films and layers was conducted by scanning electron microscopy (SEM). A Focus Ion Beam Zeiss Neon 40 instrument (Carl Zeiss, Germany) equipped with an energy dispersive X-ray (EDX) spectroscopy system and operating at 1 kV was used. Films supported onto steel sheets were mounted on a double-sided adhesive carbon disc and sputter-coated with an ultra-thin carbon layer (6-10 nm) to prevent sample charging problems. The diameter of the perforations was measured with the SmartTiff software from Carl Zeiss SMT Ltd.

Fluorescence microscopy. Imaging was performed using an Axio Observer Z1 fluorescence microscope (Carl Zeiss) confocal laser scanning microscope with a 60x oil objective. The excitation wavelength was set to 280 nm and the emission was collected at 303 and 354 nm, for tyrosine (Tyr) and tryptophan (Trp) residues, respectively.

Atomic force microscopy. AFM images of PLA nanomembranes before and after application of selective solvent etching were obtained with a Molecular Imaging PicoSPM using a NanoScope IV controller under ambient conditions. The tapping mode AFM was operated at constant deflection (*i.e.* vertical constant force with triangular shaped gold-coated silicon nitride). The row scanning

frequency was set to 0.87 or 0.68 Hz, depending on the sample response, and the physical tip sample motion speed was 10 mm/s.

Raman spectroscopy. Samples were characterized using a commercial Renishaw inVia Qontor confocal Raman microscope. The Raman setup consisted of a laser (at 785 nm with a nominal 300 mW output power) directed through a microscope (specially adapted Leica DM2700 M microscope) to the sample, after which the scattered light is collected and directed to a spectrometer with a 1200 lines·mm^{-1} grating. The exposure time was 1 s, the laser power was adjusted to 0.1% of its nominal output power depending on the sample, and each spectrum was collected with three accumulations.

FTIR spectroscopy. FTIR spectra were recorded on a FTIR Jasco 4100 spectrophotometer. The powder and films were deposited on an attenuated total reflection accessory (Top-plate) with a diamond crystal (Specac model MKII Golden Gate Heated Single Reflection Diamond ATR). Samples were evaluated using the spectra manager software and, for each sample, 32 scans were performed between 4000 and 600 cm^{-1} with a resolution of 4 cm^{-1}.

X-ray photoelectron spectroscopy. XPS analyses were performed in a SPECS system equipped with a high-intensity twin-anode X-ray source XR50 of Mg/Al (1253 eV/1487 eV) operating at 150 W, placed perpendicular to the analyzer axis, and using a Phoibos 150 MCD-9 XP detector. The X-ray spot size was 650 mm. The pass energy was set to 25 and 0.1 eV for the survey and the narrow scans, respectively. Charge compensation was achieved with a combination of electron and argon ion flood guns. The energy and emission currents of the electrons were 4 eV and 0.35 mA, respectively. For the argon gun, the energy and the emission currents were 0 eV and 0.1 mA, respectively. The spectra were recorded with a pass energy of 25 eV in 0.1 eV steps at a pressure below 6·10^{-9} mbar. These standard conditions of charge compensation resulted in a negative but perfectly uniform static charge. The C1s peak was used as an internal reference with a binding energy of 284.8 eV. High-resolution XPS spectra were acquired by Gaussian/Lorentzian curve fitting after S-shape background subtraction. The surface composition was determined using the manufacturer's sensitivity factors.

Wettability. Contact angle measurements were carried out using the water sessile drop method. Images of 0.5 μL distillated water drops were recorded after stabilization with the equipment OCA 15EC (Data-Physics Instruments GmbH, Filderstadt). SCA20 software was used to analyze the images and determine the contact angle value, which was obtained as the average of at least fifteen independent measures for each sample.

Circular dichroism. CD spectra were recorded between 190 and 260 nm at room temperature using a Jasco J-815 equipment with a protein concentration of approximately 110 µg/mL and a 0.1 cm cell path. Spectra were acquired at a scan speed of 50 nm min^{-1} with a 0.2 nm data pitch using a 2 nm bandwidth and a 4 second digital integration time. Spectra were averaged after two accumulations and corrected by subtraction of the background spectrum.

Electrochemical impedance spectroscopy. EIS measurements were performed using a conventional three-electrode cell and an AUTOLAB-302N potentiostat/galvanostat operating between the frequency range of 10^5 Hz and 10^{-2} Hz and 10 mV of amplitude for the sinusoidal voltage. All experiments were performed at room temperature with 3-layered membranes deposited onto steel and using a 500 mM NaCl electrolyte solution. Steel was used as working-electrode and platinum as counter-electrode, whereas Ag|AgCl saturated (KCl 3M) was employed as reference electrode. After data collection, EIS results were then processed and fitted to an electrical equivalent circuit (EEC).

5.3. Results and discussion

Preparation and characterization of the 3-layered film

The process used to prepare the new biomimetic membrane is schematically summarized in Figure 5.1, and experimental details are given in the Methods section. An electroactive PEDOT: PSS film of 173±19 nm in thickness was prepared as sacrificial layer by spin-coating a commercial water dispersion onto steel AISI 316 sheets (Figure 5.1a). Then, a PLA:PVA layer was deposited onto the PEDOT:PSS sheet by spin-coating a PLA:PVA mixture in hexafluoroisopropanol (HFIP) (Figure 5.1b). As PLA and PVA are immiscible polymers, the resulting PLA:PVA layer displays a phase segregation with the formation of PVA domains with dimensions similar to the entire film thickness (Figure 5.1c) [21], which is 135±18 nm.

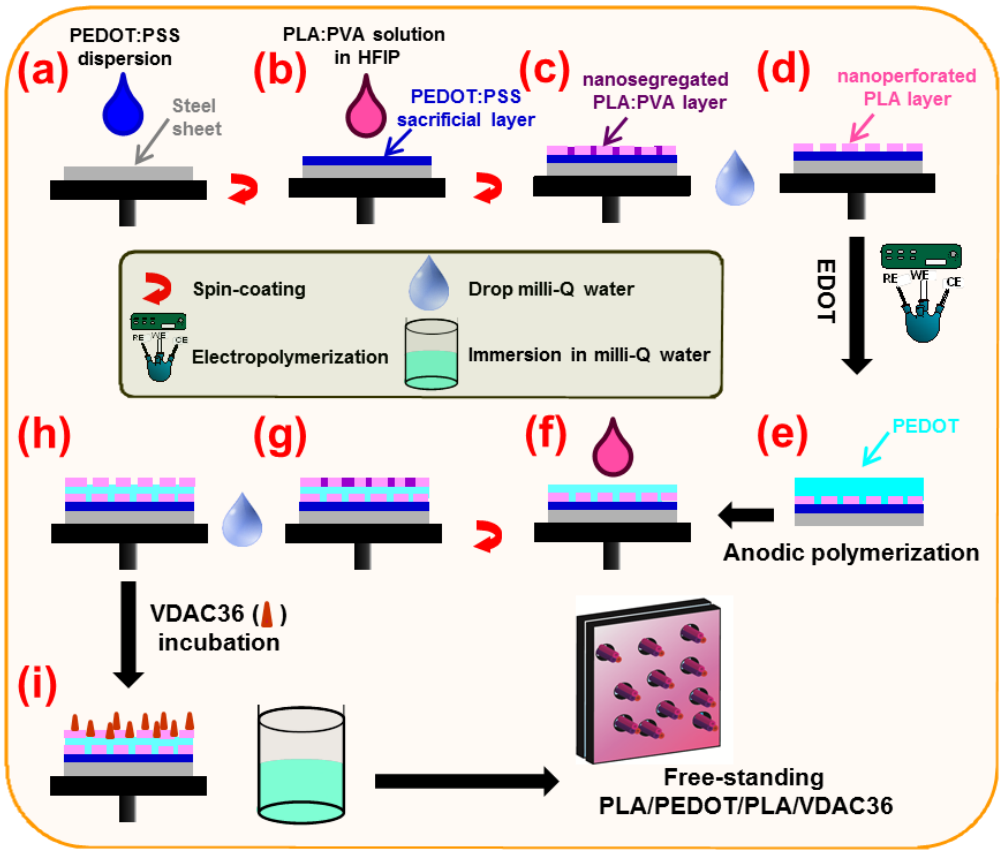

Figure 5.1: Scheme illustrating the preparation of npPLA/PEDOT/npPLA/VDAC free-standing biomimetic membranes.

Representative AFM phase images (Figure 5.2) show nanofeatures, consisting of separated PVA rounded-shape domains within the PLA matrix (lighter and darker contrast, respectively). Nanofeatures transform into nanoperforations (Figure 5.1d) by selective solvent etching, and resulting films are 114±11 nm thick. AFM phase images of npPLA are shown in Figure 5.2, while

the representative SEM micrograph displayed in Figure 5.3 illustrates the abundance and distribution of the nanoperforations, which are 49±14 nm in diameter.

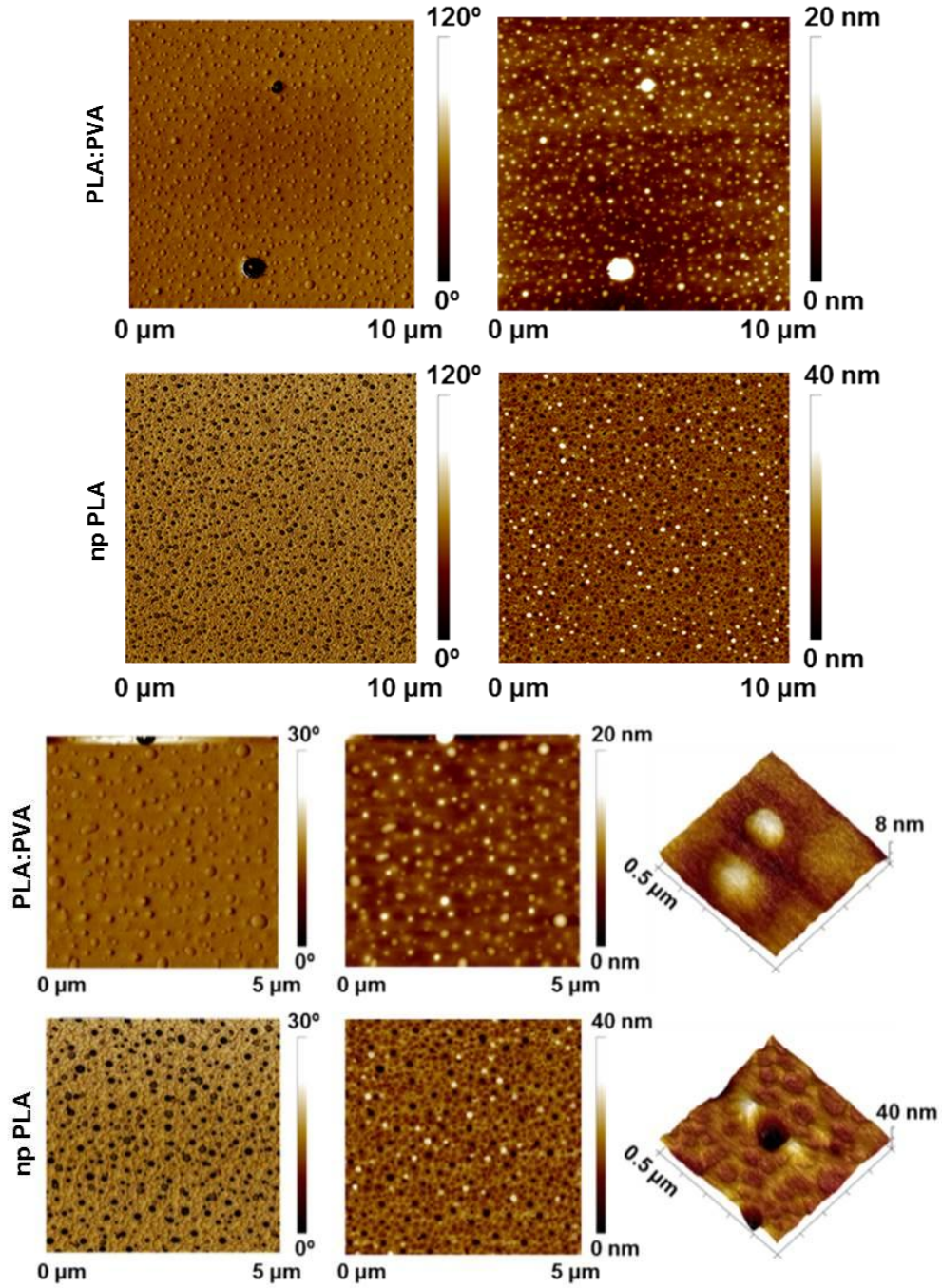

Figure 5.2: AFM phase and topographic images of PLA:PVA and npPLA films.

Nanoperforations in the PLA nanosheet were responsible of the successful anodic polymerization of PEDOT (Figure 5.1e). For this purpose, the electrode coated with PEDOT:PSS and npPLA was moved to an electrochemical cell and used as working electrode. This cell was filled with EDOT monomers and supporting electrolyte containing solution. The electropolymerization was performed under a constant potential of 1.40 V and adjusting the polymerization charge to 90 mC. Monomer molecules cross the entire thickness of the npPLA film through the nanoperforations, reaching the semiconducting PEDOT:PSS sacrificial layer. The latter was used to immobilize the PEDOT chains, forming a very cohesive system when adhering to the npPLA layer. A SEM micrograph of the PEDOT layer, which exhibited a thickness of 765±81 nm, is shown in Figure 5.3b, while Figure 5.3c, displays both the npPLA and PEDOT sides in an intentionally scratched sheet. Finally, the PEDOT layer was covered with a new nanosheet of npPLA, obtained as previously described. The morphology of the last PLA layer, with a thickness of 167±31 nm, is shown in Figure 5.3d. The diameter of the nanoperforations in the upper npPLA layer, 137±25 nm, is greater than in the first layer, evidencing that the PEDOT layer behaves as a mold in the spin-coating process.

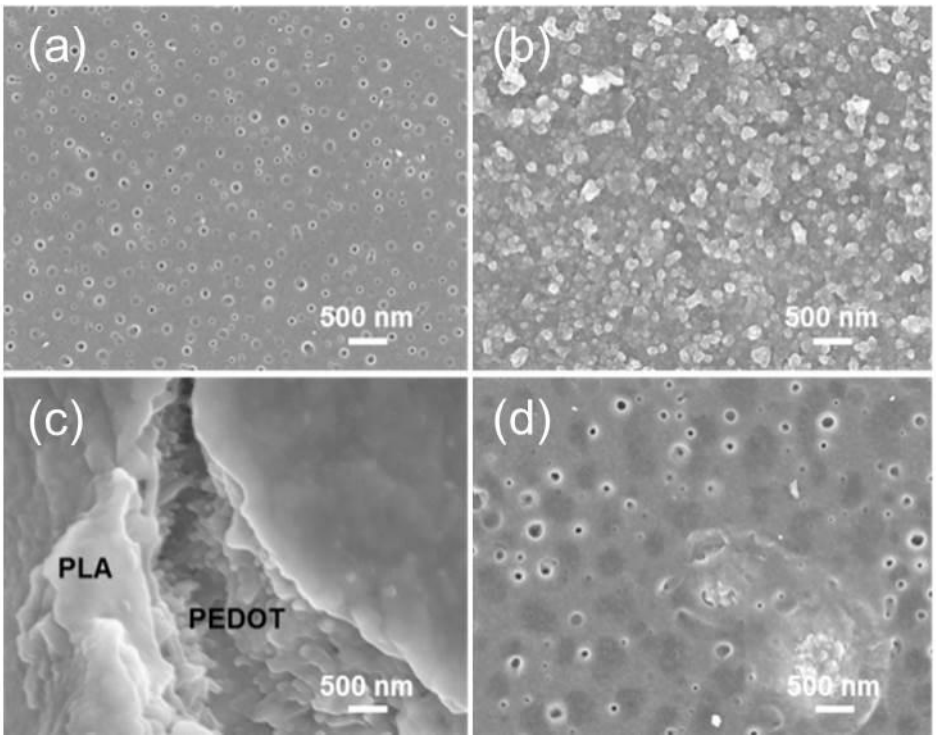

Figure 5.3: Representative high resolution SEM micrograph of: (a) the first npPLA layer, (b) the intermediate PEDOT layer, (c) the two sides of an intentionally scratched npPLA/PEDOT 2-layered film, and (d) the upper layer of the npPLA/PEDOT/npPLA 3-layered film.

Immobilization of the protein into the 3-layered film

The supported npPLA/PEDOT/npPLA 3-layered film, with a thickness of *ca*. 1.2 μm, was used to immobilize the protein as described in the experimental section. Although SEM micrographs recorded for 3-layered systems incubated in both protein and blank solutions (Figure 5.4) allowed the identification of superficial SDS crystals, frequently formed from SDS micellar solutions [22], the VDAC36 protein was not distinguished at the surface. This was attributed to its low tendency to associate into hierarchical structures. However, the successful immobilization of the protein onto the surface of the 3-layered film was proved by laser scanning confocal microscopy, visualizing the intrinsic fluorescence of VDAC36 (Figure 5.5). Comparison of the bright field images, the fluorescence images as well as the merged images recorded for 3-layered films before and after protein incubation allows identifying the Tyr and the Trp of VDAC36 in npPLA/PEDOT/npPLA/VDAC by the fluorescence at 303 and 354 nm, respectively. Apparently, the protein is homogeneously immobilized over the entire surface, without observing preferential positions.

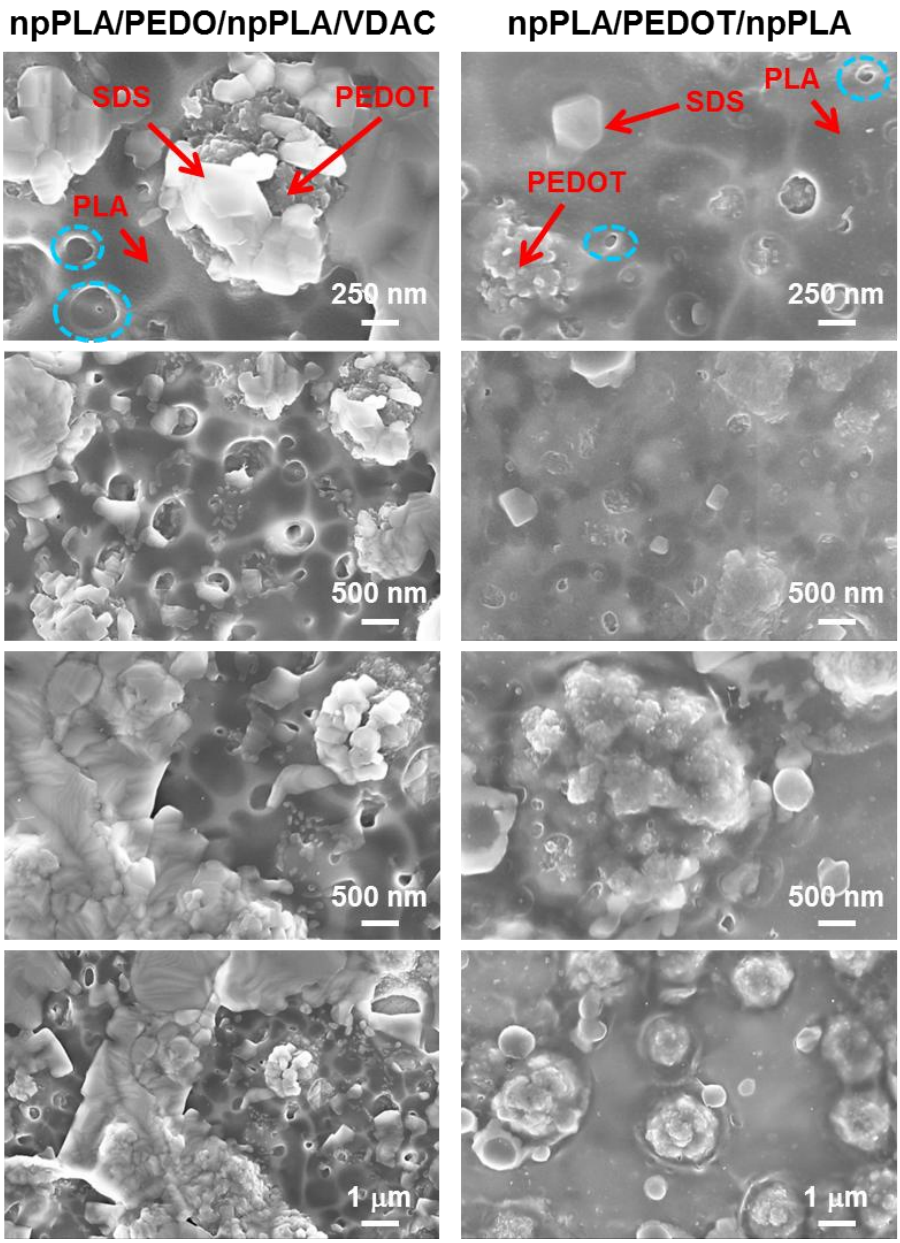

Figure 5.4: SEM micrographs with increasing magnification (bottom to top) of npPLA/PEDOT/npPLA/VDAC (left column) and npPLA/PEDOT/npPLA (right column) 3-layered films. The different elements of the film (*i.e.* npPLA of the upper layer, PEDOT clusters emerging from the intermediate layer and SDS crystals) are marked in red, while representative nanoperforations of the upper npPLA layer are marked in blue.

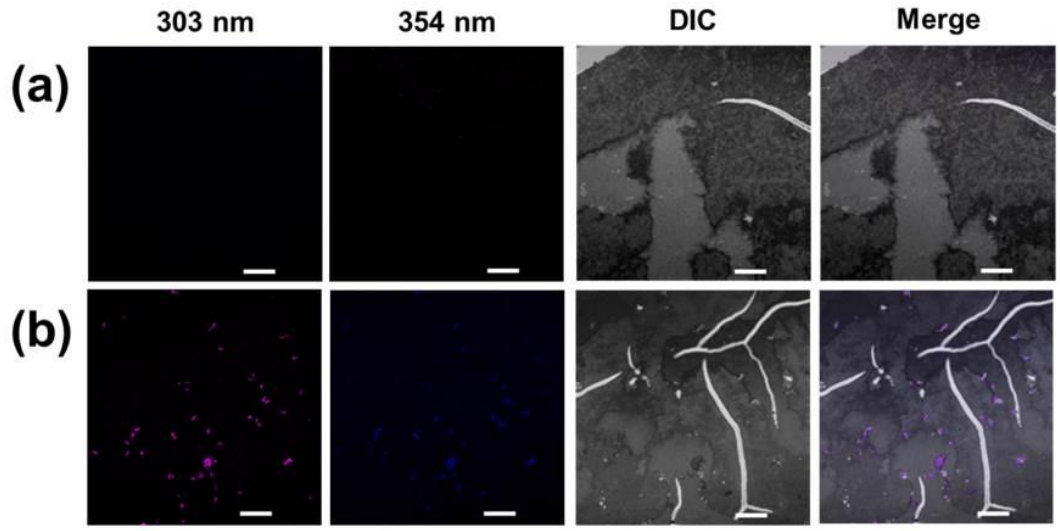

Figure 5.5: Confocal microscopy images of (a) npPLA/PEDOT/npPLA and (b) npPLA/PEDOT/npPLA/VDAC. The panels at the first and second columns correspond to the fluorescence images, the panel at the right displays the merged images. Scale bar: 10 µm.

The latter observation was corroborated by AFM. Comparison of topographic and phase AFM images recorded for npPLA/PEDOT/npPLA films before and after incubation with VDAC36 (Figure 5.6) shows that the protein was not only confined inside and around the nanopores of the outer npPLA layer but also adsorbed onto its electrochemically inactive surface. Although only the protein immobilized in the pores is expected to contribute to ion transport, regulation of the adsorption process to avoid the immobilization onto the surface is, unfortunately, a very difficult task.

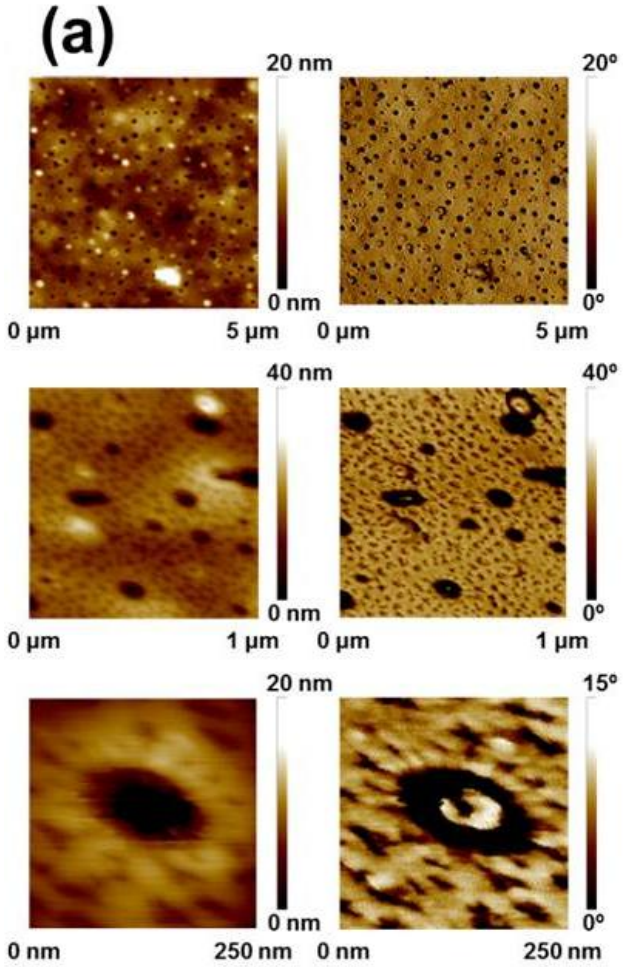
(a)
20 nm
0 nm
20°
0°
0 µm
5 µm
0 µm
5 µm
40 nm
0 nm
40°
0°
0 µm
1 µm
0 µm
1 µm
20 nm
0 nm
15°
0°
0 nm
250 nm
0 nm
250 nm

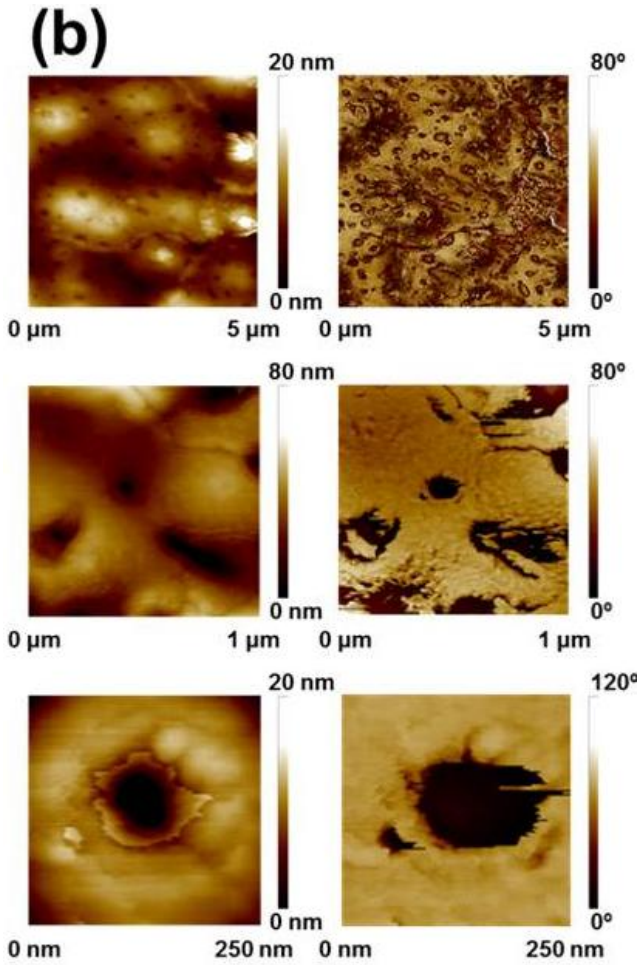

Figure 5.6: 2D topographic and phase contrast AFM images (left and right, respectively) for (a) npPLA/PEDOT/npPLA and (b) npPLA/PEDOT/npPLA/VDAC: 5x5 µm² (top), 1x1 µm² (middle) and 0.25x0.25 µm² (bottom) windows. Comparison of the images recorded for the 3-layered film reflects the apparition of small protuberances after incubation in the protein solution. These protuberances, which have been attributed to protein aggregates, are located onto the film surface and inside and around the nanopores of the outer npPLA layer.

Further characterization by XPS, contact angle measures, FTIR spectroscopy and CD unambiguously confirmed the immobilization of the protein. The atomic compositions of npPLA/PEDOT/npPLA and npPLA/PEDOT/npPLA/VDAC, as obtained by XPS, are compared in

Table **5.1**. The penetration of X-ray radiation using the conditions described in Methods section (ESI) is expected to be ~10 nm, even though in this case the penetration is unknown due to the nanoperforations at the upper layer. The content of N 1s, which is undetectable for npPLA/PEDOT/npPLA, is 0.19% for npPLA/PEDOT/npPLA/VDAC. This feature, together with the increment of O 1s content, supports the presence of the porin.

Table 5.1: Atomic percent composition obtained by XPS for the studied 3-layered films.

	C 1s	N 1s	O 1s	S 2p
npPLA/PEDOT/npPLA	72.01	0.00	27.88	0.11
npPLA/PEDOT/npPLA/VDAC	70.87	0.19	28.88	0.06

The contact angles (Θ) measured in water (Figure 5.7) also provided indirect evidences of the successful immobilization of VDAC36. The wettability of npPLA/PEDOT/npPLA (θ=61°±7°) significantly increased upon the incorporation of the protein (θ=41°±10°), which has been attributed to the effect of the hydrophilic residues found in the loops connecting the β-strands of the protein or inside the central pore.

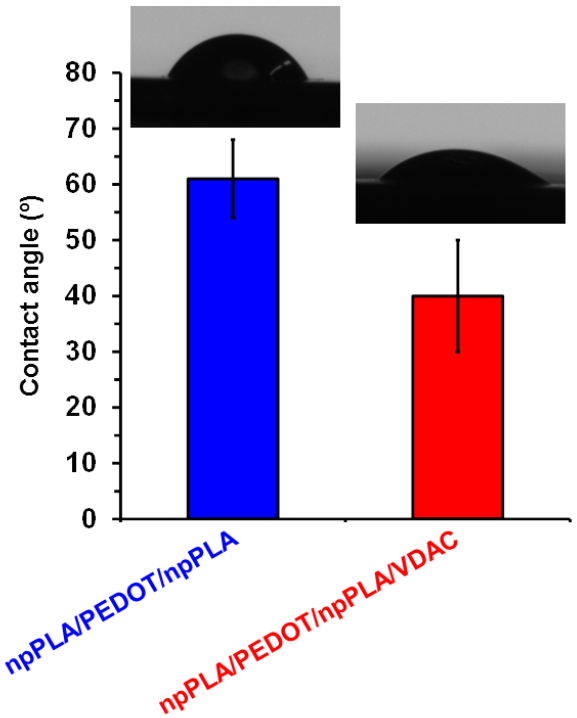

Figure 5.7: Contact angle of the 3-layered films.

Detachment of 3-layered films from steel substrates was achieved by selective elimination of the thin sacrificial layer. Although PEDOT:PSS is not soluble in water, it forms a colloidal dispersion. After immersion into milli-Q water for 12 h, films were detached from the steel substrate and easily recovered with fine-point tweezers. The resulting free-standing films, which do not deteriorate during such process, are 1.05 μm in thickness and shows excellent conformability (Figure 5.8).

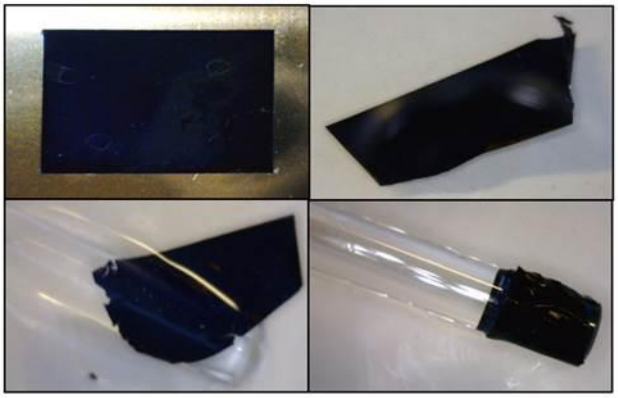

Figure 5.8: Photographs showing the robustness and conformability of free standing npPLA/PEDOT/npPLA/VDAC films.

Figure 5.9 compares the FTIR spectra from 890 to 1790 cm^{-1} of several films after detachment. Although the side chain bands of charged amino residues at ~1631 and ~1755 cm^{-1} are not identified because of the overlapping with the bands associated to the thiophene ring (C=C and C–C stretching) of PEDOT [23], it is possible, from the typical amide band, to unambiguously conclude that VDAC36 has been successfully immobilized. Indeed, the amide III and II vibrational modes of the protein, which arise from the coupling between the N−H in-plane bending and C−N stretching modes, are clearly recognizable at 1230 and 1514 cm^{-1}, respectively.

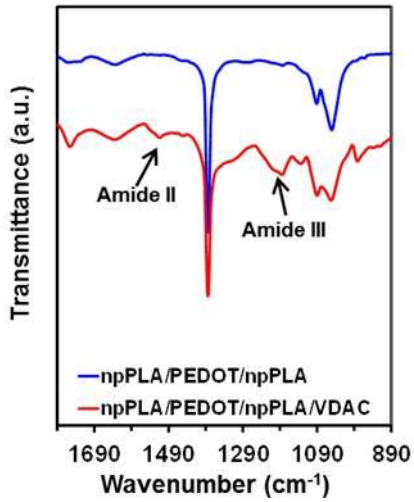

Figure 5.9: FTIR spectra of 3-layered free standing films.

The immobilized protein not only remained at the free-standing 3-layered film, as proved by FTIR spectroscopy (Figure 5.9) but also preserved its β-barrel structure. Figure 5.10 compares the CD spectra recorded for VDAC36 in five different scenarios: (i) unfolded (negative control); (ii) refolded in SDS-MPD; (iii) after immobilization onto the supported 3-layered film; and (iv) after detachment of the free-standing film. All spectra, with the exception of the unfolded protein, exhibit a broad minimum at 218-220 nm that is typically associated with β-stranded proteins [24]. The spectrum of the unfolded protein reflects structural modifications associated with the conformational lost.

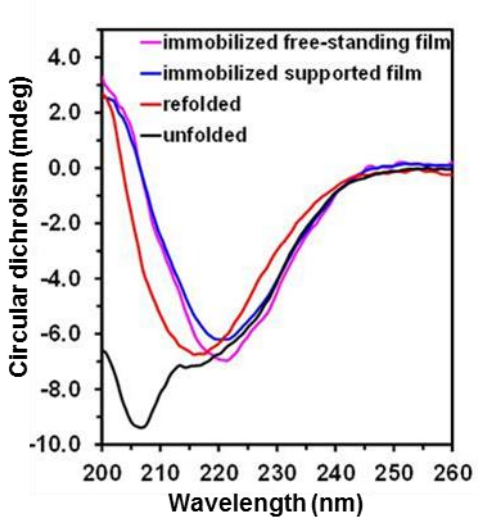

Figure 5.10: CD spectra for the VDAC36 protein: unfolded, refolded, after immobilization onto supported 3-layered films and after detachment of the 3-layered film from the steel substrate.

Influence of the protein on the film electrical response

EIS studies were conducted on npPLA/PEDOT/npPLA and npPLA/PEDOT/npPLA/VDAC to monitor the changes in resistance and capacitance caused by the 3-layered configuration containing both npPLA and CP with respect to simple membranes with only one of such components. The ion transport was evaluated by measuring the impedance for frequencies ranging from 10^{-2} to 10^{5} Hz, using a 0.5 M NaCl solution and steel electrodes. Figure 5.11 displays the recorded Nyquist and Bode plots. The EECs used to fit the experimental data and the corresponding parameters are sketched in Figure 5.12, where R_S is the electrolyte resistance and R_p represents the ability of the films to impede ion transport at the interface between the electrolyte and the membrane (*i.e.* the resistance of the film). The EECs also include double layer capacitances from both the 3-layered film and the steel electrode (CPE_{3L} and CPE_{st}, respectively) and a Warburg impedance element (W), corresponding to the diffusion of water molecules. In the case of npPLA/PEDOT/npPLA/VDAC,

both R_p and CPE_{3L} include the overall contribution of the VDAC36-integrated interface. Both CPE_{3L} and CPE_{st} were modelled using a constant phase element (CPE).

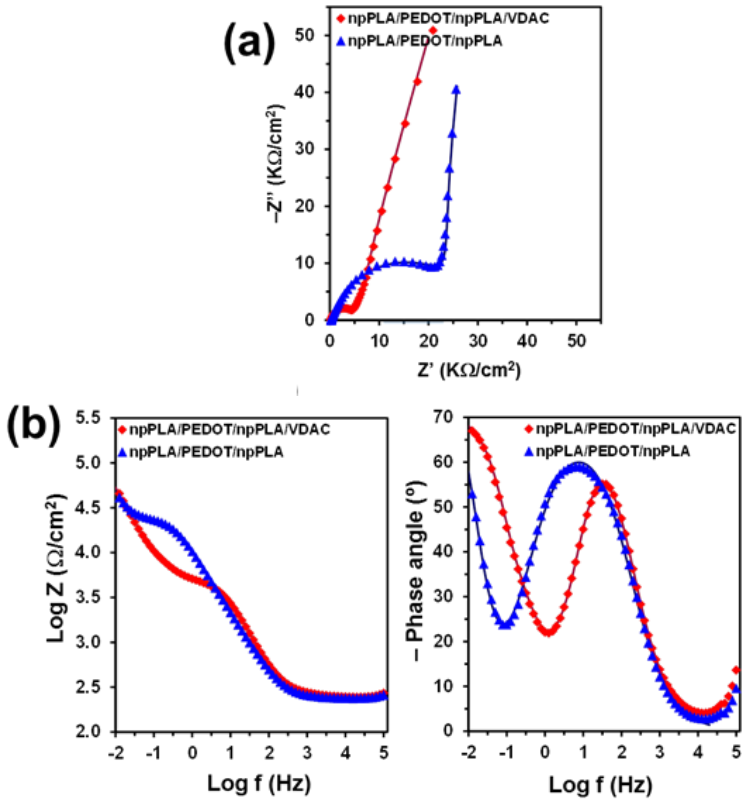

Figure 5.11: (a) Nyquist and (b) Bode plots in a 0.5 M NaCl aqueous solution. Symbols correspond to experimental data, while lines are fitted curves according to EEC.

The R_p of the 3-layered film functionalized with VDAC36 is one order of magnitude lower than that of the film without protein (*i.e.* 3.9 and 21.9 kΩ·cm^2, respectively) using a 0.5 M NaCl solution. Interestingly, the resistance of the npPLA/PEDOT/npNA/VDAC membrane is very similar to that observed for the PPy/Omp2a membrane (1.3 kΩ·cm^2) [5], though the amount of CP contained was significantly higher and was not self-supported. Similarly, the resistance reported for Omp2a protein supported onto lipid bilayers, which exhibited much less mechanical strength than polymeric nanomembranes, was of 3.7 kΩ·cm^2 [16].

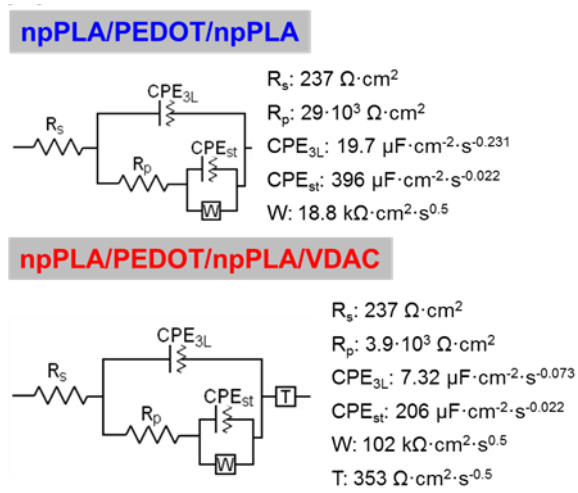

Figure 5.12: Electrical equivalent circuit (EEC) elements used for fitting experimental data recorded for npPLA/PEDOT/npPLA and npPLA/PEDOT/npPLA/VDAC.

These results confirm that npPLA/PEDOT/npNA/VDAC membranes behave as smart biomimetic membranes fulfilling the self-standing and mechanical integrity requirements of many applications in different areas of the biomedical field, such as nanofluidics, biosensing and energy conversion.

In addition to the heterogeneous characteristics of the electrode surface (i.e. roughness, porosity, reactivity), the CPE impedance is related to non-uniform diffusion across the interface. Accordingly, CPE is expressed as $[Q\cdot(j\omega)^{n}]^{-1}$, representing an ideal capacitor (n = 1), a pure resistor (n = 0) or a diffusion process (n = 0.5). For films without and with VDAC36, the value of n obtained for the CPE associated to CPE_{3L} is 0.769 and 0.927, reflecting that the protein significantly improves the capacitive behaviour of the film. The well-known supercapacitive (*i.e.* electrochemically capacitive) response of PEDOT is typically attributed to its ability to promote series of fast and reversible redox reactions [25-26]. However, our results show that the integration of the protein enhances this behaviour. This change is justified by the addition of the bounded Warburg diffusion impedance (T) element, which is characteristic of films that contain a fixed amount of electroactive material (*i.e.* films of finite thickness). The addition of T, which is usually related to the diffusion resistance of ions in doped electrodes of batteries and supercapacitors [27–29], indicates that VDAC36 induces a fast transfer and subsequent adsorption of electrolytes on the surface of the membrane. This leads to an increased CPE_{3L}, as demonstrated by the EEC parameters (Figure 5.12), indicating that npPLA/PEDOT/npPLA/VDAC membranes are potential candidates for the fabrication of bio-supercapacitors.

5.4. Conclusion

In conclusion, we have established an efficient methodology for the functional incorporation of porins in self-supported, stable, size-adaptable and conducting polymeric membranes made of PLA and PEDOT. The surface of the different layers was characterized and the nanofeatures such as nanoperforations were evidenced. The presence of the protein was demonstrated by fluorescence, FTIR and XPS. The incorporation of the VDAC36 protein is accompanied by a distinctive electrochemical behavior as demonstrated by EIS measurements. The electrical resistance of the material in a NaCl solution was greatly reduced by incorporation of the channel protein. The complete description of the electrical equivalent circuits helped to understand the exact effects of the protein on the material properties. In addition, the supercapacitive of the PEDOT layer was preserved and enhanced by the protein. The membranes developed in this work are promising electrode materials for advanced bio-supercapacitors in energy storage functions.

5.5. Bibliography

[1] R. Koebnik, K. P. Locher, and P. Van Gelder, "Structure and function of bacterial outer membrane proteins: barrels in a nutshell.," *Mol. Microbiol.*, 37, 2, 239–253, 2000.

[2] M. Grzelakowski, O. Onaca, P. Rigler, M. Kumar, and W. Meier, "Immobilized Protein-Polymer Nanoreactors," *Small*, 5, 22, 2545–2548, 2009.

[3] W. Meier, C. Nardin, and M. Winterhalter, "Reconstitution of Channel Proteins in (Polymerized) ABA Triblock Copolymer Membranes," *Angew. Chemie Int. Ed.*, 39, 24, 4599–4602, 2000.

[4] D. Wong, T.-J. Jeon, and J. Schmidt, "Single molecule measurements of channel proteins incorporated into biomimetic polymer membranes," *Nanotechnology*, 17, 15, 3710–3717, 2006.

[5] M. M. Pérez-Madrigal, L. J. del Valle, E. Armelin, C. Michaux, G. Roussel, E. A. Perpète, and C. Alemán, "Polypyrrole-Supported Membrane Proteins for Bio-Inspired Ion Channels," *ACS Appl. Mater. Interfaces*, 7, 3, 1632–1643, 2015.

[6] A. Puiggalí-Jou, M. M. Pérez-Madrigal, L. J. del Valle, E. Armelin, M. T. Casas, C. Michaux, E. A. Perpète, F. Estrany, and C. Alemán, "Confinement of a β-barrel protein in nanoperforated free-standing nanomembranes for ion transport," *Nanoscale*, 8, 38, 16922–16935, 2016.

[7] X. Zhang, W. Fu, C. G. Palivan, and W. Meier, "Natural channel protein inserts and functions in a completely artificial, solid-supported bilayer membrane.," *Nat. Sci. reports*, 3, 1, 2196, 2013.

[8] W. Xie, F. He, B. Wang, T.-S. Chung, K. Jeyaseelan, A. Armugam, and Y. W. Tong, "An aquaporin-based vesicle-embedded polymeric membrane for low energy water filtration," *J. Mater. Chem. A*, 1, 26, 7592, 2013.

[9] S. Balme, F. Picaud, S. Kraszewski, P. Déjardin, J. M. Janot, M. Lepoitevin, J. Capomanes, C. Ramseyer, and F. Henn, "Controlling potassium selectivity and proton blocking in a hybrid biological/solid-state polymer nanoporous membrane," *Nanoscale*, 5, 9, 3961, 2013.

[10] A. Puiggalí-Jou, L. J. del Valle, and C. Alemán, "Biomimetic hybrid membranes: incorporation of transport proteins/peptides into polymer supports," *Soft Matter*, 15, 13, 2722–2736, 2019.

[11] Y. Shen, W. Song, D. R. Barden, T. Ren, C. Lang, H. Feroz, C. B. Henderson, P. O. Saboe, D. Tsai, H. Yan, P. J. Butler, G. C. Bazan, W. A. Phillip, R. J. Hickey, P. S. Cremer, H. Vashisth, and M. Kumar, "Achieving high permeability and enhanced selectivity for Angstrom-scale separations using artificial water channel membranes," *Nat. Commun.*, 9, 1, 2294, 2018.

[12] C. Lang, Y. Shen, J. A. LaNasa, D. Ye, W. Song, T. J. Zimudzi, M. A. Hickner, E. D. Gomez, E. W. Gomez, M. Kumar, and R. J. Hickey, "Creating cross-linked lamellar block copolymer supporting layers for biomimetic membranes," *Faraday Discuss.*, 209, 0, 179–191, 2018.

[13] H. Wang, T.-S. Chung, Y. W. Tong, K. Jeyaseelan, A. Armugam, Z. Chen, M. Hong, and W. Meier, "Highly Permeable and Selective Pore-Spanning Biomimetic Membrane Embedded with Aquaporin Z," *Small*, 8, 8, 1185–1190, 2012.

[14] G. Roussel, E. A. Perpète, A. Matagne, E. Tinti, and C. Michaux, "Towards a universal method for protein refolding: The trimeric beta barrel membrane Omp2a as a test case," *Biotechnol. Bioeng.*, 110, 2, 417–423, 2013.

[15] A. Puiggalí-Jou, J. Medina, L. J. del Valle, and C. Alemán, "Nanoperforations in poly(lactic acid) free-standing nanomembranes to promote interactions with cell filopodia," *Eur. Polym. J.*, 75, 552–564, 2016.

[16] A. Puiggalí-Jou, J. Pawlowski, L. J. del Valle, C. Michaux, E. A. Perpète, S. Sek, and C. Alemán, "Properties of Omp2a-Based Supported Lipid Bilayers: Comparison with

Polymeric Bioinspired Membranes," *ACS Omega*, 3, 8, 9003–9019, 2018.

[17] B. W. Hoogenboom, K. Suda, A. Engel, and D. Fotiadis, "The Supramolecular Assemblies of Voltage-dependent Anion Channels in the Native Membrane," *J. Mol. Biol.*, 370, 2, 246–255, 2007.

[18] K. Zeth, "Structure and evolution of mitochondrial outer membrane proteins of β-barrel topology," *Biochim. Biophys. Acta - Bioenerg.*, 1797, 6–7, 1292–1299, 2010.

[19] M. Forte and E. Blachly-Dyson, "VDAC Channels," *IUBMB Life (International Union Biochem. Mol. Biol. Life)*, 52, 3–5, 113–118, 2001.

[20] T. Salinas, S. El Farouk-Ameqrane, E. Ubrig, C. Sauter, A.-M. M. Duchêne, and L. Maréchal-Drouard, "Molecular basis for the differential interaction of plant mitochondrial VDAC proteins with tRNAs," *Nucleic Acids Res.*, 42, 15, 9937–9948, 2014.

[21] H. Zhang and S. Takeoka, "Morphological Evolution within Spin-Cast Ultrathin Polymer Blend Films Clarified by a Freestanding Method," *Macromolecules*, 45, 10, 4315–4321, 2012.

[22] R. M. Miller, O. Ces, N. J. Brooks, E. S. J. Robles, and J. T. Cabral, "Crystallization of Sodium Dodecyl Sulfate-Water Micellar Solutions under Linear Cooling," *Cryst. Growth Des.*, 17, 5, 2428–2437, 2017.

[23] G. Fabregat, B. Teixeira-Dias, L. J. del Valle, E. Armelin, F. Estrany, and C. Alemán, "Incorporation of a Clot-Binding Peptide into Polythiophene: Properties of Composites for Biomedical Applications," *ACS Appl. Mater. Interfaces*, 6, 15, 11940–11954, 2014.

[24] J. Y. Paquet, M. A. Diaz, S. Genevrois, M. Grayon, J. M. Verger, X. De Bolle, J. H. Lakey, J. J. Letesson, and A. Cloeckaert, "Molecular, antigenic, and functional analyses of Omp2b porin size variants of Brucella spp.," *J. Bacteriol.*, 183, 16, 4839–4847, 2001.

[25] M. Rajesh, C. J. Raj, R. Manikandan, B. C. Kim, S. Y. Park, and K. H. Yu, "A high performance PEDOT/PEDOT symmetric supercapacitor by facile in-situ hydrothermal polymerization of PEDOT nanostructures on flexible carbon fibre cloth electrodes," *Mater. Today Energy*, 6, 96–104, 2017.

[26] D. Aradilla, F. Estrany, and C. Alemán, "Symmetric Supercapacitors Based on Multilayers of Conducting Polymers," *J. Phys. Chem. C*, 115, 16, 8430–8438, 2011.

[27] N. Phattharasupakun, J. Wutthiprom, S. Kaenket, T. Maihom, J. Limtrakul, M. Probst, S. S. Nagarkar, S. Horike, and M. Sawangphruk, "A proton-hopping charge storage mechanism of ionic one-dimensional coordination polymers for high-performance supercapacitors," *Chem. Commun.*, 53, 86, 11786–11789, 2017.

[28] D. Kuzum, H. Takano, E. Shim, J. C. Reed, H. Juul, A. G. Richardson, J. de Vries, H. Bink, M. A. Dichter, T. H. Lucas, D. A. Coulter, E. Cubukcu, and B. Litt, "Transparent and flexible low noise graphene electrodes for simultaneous electrophysiology and neuroimaging.," *Nat. Commun.*, 5, 5259, 2014.

[29] K. C. Tully, J. F. Whitacre, and S. Litster, "Spatiotemporal electrochemical measurements across an electric double layer capacitor electrode with application to aqueous sodium hybrid batteries," *J. Power Sources*, 248, 348–355, 2014.

6. Enhanced biomimetic membrane made of PLA, PEDOT-P3DT and VDAC36

6. Enhanced biomimetic membrane made of PLA, PEDOT-P3DT and VDAC36

Summary

The transport of metabolites across robust, flexible and free-standing biomimetic membranes made of three perforated poly(lactic acid) (pPLA) layers, separated by two anodically polymerized conductive layers of poly(3,4-ethylenedioxythiophene-co-3-dodecylthiophene), and functionalized on the external pPLA layers with a voltage dependent anion channel (VDAC) protein, has been demonstrated in the previous section. The three pPLA layers offer robustness and flexibility to the bioactive platform and the possibility of obtaining conducing polymer (CP) layers by in situ anodic polymerization. The incorporation of dodecylthiophene units, which bear a 12 carbon atoms long linear alkyl chain, to the conductive layers allows mimicking the amphiphilic environment offered by lipids in cells. This increases by 32% the efficiency of the functionalization with the protein, which is preferably immobilized inside the PLA perforations, with respect to the system without dodecylthiophene units. Electrochemical impedance measurements in NaCl and adenosine triphosphate (ATP) solutions, using protein-functionalized and non-functionalized (control) free-standing membranes, prove that the integration of the VDAC porin considerably increases the membrane conductivity and facilitates the electrolyte diffusion, the latter being not detected for control membranes.

6.1. Introduction

Biomimetics takes advantage of the natural structures found in biological systems permitting a nanoscopic development of functional materials. Within this context, nanomaterials based on proteins offer countless potential nano-sized devices such as nanoreactors [1], filtration devices [2], nanosensors [3-4], or drug delivery systems [5]. Many of these applications usually require channel shaped components, which provide nanoscopic pathways for the passage of ions and small molecules. Appropriately, a class of outer membrane proteins (OMPs) found in *gram*-negative bacteria and mitochondria, called porins, can naturally form β-barrel channels [6]. They act as the gates of the cell membrane. The majority of the porins does not present any particular selectivity and allows the passive diffusion of various hydrophilic solutes, such as ions, sugars, amino acids and ATP [7].

The outside facing part of β-barrel channels is hydrophobic to match the alkyl chains of the membrane lipids, while the internal water-filled part contains charged and hydrophilic residues. The size of the pore, which usually ranges from 10 to 40 Å, prevents bulky molecules to be diffused and the internal hydrophilic region defines the permeation mechanism of species crossing the channel [8]. In addition, β-barrels exhibit exceptional robustness and stability over time and temperature [9-10]. Those features make porins competitive for their insertion in non-biological synthetic environment such as polymers. From such perspective, the approaches used to modify polymeric membranes, which can be free-standing or tethered onto solid supports, with functional biomolecules are those based on the utilization of amphiphilic copolymers and nanostructured polymers [3].

In a recent study, ion-responsive hybrid nanomembranes (NMs) were developed by combining poly(*N*-methylpyrrole) (PNMPy), a conducting polymer (CP) that was electrochemically synthesized onto a rigid stainless steel electrode, with the Omp2a porin [11]. Electrochemical studies on the resulting system (PNMPy/Omp2a) showed the activity of the protein to promote the passive transport of K^+ through the CP membrane. More recently, another hybrid NM was engineered by immobilizing the same protein onto nanoperforated poly(lactic acid) (pPLA) NMs, the resulting system being denoted npPLA/Omp2a [12]. Immobilization of the protein around and inside the nanoperforations, which exhibited an average diameter of 51 ± 22 nm and a depth of ~100 nm, greatly increased the material conductivity and selectivity against some ions. Despite the capacity of pPLA and pPLA/Omp2a NMs to be free-standing, the difficulties associated with their handling limited ion diffusion and electrical measurements, which were conducted using NMs supported onto ITO substrates [12]. Under these conditions, the conductivity of pPLA/Omp2a

membranes was comparable to that of the same protein supported onto lipid bilayers (LB) (LB/Omp2a) [13]. However, the suppression of the solid support to have biomimetic and flexible platforms with conducting channels for the metabolite transport is highly desirable.

Taking advantages of previous studies based on PNMPy/Omp2a, npPLA/Omp2a and LB/Omp2a, the novelty of the present work relies on the design of an advanced functional platform by immobilizing porin proteins onto a smart free-standing biomimetic membrane. This biomimetic membrane consists of three PLA layers with sub-micrometric perforations (pPLA layers) separated by two layers of a CP, which was prepared by electropolymerization. Although poly(3,4-ethylenedioxythiophene) (PEDOT) is the most stable and electroactive heterocyclic CP, [14–18] in this wor the two conducting layers have been prepared using a copolymer (COP) of 3,4-ethylenedioxythiophene (EDOT) and 3-dodecylthiophene (3DT). The incorporation of 3DT units, which bear a 12 carbon atoms long linear alkyl chain (Figure 6.1), is aimed to mimic the natural amphiphilic environment (*i.e.* lipids) required by OMPs, without losing of the excellent conductive properties of PEDOT.

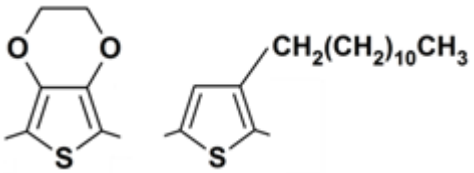

Figure 6.1: Chemical structure of the 3,4-ethylenedioxythiophene (EDOT; left) and 3-dodecylthiophene (3DT; right) repeat units.

The resulting free-standing 5-layered membrane, hereafter named 5-pPLA/COP, has been transformed into 5-pPLA/COP/VDAC by immobilizing a Voltage Dependent Anion Channel (VDAC) protein at the external pPLA layers. VDACs are porins found in the outer mitochondrial membrane of all eukaryotic cells and are associated with the permeability of the mitochondria [19] and regulate the diffusion of ions and metabolites such as nicotinamide adenine dinucleotide hydrogen (NADH) or adenosine triphosphate (ATP) [20]. The protein used to prepare 5-pPLA/COP/VDAC is VDAC36 from *Solanum tuberosum*, a plant model organism [21]. Although the molecular weight of this voltage-dependent anion selective porin is similar to that of Omp2a (36 and 39 kDa, respectively), these two proteins highly differ in the diameter of their channel. The effective diameter of the protein channel of VDAC36 and Omp2a is about 2.0 and 1.2 nm, respectively, and, therefore, the former is expected to allow the diffusion of larger solutes than the latter [22-23]. In order to ascertain the influence of the dodecyl side groups in the functionalized device, the performance of 5-pPLA/COP/VDAC and 5-pPLA/PEDOT/VDAC (Figure 6.2), in

which the two COP layers have been substituted by the PEDOT homopolymer, has been compared. Moreover, the benefits provided by the VDAC36 protein have been evaluated by comparing the transport of ions across protein functionalized and non-functionalized free-standing membranes, the latter being named 5-pPLA/COP and 5-pPLA/PEDOT.

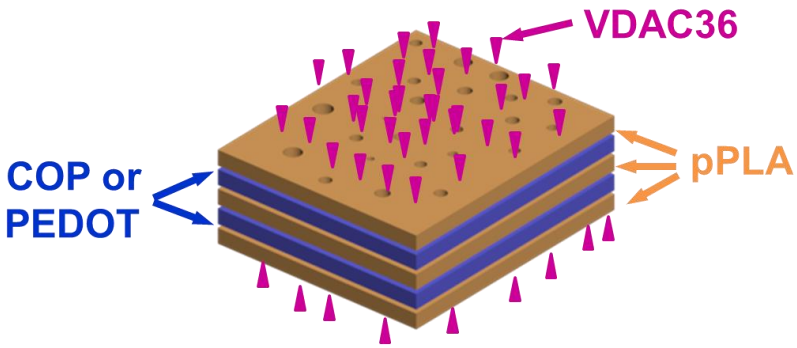

Figure 6.2: Representation of the 5-pPLA/COP/VDAC and 5-pPLA/PEDOT/VDAC membranes.

The 5-pPLA/COP/VDAC system shows the handling advantages of free-standing multi-layered films, integrates nanosheets of insulating polymers with electropolymerized CP layers through the perforations induced in the former, and brings together the benefits associated to each component: the good mechanical integrity of biodegradable PLA, the good conductive and electrochemical response of PEDOT copolymers, the biomimetic environment created by 3DT units, and the ability to regulate the diffusion ATP ions of VDAC36. As a result, hybrid 5-pPLA/COP/VDAC represents a significant improvement with respect to nanomembranes previously engineered for metabolite transport.

6.2. Methods

Materials. PEDOT:poly(styrene sulfonate) (PSS) 1.3 wt. % dispersion in water, EDOT and 3DT monomers, poly(vinyl alcohol) (PVA) 87-89% hydrolyzed and lithium perchlorate ($LiClO_4$) were purchased from Sigma-Aldrich (USA); $LiClO_4$ was stored at 80 °C before its use. PLA 2002D pellets were supplied by Nupik International (Polinyà, Spain). Acetonitrile and hexafluoroisopropanol (HFIP) were purchased from Panreac Quimica S.A.U. (Spain).

Synthesis of PEDOT and COP. Both PEDOT and COP were prepared by anodic polymerization using an Autolab PGSTAT302N controlled by the NOVA software. Polymerizations were carried out by chronoamperometry (CA) in a three-electrode cell filled with a 0.1 M $LiClO_4$ acetonitrile solution containing 10 mM EDOT for PEDOT or 7 mM EDOT + 3 mM 3DT for COP. In both

cases, a constant potential of +1.40 V was applied and the polymerization charge was adjusted to 30 mC. Polished steel AISI 304 sheets (1×1 cm^2) were employed as working and counter electrodes, while the reference electrode was an Ag|AgCl standard electrode (KCl 3M).

Synthesis of 5-layered free-standing films. Films containing 3 layers of pPLA separated by 2 layers of PEDOT or COP were prepared by combining the spin-coating and the anodic polymerization (CA) techniques. In brief, a steel sheet (AISI 304) of 3□3 cm2 was coated with a sacrificial layer of PEDOT:PSS by spin-coating deposition (1200 rpm for 60 s). Then, a PLA:PVA layer was generated onto the sacrificial layer by spin-coating (1200 rpm for 60 s) a 80:20 v/v mixture of PLA (10 mg/mL) and PVA (10 mg/mL) HFIP solutions. The perforated PLA layer (pPLA) was obtained by removing the PVA domains via water etching. The resulting PEDOT:PSS/pPLA bilayer was used as working electrode for the anodic polymerization of COP or PEDOT doped with ClO4–, as described before. Afterwards, the following pPLA, COP or PEDOT layers were obtained by iterating this procedure. Then, 5-layered films of composition pPLA/COP/pPLA/COP/pPLA (5-pPLA/COP) and pPLA/PEDOT/pPLA/PEDOT/pPLA (5-pPLA/PEDOT), still supported onto the PEDOT:PSS-coated steel substrate, were achieved. These supported membranes were easily detached from the metallic substrate by selective elimination of the PEDOT:PSS sacrificial layer. This was achieved by submerging the supported membranes into milli-Q water for 24 h. Finally, 5-layered membranes were completely detached from the steel substrate with the help of tweezers, and converted into self-supported multi-layered films.

Expression and purification of the VDAC36 protein. *Escherichia coli* BL21 (DE3) bacteria were transformed to produce 6 His-tagged VDAC36 proteins in inclusion bodies. Bacteria were then lysed and centrifuged to obtain the final pellet corresponding to the non-purified proteins. VDAC36 was then purified by Ni^{2+} affinity column. VDAC36 was eluted and the buffer was exchanged to 20 phosphate, 60 mM SDS and 1.5 M MPD with a PD10 desalting column.

Functionalization of 5-pPLA/COP and 5-pPLA/PEDOT membranes. In order to integrate the porin, the VDAC36 protein was incubated with the free-standing 5-pPLA/COP and 5-pPLA/PEDOT membranes. Films were placed in 1 mL of a protein solution, which contained 0.85 mg/mL VDAC36, 60 mM SDS and 1.5 M MPD, for 12 h at room temperature. The resulting 5-pPLA/COP/VDAC and 5-pPLA/PEDOT/VDAC functionalized membranes were rinsed three times with milli-Q water to remove residues. Blank (non-functionalized) 5-pPLA/COP and 5-pPLA/PEDOT membranes were obtained using the same solution (i.e. 60 mM SDS and 1.5 M MPD) but without VDAC36.

The concentration of immobilized protein was determined using a UV–Vis Cary 100 Bio spectrophotometer (Agilent, USA) and a 1 cm length quartz cuvette. The absorbance from 250 to 300 nm was recorded for the protein solutions before and after incubation with the polymeric membranes. The spectra for the solutions after incubation were corrected by subtracting the spectra of the rinsing solutions.

FTIR spectroscopy. FTIR spectra were recorded on a Nicolet 6700 spectrophotometer by transmittance. For this purpose, the films were removed from the substrate, mixed with KBr and compressed to create discs, which were measured at a 4 cm^{-1} resolution (64 scans).

X-ray photoelectron spectroscopy (XPS). X-ray photoelectron spectroscopy (XPS) analyses were performed in a SPECS system equipped with a high-intensity twin-anode X-ray source XR50 of Mg/Al (1253 eV/1487 eV) operating at 150 W, placed perpendicular to the analyzer axis, and using a Phoibos 150 MCD-9 XP detector. The X-ray spot size was 650 mm. The pass energy was set to 25 and 0.1 eV for the survey and the narrow scans, respectively. Charge compensation was achieved with a combination of electron and argon ion flood guns. The energy and emission currents of the electrons were 4 eV and 0.35 mA, respectively. For the argon gun, the energy and the emission currents were 0 eV and 0.1 mA, respectively. The spectra were recorded with a pass energy of 25 eV in 0.1 eV steps at a pressure below $6 \cdot 10^{-9}$ mbar. These standard conditions of charge compensation resulted in a negative but perfectly uniform static charge. The C1s peak was used as an internal reference with a binding energy of 284.8 eV. High-resolution XPS spectra were acquired by Gaussian/Lorentzian curve fitting after S-shape background subtraction. The surface composition was determined using the manufacturer's sensitivity factors.

Scanning electron microscopy (SEM). The morphology of the different samples was studied by scanning electron microscopy (SEM). Micrographs were acquired in a Focused Ion Beam Zeiss Neon 40 equipped with an EDX spectroscopy system, operating at 2 or 5 kV, depending on the sensitivity to beam degradation of the studied systems.

Contact angle. The wettability of the NMs was analysed by a sessile water drop method with the equipment OCA 20 (DataPhysics Instruments GmbH, Filderstadt). Images of 5 µL milli-Q water drops onto the samples surfaces were recorded after stabilization (5 s) with the software SCA20. The contact angle (θ) value for each sample was expressed as the average of at least 10 independent measures ± the corresponding standard deviation.

Profilometry. Film thickness and roughness measurements were carried out using a Dektak 150 stylus profilometer (Veeco, Plainview, NY). Conducted using the following settings: tip radius = 2.5 μm; stylus force = 3 mg; scan length = 1000 μm; speed = 33 μm s^{-1}.

Electrochemical measurements. The electroactivity and electrostability of the prepared NMs were studied by cyclic voltammetry (CV) through direct measure of the anodic and cathodic areas in the control voltammograms using the Nova software. A three-cell electrode was used with phosphate buffer saline (PBS) 0.1 M (pH 7.4) as electrolyte solution. The initial and final potential was –0.20 V, while the reversal potential was 1.00 V. A scan rate of 50 mV/s was used in all cases. All experiments were repeated three times.

Electrochemical impedance spectroscopy (EIS). The electroactivity and electrostability of the new platforms were studied by cyclic voltammetry (CV) through direct measure of the anodic and cathodic areas in the control voltammograms using an Autolab PGSTAT302N potentiostat controlled by the NOVA software. A three-cell electrode composed by the free-standing NMs as working electrode (WE), platinum wire as counter-electrode, and a reference electrode of Ag□AgCl (KCl, 3M), was used. The electrolyte solution was composed of 0.1 M phosphate buffer saline (PBS) solution (pH 7.4). The initial and final potential was –0.20 V, while the reversal potential was 1.00 V. A scan rate of 50 mV/s was used in all cases. All experiments were repeated three times.

Electrochemical impedance spectroscopy (EIS) measurements were performed using a conventional three-electrode cell and an AUTOLAB-302N potentiostat/galvanostat operating between the frequency range of 105 Hz and 10-2 Hz and 10 mV of amplitude for the sinusoidal voltage. All experiments were performed at room temperature with 5-layered free-standing membranes. For the EIS assays the electrolyte solutions were: 0.5 M NaCl, 0.5 M ATP and 0.1 M ATP. Platinum wire was used as counter-electrode, whereas Ag|AgCl saturated (KCl 3M) was employed as reference electrode.

6.3. Results and discussion

Characterization of COP and PEDOT

In order to facilitate the identification of the CP layers in 5-layered membranes, COP and PEDOT films were characterized using FTIR and SEM. Figure 6.3 compares the FTIR spectra recorded for COP and PEDOT, both showing the polythiophene characteristic bands. COP and PEDOT spectra show the asymmetric and symmetric stretching vibrations of the methylene groups at 2916-2864 cm^{-1}, even though these are more intense for the former than for the latter due to the long alkyl chain

of 3DT monomers. Moreover, the COP also presents a small band at 729 cm^{-1}, which has been attributed to the rocking of the methylene groups [24-25]. Besides, the absorption bands displayed at 1648 cm^{-1} and 1520 cm^{-1} correspond to the vibrations of the aromatic thiophene ring, whereas the bands at 1086 cm^{-1} and 620 cm^{-1} have been attributed to the ethylenedioxy group (C–O–C stretching) and the C–S characteristic peak of the thiophene ring, respectively [26].

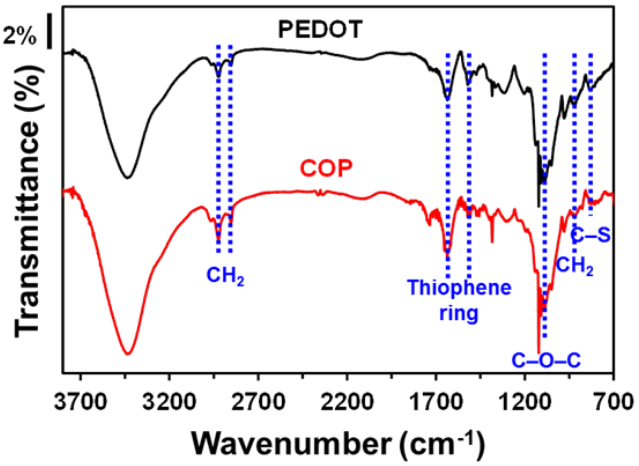

Figure 6.3: FTIR spectra of PEDOT and COP.

On the other hand, the successful incorporation of 3DT units to COP chains was also corroborated by XPS analyses (Table 6.1). For PEDOT, the S 2p / C 1s ratio is 0.15, which almost matches the theoretical value of 0.16. For COP, the experimental and theoretical S 2p / C 1s ratios decrease to 0.11 and 0.09, respectively, the difference between them being essentially attributed to: (i) the overoxidation of 3DT units (i.e. the β or β' position of the thiophene ring are free in 3DT units, while they are blocked in EDOT units), which also affects the O 1s content; and/or (ii) the content of EDOT units in COP chains is slightly higher than the content of 3DT units (i.e. 1.2 times, if the influence of factor (i) is neglected). Comparison of the theoretical and experimental O 1s / C 1s ratios for PEDOT) indicates that the content of O 1s is higher than expected, evidencing the adsorption of CO2 and water molecules (i.e. PEDOT is a hydrophilic polymer) from the atmosphere. Considering that the adsorption of CO2 and water is similar for PEDOT and COP, the experimental value of the O 1s / C 1s ratio obtained for the latter, which is significantly higher than the theoretical one, confirms the overoxidation of the 3DT units.

Table 6.1: Atomic percent composition (C 1s, S 2p and O 1s) obtained by XPS for PEDOT and COP films. Theoretical and experimental S 2p / C 1s ratios are displayed for comparison.

Sample	C 1s	S 2p	O 1s	S/C Theo. ratio (%)	S/C Exp. ratio (%)
PEDOT	62.74	9.24	28.02	0.16	0.15
COP	65.47	7.37	27.16	0.09	0.11

The surface morphologies of COP and PEDOT films are compared in Figure 6.4. As shown in SEM micrographs, both materials exhibit a typical coral-like morphology. In recent studies phase contrast AFM images were used to identify a phase segregation phenomenon in poly(3,4-ethylenedioxythiophene-co-N-methylpyrrole), P(EDOT-co-NMPy),28 in which EDOT- and NMPy-rich blocks organized in separated phases. Comparison of the phase contrast AFM images obtained for COP and PEDOT (Figure 6.5) does not allow detecting phase segregation, suggesting that the distribution of EDOT and 3DT units in COP chains is very homogeneous [27].

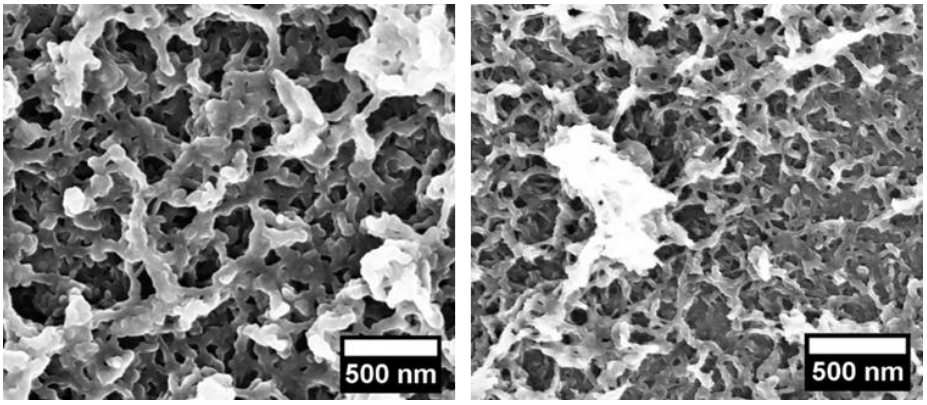

Figure 6.4: Representative SEM images of (left) PEDOT and (right) COP.

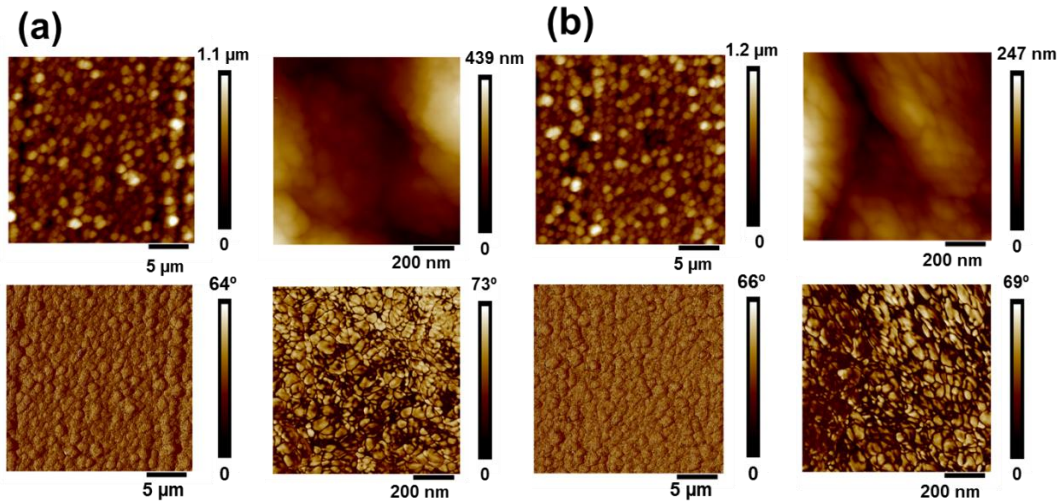

Figure 6.5: Representative height and phase contrast AFM images of (a) COP and (b) PEDOT.

The incorporation of the long alkyl chains to the polythiophene backbone affects the thickness, the surface topography and the water wettability of the films. Although COP and PEDOT films were prepared using identical conditions, the average thickness of the former is more than twice that of the latter (*i.e.* 381 ± 59 and 171 ± 26 nm, respectively). Similarly, the root-mean-square roughness (Rq) values reflects a smoother surface for COP than for PEDOT (*i.e.* Rq= 235 ± 68 and 311 ± 31 nm, respectively). Moreover, the water contact angle (WCA) increased from 57° ± 5º for PEDOT to 64° ± 7º for COP.

Finally, control voltammograms of COP and PEDOT films deposited onto steel sheets were conducted in 0.1 M PBS to study the effect of the 3DT units on the electroactivity and electrostability of the samples. As shown in Figure 6.6, the charge stored in both samples is similar, indicating that the incorporation of thiophene monomers bearing alkyl chain does not significantly affect the electroactivity of the film. After 25 consecutive oxidation–reduction cycles (solid lines) the loss of electrochemical activity is 31% ± 3% and 28% ± 13% for COP and PEDOT, respectively.

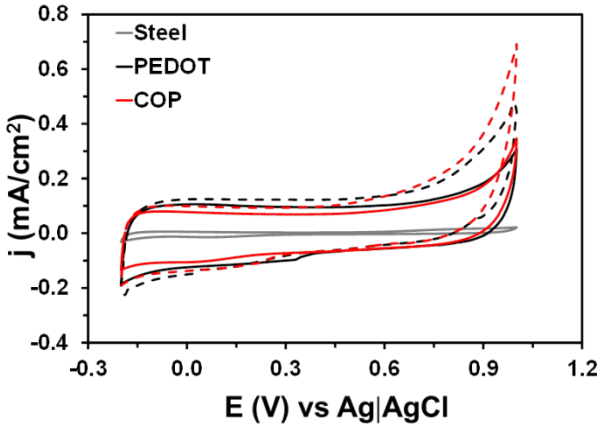

Figure 6.6: First control voltammogram (dashed lines) and voltammogram after 25 consecutive oxidation–reduction cycles (solid lines) in PBS 0.1 M for steel, PEDOT and COP.

Free-standing 5-layered membranes

Supported 5-pPLA/COP and 5-pPLA/PEDOT free-standing membranes were prepared by alternating spin-coated pPLA and electropolymerized conductive COP or PEDOT layers, as previously described in the method section. When spin-coating the 1st pPLA layer onto the PEDOT:PSS sacrificial layer (thickness: 302 ± 3 nm), the strategy of using two immiscible polymers (PLA:PVA, 80:20 v/v) resulted in the formation of segregated pseudo-spherical domains, as shown in Figure 6.7a. The diameter of such features was adjusted to the entire film thickness by regulating the operational conditions of the spin-coating process (*i.e.* time and angular speed) and the concentration of the less abundant polymer (PVA) in the feeding mixture. Afterwards, PVA domains were successfully removed by solubilizing them in water and perforations of 462 ± 219 nm in diameter were obtained.It is worth noting that the formation of such perforations is required for successful electropolymerization of the 2nd conducting layer (*i.e.* the access of the 3DT and EDOT monomers to the conducting PEDOT:PSS sacrificial layer, which acts as working electrode in the electropolymerization, is possible because of the perforations.

The surface morphology of COP and PEDOT in the 2nd layers, which was checked by SEM (Figure 6.7c and d, respectively), very similar to that displayed by the CPs directly generated onto steel substrates. This demonstrates that perforations were successfully formed by phase segregation in the 1st pPLA layer. The absence of perforations in the PLA layer was found to preclude the formation of homogeneous CP layers since the microstructure of the former hinders the action of the PEDOT:PSS working electrode in the anodic polymerization process. SEM micrographs displayed in Figure 6.7e and f show the morphology of the 3rd pPLA layer deposited onto the 2nd COP and PEDOT layers, respectively. In both cases rounded-shape perforations with average diameter of 245 ± 96 nm,

respectively, are observed. As shown in Figure 6.7, the 4th COP and PEDOT layers were successfully generated onto the 3rd pPLA layer, evidencing that 3DT and/or EDOT monomers were able to access the CP chains deposited in the 2nd layer through the perforations of the 3rd pPLA layer. Finally, Figure 6.7i and j show the morphology of the outer pPLA layer (*i.e.* the fifth layer of the 5-pPLA/COP and 5-pPLA/PEDOT biomimetic membranes). In this case, the average diameter of the perforations increased o 321 ± 150 nm and 403 ± 294 nm, respectively. The diameter of the perforations in the 3rd and 5th pPLA layers is affected by the morphology and topography of the previous CP layers. Indeed, the diameter of the perforations is smaller in 5-pPLA/COP than in 5-pPLA/PEDOT since the surface roughness is lower for COP layers than for PEDOT layers. Besides, the 4th COP or PEDOT layer can be observed through the perforations of the outer pPLA layer in Figure 6.7i and j.

The total thickness of 5-pPLA/COP films is 998 nm ± 57nm, while that of 5-pPLA/PEDOT is 741 nm ± 23 nm. These values are consistent with the sum of the thciknessses obtained for single-layered films: COP and PEDOT supported onto steel (*i.e.* 381 ± 59 and 171 ± 26 nm, respectively) and the pPLA spin-coated using a v/v 80:20 PLA:PVA mixture (*i.e.* 170 ± 14 nm) [28]. Similarly, the surface roughness is significantly higher for 5-pPLA/COP (Rq= 418 nm ± 76 nm) than for 5-pPLA/PEDOT (Rq= 185 nm ± 50 nm), which differs from the results discussed for the CPs directly generated onto steel. This has been attributed to the templating effect induced by the alkyl chains of the COP when it grows onto elastic pPLA membranes. On the other hand, the water wettability, which is mainly controlled by the outer pPLA layer, is pretty similar for the two 5-layered systems (θ = 88º ± 6º and 85º ± 8º for 5-pPLA/PEDOT and 5-pPLA/COP, respectively).

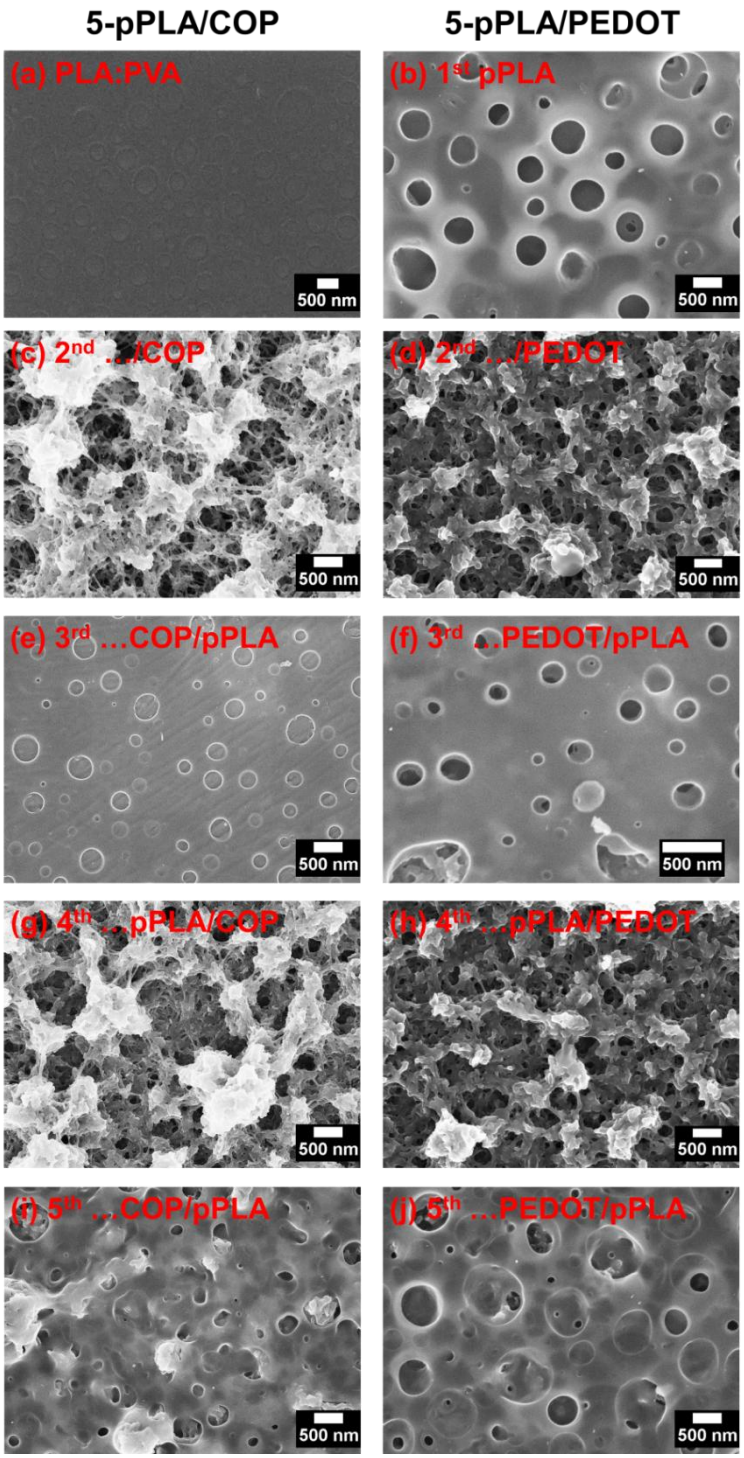

Figure 6.7: SEM images of the five layers involved in 5-pPLA/COP and 5-pPLA/PEDOT systems. (a) spin-coated 80:20 PLA:PVA layer. (b) 1st pPLA layer after elimination of PVA by water etching. (c) 2nd COP or (d) PEDOT layer electropolymerized onto the 1st pPLA layer. 3rd pPLA layer spin-coated onto the 2nd (e) COP or (f) PEDOT layer. 4th (g) COP or (h) PEDOT layer electropolymerized onto the 3rd pPLA layer. 5th pPLA layer spin-coated onto the 4th (i) COP or (j) PEDOT layer.

The electroactivity and electrostability of the two 5-layered membranes have been examined to confirm the efficiency of the oxidation-reduction processes when insulating PLA sheets separate the CP layers. Figure 6.8 compares the cyclic voltammograms recorded in PBS 0.1 M for free-standing 5-layered membranes. As expected, the electrochemical activity is lower for free-standing membranes than for CP films supported on steel substrate due to the presence of pPLA layers. The loss of electrochemical activity (LEA) after 25 consecutive redox cycles is lower for 5-pPLA/PEDOT than for 5-pPLA/COP (LEA = 1% and 17%, respectively). Additionally, the robustness and flexibility of the free-standing membranes were observed by the manipulation of the films. Then, Figure 6.9 shows digital camera images of a 5-pPLA/COP membrane, which was fabricated and detached. The sequence of images reveals that the free-standing films are not only manageable and robust but they are also very flexible. Figure 6.9 shows the aspiration process of a film, with an area of 0.5 cm^2, floating in water into a pipette with a tip diameter of 1.5 mm. Due to its outstanding flexibility, the 5-layered membrane does not obstruct the pipette tip but, instead is completely introduced and delivered from it without damage. After release into the solvent, the film slowly tends to recover its original shape. Then, the film can be dried for manipulation without damaging its structure. This process (*i.e.* aspiration, release, shape recovery and drying step) can be repeated at least five times without any damage to the membrane. The same behaviour was obtained for 5-pPLA/PEDOT films (not shown here).

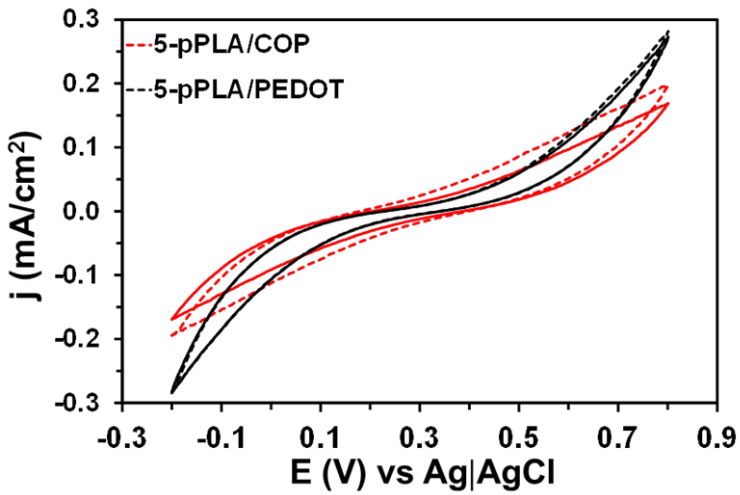

Figure 6.8: First control voltammogram (dashed lines) and voltammogram after 25 consecutive oxidation–reduction cycles (solid lines) in PBS 0.1 M for free-standing 5-pPLA/COP and 5-pPLA/PEDOT films.

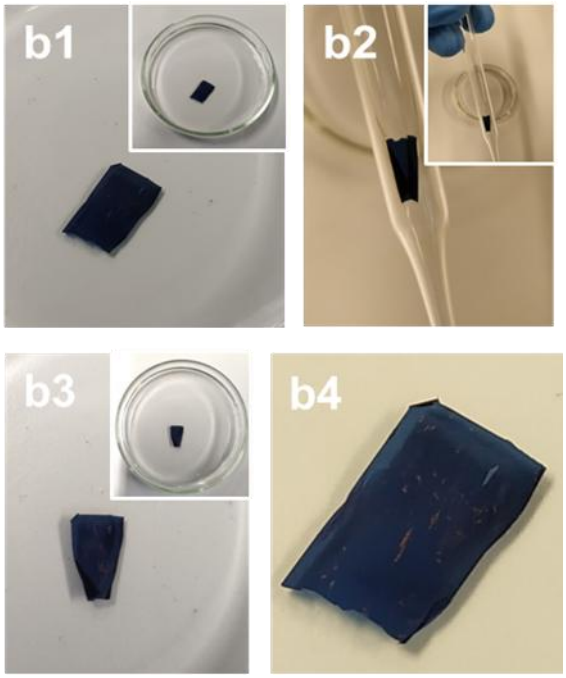

Figure 6.9: Digital camera images of a 5-pPLA/COP free-standing film immersed in water (b1); aspired film floating in water into a pipette (b2); aspect of the film while it recovers the shape once it has been released (b3); and dried film after having completely recovered the shape (b4).

Functionalization of 5-layered membranes with proteins

The VDAC36 porin was incorporated to free-standing 5-pPLA/COP and 5-pPLA/PEDOT by incubating for 12 hours the free-standing membranes in a 0.85 mg/mL protein solution with 60 mM SDS and 1.5 M MPD. After rinsing with milli-Q water, the successful immobilization of the protein on the membranes was examined by FTIR spectroscopy. The FTIR spectra of 5-pPLA/COP and 5-pPLA/PEDOT before and after functionalization are compared in Figure 6.10. Unfortunately, the bands associated to the amide I, which mainly corresponds to the C=O stretching) and side chain bands of charged amino residues (all them between 1600 and 1750 cm^{-1}) cannot be used for protein identification due to the overlapping with the bands associated to the aromatic thiophene ring (C=C and C–C stretching) of COP or PEDOT (Figure 6.3). However, the amide II band, which results from the N–H bending and the C–N stretching vibrations, and the amide III band which is a very complex band that comes from a mixture of several coordinate displacements (*i.e.* N–H in plane bending coupled with C–N stretching and, also C–H and N–H deformation vibrations) are clearly recognizable at 1517 and 1200-1300 cm^{-1}, respectively. Thus, the latter bands, which do not appear in the free-protein 5-pPLA/COP and 5-pPLA/PEDOT samples, are indicators of the VDAC36 presence onto the films.

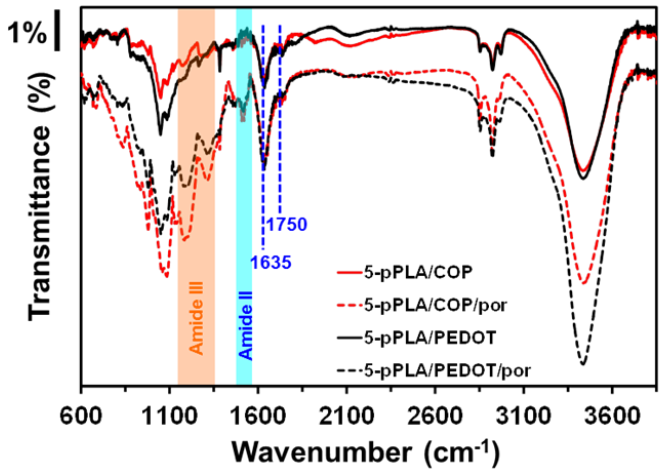

Figure 6.10: FTIR spectra of the 5-layered films before and after incorporation of the VDAC36 protein. The amide II and amide III protein bands are highlighted.

The chemical structure of functionalized 5-layered membranes was further characterized by XPS. Table 6.2 compares the surface atomic compositions of 5-pPLA/COP/VDAC and 5-pPLA/PEDOT/VDAC with those of the corresponding controls, which were prepared incubating the free-standing membranes in a 60 mM SDS and 1.5 M MPD solution without protein. Whilst the penetration of X-ray radiation is expected to be ~10 nm, here the penetration is unknown due to both the nanometric thickness of the layers and the filling of the perforations of the outer pPLA layers (see below). The N 1s detected in the composition of 5-pPLA/COP and 5-pPLA/PEDOT controls has been attributed to the usual N_2 contamination from air. However, the N 1s increases from 0.63-0.64% in the control samples to 0.89% and 0.85% in 5-pPLA/COP/VDAC and 5-pPLA/PEDOT/VDAC, respectively, supporting the successful integration of the VDAC36 onto the surface of the films.

Table 6.2: Atomic percent composition (C 1s, O 1s, S 2p and N 1s) obtained by XPS for control and functionalized 5-layered films.

Sample	C 1s (%)	O 1s (%)	S 2p (%)	N 1s (%)
5-pPLA/COP (control)	57.71	35.24	6.42	0.63
5-pPLA/COP/VDAC	69.66	22.30	7.48	0.89
5-pPLA/PEDOT (control)	66.05	27.27	6.05	0.64
5-pPLA/PEDOT/VDAC	63.30	30.03	5.62	0.85

Figure 6.11 displays the high-resolution XPS spectra in the S 2p region for functionalized and control films, which show the spin-split sulphur coupling S $2p_{3/2}$ and S $2p_{1/2}$ with a separation of 1.2 eV. The spectrum recorded for the 5-pPLA/COP control sample reveals two peaks, which transform into six (A-F) after deconvolution (3 for S $2p_{3/2}$ and 3 for S $2p_{1/2}$). The peak at 167.9 eV (after deconvolution A and B at 167.7 and 168.9 eV, respectively) corresponds to the $–SO_3^-$ of the SDS used in the incubation buffer. The second peak at 163.7 eV has been associated to the signals of the thiophene rings: the C–S–C bond (C and D at 163.2 and 164.4 eV, respectively) and its homologous with positively charged sulphur, $C–S^+–C$ (E and F at 164.2 and 165.4 eV, respectively) [29]. The same trends are observed in the spectrum obtained for the 5-pPLA/PEDOT control, the only difference with respect to 5-pPLA/COP being that the binding energies of the peaks from the experimental profile and from deconvolution decrease by ~1.1 eV. For both control films, the sulphur content at the surface originating from SDS was slightly higher than from the CP (Table 6.3).

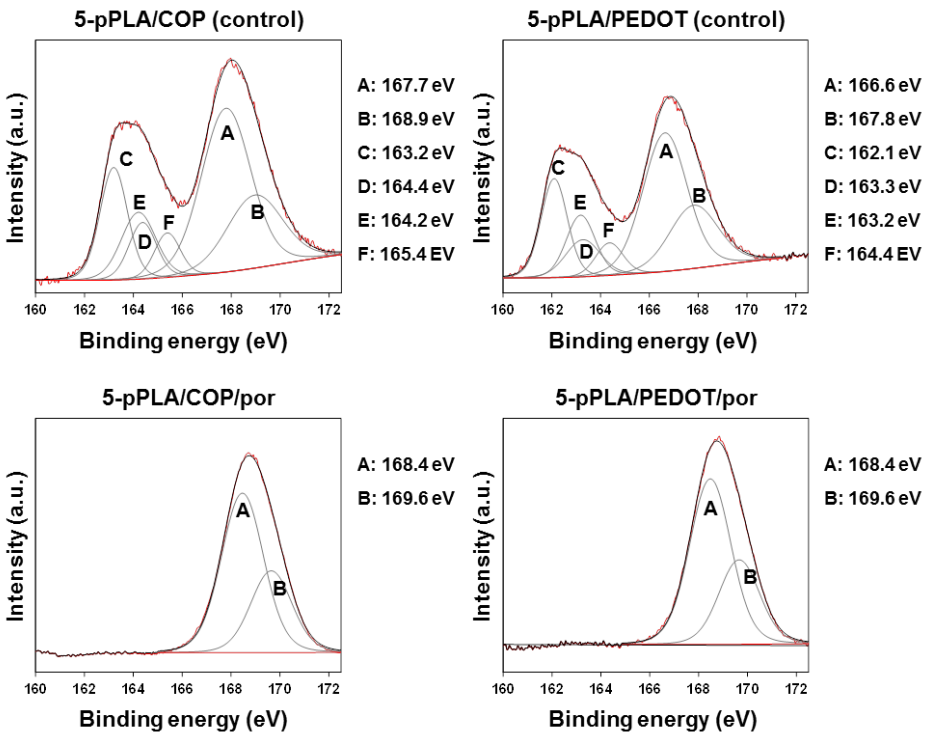

Figure 6.11: High-resolution XPS spectra in the S 2p region for 5-pPLA/COP and 5-pPLA/PEDOT control films (*i.e.* samples incubated in a 60 mM SDS and 1.5 M MPD aqueous solution without protein) and functionalized 5-pPLA/COP/VDAC and 5-pPLA/PEDOT/VDAC films (*i.e.* films incubated in a 60 mM SDS and 1.5 M MPD aqueous solution with 0.85 mg/mL VDAC36). The recorded spectrum is displayed in black, the curves coming from the deconvolution are shown in gray, and red lines correspond to the background and profile obtained by summing the curves from deconvolution.

Table 6.3: Distribution of the S 2p atomic percent composition as obtained by XPS for control and functionalized 5-layered films.

Sample	S 2p (%) 166.9 eV	S 2p (%) 162.4 eV
5-pPLA/COP (control)	59.92	40.08
5-pPLA/COP/VDAC	100	0
5-pPLA/PEDOT (control)	58.27	41.73
5-pPLA/PEDOT/VDAC	100	0

Interestingly, biofunctionalized 5-pPLA/COP/VDAC and 5-pPLA/PEDOT/VDAC films do not show the peak associated to the CP. Thus, the only detected peak, which appears at 168.8 eV, corresponds to the detergent of the solution used for the incubation of the protein. As shown in the SEM micrographs discussed above (Figure 6.7), the CP layers are accessible through the perforations in the outer pPLA layers before functionalization. Accordingly, the disappearance of the thiophene peak from the XPS spectra in the S 2p region indicates that the protein fills the perforations and adsorbs on the underlying CP layer, occulting the presence of COP or PEDOT. Although these results demonstrate the immobilization of VDAC36 inside the perforations, looking for the accessible CP chains, its adsorption onto the PLA at surface of the outer layers cannot be ruled out. However, it is well-known that the physical immobilization of proteins and protein aggregates on flat surfaces, as for example the spin-coated PLA, is more difficult than onto rough surfaces, as for example the electropolymerized CP [30].

In order to quantify the amount of VDAC36 retained by the films, the solutions containing the protein were analyzed by UV absorbance. More specifically, the absorbance at 280 nm was determined for the protein solution before and after films incubation, correction of the rinsing solutions being applied to the latter. The VDAC36 molar extinction coefficient, calculated by the ProtParam software, is 20400 $M^{-1}cm^{-1}$ [31]. The original concentration was 0.847 mg/mL. After incubation, the concentrations were 0.825 and 0.830 mg/mL for the 5-pPLA/COP and 5-pPLA/PEDOT, respectively. Accordingly, the quantity of protein retained by the 5-pPLA/COP/VDAC and 5-pPLA/PEDOT/VDAC films is 2.704 and 2.043 µg/cm², respectively. This result indicates that the protein retention increased by 32% when 3DT units were incorporated to the CP layers, demonstrating the importance of the lipid-like environment for the incorporation of the porins to artificial membranes.

EIS measurement of 5-pPLA/COP/VDAC biosensor

EIS measurements were performed to study the effectiveness of the protein activity on the ion transport across the bioactivated free-standing membranes. Both functionalized and control free-standing membranes were considered by using three different electrolyte solutions: 0.5 M NaCl, 0.5 M ATP and 0.1 M ATP. The 0.5 M NaCl solution was selected as the standard to assess the membrane resistance and for further comparison to the results from previous works involving biomimetic membranes made of polymers and porins. Instead, the ATP electrolyte was examined to take profit of the main VDAC function *in vivo*, which is the transport of this metabolite across the mitochondrial membranes. Accordingly, 5-pPLA/COP/VDAC and, especially, 5-pPLA/PEDOT/VDAC films are expected to behave as biosensors of relevant cellular compounds. The results were expressed as solution resistance (R_s), membrane resistance (R_M) and membrane capacitance, *i.e.* the capacitance of real systems (CPE, constant phase element), by using the simple Randles electrical circuit.

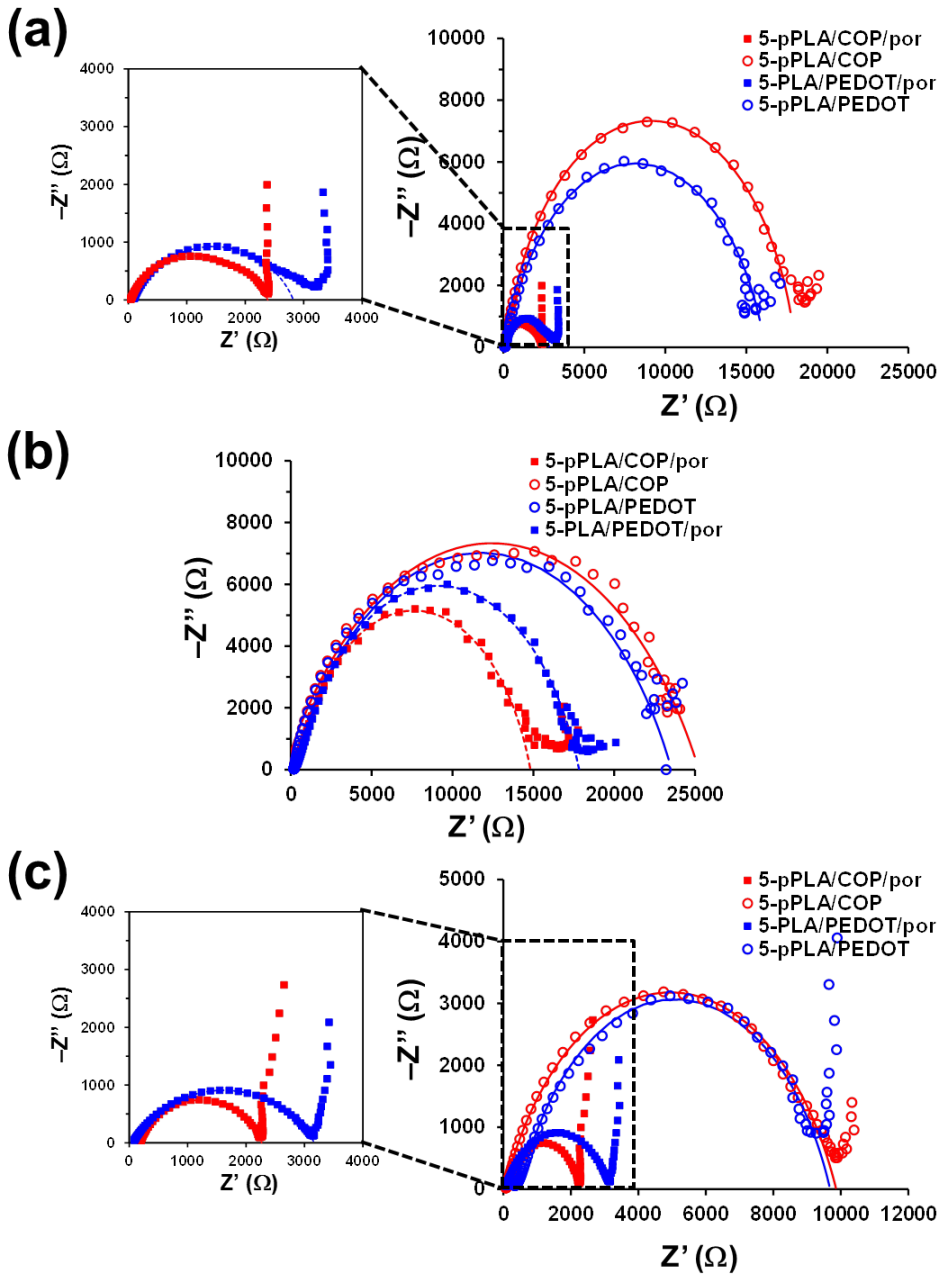

Figure 6.12: Nyquist plots for non-functionalized (control) and VDAC36-functionalized free-standing 5-layered membranes in (a) 0.5 M NaCl, (b) 0.5 M ATP and (c) 0.1 M ATP aqueous solutions.

Figure 6.12 displays the collected impedance (*Z*) data as a Nyquist plot for the three studied electrolyte solutions, while the corresponding Bode plots (both impedance and phase angle results) are provided in Figure 6.13. Nyquist plots for functionalized membranes show a low capacitive semicircle in the high-frequency range and a straight ascending vertical line (almost 90º to the real axis) in the low-frequency range. This vertical line, which can be described as a "*capacitive spike*", is consistent with a pure capacitor and reflect the diffusion of electrolytes. On the other hand, Nyquist plots for control 5-pPLA/COP and 5-pPLA/PEDOT membranes consist of a large semicircle (*i.e.* high capacitance), which extends from the high frequency to the low frequency range. The diameter of the semicircle, which is very sensitive to the microstructure of the membrane, is directly proportional to the membrane resistance. Accordingly, the results displayed in Figure 6.12 indicate that the incorporation of the VDAC36 protein inside the pores considerably increases the membrane conductivity. Besides, the Nyquist plots obtained for non-functionalized membranes in 0.5 M NaCl and 0.5 M ATP do not show any straight line ascending in the low frequency range indicating that diffusion is hindered in these systems.

The impedance of the Bode plot shows that, in all cases, the solution resistance dominates at high frequency, while the sum of the solution resistance and the membrane resistance predominates at low frequency. Accordingly, in the low frequency range, functionalized and control membranes show differences in the electrolyte–membrane interface. In the log |Z| vs log *f* plots (Figure 6.13), a shoulder between 10^2 and 10^4 appears for functionalized membranes, which corresponds to the parallel association of the membrane resistance and the membrane capacitance. Such a shoulder is associated to one time constant in the phase angle Bode plotn and it appears at lower log |Z| values for control membranes than for bioactivated membranes, reflecting the role of the porin in the diffusion of ions.

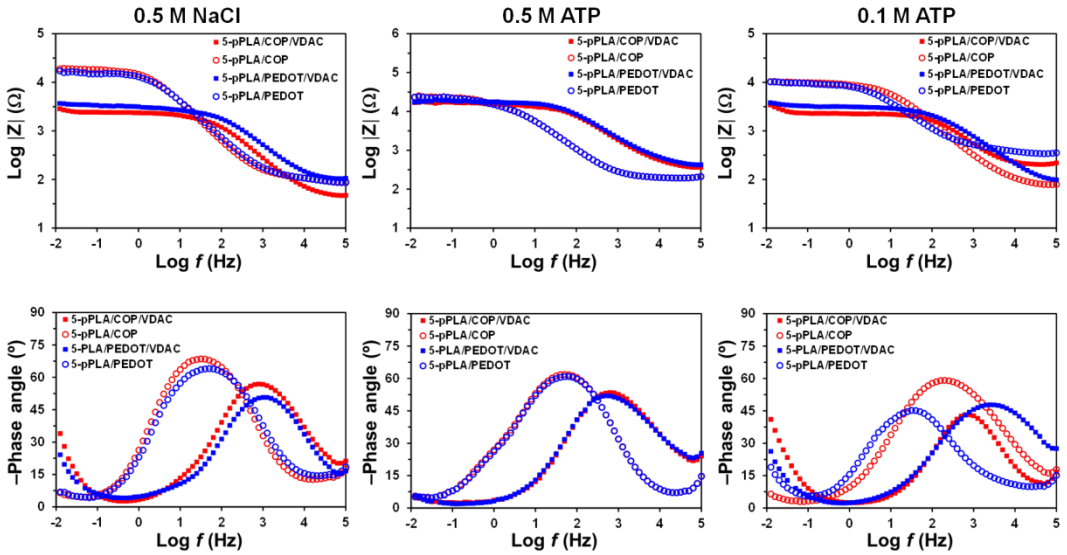

Figure 6.13: Bode plots for non-functionalized (control) and VDAC36-functionalized free-standing 5-layered membranes in 0.5 M NaCl, 0.5 M ATP and 0.1 M ATP aqueous solutions.

The noisy points that appear in the low frequency range of Nyquist plots, especially for 0.5 M ATP solution, has been associated to the free-standing nature of the membrane. This makes difficult the fitting of the experimental data to a proposed electric equivalent circuit (EEC) for explaining the whole EIS profiles. In order to overcome this drawback, the simplified Randles EEC (Figure 6.14) has been used to obtain the electrolyte resistance (R_s), the membrane resistance (R_M), which represents the ability of the membrane to impede ion transport at the interface, and the double layer capacitance (C_{dl}) in parallel with R_M, which can store only charge and ion movement. At high frequencies C_{dl} is close to 0 and the main contribution comes from R_s (*i.e.* the solution acts as an Ohmic resistor). Accordingly, the semicircles start at R_s (Figure 6.12). At high frequencies, C_{dl} has very high impedance values and all the current goes through R_M. Therefore, the impedance contribution at the point where the right end of the semi-circle intercepts the y-axis is $R_s + R_M$. C_{dl} has been modelled as a constant phase element (CPE), which represents the capacitance of real systems, as explained above). Thus, CPE represents the ability of the system to store charge, taking into account the contribution of all membrane components. In addition to the heterogeneity of the surface (*i.e.* roughness, porosity, reactivity), the CPE impedance (Z_{CPE}) is related to non-uniform diffusion across the interface. Mathematically, Z_{CPE} is expressed as $[Q(i\cdot\omega)^n]^{-1}$, where Q is the capacitance, i the imaginary number, ω the angular frequency, and n the exponent representing a pure capacitor ($n = 1$), a pure resistor ($n = 0$) or a diffusion process ($n = 0.5$) [32]. Both R_M and CPE are expected to include the contribution of the VDAC36-integrated protein for 5-pPLA/COP/VDAC and 5-pPLA/PEDOT/VDAC membranes.

The parameters obtained from the best fitting of the experimental data in the semicircle to the Randles EEC are listed in Table 6.4. The presence of COP in membranes slightly increases the resistance of non-functionalized membranes, as R_M is higher for 5-pPLA/COP than for 5-pPLA/PEDOT by 11%, 7% and 4% in 0.5 M NaCl, 0.5 M ATP and 0.1 M ATP, respectively. This has been attributed to differences in the electrical conductivity of the CP matrices (*i.e*. the electrical conductivity is lower for COP than for PEDOT). The low conductivity of poly(3-alkylthiophene) in comparison to PEDOT was previously studied, being attributed to the self-rigidification of the thiophene ring in the latter [33]. More specifically, in PEDOT the π-conjugation induced by the geometric restrictions imposed by the cyclic substituent and the electron-donating effects of the oxygen atoms produce a gain in aromaticity and favorable electrostatic interactions when planarity is reached. This gain is not achieved in poly(3-alkylthiophene), which reduces the aromaticity and the effective conduction pathways. On the other hand, the capacitive behavior of the non-functionalized films is very similar, independently of the CP used for the 2nd and 4th layer.

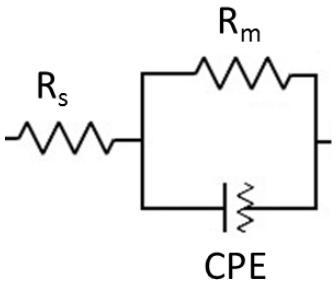

Figure 6.14: Randles electrical equivalent circuit (EEC) used to fit the experimental data in the semicircle of the Nyquist plots.

Table 6.4: Resistance of the electrolytic solution (Rs), resistance of the membrane (R_M) and constant phase element (CPE) with the exponent parameter *n* for the different functionalized and non-functionalized (control) free-standing 5-layered membranes. Data were obtained by fitting the semicircle of the Nyquist plots from EIS measurements to a simple Randles circuit. The percentages in parenthesis indicate the resistance reduction for the membranes with the same CP after incorporation of the protein.

Sample	R_s (Ω)	R_M (kΩ·cm²)	CPE (μF.s^n)	*n*
		NaCl (0.5 M)		
5-pPLA/COP/VDAC	102	2.36 (87%)	1.07	0.732
5-pPLA/COP	102	17.85	4.61	0.876
5-pPLA/PEDOT/VDAC	102	2.69 (83%)	0.53	0.768
5-pPLA/PEDOT	102	16.03	4.50	0.814
		ATP (0.5 M)		
5-pPLA/COP/VDAC	431	14.40 (43%)	0.12	0.790
5-pPLA/COP	431	25.12	5.00	0.689
5-pPLA/PEDOT/VDAC	431	17.40 (26%)	0.16	0.766
5-pPLA/PEDOT	431	23.52	4.64	0.679
		ATP (0.1 M)		
5-pPLA/COP/VDAC	202	2.07 (78%)	0.53	0.794
5-pPLA/COP	202	9.53	4.72	0.674
5-pPLA/PEDOT/VDAC	202	3.11 (66%)	0.35	0.751
5-pPLA/PEDOT	202	9.18	4.60	0.653

After the incorporation of the VDAC proteins, the diameter of the semi-circle decreases drastically. This reflects an enhanced flow of charges at the electrolyte–membrane interface, as well as an increment of current crossing the nanomaterial, both phenomena leading to a great reduction of R_M when compared to the protein-free systems. The membrane resistance decay increases with the conductivity of the electrolyte solution. Moreover, the initial hypothesis that the incorporation of 3DT units would help to retain a higher amount of protein and to keep it in its active form is fully supported by the EIS results. Indeed, the combination of COP and VDAC36 leads to a greater resistance reduction when combined with PEDOT.

Figure 6.15 compares the resistance of free-standing membranes studied in this work with that of supported membranes reported in literature, before and after functionalization with porins. In all cases, R_M was determined by EIS using NaCl as emectrolyte. The resistance of the free-standing 5-layered membranes functionalized with VDAC36 is slightly higher than previous obtained supported PNMPy/Omp2a [11] and pPLA/Omp2a [12] membranes (R_M =

0.6 and 0.3 kΩ·cm², respectively). The latter were made by immobilizing the pore-forming Omp2a protein over a PNMPy film electropolymerized onto a rigid steel electrode and over a pPLA film spin-coated onto an ITO substrate, respectively. The thickness of the PNMPy and pPLA films (~300 and 110 ± 7 nm, respectively) was reported to be similar to those of the CP and pPLA layers in the 5-layered membrane developed in this work. Hence, the higher resistance of the free-standing films has been essentially attributed to the fact that supported membranes do not suffer drawbacks associated to the manipulation of thin free-standing films, like the folds inducing local changes in the resistance. In order to confirm this assumption, the R_M of supported 5-pPLA/PEDOT/VDAC and 5-pPLA/PEDOT membranes were determined by EIS in 0.5 M NaCl solution. As shown in Figure 6.15, the measured resistance (R_M = 1.9 and 16.7 kΩ·cm²) was lower than those obtained for the corresponding free-standing films. This indicates that the self-supporting capacity only produces a small increment in the resistance.

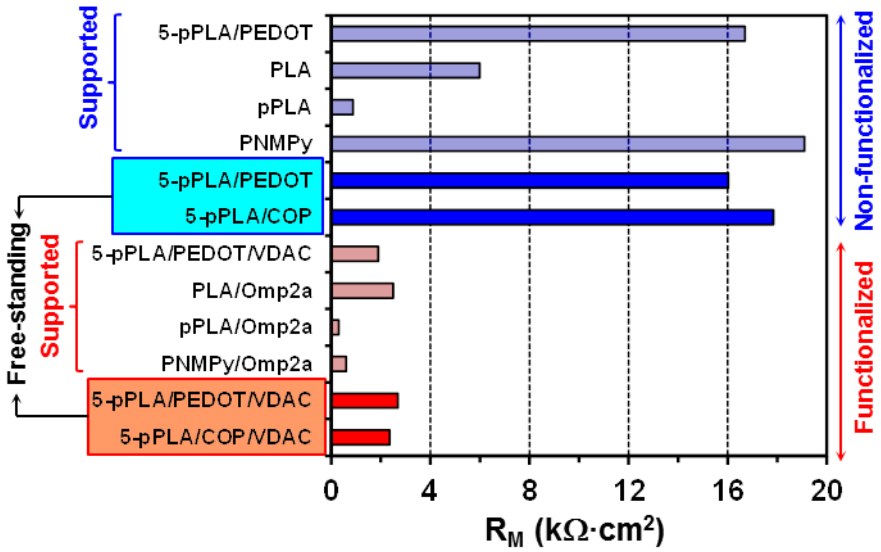

Figure 6.15: Comparison of the membrane resistance (R_M) values obtained in this work for free-standing 5-pPLA/COP/VDAC and 5-pPLA/PEDOT/VDAC, 5-pPLA/COP and 5-pPLA/PEDOT membranes with those obtained for supported functionalized and non-functionalized membranes. R_M values were determined by EIS using a 0.5 M NaCl electrolyte solution in all cases with exception of the supported PNMPy and PNMPy/Omp2a membranes, for which a 0.14 M NaCl electrolyte solution was used.

On the other hand, Table 6.4 shows that, independently of the electrolyte solutions, CPE decreases after the integration of VDAC36, indicating that protein-promoted ion diffusion causes a loss of capacitance. For the study in 0.5 M NaCl, the increasing contribution of the diffusion process is also reflected by the reduction of the *n* exponent (see Z_{CPE} expression). The opposite behavior is observed in the ATP solutions for which the *n* value is higher for

the functionalized membranes than for the control ones. This difference has been attributed not only to the ATP diffusion coefficient, which is much lower than that of Cl^- (3.10^{-6} and $2.03\ 10^{-5}$ cm^2/s for ATP and Cl^-, respectively) but also to the binding affinity of ATP with VDAC proteins [34–36].

Overall, results demonstrate that the VDAC36 protein was successfully integrated into the 5-layered 5-pPLA/COP membrane. The incorporated protein induced electrochemical changes in the behaviour of the membrane by retaining its function and promoting the diffusion of ions, especially of ATP. The results also suggest that hybrid 5-pPLA/COP/VDAC films behave as smart capacitive membranes fulfilling the free-standing and mechanical integrity requirements of many applications.

6.4. Conclusion

In the present study, a free-standing and conducting polymeric membrane with protein proteins immobilized has been developed and proved to be efficient for transport of ATP and NaCl, for the first time. The VDAC36 protein has been immobilized at the external layers of free-standing 5-pPLA/COP membranes. The retention of such protein has been found to be higher for COP- than for PEDOT-containing membranes, indicating that the dodecyl alkyl chains successfully mimic the lipophilic environment of cell membranes. The incorporation of the porin, which retains its function, has induced important electrochemical changes in the membrane resistance and capacitance, promoting the diffusion of ions, especially of ATP. In conclusion, the hybrid system obtained by combining synthetic polymers (CP and biodegradable PLA) and porin proteins is well-suited for the development of flexible biosensors with fully functional transmembrane ion channels. The new platform is free-standing and flexible, and can be applied in many biomedical technologies, opening new frontiers for the future development of high-throughput screening assays.

6.5. Bibliography

[1] Dennis M. Vriezema, Marta Comellas Aragonès, Johannes A. A. W. Elemans, Jeroen J. L. M. Cornelissen, and Alan E. Rowan, and R. J. M. Nolte*, "Self-Assembled Nanoreactors," 2005.

[2] J. R. Werber, C. O. Osuji, and M. Elimelech, "Materials for next-generation desalination and water purification membranes," *Nat. Rev. Mater.*, 1, 5, 16018, 2016.

[3] A. Puiggalí-Jou, L. J. del Valle, and C. Alemán, "Biomimetic hybrid membranes: incorporation of transport proteins/peptides into polymer supports," *Soft Matter*, 15, 13, 2722–2736, 2019.

[4] Y.-R. Kim, S. Jung, H. Ryu, Y.-E. Yoo, S. M. Kim, and T.-J. Jeon, "Synthetic biomimetic membranes and their sensor applications.," *Sensors (Basel).*, 12, 7, 9530–50, 2012.

[5] S. Mura, J. Nicolas, and P. Couvreur, "Stimuli-responsive nanocarriers for drug delivery," *Nat. Mater.*, 12, 11, 991–1003, 2013.

[6] R. Koebnik, K. P. Locher, and P. Van Gelder, "Structure and function of bacterial outer membrane proteins: barrels in a nutshell.," *Mol. Microbiol.*, 37, 2, 239–253, 2000.

[7] S. Galdiero, A. Falanga, M. Cantisani, R. Tarallo, M. Elena Della Pepa, V. D'Oriano, M. Galdiero, M. E. Della Pepa, V. D'Oriano, and M. Galdiero, "Microbe-Host Interactions: Structure and Role of Gram-Negative Bacterial Porins," *Curr. Protein Pept. Sci.*, 13, 8, 843–854, 2012.

[8] O. Ahumada, M. M. Pérez-Madrigal, J. Ramirez, D. Curcó, C. Esteves, A. Salvador-Matar, G. Luongo, E. Armelin, J. Puiggalí, and C. Alemán, "Sensitive thermal transitions of nanoscale polymer samples using the bimetallic effect: Application to ultra-thin polythiophene," *Rev. Sci. Instrum.*, 84, 5, 053904, 2013.

[9] J. H. Kleinschmidt, "Folding and Stability of Monomeric β-Barrel Membrane Proteins," in *Protein-Lipid Interactions*, Weinheim, FRG: Wiley-VCH Verlag GmbH & Co. KGaA, 2006, 27–56.

[10] M. Lopes-Rodrigues, A. Puiggalí-Jou, D. Martí-Balleste, L. J. del Valle, C. Michaux, E. A. Perpète, and C. Alemán, "Thermomechanical Response of a Representative Porin for Biomimetics," *ACS Omega*, 3, 7, 7856–7867, 2018.

[11] M. M. Pérez-Madrigal, L. J. del Valle, E. Armelin, C. Michaux, G. Roussel, E. A. Perpète, and C. Alemán, "Polypyrrole-Supported Membrane Proteins for Bio-Inspired Ion Channels," *ACS Appl. Mater. Interfaces*, 7, 3, 1632–1643, 2015.

[12] A. Puiggalí-Jou, M. M. Pérez-Madrigal, L. J. del Valle, E. Armelin, M. T. Casas, C. Michaux, E. A. Perpète, F. Estrany, and C. Alemán, "Confinement of a β-barrel protein in nanoperforated free-standing nanomembranes for ion transport," *Nanoscale*, 8, 38, 16922–16935, 2016.

[13] A. Puiggalí-Jou, J. Pawlowski, L. J. del Valle, C. Michaux, E. A. Perpète, S. Sek, and C. Alemán, "Properties of Omp2a-Based Supported Lipid Bilayers: Comparison with Polymeric Bioinspired Membranes," *ACS Omega*, 3, 8, 9003–9019, 2018.

[14] O. Bubnova, Z. U. Khan, H. Wang, S. Braun, D. R. Evans, *et al.*, "Semi-metallic polymers," *Nat. Mater.*, 13, 2, 190–194, 2014.

[15] L. V. Kayser and D. J. Lipomi, "Stretchable Conductive Polymers and Composites Based on PEDOT and PEDOT:PSS," *Adv. Mater.*, 31, 10, 1806133, 2019.

[16] L. D. Sappia, E. Piccinini, W. Marmisollé, N. Santilli, E. Maza, S. Moya, F. Battaglini, R. E. Madrid, and O. Azzaroni, "Integration of Biorecognition Elements on PEDOT Platforms through Supramolecular Interactions," *Adv. Mater. Interfaces*, 4, 17, 1700502, 2017.

[17] L. Groenendaal, F. Jonas, D. Freitag, H. Pielartzik, and J. R. Reynolds, "Poly(3,4-ethylenedioxythiophene) and Its Derivatives: Past, Present, and Future," *Adv. Mater.*, 12, 7, 481–494, 2000.

[18] D. Aradilla, F. Estrany, and C. Alemán, "Symmetric Supercapacitors Based on Multilayers

of Conducting Polymers," *J. Phys. Chem. C*, 115, 16, 8430–8438, 2011.
[19] B. W. Hoogenboom, K. Suda, A. Engel, and D. Fotiadis, "The Supramolecular Assemblies of Voltage-dependent Anion Channels in the Native Membrane," *J. Mol. Biol.*, 370, 2, 246–255, 2007.
[20] K. Zeth, "Structure and evolution of mitochondrial outer membrane proteins of β-barrel topology," *Biochim. Biophys. Acta - Bioenerg.*, 1797, 6–7, 1292–1299, 2010.
[21] T. Salinas, S. El Farouk-Ameqrane, E. Ubrig, C. Sauter, A.-M. M. Duchêne, and L. Maréchal-Drouard, "Molecular basis for the differential interaction of plant mitochondrial VDAC proteins with tRNAs," *Nucleic Acids Res.*, 42, 15, 9937–9948, 2014.
[22] S. Hiller, R. G. Garces, T. J. Malia, V. Y. Orekhov, M. Colombini, and G. Wagner, "Solution Structure of the Integral Human Membrane Protein VDAC-1 in Detergent Micelles," *Science (80-.).*, 321, 5893, 1206–1210, 2008.
[23] M. Colombini, "The VDAC channel: Molecular basis for selectivity," *Biochim. Biophys. Acta - Mol. Cell Res.*, 1863, 10, 2498–2502, 2016.
[24] L. D. L. Ferreira, H. Daniel, and R. Calado, "Electrochromic and spectroelectrochemical properties of polythiophene β -substituted with alkyl and alkoxy groups," 2017.
[25] R. Singhal, W. Takashima, K. Kaneto, and S. B. Samanta, "Langmuir – Blodgett films of poly (3-dodecyl thiophene) for application to glucose biosensor," 86, 42–48, 2002.
[26] J. Zhang, Z. Han, M. Chen, X. Yang, and W. Cao, "Synthesis and application in solar cell of poly(3-dodecylthiophene)/titanium dioxide nanocomposite," *J. Phys. Chem. Solids*, 71, 9, 1316–1323, 2010.
[27] N. Borras, F. Estrany, and C. Alemán, "Nanophase-segregation in the dielectric layer enhances the charge storage capacity of polymeric electrochemical supercapacitors," *Org. Electron.*, 51, 322–331, 2017.
[28] A. Puiggalí-Jou, J. Medina, L. J. del Valle, and C. Alemán, "Nanoperforations in poly(lactic acid) free-standing nanomembranes to promote interactions with cell filopodia," *Eur. Polym. J.*, 75, 552–564, 2016.
[29] J. Zhao, B. Guan, C. Ma, B. Hu, and H. Zhang, "Effect of elemental sulfur in precursors on the pore structure and surface chemical characteristics of high-surface area activated carbon," *J. Saudi Chem. Soc.*, 21, 6, 691–697, 2017.
[30] K. Rechendorff, M. B. Hovgaard, M. Foss, A. V. P. Zhdanov, and F. Besenbacher, "Enhancement of Protein Adsorption Induced by Surface Roughness," 2006.
[31] V. K. Garg, H. Avashthi, A. Tiwari, P. A. Jain, P. W. Ramkete, A. M. Kayastha, and V. K. Singh, "MFPPI - Multi FASTA ProtParam Interface.," *Bioinformation*, 12, 2, 74–77, 2016.
[32] P. Córdoba-Torres, "Relationship between constant-phase element (CPE) parameters and physical properties of films with a distributed resistivity," *Electrochim. Acta*, 225, 592–604, 2017.
[33] J. Poater, J. Casanovas, M. Solà, and C. Alemán, "Examining the Planarity of Poly(3,4-ethylenedioxythiophene): Consideration of Self-Rigidification, Electronic, and Geometric Effects," *J. Phys. Chem. A*, 114, 2, 1023–1028, 2010.
[34] T. Rostovtseva and M. Colombini, "VDAC channels mediate and gate the flow of ATP: implications for the regulation of mitochondrial function," *Biophys. J.*, 72, 5, 1954–1962, 1997.
[35] G. . Smith and M. S. . Sansom, "Effective diffusion coefficients of K+ and Cl− ions in ion channel models," *Biophys. Chem.*, 79, 2, 129–151, 1999.
[36] A. K. S. Camara, Y. Zhou, P.-C. Wen, E. Tajkhorshid, and W.-M. Kwok, "Mitochondrial VDAC1: A Key Gatekeeper as Potential Therapeutic Target.," *Front. Physiol.*, 8, 460, 2017.

7. Conclusion

7. Conclusion

Each part of the thesis contains its own specific conclusion related to the undergone studies. The present section that concludes the whole thesis shall summarize the goals achieved.

The first task was to further characterize the latest hybrid nanomaterial prepared by the IMEM laboratory. It was a nanofilm of perforated PLA loaded with the porin Omp2a. More precisely, the thermomechanical properties of the compounds (*i.e.* Omp2a and PLA) present in the material were investigated. For this purpose, we took advantage of the innovative SCALA device installed in our infrastructure. Using this method, silicon microcantilevers were coated with proteins or polymers. The thermal properties of the protein Omp2a were studied against temperature. Standard methods such as FTIR, CD and DLS were also performed to complement the SCALA measurement. The results demonstrated the high stability of β-barrel proteins up to 100°C as well as the aggregates rearrangement before loss of structural content in the protein. This work also established an efficient protocol for the future studies of biomolecules tethered to silicon substrates.

In the next study, the microcantilevers were covered with different types of nanomodified PLA films. The effect of nanopores and nanoperforations on the thermomechanical properties was investigated. The apparent glass transition and the cold crystallization temperature increased with the presence of such nanofeatures. After that, the films were loaded with two drugs: curcumin and stiripentol. Both form nanodomains composed of drug aggregates, consequently affecting the intermolecular interactions within the film. The effect on the glass transition temperature is function of the size and abundance of the nanodomains which is a promising result to modulate the properties of functional nanomaterials.

On the road to produce functional nanomaterials made of polymers and VDAC36, another pore-forming protein, the first step was to obtain large amounts of the biomolecule. For this, the transformation of competent bacteria that would produce the protein VDAC36 was accomplished. The procedure to obtain Omp2a was already known while the one for VDAC36 was established. The subsequent overexpression and affinity purification steps were successfully completed to obtain a sufficient amount of proteins for the following studies. The proteins were refolded by using the SDS-MPD developed in the CPB laboratory of the University of Namur.

Using spectroscopic methods, the VDAC36 secondary structure was determined and compared to a 3D model of the protein we have built. By addition of MPD to the SDS buffer, the protein recovered a β-barrel structure with a β-sheet content similar to the calculated value from the model. The

7. Conclusion

VDAC was characterized in different refolding solutions in order to select the optimal conditions to preserve the most the β-barrel structure. The formation of oligomers was investigated by cross-linking experiments, revealing the presence of dimers and tetramers. The latter showed instability against reducing agent, decomposing into dimers upon addition of β-mercaptoethanol. This result raised the hypothesis of a disulphide intermolecular bond, supported by a dimer theoretical model. Finally, VDAC36 was reconstituted into size-controlled liposomes made by extrusion and the size of the channel was determined to be 2.0-2.7 nm. The VDAC36 being fully described, and available in its active form, the next step focused on the development of the material that would contain the protein.

The stacking of PLA and PEDOT nanofilms was performed to take profit of the promising PEDOT electrochemical features and the mechanical integrity and robustness of PLA. The PLA layers were prepared by spin-coating and nanoperforation by solvent etching. It allowed the PEDOT to grow by electropolymerization and cover the entire surface of PLA. The new layer was then covered by a new layer of PLA with nanoperforations where the protein was integrated. The electron microscopy studies revealed the correct superposition of each layer. Fluorescence, FTIR and XPS evidenced the presence of VDAC36 in the material. EIS was performed to thoroughly describe the electrical properties of the new multi-layered material. The addition of VDAC36 into the material decreased the electrical resistance and enhanced the supercapacitive properties of the material. Moreover, the electrical equivalent circuit helped to evidence the ion diffusion process after integration of the protein.

The results of the 3-layered PLA/PEDOT membrane motivated us to consider some optimizations such as a higher robustness and higher content of retained protein. For the first goal, the membrane was extended from three to five layers by alternating PLA and PEDOT. For the latter, PEDOT was mixed with P3DT which contains a 12 carbon long alkyl chain instead of the ethylenedioxy group. Doing so, the monomer is mimicking the structure of the lipids present in the cell membrane. By providing a more suitable environment for the protein, it was expected to integrate more proteins in the material but also enhancing their activity. Both goals could be achieved and the response of the material in different electrolyte solutions was again monitored by EIS. The results were similar but more intense than the ones observed for the 3-layers material: a decrease in the resistance and an enhancement of the capacitive properties. Using biomolecules diffusing through the channel such as ATP, the electrical response given by the hybrid membrane differed according to the concentration of the electrolyte. Those promising results pave the way for the development of biosensing nanodevices.

7.1. Specific conclusions

2. Thermomechanical response of Omp2a

- Using CD and FTIR, the unfolding temperature of Omp2a was estimated to be 90°C.
- The effective diameter of Omp2a measured by DLS increased from 6.1 nm at 20°C to 12.6 nm at 60°C. This change was attributed to the formation of oligomers triggered by the rise of temperature.
- Contact angle as well as XPS measurements confirmed the linking of the proteins onto the silicon cantilevers.
- The SCALA equipment recorded the thermomechanical transitions of Omp2a. Four regimes were identified above 40°C. First, the interactions protein-substrate and protein-protein were slightly altered. Then, the proteins formed bigger aggregates and the latter were reorganized when the temperature continues increasing. Finally, above 105°C the protein was unfolded.

3. Effect of nanofeatures on the thermal transitions of PLA films

- Using SCALA, the glass transition temperature (T_g) for ultra-thin films of PLA and PVA were determined to be 51°C and 87°C, respectively.
- The T_g was affected by the presence of nanoperforations in the films. For 10 and 20% of perforations, the T_g were 58°C and 63°C, respectively. The changes were due to the additional interactions at the interface polymer-air.
- The T_g of PLA films loaded with 10% curcumin was measured at 60°C. With 20% of curcumin, T_g dropped to 48°C.
- The T_g of PLA films loaded with 10% stiripentol was measured at 61°C. With 20% of stiripentol, T_g dropped to 54°C.

4. Structural and functional characterization of VDAC36

- The VDAC36 protein was expressed in *E. coli*, purified by chromatography and the optimal refolding conditions (20 mM phosphate pH 8, 66 mM NaCl, 60 mM SDS and 1.5 M MPD) were determined by CD and intrinsic fluorescence.
- A 3D molecular model was built by threading to compare with the experimental results. The model presented a 64% of β-sheet content (vs 68% in the experimental data). In the model, the diameter of the pore was 1.56 nm and increased to 2.16 nm by removing the inner α-helix.

- Using cross-linkers, the VDAC36 was proved to form dimers and tetramers. The latter were not stable in presence of a reducing agent, suggesting the presence of an intermolecular disulphide bond.
- The presence of the disulphide bond could be supported by a modelling study.
- VDAC proteins were reconstituted into 150 nm diameter liposomes to perform swelling assays. Doing so, the diameter of the protein channel was determined to be comprised between 2.0 and 2.7 nm.
- Docking studies revealed the key residues able to bind ATP inside the pore: Lys-13, Arg-16, Asp-10, Arg-21 and Lys-28.

5. Biomimetic hybrid membranes made of PLA, PEDOT and VDAC36

- The membranes were self-standing with a thickness of 1.2 µm.
- The protein insertion into the film was verified by FTIR, fluorescence and XPS.
- The impedance measurements were useful to completely describe the electrical equivalent circuit of the membrane with the presence of resistances for the electrolyte solution and the membrane as well as constant phase elements (capacitance). A Warburg element was also present corresponding to the diffusion of water molecules.
- After integration of the protein, the resistance decreased from 21.9 to 3.9 kΩ. The capacitive behaviour of the membrane was also enhanced.
- A new element appeared in the equivalent circuit with the presence of VDAC36, evidencing the diffusion of ions.

6. Enhanced biomimetic membrane made of PLA, PEDOT-P3DT and VDAC36

- The 5-layered films were free-standing and showed good robustness and mechanical integrity allowing easy manipulation.
- The addition of 3DT in the conductive layers increased the thickness of the film from 741 to 998 nm.
- The surface of the conductive layer was smoother for the copolymer than the homopolymer and the wettability slightly increased.
- The presence of 3DT did not affect the electroactivity of the material but the amount of protein retained increased by 32% using the copolymer rather than the homopolymer.
- The protein immobilization was demonstrated by FTIR and XPS. It was shown that the proteins fill the nanoperforations present on the PLA surfaces.
- After addition of the protein, the resistance of the membrane was decreased by 87% in 0.5 M NaCl.
- In 0.5 M NaCl, the capacitive behaviour of the membrane was reduced due to the promoted ion diffusion process induced by the protein.
- The resistance of the material, after addition of VDAC36, was reduced by 43 and 78% in 0.5 and 0.1 M ATP.
- The ion diffusion process was less marked in ATP solutions due to the affinity of VDAC36 to interact with its natural substrate.